

SPIN-ORBIT COUPLING AND TIDAL DISSIPATION IN HOT JUPITER SYSTEMS

A Dissertation

Presented to the Faculty of the Graduate School

of Cornell University

in Partial Fulfillment of the Requirements for the Degree of

Doctor of Philosophy

by

Natalia Igorevna Shabaltas

August 2015

© 2015 Natalia Igorevna Shabaltas

ALL RIGHTS RESERVED

SPIN-ORBIT COUPLING AND TIDAL DISSIPATION IN HOT JUPITER
SYSTEMS

Natalia Igorevna Shabaltas, Ph.D.

Cornell University 2015

Hot Jupiters are giant planets located extremely close to their host stars, with orbital periods less than 5 days. Many aspects of hot Jupiter (HJ) formation remain unclear, but several clues, such as the observed misalignment between their orbital axes and their hosts' spin axes, point to a dynamical origin. In the first portion of this work we explore the stellar spin-orbit dynamics of one such dynamical formation channel, the Lidov-Kozai mechanism. We show that the coupling between the stellar spin and the planet orbit can lead to complex, and sometimes chaotic, behavior of the stellar spin vector. Many features of this behavior arise due to a set of resonances between the stellar spin axis precession timescale and the Lidov-Kozai timescale. Under the assumption that the stellar quadrupole does not induce precession in the planet's orbit, given a system with a set of initial parameters, we show that it is possible to predict whether the system can attain high spin-orbit misalignments. In the second portion of this work, we discuss tidal dissipation in giant planets, another aspect that is crucial to dynamical HJ formation theories. We show that tidal dissipation in the cores of giant planets can be significant, and can help reconcile inconsistencies in the tidal dissipation efficiencies inferred from observations of Jupiter's moons and from high-eccentricity HJ migration theories. Finally, we improve upon existing core tidal dissipation theories by presenting semi-analytical formulae for dissipation in a core surrounded by a polytropic $n = 1$ envelope.

BIOGRAPHICAL SKETCH

Natalia Igorevna Shabaltas (Storch) was born in 1987 in Novosibirsk, Russia. She was born on September 1, which in Russia is known as the Day of Knowledge, so nobody was particularly surprised that she loved school, and later wanted to become a scientist.

In the year 2000, Natalia and her parents moved to California, USA, eventually settling in sunny Santa Barbara. In 2005, Natalia entered the Creative Studies College at the University of California, Santa Barbara, as a physics major. There she met Isaac Storch, who would later become her husband.

In her junior year at university Natalia dabbled in experimental biophysics research under the direction of Professor Omar Saleh, but quickly decided that pipetting, and indeed, most aspects of experimental physics, were not for her. She then began her senior thesis work with Professor Omer Blaes, who first exposed her to the wonders of theoretical astrophysics research; there was no going back after that.

In 2009, Natalia and Isaac both entered Cornell University as graduate students in Physics. In 2010, Natalia began her research work with Professor Dong Lai, working first on neutron stars and later on exoplanets.

In 2012, Natalia married Isaac and took his last name. They remain happily married to date.

In her spare time, Natalia enjoys reading, writing haiku, watching her husband play video games, hanging out with cats (and occasionally people), and baking healthy desserts.

This 2015 thesis work marks the completion of Natalia's Ph.D. journey. She will begin work as a postdoctoral prize fellow at Caltech in September, 2015.

“So much universe, and so little time.”

—Sir Terry Pratchett (1948–2015)

ACKNOWLEDGEMENTS

First and foremost, I thank my advisor, Professor Dong Lai. Dong believed in me even when I didn't believe in myself. He was patient with me when I needed patience, and pushed me (just a little) when I needed to be pushed. He taught me what it means to be a scientist, the importance of asking questions, and perseverance in pursuing answers. Although I still have far to go in my quest toward being a successful scientist, Dong has helped lay a foundation that is sure to help me at every step of my journey.

I thank my coworker and collaborator, Kassandra Anderson, for helping bring our *Science* paper to life.

I thank the members of my Special Committee, Professors Saul Teukolsky and Ritchie Patterson, for their guidance and support through the years.

I thank my husband, Isaac Storch, who was going through his own Ph.D. journey at the same time as I was. I daresay we did a good job of supporting each other through it all. Isaac put up with having to buy takeout for dinner whenever I was too tired to cook, and tried his best to listen to my convoluted stories about the projects I was working on. He also helped me remember that, no matter how frustrated I might be with my projects, I still, on a basic level, enjoy doing and talking about science. I thank him for that.

I thank my parents, Igor and Inna Shabaltas, for never for a second doubting my ability to earn a Ph.D. Their unwavering certainty bolstered mine when mine was failing.

I thank my Dad for being the one that made our dream of moving to America a reality. Without him, this thesis work would not exist. I thank him also for playing World of Warcraft with me, which often gave me a much-needed reprieve from banging my head against astrophysics puzzles.

I thank my Mom for instilling in me an unquenchable desire to excel, and the drive to always do my best work. I thank her, also, for sending me many pictures of the family cat, Mitya, which cheered me up and got me through many a frustrating moment.

I thank my undergraduate advisor, Professor Omer Blaes, for first exposing me to the wonderful world of theoretical astrophysics, for suggesting I work with Dong, and for giving me much-needed advice when I began to doubt myself.

Finally, I thank my friends. Hannah Savage, for managing to support me despite being on the west coast. Ted Tao, for keeping in touch and telling me I can do it. Dave Tsang, for fun stories about working with Dong. My past and present Ithaca friends, Mike Bono, Daniel Citron, Jenni Drewes, Diwakar Gupta, Jesse Hopkins, Kathryn McGill, Christopher Monson, Veronica Pillar, Sam Posen, Everett Schlawin, and many others, for evenings spent talking and watching TV shows. I thank (Dr.) Mike Bono in particular for making my thesis writing process a breeze by providing a working, perfectly formatted LaTeX template.

TABLE OF CONTENTS

Biographical Sketch	iii
Dedication	iv
Acknowledgements	v
Table of Contents	vii
List of Figures	x
1 Introduction	1
2 Chaotic Dynamics of Stellar Spin in Binaries and the Production of Misaligned Hot Jupiters	4
2.1 Abstract	4
2.2 Introduction	4
2.3 Lidov-Kozai Cycles and Spin-Orbit Coupling	7
2.4 Numerical Exploration	9
2.5 Tidal dissipation and memory of chaotic evolution	14
2.6 Discussion	18
2.7 Acknowledgements	21
2.8 Supplementary Materials	21
2.8.1 Materials and Methods	21
2.8.2 Supplementary Figures	24
2.8.3 Toy Model	27
3 Chaotic Dynamics of Stellar Spin Driven by Planets Undergoing Lidov-Kozai Oscillations: Resonances and Origin of Chaos	34
3.1 Abstract	34
3.2 Introduction	35
3.3 Review of the Physical System and Ingredients	40
3.3.1 Lidov-Kozai (LK) Oscillations	40
3.3.2 Stellar spin precession	43
3.4 Hamiltonian Formulation of Spin Dynamics and Resonances	45
3.4.1 The Spin Hamiltonian	45
3.4.2 The Rescaled Hamiltonian	47
3.4.3 Fourier Decomposition and Resonances	48
3.5 Dynamics of a Single Resonance	51
3.6 Onset of Chaos: Two or More Resonances	58
3.7 Application to the Full Problem of Lidov-Kozai driven Spin Precession	60
3.8 Adiabatic Resonance Advection	66
3.9 Conclusion	72
3.10 Acknowledgments	73

4	Dynamics of Stellar Spin Driven by Planets Undergoing Lidov-Kozai Oscillations: Paths to Misalignment	75
4.1	Abstract	75
4.2	Introduction	76
4.3	LK-Driven Spin Dynamics: Review	77
4.3.1	Lidov-Kozai oscillations	77
4.3.2	Stellar Spin Precession	79
4.3.3	Hamiltonian Spin Dynamics	81
4.4	Effect of Short-Range Forces	85
4.5	Non-dissipative Regime Classification	90
4.5.1	Non-adiabatic Regime: $\bar{A} \lesssim 1$	90
4.5.2	Adiabatic Regime: $\bar{A} \gtrsim 1$	93
4.5.3	The initially-aligned trajectory	94
4.6	Inclusion of Tides: Paths to Misalignment	96
4.6.1	Varying the stellar spin period	97
4.6.2	Non-adiabatic behavior: bimodality	100
4.6.3	Stationary adiabatic behavior	103
4.6.4	Adiabatic advection	104
4.7	Predictive Power	107
4.8	Discussion and Conclusion	111
4.8.1	Complications due to feedback	111
4.8.2	Primordial misalignment	112
4.8.3	Summary of key findings	113
5	Viscoelastic Tidal Dissipation in Giant Planets and Formation of Hot Jupiters Through High-Eccentricity Migration	115
5.1	Abstract	115
5.2	Introduction	116
5.3	Evolution of Eccentric Systems with General Tidal Responses	120
5.4	Viscoelastic Dissipation in Giant Planets with Rocky Cores	124
5.4.1	Viscoelastic Solid Core	124
5.4.2	Application to a giant planet with a rocky core	126
5.4.3	The specific case of Jupiter	128
5.5	High-eccentricity migration of a giant planet with a rocky core	130
5.5.1	Orbital Evolution	130
5.5.2	Tidal heating of giant planets during migration	133
5.6	Conclusion	136
5.7	Acknowledgments	138
5.8	Appendix: Spin Equilibrium/Pseudosynchronization in Viscoelastic Tidal Models	138

6 Analytical Model of Tidal Distortion and Dissipation for a Giant Planet with a Viscoelastic Core	144
6.1 Abstract	144
6.2 Introduction	144
6.3 Setup and Schematic Solution	146
6.3.1 Equilibrium Structure	147
6.3.2 Tidal Perturbation	148
6.4 Analytical Love Number Formulae	150
6.4.1 Non-dissipative tide	150
6.4.2 Dissipative tide	151
6.5 Applications of Love Number Formulae	152
6.5.1 Non-dissipative elastic core	153
6.5.2 Dissipation of viscoelastic core	155
6.5.3 Comparison with planet models with uniform-density envelope	156
6.5.4 Application to Super-Earths	159
6.6 Conclusion	160
6.7 Acknowledgments	161
7 Conclusion	162
Bibliography	164

LIST OF FIGURES

2.1	Sample evolution curves for the “pure” Lidov-Kozai system, demonstrating how the stellar spin evolves through LK cycles	10
2.2	Sample surfaces of section demonstrating the presence or lack of chaos in the stellar spin evolution	12
2.3	Lyapunov analysis of spin dynamics with and without short-range forces	13
2.4	“Bifurcation” diagram of spin-orbit misalignment angle vs planet mass, including all short-range effects	15
2.5	Two “bifurcation” diagrams of the final spin-orbit misalignment angle (top) and semi-major axis (bottom) vs planet mass for a small range of initial planet-binary inclinations, including the effects of tidal dissipation and stellar spindown	18
2.6	Distribution of the final spin-orbit misalignment angles as a function of planet mass, including the effects of tidal dissipation and stellar spin down, for initial planet-binary inclinations θ_{lb}^0 in the range $85^\circ - 89^\circ$	19
2.7	Breakdown of parameter space into the three regimes of spin evolution	26
2.8	Orbital trajectories in $e - \omega$ phase space	27
2.9	Sample evolution curves for a trajectory in a periodic island of regime II	28
2.10	Sample orbital and spin evolution, including tidal dissipation and stellar spindown	29
2.11	Toy model angles θ_{sl} and θ_{sb} evaluated at maximum eccentricity .	31
2.12	Toy model angles θ_{sl} and θ_{sb} as functions of time	32
2.13	Toy model Lyapunov analysis	33
3.1	“Bifurcation” diagram of the spin-orbit misalignment angle versus planet mass and the adiabaticity parameter ϵ	38
3.2	Plots of the “shape” functions $\beta(\tau)$ (blue), $\gamma(\tau)$ (red), and $\psi(\tau)$ (brown)	46
3.3	Fourier coefficients as a function of the resonance number N	49
3.4	Sample constant-energy curves for the $N = 0$ single-resonance Hamiltonian	50
3.5	Comparison of the exact resonance locations and widths with simple analytical estimates	52
3.6	Sample separatrices for resonances of different N ’s	53
3.7	Surfaces of section for two different pairs of resonances	54
3.8	Surfaces of section for two pairs of resonances put together, with their respective analytically computed separatrices	56
3.9	Surfaces of section computed using the exact Hamiltonian (top panels) and using the approximate Hamiltonian(bottom panels)	56

3.10	Demonstration of how overlapping resonances can explain several features of the $\epsilon = 0.02$ surface of section	61
3.11	Outermost boundaries of the chaotic region as a function of ϵ	62
3.12	“Bifurcation” diagram of spin-orbit misalignment angle versus the adiabaticity parameter ϵ	63
3.13	Zoom in on Fig. 3.12 in the region $0.04 < \epsilon < 0.07$	66
3.14	Zoom in on Fig. 3.12 in the region $0.025 < \epsilon < 0.0286$	67
3.15	Demonstration of how the variation of resonances with ϵ leads to the peculiar oscillatory behavior seen in Fig. 3.14	68
3.16	Sample time evolution demonstrating non-chaotic drift of an initially aligned system toward higher misalignment angles	69
3.17	Proof of concept for “adiabatic resonance advection”	71
4.1	Shape functions β , γ , and ψ as a function of the rescaled time variable τ	87
4.2	N_{\max} as a function of initial inclination	88
4.3	Locations of several resonances, labeled on the right-hand side with their corresponding N , for the shape functions presented in Fig. 4.1	89
4.4	Sample separatrices in phase space for $M_p = 5M_J$, $\theta_{lb,0} = 89^\circ$ and, top to bottom, $P_* = 50, 25, 20, 3$, and 1.7 days.	91
4.5	Maximum widths of each of the sample separatrices presented in Fig. 4.4 as a function of stellar spin period for $\theta_{lb,0} = 89^\circ$, $M_p = 5M_J$	95
4.6	Final spin-orbit misalignments after tidal dissipation, as a function of stellar spin period, for $M_p = 5M_J$, $\theta_{lb,0} = 89^\circ$, $a_0 = 1.5$ AU, $a_b = 300$ AU.	98
4.7	Sample evolution trajectories, including tidal dissipation, for $\theta_{lb,0} = 89^\circ$, $M_p = 5M_J$ and three different values of the stellar spin period.	99
4.8	Demonstration of the process that gives rise to the bimodality found in the non-adiabatic regime of Fig. 4.6.	101
4.9	Demonstration of the process of adiabatic advection by an $N = -2$ resonance.	105
4.10	Demonstration of the process of adiabatic advection by an $N = -1$ (top) and an $N = -3$ (bottom) resonance.	106
4.11	Final spin-orbit misalignment angle as a function of initial inclination $\theta_{lb,0}$, for two different planet masses and two stellar spin periods.	108
4.12	Compilation of the outcomes of a suite of time evolutions with variable initial conditions, plotted in $N_{\max,0}$ vs \bar{A}_0 space	110
5.1	Theoretical curves for the tidal Love number of a Jupiter-mass planet as a function of the tidal forcing frequency	129

5.2	Ratio of the pseudosynchronized spin frequency Ω_{ps} to the pericenter frequency Ω_{peri} for each of the viscoelastic models of Figure 5.1	131
5.3	Ratio of the orbital decay rate \dot{a} for different viscoelastic tidal dissipation models and \dot{a}_{weak} for the weak friction theory as a function of eccentricity	132
5.4	Eccentricity as a function of time, for an initial eccentricity of 0.9945 and a final mean motion period of 5 days	132
5.5	Core luminosity due to viscoelastic tidal dissipation in a Jupiter-mass gas giant; Evolution of radius vs time for each of the models (top), assuming an initial eccentricity of 0.9945 and a final circularized orbital period of 5 days.	135
5.6	Theoretical curves for the tidal Love number of a Jupiter-mass planet as a function of the tidal forcing frequency	139
5.7	Tidal torque on the planet as a function of the spin frequency for different values of eccentricity and different tidal dissipation models.	141
5.8	Tidal torque on the planet as a function of the ratio of spin frequency to pericenter frequency for $e = 0.8$ and different tidal dissipation models.	142
6.1	Sample tidal Love numbers h_{2c} (top) and k_2 (bottom) for a gas giant with mass M_J , radius R_J , and core density $\rho_c = 6 \text{ g cm}^{-3}$. .	154
6.2	Sample tidal Love numbers h_{2c} (top) and k_2 (bottom) for a gas giant with mass M_J , radius R_J , and core mass $M_c = 5M_\oplus$	155
6.3	Sample tidal dissipation rates for a gas giant with mass M_J , radius R_J with an $n = 1$ envelope	157
6.4	Comparison of tidal response curves for a gas giant with mass M_J , radius R_J with an $n = 1$ envelope vs $n = 0$ envelope	158
6.5	Tidal response for a super-Earth analogue similar to Kepler-11d, assuming an $n = 1$ envelope.	159

CHAPTER 1

INTRODUCTION

The discovery that as many as 1% of solar-type stars host giant Jupiter-sized planets with periods of only 1 – 5 days (Udry and Santos, 2007) has in many ways revolutionized our understanding of planetary system formation processes. In fact, these “hot Jupiters” (HJs) were the first indication of just how *little* we understand about planet formation. Before their discovery, when the Solar System was our only example of a planetary system, it was thought that planet formation – or, at least, what kinds of planets form where – was fairly clear-cut, with rocky planets close to the Sun (inside the snow line, the distance beyond which water and other volatiles can condense into solid form), and gas and ice giants outside the snow line. The discovery of HJs turned all of that on its head and has led to a wealth of interesting and innovative theoretical work.

The extreme proximity of HJs to their host stars is not their only peculiar feature. While many HJs reside on circular orbits, a non-negligible fraction of them have orbital eccentricities in excess of 0.1, with some as high as 0.4 (Udry and Santos, 2007). Furthermore, many HJs have been found to have orbital axes that are misaligned relative to the spin axes of their host stars (Albrecht et al., 2012; Hébrard et al., 2008, 2010; Narita et al., 2009; Triaud et al., 2010; Winn et al., 2009). Though several potential ways of generating primordial spin-orbit misalignment (Bate et al., 2010; Batygin, 2012; Batygin and Adams, 2013; Lai, 2014; Lai et al., 2011; Spalding and Batygin, 2014) and eccentricity (Tsang et al., 2014) have now been proposed, these observations generally point to a dynamical origin for these enigmatic planets.

Any dynamical process thought to be responsible for creating hot Jupiters

typically consists of several steps. First, a giant planet (a proto-HJ) forms at a few AU's distance from their host star, just like the giant planets in our Solar System. Second, a dynamical interaction throws the proto-HJ into a highly eccentric orbit. Potential such interactions include planet-planet interactions or scattering (Chatterjee et al., 2008; Ford and Rasio, 2008; Jurić and Tremaine, 2008; Petrovich, 2015*a*; Rasio and Ford, 1996; Weidenschilling and Marzari, 1996; Zhou et al., 2007), secular chaos (Wu and Lithwick, 2011), and the Lidov-Kozai effect induced by a distant companion (Correia et al., 2011; Fabrycky and Tremaine, 2007; Naoz et al., 2012; Petrovich, 2015*b*; Storch et al., 2014; Wu and Murray, 2003). After the proto-HJ has been thrown into an eccentric orbit, tidal dissipation in its interior at periastron acts to remove energy from its orbit and bring the planet closer and closer to its host.

This thesis work focuses on one particular method of eccentricity excitation: the Lidov-Kozai mechanism [also erroneously known as Kozai, or Kozai-Lidov; Kozai (1962); Lidov (1962)] induced by a distant stellar companion. This mechanism, described in detail in chapters 2 and 3, provides a natural and generally robust means of generating spin-orbit misalignment. However, the process of generating misalignment is far from trivial, due to complications arising from coupling between the planet orbital angular momentum vector and the stellar spin vector. The dynamics arising from this coupling are the focus of chapters 2, 3, and 4 of this work.

The tidal dissipation step of HJ formation is also not trivial. It has long been known that the tidal dissipation efficiency of our own Jupiter, obtained typically by considering the present positions of the Galilean moons (Goldreich and Soter, 1966; Yoder and Peale, 1981), and more recently by fitting to direct astro-

metric measurements of their movement (Lainey et al., 2009), cannot be easily explained by the simple turbulent viscosity in Jupiter’s fluid envelope (Goldreich and Nicholson, 1977). Furthermore, in context of the standard formalism for tidal dissipation, the so-called weak friction theory (Alexander, 1973; Eggleton et al., 1998; Hut, 1981), the constraints placed on Jupiter’s tidal dissipation are incompatible with constraints placed on the dissipation in HJs based on the maximum lifetimes of their host stars. Chapters 5 and 6 of this work present one means of alleviating both of these issues by considering dissipation that happens in the (hypothetically present) solid core of the giant planet, rather than in its envelope.

Recently, it has been suggested that there may not be a universal channel through which HJs are formed (Dawson and Murray-Clay, 2013; Dong et al., 2014; Knutson et al., 2014). Although as many as 50% of stars hosting hot Jupiters may have stellar companions (Knutson et al., 2014), the distributions of HJ semi-major axes obtained from simulations of the Lidov-Kozai mechanism are not currently compatible with the observed distribution. Nevertheless, simulations point to the Lidov-Kozai mechanism being robust enough that at least a *sub*-population of HJs could potentially be formed through it. Unfortunately, the current numbers of known HJs are not high enough to be able to identify different sub-populations. Nevertheless, because HJs make prime targets for ground-based radial velocity surveys, more and more of them should be discovered in the coming years, and our statistics will slowly but surely improve. If/when the Lidov-Kozai sub-population of HJs is discovered, one hopes that the work presented herein will be at least a little useful in characterizing it.

CHAPTER 2

CHAOTIC DYNAMICS OF STELLAR SPIN IN BINARIES AND THE PRODUCTION OF MISALIGNED HOT JUPITERS

2.1 Abstract

Many exoplanetary systems containing hot Jupiters are observed to have highly misaligned orbital axes relative to the stellar spin axes. Lidov-Kozai oscillations of orbital eccentricity/inclination induced by a binary companion, in conjunction with tidal dissipation, is a major channel for the production of hot Jupiters. We demonstrate that gravitational interaction between the planet and its oblate host star can lead to chaotic evolution of the stellar spin axis during Lidov-Kozai cycles. As parameters such as the planet mass and stellar rotation period vary, periodic islands can appear in an ocean of chaos, in a manner reminiscent of other dynamical systems. In the presence of tidal dissipation, the complex spin evolution can leave an imprint on the final spin-orbit misalignment angles.

2.2 Introduction

About 1% of solar-type stars host giant planets with periods of ~ 3 days (Udry and Santos, 2007). These “hot Jupiters” could not have formed *in situ*, given the large stellar tidal gravity and radiation fields close to their host stars. Instead, they are thought to have formed beyond a few astronomical units (AU)

The contents of this chapter are adapted from an article published in *Science* magazine as "Chaotic Dynamics of Stellar Spin in Binaries and the Production of Misaligned Hot Jupiters" (Storch et al., 2014)

and migrated inward. However, the physical mechanisms of the migration remain unclear. In the last few years, high stellar obliquities have been observed in many hot Jupiter systems, i.e., the spin axis of the host star and the planetary orbital angular momentum axis are misaligned (Albrecht et al., 2012; Hébrard et al., 2008, 2010; Narita et al., 2009; Triaud et al., 2010; Winn et al., 2009). Planet migration in protoplanetary disks (Goldreich and Tremaine, 1980; Lin et al., 1996) is usually expected to produce aligned orbital and spin axes [however, see Bate et al. (2010); Batygin (2012); Batygin and Adams (2013); Lai (2014); Lai et al. (2011)], so the observed misalignment suggests that other formation channels may be required, such as strong planet-planet scatterings (Ford and Rasio, 2008; Jurić and Tremaine, 2008), secular interactions/chaos between multiple planets (Nagasawa et al., 2008; Wu and Lithwick, 2011), and the Lidov-Kozai (LK) effect induced by a distant companion (Correia et al., 2011; Fabrycky and Tremaine, 2007; Naoz et al., 2012; Wu and Murray, 2003). Other observations suggest that multiple formation channels of hot Jupiters may be required (Dawson and Murray-Clay, 2013; Dong et al., 2014; Knutson et al., 2014).

In the “LK+tide” scenario, a giant planet initially orbits its host star at a few AU and experiences secular gravitational perturbations from a distant companion (a star or planet). When the companion’s orbit is sufficiently inclined relative to the planetary orbit, the planet’s eccentricity undergoes excursions to large values, while the orbital axis precesses with varying inclination. At periastron, tidal dissipation in the planet reduces the orbital energy, leading to inward migration and circularization of the planet’s orbit.

As the planet approaches the star in an LK cycle, the planet-star interaction torque due to the rotation-induced stellar quadrupole makes the stellar spin and

the planetary angular momentum axes precess around each other. Although the equations for such precession in the context of triple systems are known (Correia et al., 2011; Eggleton and Kiseleva-Eggleton, 2001), previous works on the “LK+tide” migration either neglected such spin-orbit coupling or included it without systematically examining the spin dynamics or exploring its consequences for various relevant parameter regimes (Correia et al., 2011; Fabrycky and Tremaine, 2007; Lithwick and Wu, 2014; Naoz et al., 2012; Wu and Murray, 2003). However, the stellar spin has the potential to undergo rich evolution during the Lidov-Kozai migration, which may leave its traces in the spin-orbit misalignments in hot Jupiter systems. Indeed, there are several examples of chaotic spin-orbit resonances in the Solar system. For instance, Saturn’s satellite Hyperion experiences chaotic spin evolution due to resonances between spin and orbital precession periods (Wisdom et al., 1984). The rotation axis of Mars undergoes chaotic variation as well, as a result of resonances between the spin precession and a combination of orbital precession frequencies (Laskar and Robutel, 1993; Touma and Wisdom, 1993).

We demonstrate here that gravitational interaction between the stellar spin and the planetary orbit can indeed induce a variety of dynamical behavior for the stellar spin evolution during LK cycles, including strongly chaotic behavior (with Lyapunov times as short as a few Myr) and perfectly regular behavior in which the stellar spin stays aligned with the orbital axis at all times. We show that in the presence of tidal dissipation the memory of chaotic spin evolution can be preserved, leaving an imprint on the final spin-orbit misalignment angles.

2.3 Lidov-Kozai Cycles and Spin-Orbit Coupling

We consider a planet of mass M_p initially in a nearly circular orbit around a star of mass M_* at a semi-major axis a , with a distant binary companion of mass M_b , semi-major axis a_b and eccentricity e_b , which we set to 0. In that case, if the planet's initial orbital inclination relative to the binary axis, denoted by θ_{lb}^0 , falls within the range $\{40^\circ, 140^\circ\}$, the distant companion induces cyclic variations in planetary orbit inclination and eccentricity, with a maximum eccentricity of $e_{\max} \simeq \sqrt{1 - (5/3) \cos^2 \theta_{lb}^0}$ (Kozai, 1962; Lidov, 1962). These LK cycles occur at a characteristic rate given by

$$\begin{aligned} t_k^{-1} &= n \left(\frac{M_b}{M_*} \right) \left(\frac{a}{a_b} \right)^3 \\ &= \left(\frac{2\pi}{10^6 \text{yr}} \right) \left(\frac{M_b}{M_*} \right) \left(\frac{M_*}{M_\odot} \right)^{1/2} \left(\frac{a}{1 \text{AU}} \right)^{3/2} \left(\frac{a_b}{100 \text{AU}} \right)^{-3}, \end{aligned} \quad (2.1)$$

where $n = 2\pi/P$ is the mean motion of the planet (P is the orbital period). Note, however, that the presence of short-range forces, such as General Relativity and tidal distortions, tend to reduce the maximum attainable eccentricity, so that the actual e_{\max} may be smaller than the “pure” (i.e. without short-range forces) LK value given above (Fabrycky and Tremaine, 2007; Holman et al., 1997; Wu and Murray, 2003). Along with the eccentricity and inclination variations, the planet orbital angular momentum vector precesses around the binary axis ($\hat{\mathbf{L}}_b$) at an approximate rate which, in the absence of tidal dissipation, is given by (Sec. 2.8.1)

$$\Omega_{pl} \approx \frac{3}{4} t_k^{-1} \cos \theta_{lb}^0 \sqrt{1 - e_0^2} \left[1 - 2 \left(\frac{1 - e_0^2}{1 - e^2} \right) \frac{\sin^2 \theta_{lb}^0}{\sin^2 \theta_{lb}} \right], \quad (2.2)$$

where e_0 is the initial eccentricity. Because of the rotation-induced stellar quadrupole, the planet induces precession in the stellar spin orientation, gov-

erned by the equation

$$\frac{d\hat{\mathbf{S}}}{dt} = \Omega_{ps}\hat{\mathbf{L}} \times \hat{\mathbf{S}}. \quad (2.3)$$

Here $\hat{\mathbf{S}}$ and $\hat{\mathbf{L}}$ are unit vectors along the stellar spin and planet orbital angular momentum axes, respectively, and the precession frequency Ω_{ps} is given by

$$\begin{aligned} \Omega_{ps} &= -\frac{3GM_p(I_3 - I_1)}{2a^3(1 - e^2)^{3/2}} \frac{\cos\theta_{sl}}{S} \\ &= -2.38 \times 10^{-8} \left(\frac{2\pi}{\text{yr}}\right) \frac{1}{(1 - e^2)^{3/2}} \left(\frac{2k_q}{k_*}\right) \left(\frac{10^3 M_p}{M_*}\right) \left(\frac{M_*}{M_\odot}\right)^{1/2} \times \\ &\quad \times \left(\frac{\hat{\Omega}_*}{0.1}\right) \left(\frac{a}{1\text{AU}}\right)^{-3} \left(\frac{R_*}{R_\odot}\right)^{3/2} \cos\theta_{sl}, \end{aligned} \quad (2.4)$$

where I_3 and I_1 are principal moments of inertia of the star, S is its spin angular momentum, $\hat{\Omega}_* \equiv \Omega_* / \sqrt{GM_*/R_*^3}$ is its spin frequency in units of the breakup frequency, R_* is the stellar radius, θ_{sl} is the angle between the stellar spin and planet angular momentum axes, and we have used $(I_3 - I_1) \equiv k_q M_* R_*^2 \hat{\Omega}_*^2$ and $S \equiv k_* M_* R_*^2 \Omega_*$. For a solar-type star, $k_q \approx 0.05$, and $k_* \approx 0.1$ (Claret and Gimenez, 1992). The stellar quadrupole also affects the planet's orbit, by introducing additional periastron advance, at a rate of order $-\Omega_{ps} S / (L \cos\theta_{sl})$ (where $L \equiv M_p \sqrt{GM_* a(1 - e^2)}$ is the orbital angular momentum), and making $\hat{\mathbf{L}}$ precess around $\hat{\mathbf{S}}$ at the rate $(S/L)\Omega_{ps}$ (Sec. 2.8.1).

During the LK cycle, orbital eccentricity varies widely from 0 to e_{\max} , and thus Ω_{ps} and Ω_{pl} change from $\Omega_{ps,0}$ and $\Omega_{pl,0}$ to $\Omega_{ps,\max}$ and $\Omega_{pl,\max}$, respectively. However, Ω_{ps} is more sensitive to eccentricity variation than Ω_{pl} , and attains a larger range of values. We therefore expect three qualitatively different regimes for the spin evolution.

Regime I, $|\Omega_{ps,\max}| \lesssim |\Omega_{pl,\max}|$ (“nonadiabatic”): $|\Omega_{ps}|$ is always smaller than $|\Omega_{pl}|$. We expect $\hat{\mathbf{S}}$ to effectively precess around $\hat{\mathbf{L}}_b$, the binary angular momentum axis (about which $\hat{\mathbf{L}}$ is precessing), maintaining an approximately constant

angle θ_{sb} .

Regime II, $|\Omega_{\text{ps},\text{max}}| \gtrsim |\Omega_{\text{pl},\text{max}}|$ and $|\Omega_{\text{ps},0}| \lesssim |\Omega_{\text{pl},0}|$ (“transadiabatic”): A secular resonance occurs when the stellar precession rate approximately matches the orbital precession rate ($|\Omega_{\text{ps}}| \approx |\Omega_{\text{pl}}|$). As the eccentricity varies from 0 to e_{max} during the LK cycle, the system transitions from nonadiabatic to adiabatic. We expect this resonance crossing to lead to complex and potentially chaotic spin evolution.

Regime III, $|\Omega_{\text{ps},0}| \gtrsim |\Omega_{\text{pl},0}|$ (“adiabatic”): $|\Omega_{\text{ps}}|$ is always larger than $|\Omega_{\text{pl}}|$. We expect the spin axis to follow $\hat{\mathbf{L}}$ adiabatically, maintaining an approximately constant spin-orbit misalignment angle θ_{sl} .

For a given planet semi-major axis a and binary semi-major axis a_b , the division between different regimes depends on the product of planet mass and stellar spin (Fig. 2.7). In particular, systems with low M_p and Ω_* lie in Regime I, while those with large M_p and Ω_* lie in Regimes II and III.

2.4 Numerical Exploration

We first study the evolution of stellar spin in “pure” LK cycles: we integrate Eq. (2.3) together with the evolution equations for the planet’s orbital elements, driven by the quadrupole potential from the binary companion (Sec. 2.8.1), but excluding all short-range forces. Although at the octupole level the companion may induce chaotic behavior in the planet orbit (Ford et al., 2000; Katz et al., 2011; Naoz et al., 2011, 2013), the effect is negligible if $a e_b / [a_b(1 - e_b^2)] \ll 0.01$ and is completely suppressed for $e_b = 0$. To isolate the dynamics of stellar

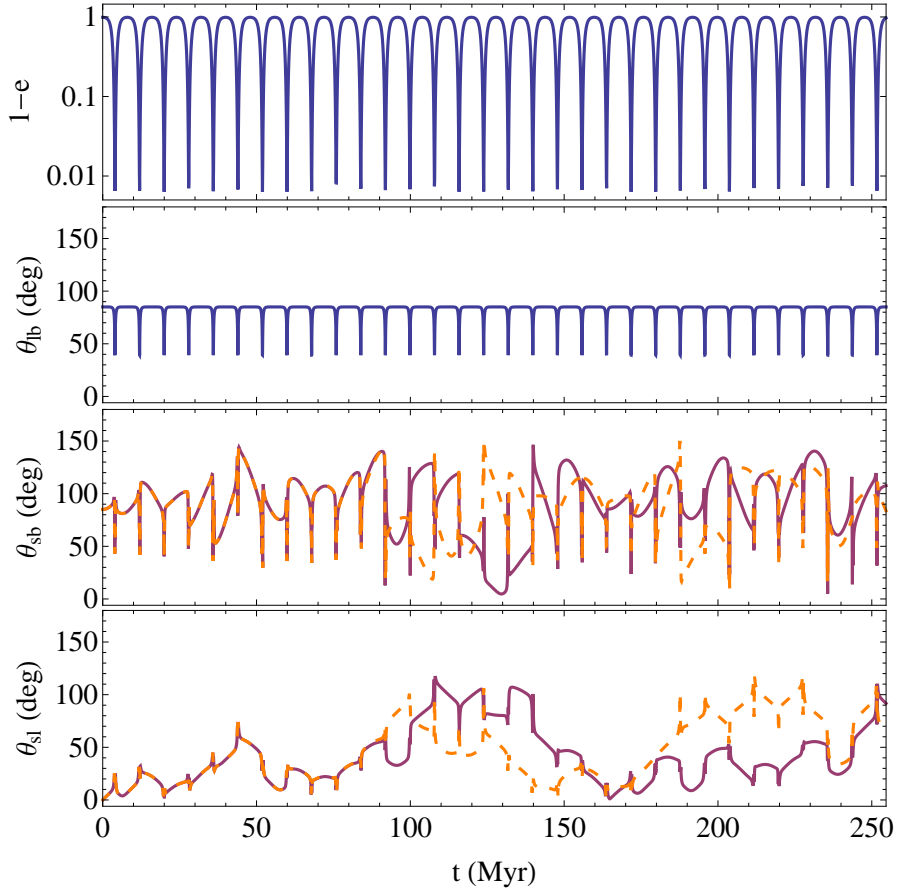


Figure 2.1: Sample evolution curves for the “pure” Lidov-Kozai system, demonstrating how the stellar spin evolves through LK cycles. The parameters for this run are $a = 1 \text{ AU}$, $a_b = 200 \text{ AU}$, $e_b = 0$, $M_\star = M_b = 1M_\odot$, $\hat{\Omega}_\star = 0.05$, $M_p = 4.6M_J$, and initial $e_0 = 0.01$, $\theta_{lb}^0 = 85^\circ$. The spin’s erratic evolution is suggestive of chaos; we therefore plot a “real” trajectory (red solid lines) and a “shadow” trajectory (orange dashed lines), used to evaluate the degree of chaotic behavior. The trajectories are initialized such that the “real” starts with \hat{S} parallel to \hat{L} , and the “shadow” with \hat{S} misaligned by 10^{-6} deg with respect to \hat{L} . This figure corresponds to the orange scatter plot of Fig. 2.2 and the orange curve of Fig. 2.3 (left). The spin evolution is highly chaotic.

spin evolution, we exclude the precession of \hat{L} around \hat{S} and all other short-range forces; thus, while the planet orbit influences the stellar spin, the stellar spin does not affect the orbit in any way. We consider different combinations of planet mass and stellar rotation rate to illustrate the different regimes described above (we consider $M_* = M_b = 1M_\odot$ and $R_* = 1R_\odot$ in all the examples shown in this paper). We present four “canonical” cases that encapsulate the range of the observed spin dynamics, including a sample trajectory in the transadiabatic regime (Regime II) (Fig. 2.1).

We find excellent agreement with the qualitative arguments outlined above. In Regime I (“nonadiabatic”, Fig. 2.2, top left) the spin evolution is regular and periodic. While we do not plot the spin-binary misalignment angle (θ_{sb}), it indeed stays constant. The “adiabatic” regime (Fig. 2.2, bottom right) is difficult to access for trajectories that start with high initial misalignment of \hat{S} and \hat{L} , due to the $\cos \theta_{\text{sl}}$ factor in the spin precession frequency. Those trajectories that start with low initial θ_{sl} (or with θ_{sl}^0 close to 180°) maintain that angle, as expected. In Regime II (“transadiabatic”), two different types of behavior are observed. For most parameters that fall within this regime, the spin evolution is strongly chaotic, as indicated by the large degree of scatter that fills up the phase space (Fig. 2.2, top right and bottom left). However, periodic islands exist in the middle of this chaos, in which the stellar spin behavior is regular (Fig. 2.2, bottom left; Fig. 2.9).

Since the stellar spin and planet orbital axes in real physical systems typically start out aligned, we specialize to the trajectories with $\theta_{\text{sl}}^0 = 0$ for the remainder of this paper. To assess the degree of chaos in each of the sample cases (Fig. 2.2), we evolve a “shadow” trajectory in addition to the real one (Fig. 2.1),

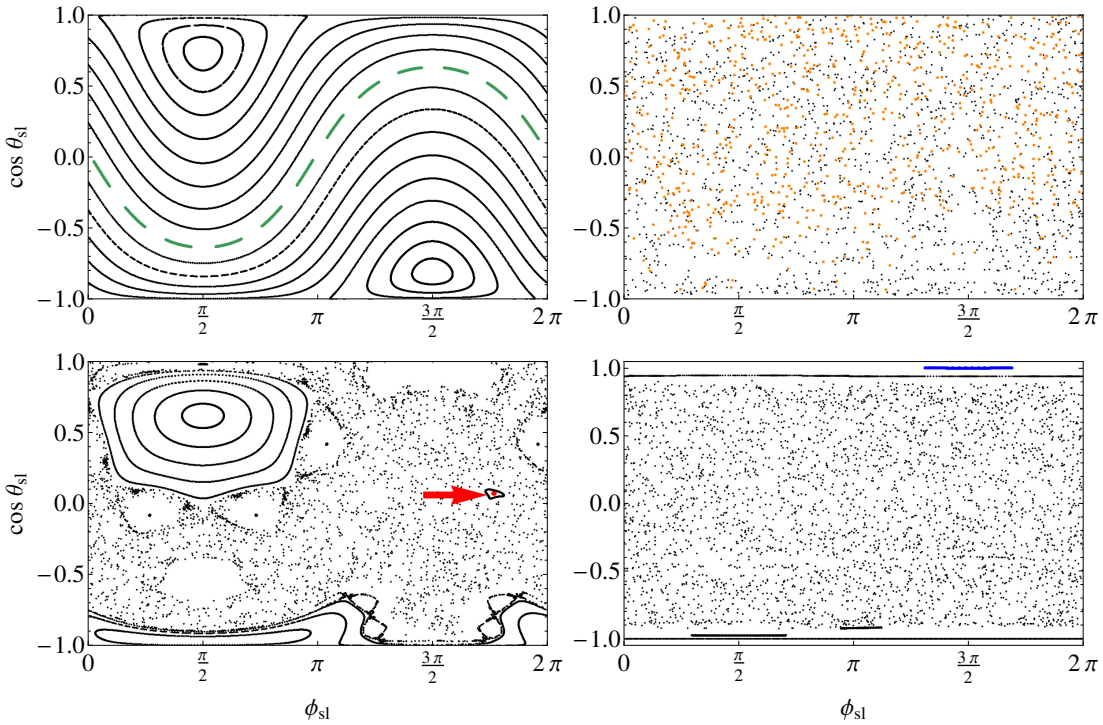


Figure 2.2: Surfaces of section of the angle (θ_{sl}) between $\hat{\mathbf{S}}$ and $\hat{\mathbf{L}}$ vs the precessional phase (ϕ_{sl}) of $\hat{\mathbf{S}}$ around $\hat{\mathbf{L}}$ for the “pure” LK system, demonstrating the presence or lack of chaos in the stellar spin evolution. In all of these sample cases, $a = 1 \text{ AU}$, $a_b = 200 \text{ AU}$, $e_b = 0$, $M_* = M_b = 1 M_\odot$, and $e_0 = 0.01$, $\theta_{\text{lb}}^0 = 85^\circ$. Each panel is composed of multiple unique trajectories, corresponding to different initial θ_{sl}^0 (with the initial spin-binary angle θ_{sb}^0 ranging from 0 to π , and assuming $\hat{\mathbf{S}}$ is initially in the same plane as $\hat{\mathbf{L}}$ and $\hat{\mathbf{L}}_b$). In each panel the colored trajectory indicates the one with $\theta_{\text{sl}}^0 = 0$. Each case is evolved for 12.7 Gyr, corresponding to ~ 1500 LK cycles. Each point in a trajectory is recorded at the argument of pericenter $\omega = \pi/2(+2\pi n$, with n an integer), corresponding to every other eccentricity maximum (Fig. 2.8). *Top left:* Regime I (nonadiabatic); $\hat{\Omega}_* = 0.003$, $M_p = 1 M_J$. We show 18 unique trajectories, with θ_{sb}^0 ranging from 5° to 175° ; the green line corresponds to $\theta_{\text{sl}}^0 = 0$. The “equilibrium” states at $(\theta_{\text{sl}}, \phi_{\text{sl}}) \approx (40^\circ, 90^\circ)$ and $(40^\circ, 270^\circ)$ correspond to $\hat{\mathbf{S}}$ parallel and anti-parallel to $\hat{\mathbf{L}}_b$. *Top right:* Regime II (transadiabatic); $\hat{\Omega}_* = 0.05$, $M_p = 4.6 M_J$; the orange dots show $\theta_{\text{sl}}^0 = 0$, while the black dots are a composite of several different θ_{sl}^0 . *Bottom left:* Regime II (transadiabatic); $\hat{\Omega}_* = 0.03$, $M_p = 1.025 M_J$; 11 periodic or quasi-periodic trajectories and a composite chaotic region. The red dot at $(\cos \theta_{\text{sl}}, \phi_{\text{sl}}) \approx (0.06, 1.8\pi)$ (see arrow) corresponds to a periodic island with $\theta_{\text{sl}}^0 = 0$. *Bottom right:* Regime III (onset of adiabaticity); $\hat{\Omega}_* = 0.05$, $M_p = 20 M_J$; 5 quasi-periodic trajectories and a composite chaotic region. The blue line corresponds to $\theta_{\text{sl}}^0 = 0$. Note that while both the orange and red cases are in Regime II, the orange one is highly chaotic, and the red resides in a periodic island.

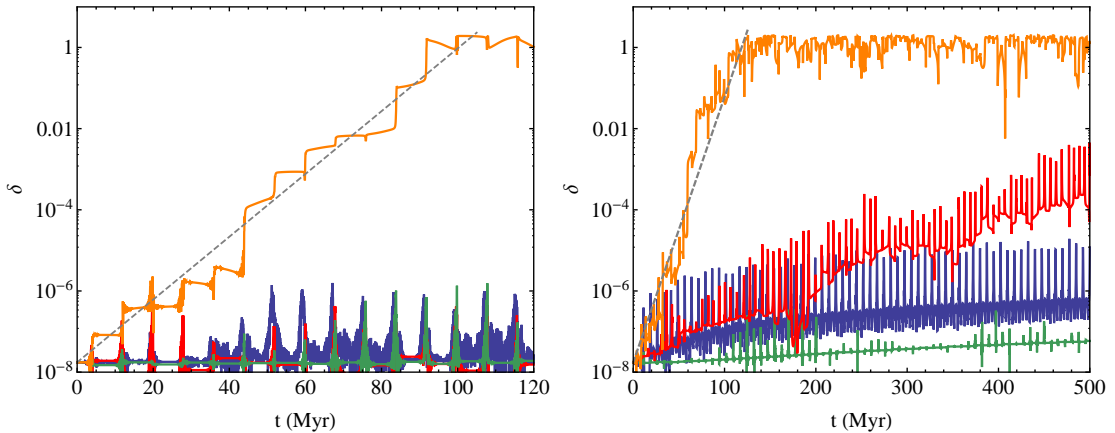


Figure 2.3: *Left panel:* Distance between two phase space trajectories, starting at slightly different initial spin orientations, for the “pure” Lidov-Kozai system. The first (real) starts with $\hat{\mathbf{S}}$ parallel to $\hat{\mathbf{L}}$, the other (shadow) with $\hat{\mathbf{S}}$ misaligned by 10^{-6} deg with respect to $\hat{\mathbf{L}}$, for each of the sample $\theta_{\text{sl}}^0 = 0$ cases depicted in Fig. 2.2. The phase space distance is calculated as $\delta = |\hat{\mathbf{S}}_{\text{real}} - \hat{\mathbf{S}}_{\text{shadow}}|$ and therefore has a maximum value of 2. The lines are color-coded to correspond to each of the cases of Fig. 2.2. The grey dashed line demonstrates that for the chaotic orange curve, $\delta \propto e^{\lambda t}$, with $\lambda \sim 0.18 \text{ Myr}^{-1}$. *Right panel:* Same as left, but including orbit precession due to stellar quadrupole and periastron advances due to General Relativity, stellar quadrupole, planet oblateness, and static tides in the planet. The orange curve shows chaotic growth with $\lambda \sim 0.15 \text{ Myr}^{-1}$. The red curve, which is periodic on the left, is mildly chaotic here, with $\lambda \sim 0.02 \text{ Myr}^{-1}$.

with initial conditions very close to the original ones, and monitor how fast the two trajectories diverge, particularly in the spin direction. As expected, three out of four of our sample cases do not exhibit chaos, while the fourth, in the transadiabatic regime, is strongly chaotic, with a Lyapunov time of $\lambda^{-1} \sim 5.6$ Myr, corresponding to only ~ 1 LK cycle (Fig. 2.3, left).

Next we include the precession of $\hat{\mathbf{L}}$ about $\hat{\mathbf{S}}$ and other short range forces (periastron advances due to General Relativity, stellar quadrupole, planet’s rotational bulge, and tidal distortion of the planet) (Fabrycky and Tremaine, 2007; Wu and Murray, 2003) in our calculations. We find that including these short-range forces for our four sample cases (Fig. 2.3, right) does not change our gen-

eral conclusion that chaotic evolution occurs in the transadiabatic regime, although it can shift the locations (in the parameter space) of periodic islands.

Clearly, the stellar spin behavior in the transadiabatic regime is very complex: highly chaotic for certain parameters, more regular for others. To explore this diversity further, we construct a “bifurcation” diagram (Fig. 2.4), with which we could examine the degree of chaos over a large range of parameter values (particularly the planet mass). Visualized in this way, the topology of the chaos is more obvious: most of the mass bins are highly chaotic, but they are interspersed with individual, isolated quasiperiodic islands. To better understand this complex topology, we have developed a simpler analytical toy model that captures many of the features of this system (Sec. 2.8.3).

Wide-spread chaos in dynamical systems is typically driven by overlapping resonances (Chirikov, 1979). Repeated secular spin-orbit resonance crossings ($|\Omega_{\text{ps}}| \sim |\Omega_{\text{pl}}|$) during LK cycles play an important role in producing the observed chaotic spin behavior. On the other hand, LK cycles themselves result from the near $1 : 1$ resonance ($\dot{\varpi} = \dot{\Omega}$) between the longitude of the periapse ϖ and the longitude of the ascending node Ω of the planet’s orbit. The back-reaction of the stellar spin on the orbit can naturally couple these two resonances. We suggest that all these effects are important in the development of the chaotic stellar spin evolution.

2.5 Tidal dissipation and memory of chaotic evolution

Having explored in some detail the variety of behaviors exhibited by stellar spin during LK cycles, we now assess the impact of this evolution on the production

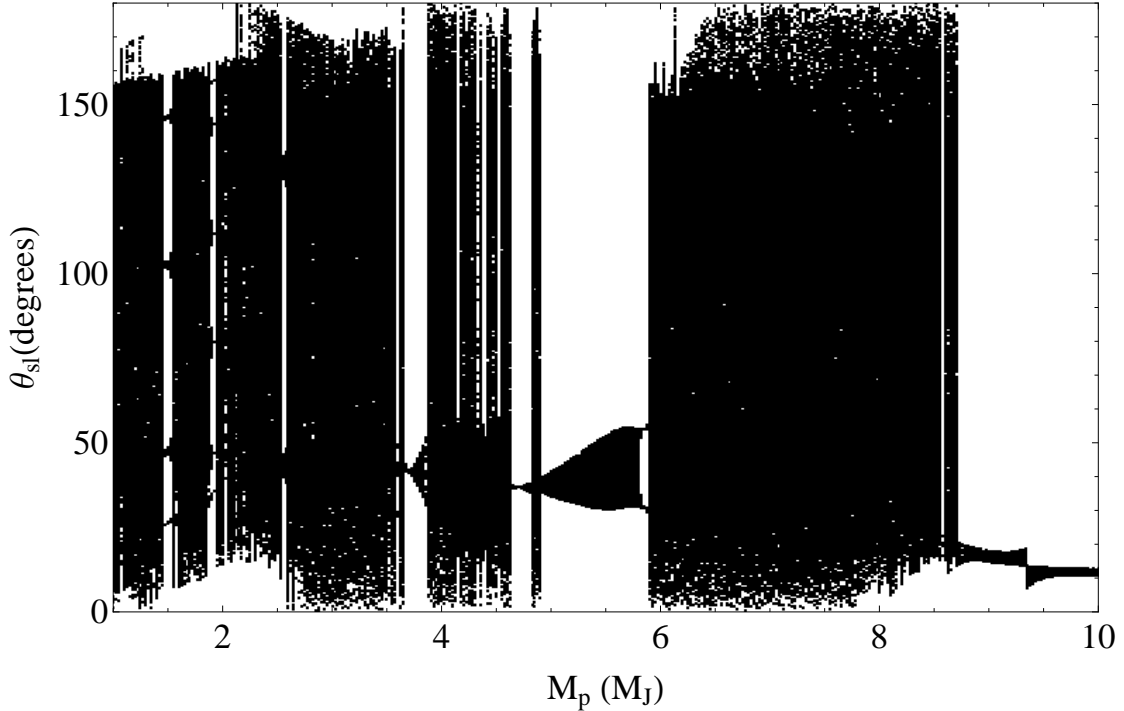


Figure 2.4: “Bifurcation” diagram of spin-orbit misalignment angle vs planet mass, including all short-range effects. The procedure described in Fig. 2.2 is carried out for each value of planet mass: the spin-orbit misalignment angle is recorded at every other eccentricity maximum for ~ 1500 LK cycles. The parameters for this plot are $a = 1$ AU, $a_b = 200$ AU, $e_0 = 0.01$, $\theta_{\text{lb}}^0 = 85^\circ$, $\hat{\Omega}_* = 0.03$. High degree of scatter in a single mass bin indicates highly chaotic behavior. Note that multiple quasiperiodic islands appear in the middle of highly chaotic regions.

of hot Jupiters, particularly on their final stellar spin-orbit misalignment angles, by adding tidal dissipation to our equations. We employ the standard weak friction model of tidal dissipation in giant planets with constant tidal lag time (Alexander, 1973; Hut, 1981). In order to ensure that all our runs lead to circularized planets and a final θ_{sl} within about 10^{10} yrs, we enhance tidal dissipation by a factor of 14 (Fig. 2.5, left) and 1400 (Fig. 2.5, right) relative to the fiducial value for Jupiter (Storch and Lai, 2014) (Sec. 2.8.1). As long as the tidal evolution timescale of the orbit is much longer than the Lyapunov time for the chaotic spin evolution, we do not expect this enhancement to have major qualitative effect

on the final observed spin-orbit misalignment angle.

Tidal dissipation leads to a gradual decrease in the proto-hot Jupiter’s semi-major axis and eventual circularization close to the host star (Fig. 2.10). As the planet’s orbit decays, LK cycles become suppressed by short-range forces. Also, as the semi-major axis decays, $|\Omega_{\text{ps}}/\Omega_{\text{pl}}|$ increases. Thus, even if we choose initial conditions that lie squarely in the nonadiabatic regime (Regime I), as a decreases, all trajectories will eventually go through the $|\Omega_{\text{ps}}| = |\Omega_{\text{pl}}|$ secular resonance and end up fully adiabatic. At that point, the spin-orbit misalignment angle freezes out to some final, constant value $\theta_{\text{sl}}^{\text{f}}$.

In all of the numerical examples of non-dissipative evolution discussed above, we have held the value of the stellar spin rate Ω_* constant. However, because the divisions between different spin evolution regimes depend on Ω_* , stellar spindown can potentially have a substantial effect on the degree of chaos in the system. Isolated solar-type stars spin down via magnetic braking associated with the stellar wind (Gallet and Bouvier, 2013). For simplicity, we use the empirical Skumanich Law (Skumanich, 1972) to add stellar spindown to our evolution equations, starting with an initial spin period of 2.3 days; the final spin period (at $t = 5$ Gyr) is 28 days.

To assess the influence of chaotic stellar spin evolution on the final distribution of spin-orbit misalignment angles, we create a different kind of “bifurcation” diagram (Fig. 2.5). As in the non-dissipative case (Fig. 2.4), we consider a range of planet masses. For each M_p , we take a set of initial conditions that are identical in all but the initial orbit-binary misalignment angle θ_{lb} , which we randomly choose from a very small range: $\theta_{\text{lb}}^0 \in \{86.99^\circ, 87.01^\circ\}$ (Fig. 2.5, left) and $\theta_{\text{lb}}^0 \in \{84.95^\circ, 85.05^\circ\}$ (Fig. 2.5, right). We evolve these trajectories until the

hot Jupiter circularizes and θ_{sl} reaches its final value. We find that the scatter in $\theta_{\text{sl}}^{\text{f}}$ depends on the planet mass. The scatter generally increases with increasing M_p , but drops sharply in the adiabatic regime (for $M_p \gtrsim 4.4M_J$ in the left panel of Fig. 2.5). There also exist quasiperiodic islands, where $\theta_{\text{sl}}^{\text{f}}$ has a rather small spread. Also, a range of misalignment angles around 90° appears to be excluded, with this range decreasing with increasing planet mass. Given the very small range of initial conditions, the evolution of any regular, non-chaotic system should result in only *one* final misalignment angle. Therefore, we suggest that this bimodality is the result of the system passing through the $|\Omega_{\text{ps}}| \sim |\Omega_{\text{pl}}|$ secular resonance, and the complex and possibly chaotic dynamics that occur during that time. We tentatively attribute the decrease of bimodality with increasing mass to an increase in chaotic behavior. The final semi-major axis a_{f} also exhibits “chaotic” spreads and periodic islands. Thus, in effect, the final distributions of $\theta_{\text{sl}}^{\text{f}}$ and a_{f} carry an imprint of the spin’s past chaotic evolution.

As a final step, we run a “mini” population synthesis calculation, for a fixed value of a_0 and a_b and a broader range of initial orbital inclinations (Fig. 2.6). A sharp contrast exists between the distribution of final spin-orbit misalignment angles at low M_p and high M_p . At low M_p a bimodal distribution of $\theta_{\text{sl}}^{\text{f}}$ is produced (this bimodality has been found in some previous population synthesis calculations (Correia et al., 2011; Fabrycky and Tremaine, 2007)). At high M_p the evolution is mostly adiabatic, producing very little spin-orbit misalignment. This is a clear signature of the complex spin evolution in the observed stellar obliquity. Other factors, such as the stellar spindown rate and planetary tidal dissipation rate, can also affect the final misalignment distribution.

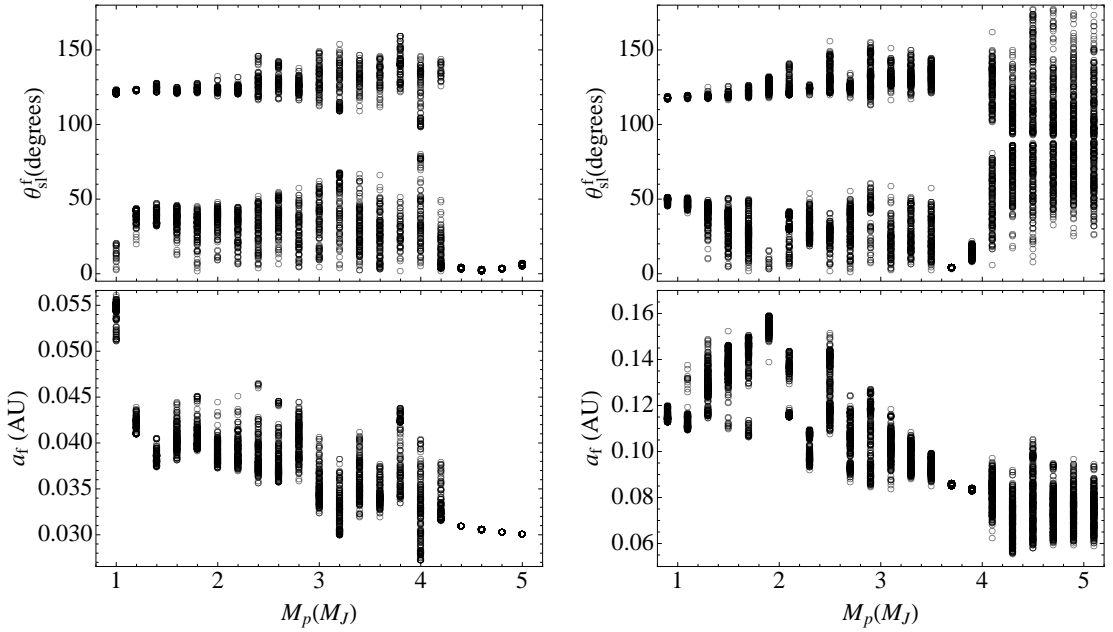


Figure 2.5: Two “bifurcation” diagrams of the final spin-orbit misalignment angle (top) and semi-major axis (bottom) vs planet mass for a small range of initial planet-binary inclinations, including the effects of tidal dissipation and stellar spindown. Here $a_b = 200$ AU, $e_0 = 0.01$, $\hat{\Omega}_{*,0} = 0.05$. Each data point represents the outcome of a single complete run starting with $a_0 = 1.5$ AU (left) and $a_0 = 1$ AU (right) and ending when the planet has sufficiently circularized (final eccentricity $e_f \leq 0.1$) and the final spin-orbit angle θ_{sl}^f is attained. For each run, we randomly select an initial inclination θ_{lb}^0 from the range $86.99^\circ - 87.01^\circ$ (left) and $84.95^\circ - 85.05^\circ$ (right). Each mass bin contains ~ 200 points. The degree of scatter in θ_{sl}^f generally increases with increasing M_p , but drops sharply in the adiabatic regime (for $M_p \gtrsim 4.4 M_J$ in the left panel). Quasiperiodic islands are still present (e.g. at $\sim 3.8 M_J$ in the right panel).

2.6 Discussion

The discovery of spin-orbit misalignment in close-in exoplanetary systems in the last few years was a major surprise in planetary astrophysics. Much of the recent theoretical work has focused on the non-trivial evolution of the planetary orbit (such as orbital flip) due to few-body gravitational interactions (Katz et al., 2011; Lithwick and Wu, 2014; Naoz et al., 2011). However, as we have shown here, the spin axis of the host star can undergo rather complex and chaotic evo-

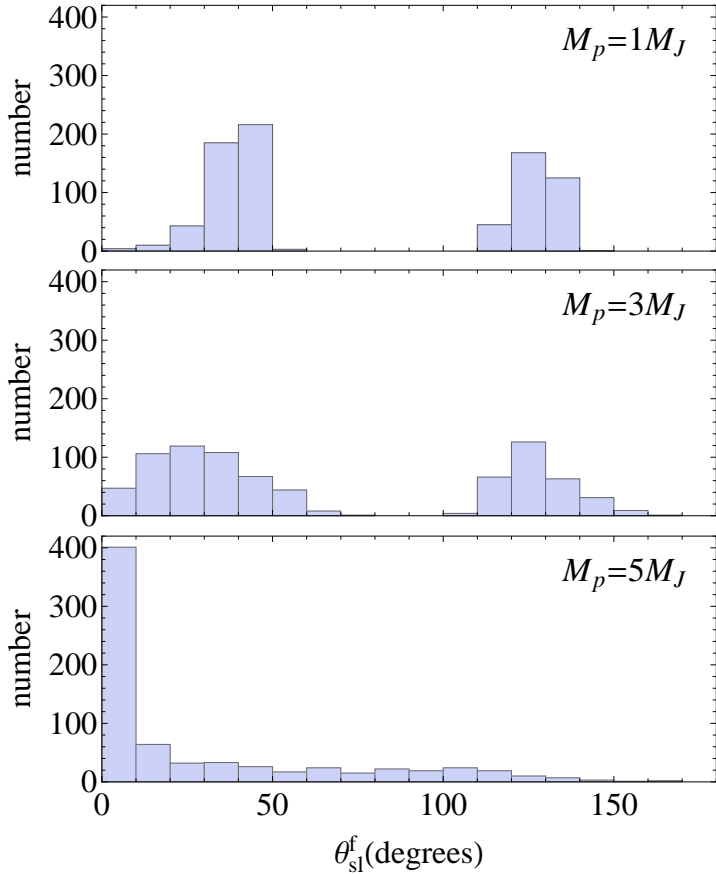


Figure 2.6: Distribution of the final spin-orbit misalignment angles as a function of planet mass, including the effects of tidal dissipation and stellar spin down, for initial planet-binary inclinations θ_{lb}^0 in the range $85^\circ - 89^\circ$. Here $a_0 = 1.5$ AU, $a_b = 200$ AU, $e_0 = 0.01$, $\hat{\Omega}_{*,0} = 0.05$. Each evolutionary trajectory is integrated until it has sufficiently circularized ($e_f \leq 0.1$), for a maximum of 5 Gyr. If by the end of 5 Gyr the planet is not circularized, it is discarded. Note that the bimodality featured in Fig. 2.5 is still present here, despite the wider range of initial inclinations. At $M_p = 5M_J$ the evolution is mostly adiabatic, and therefore it is difficult to generate misalignment.

lution, depending on the planetary mass and the stellar rotation rate. In many cases, the variation of the stellar spin axis relative to the binary axis is much larger than the variation of the orbital axis. Therefore, to predict the final spin-orbit misalignments of hot Jupiter systems in any high-eccentricity migration scenario, it is important to properly account for the complex behavior of stellar spin evolution.

In the above, we have focused on the Lidov-Kozai mechanism for the formation of hot Jupiters, but similar consideration can be applied to the formation of short-period stellar binaries (Fabrycky and Tremaine, 2007). Indeed, spin-orbit misalignment angles have been measured for a number of close-in stellar binaries (Albrecht et al., 2009, 2014; Triaud et al., 2013). Because of the much larger stellar spin precession rate in stellar binaries compared to the star-planet systems, the stellar spin evolution is expected to be largely in the adiabatic regime (depending on various parameters; Fig. 2.7), in which case the observed spin-orbit misalignment angles in close binaries would reflect their initial values at formation.

It is a curious fact that the stellar spin axis in a wide binary (~ 100 AU apart) can exhibit such a rich, complex evolution. This is made possible by a tiny planet ($\sim 10^{-3}$ of the stellar mass) that serves as a link between the two stars: the planet is “forced” by the distant companion into a close-in orbit, and it “forces” the spin axis of its host star into wild precession and wandering.

The “binary+planet+spin” system studied in this paper exhibits many intriguing dynamical properties. While we have provided a qualitative understanding for the emergence of chaos in this system in terms of secular resonance crossing, much remains to be understood theoretically. Most remarkable

is the appearance of periodic islands as the system parameters (planet mass and stellar spin) vary – a feature reminiscent of some well-known chaotic systems (Lichtenberg and Lieberman, 1992; Strogatz, 1994).

2.7 Acknowledgements

We thank Konstantin Batygin, Dan Fabrycky, Matt Holman and Diego Muñoz for useful discussions. This work has been supported in part by NSF grants AST-1008245, AST-1211061 and NASA grants NNX12AF85G, NNX14AG94G. K.R.A. is supported by the NSF Graduate Research Fellowship Program under Grant No. DGE-1144153.

2.8 Supplementary Materials

2.8.1 Materials and Methods

For the “pure” Lidov-Kozai problem discussed in the earlier part of the main text, we integrate the standard quadrupole Lidov-Kozai equations for the planet’s orbital elements (assuming $M_p \ll M_*, M_b$). These are given by

$$\begin{aligned} \frac{de}{dt} &= t_k^{-1} \frac{15}{8} e \sqrt{1 - e^2} \sin 2\omega \sin^2 \theta_{lb}, \\ \frac{d\Omega}{dt} &= t_k^{-1} \frac{3}{4} \frac{\cos \theta_{lb} (5e^2 \cos^2 \omega - 4e^2 - 1)}{\sqrt{1 - e^2}}, \\ \frac{d\theta_{lb}}{dt} &= -t_k^{-1} \frac{15}{16} \frac{e^2 \sin 2\omega \sin 2\theta_{lb}}{\sqrt{1 - e^2}}, \\ \frac{d\omega}{dt} &= t_k^{-1} \frac{3 [2(1 - e^2) + 5 \sin^2 \omega (e^2 - \sin^2 \theta_{lb})]}{4\sqrt{1 - e^2}}, \end{aligned} \quad (2.5)$$

where e is the planet's orbital eccentricity, θ_{lb} is the angle between the planet orbital angular momentum axis and the binary axis $\hat{\mathbf{L}}_b$, Ω is the longitude of the ascending node, ω is the argument of periastron, and t_k^{-1} is the characteristic LK rate, given by Eq. (2.1) of the main text. We choose the binary orbital plane to be the invariant plane. In all the cases we consider, we take as our initial condition $\Omega_0 = 0$ and $\omega_0 = 0$ (thus, ω always circulates rather than librates; see Fig. 2.8). Note, however, that this is not a particularly special choice, since for the initial inclinations θ_{lb} we consider ($85^\circ - 89^\circ$) the maximum eccentricity is the same for the circulating and librating cases, and the rates of precession of the node (Ω_{pl} , Eq. 2.2) are only slightly different.

We evolve the precession of the stellar spin according to the equation

$$\frac{d\hat{\mathbf{S}}}{dt} = \Omega_{ps}\hat{\mathbf{L}} \times \hat{\mathbf{S}}, \quad (2.6)$$

where Ω_{ps} is given by Eq. (2.4), and $\hat{\mathbf{L}} = (\sin \theta_{lb} \sin \Omega, -\sin \theta_{lb} \cos \Omega, \cos \theta_{lb})$ in the inertial frame where the z -axis is parallel to the binary axis $\hat{\mathbf{L}}_b$.

In the latter part of the main text, we add short-range forces to our system. We use the expressions given in Wu and Murray (2003) for periastron advances due to General Relativity, planet spin-induced quadrupole, and static tide in the planet. We also add nodal and apsidal precession of the planetary orbit due to the spin-induced stellar quadrupole. This introduces the following terms to the orbital evolution equations:

$$\begin{aligned} \frac{d\omega}{dt} &= \omega_* \left(1 - \frac{3}{2} \sin^2 \theta_{sl} - \frac{\cos \theta_{lb}}{\sin \theta_{lb}} \cos \theta_{sl} \frac{\partial \cos \theta_{sl}}{\partial \theta_{lb}} \right), \\ \frac{d\Omega}{dt} &= \omega_* \frac{\cos \theta_{sl}}{\sin \theta_{lb}} \frac{\partial \cos \theta_{sl}}{\partial \theta_{lb}}, \\ \frac{d\theta_{lb}}{dt} &= -\omega_* \frac{\cos \theta_{sl}}{\sin \theta_{lb}} \frac{\partial \cos \theta_{sl}}{\partial \Omega}, \end{aligned} \quad (2.7)$$

where

$$\begin{aligned}\cos \theta_{\text{sl}} &= \hat{\mathbf{L}} \cdot \hat{\mathbf{S}} = S_x \sin \theta_{\text{lb}} \sin \Omega - S_y \sin \theta_{\text{lb}} \cos \Omega + S_z \cos \theta_{\text{lb}}, \\ \frac{\partial \cos \theta_{\text{sl}}}{\partial \theta_{\text{lb}}} &= S_x \cos \theta_{\text{lb}} \sin \Omega - S_y \cos \theta_{\text{lb}} \cos \Omega - S_z \sin \theta_{\text{lb}}, \\ \frac{\partial \cos \theta_{\text{sl}}}{\partial \Omega} &= S_x \sin \theta_{\text{lb}} \cos \Omega + S_y \sin \theta_{\text{lb}} \sin \Omega,\end{aligned}\quad (2.8)$$

and $\omega_* = -\Omega_{\text{ps}} S / (L \cos \theta_{\text{sl}})$.

Finally, we add tidal dissipation in the planet to our equations. We use the standard weak friction tidal dissipation model (Alexander, 1973; Hut, 1981):

$$\frac{1}{a} \frac{da}{dt} = \frac{1}{t_a} \frac{1}{(1-e^2)^{15/2}} \left[(1-e^2)^{3/2} f_2(e) \frac{\Omega_{\text{s,p}}}{n} - f_1(e) \right], \quad (2.9)$$

$$\frac{1}{e} \frac{de}{dt} = \frac{11}{4} \frac{1}{t_a} \frac{1}{(1-e^2)^{13/2}} \left[(1-e^2)^{3/2} f_4(e) \frac{\Omega_{\text{s,p}}}{n} - \frac{18}{11} f_3(e) \right], \quad (2.10)$$

where a is the semi-major axis, $\Omega_{\text{s,p}}$ is the spin rate of the planet, the functions $f_1 - f_4$ are defined as

$$\begin{aligned}f_1(e) &= 1 + \frac{31}{2} e^2 + \frac{255}{8} e^4 + \frac{185}{16} e^6 + \frac{25}{64} e^8, \\ f_2(e) &= 1 + \frac{15}{2} e^2 + \frac{45}{8} e^4 + \frac{5}{16} e^6, \\ f_3(e) &= 1 + \frac{15}{4} e^2 + \frac{15}{8} e^4 + \frac{5}{64} e^6, \\ f_4(e) &= 1 + \frac{3}{2} e^2 + \frac{1}{8} e^4,\end{aligned}\quad (2.11)$$

(2.12)

and t_a is a characteristic timescale, given by

$$\frac{1}{t_a} = 6k_2 \Delta t_L \left(\frac{M_*}{M_p} \right) \left(\frac{R_p}{a} \right)^5 n^2, \quad (2.13)$$

where n is the mean motion of the planet, k_2 is the tidal Love number and Δt_L is the tidal lag time. For Jupiter, $k_2 = 0.37$ and we take $\Delta t_L = 0.1$ s (corresponding to $k_2/Q \approx 10^{-5}$ at a tidal forcing period of 6.5 hours). We therefore use $\Delta t_L =$

0.1χ s, where χ is a tidal enhancement factor, which we take to be 14 for Fig. 2.5 (left) and 1400 for Fig. 2.5 (right), in order to ensure that the planets in our test cases circularize within the lifetime of their host stars. For all the sample cases considered in this work, we assume the planet spin to be pseudosynchronous with the orbit, i.e. $\Omega_{s,p}/n = f_2(e)/[(1 - e^2)^{3/2} f_5(e)]$, with $f_5(e) = 1 + 3e^2 + (3/8)e^4$. Relaxing this assumption does not qualitatively change our results. (For pseudosynchronous spin, the periastron advance due to planet's rotation bulge is always smaller than that due to tidal distortion.)

Equivalent evolution equations for the spin-triple system can be found in Correia et al. (2011) and Eggleton and Kiseleva-Eggleton (2001).

2.8.2 Supplementary Figures

In this section we provide several supplementary figures that facilitate deeper understanding of the rich dynamics exhibited by the stellar spin during LK cycles and migration.

As stated in the main text, the division between different regimes of stellar spin behavior depends on the planet semi-major axis, binary semi-major axis, and the product of planet mass and stellar spin frequency. In Fig. 2.7, we illustrate these divisions in the $a_b - a$ space for several different values of $\hat{M}_p \equiv (\hat{\Omega}_*/0.05)(M_p/M_J)$. We note that for real systems, short-range effects due to General Relativity (GR) and tidal/rotation distortion of the planet may affect the LK cycles. For the parameter space explored in this paper, the GR effect dominates. When the LK precession frequency $\dot{\omega}_k \sim t_k^{-1}(1 - e^2)^{3/2}$ becomes comparable to the GR-induced precession frequency $\dot{\omega}_{GR}$, the LK cycle

is arrested. In this case, the maximum eccentricity achieved during an LK cycle is reduced, and any planet undergoing LK cycles in will fail to become a hot Jupiter if $r_p = a(1 - e_{\max})$ is larger than ~ 0.1 AU. Thus, the effect of GR can restrict the available parameter space in which adiabatic evolution (regime III) happens *and* a hot Jupiter is created. However, the presence of short-range forces and tidal dissipation also alters the topology of the chaos in the parameter space, making it difficult to draw a direct connection between the regime divisions in the “pure” LK system and the results of our dissipative simulations. In fact, the results of Fig. 2.5 (left) demonstrate that, indeed, it is possible for hot Jupiters to experience adiabatic evolution.

In order to explore the three regimes of stellar spin evolution, we create surfaces of section (Fig. 2.2) by sampling the spin trajectory every time the orbital trajectory comes back to the same region of phase space. In Fig. 2.8 we show the orbital trajectory in phase space, with and without short-range forces, and mark the point at which we choose to sample the spin evolution.

In the main text, we demonstrate that in the “transadiabatic” regime (regime II), stellar spin has the potential to undergo both chaotic motion and regular quasiperiodic motion, depending on the parameters of the system. In Fig. 2.1 we present an example of a chaotic trajectory. Here, in Fig. 2.9 we present an example of a periodic transadiabatic trajectory: even at late times, the “real” and “shadow” trajectories match perfectly.

Finally, in Fig. 2.10 we present a sample time evolution for the LK problem with added short-range forces, tidal dissipation and stellar spindown, showing how the final semi-major axis a_f and spin-orbit misalignment angle θ_{sl}^f are attained. Each point in Fig. 2.5 represents the result of such evolution.

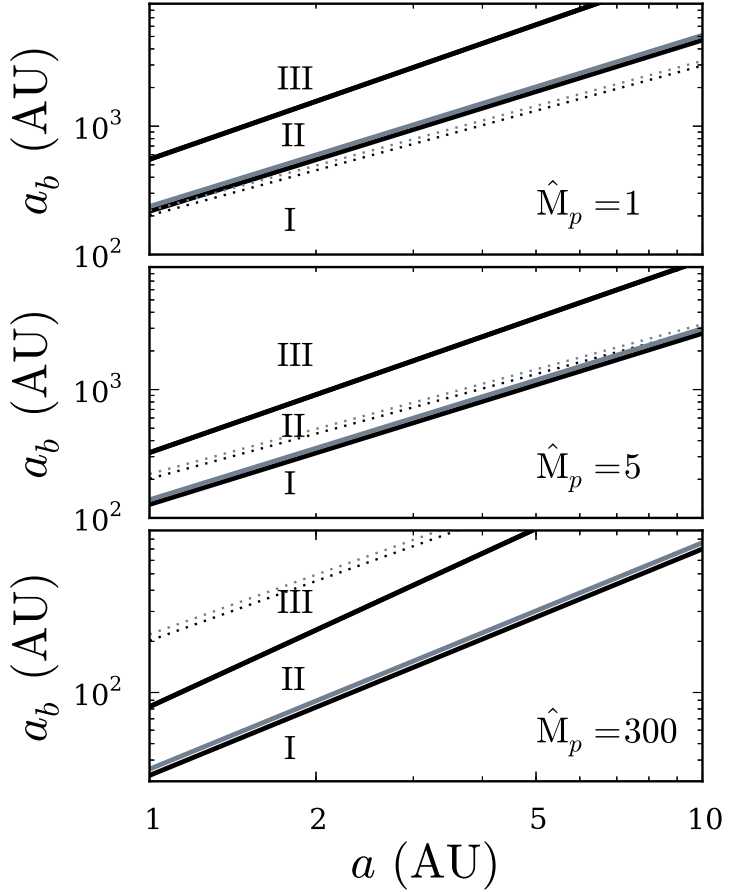


Figure 2.7: Breakdown of parameter space into the three regimes of spin evolution, as discussed in the text. *Black:* for a periastron distance of $r_p = a(1 - e_{\max}) = 0.03$ AU; *gray:* for $r_p = 0.05$ AU. Here $\hat{M}_p = (\hat{\Omega}_*/0.05)(M_p/M_J)$. The regimes are determined by the relative values of the stellar spin precession frequency Ω_{ps} and the nodal precession frequency Ω_{pl} of the planet's orbit. Note that Ω_{ps} depends on $\cos \theta_{\text{sl}}$, and for concreteness we use $\cos \theta_{\text{sl}} = 1$. Ω_{pl} is a complicated function of eccentricity and θ_{lb} (Eq. 2.2), which we approximate as $\Omega_{\text{pl}} \approx -t_k^{-1}/(1 - e^2)$ in making this figure. The lines separating Regimes I and II are given by $|\Omega_{\text{ps},\max}| \approx 0.5|\Omega_{\text{pl},\max}|$, where $\Omega_{\text{ps},\max}$ and $\Omega_{\text{pl},\max}$ are equal to Ω_{ps} and Ω_{pl} evaluated at $(1 - e_{\max}) = r_p/a$. The line separating Regimes II and III is given by $|\Omega_{\text{ps},0}| \approx 2|\Omega_{\text{pl},0}|$, where $\Omega_{\text{ps},0}$, $\Omega_{\text{pl},0}$ are equal to Ω_{ps} and Ω_{pl} evaluated at $e = 0$. The dotted lines mark the boundary at which the effect of GR becomes significant, approximated by $\dot{\omega}_{\text{GR}} \approx t_k^{-1}(1 - e_{\max}^2)^{-1/2}$. Above the dotted lines, GR will suppress the LK cycles, so that the system cannot reach the specified r_p . In Regimes I and III the spin precession frequency never overlaps with the nodal precession frequency, and the spin evolution is expected to be regular and periodic. In Regime II, the two frequencies are equal for some value of e during the LK cycle, and therefore secular spin-orbit resonance develops, potentially leading to chaos. Note that the parameters shown in the lowest panel ($\hat{M}_p = 300$) correspond to a low-mass star rather than a planet.

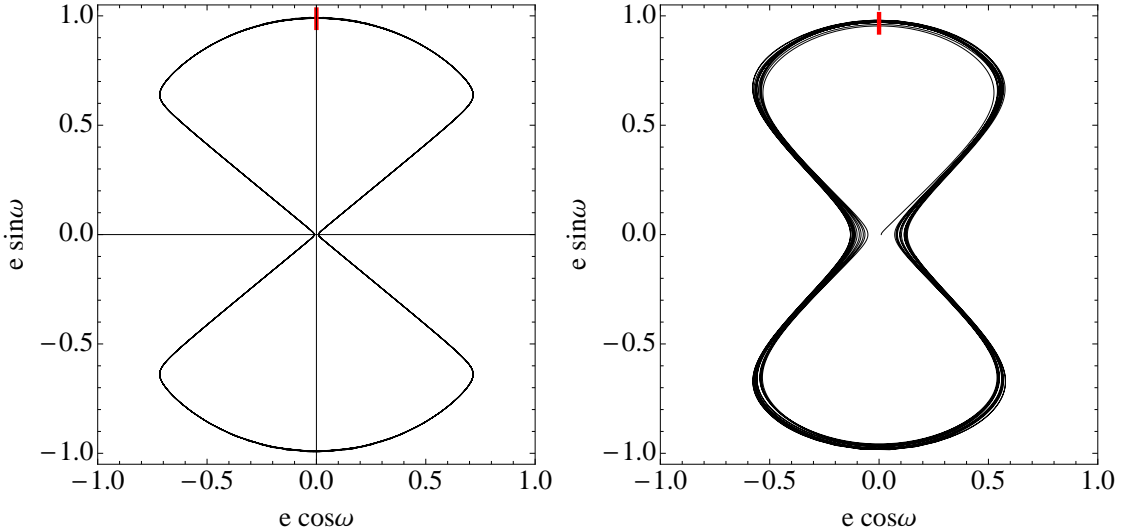


Figure 2.8: Orbital trajectory in $e - \omega$ phase space, for the “pure” LK problem (left), and with the addition of short-range forces (right). ω circulates with a period that is twice the period of the eccentricity oscillations. In red, we mark the point in the trajectory where we choose to sample the spin evolution in generating Figs. 2.2 and 2.4: i.e., every time the trajectory passes that point, we record the stellar spin orientation.

2.8.3 Toy Model

We consider a toy model in order to gain a better understanding of the dynamical behavior of the “real” LK system with stellar spin evolution (i.e. the system on which we focused in the main text). In this model, the stellar spin axis \hat{S} satisfies Eq. (2.6), and the orbital axis \hat{L} evolves according to

$$\frac{d\hat{L}}{dt} = \Omega_{\text{pl}} \hat{L}_b \times \hat{L}, \quad (2.14)$$

where we have neglected the back-reaction torque of the stellar spin on the planetary orbit (this back-reaction can be included but it does not introduce qualitatively new features when $L \gg S$), and the nutation of the orbital angular momentum vector \hat{L} . The external binary axis \hat{L}_b is fixed in time, and the angle between \hat{L} and \hat{L}_b is constant. The spin precession rate Ω_{ps} is a function of eccentricity (and time) [see Eq. (2.4)]. In the case of pure LK oscillations (i.e.

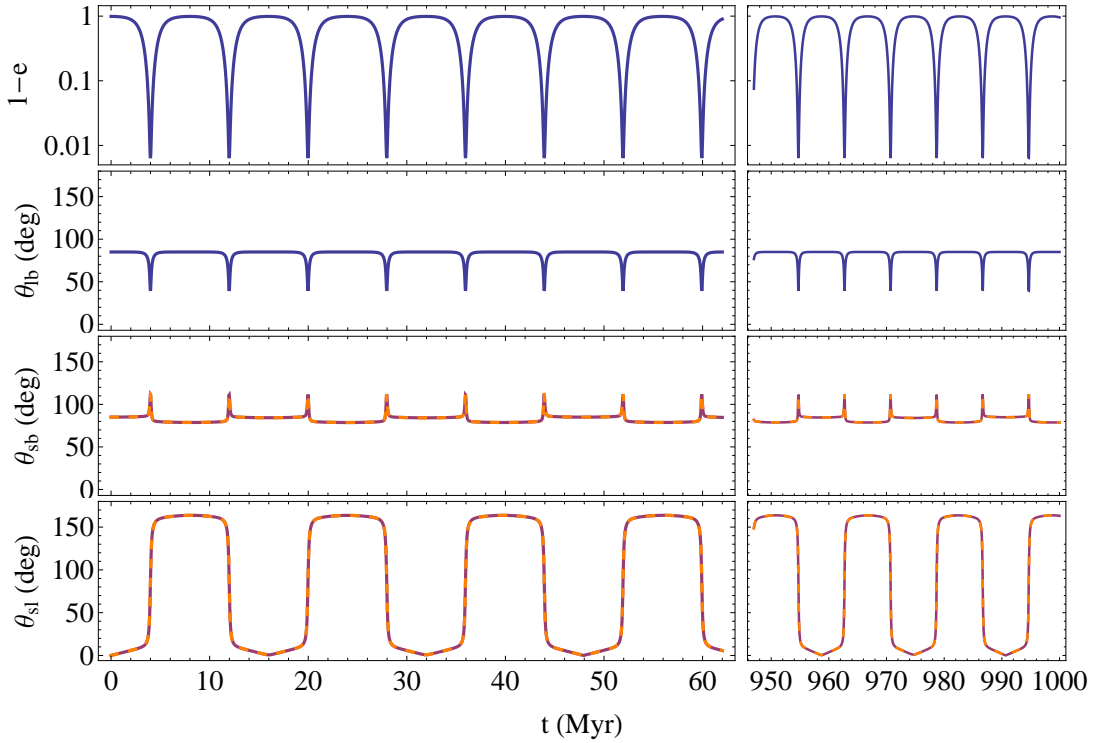


Figure 2.9: Sample evolution curves for a trajectory in a periodic island of regime II, demonstrating how the stellar spin evolves through many LK cycles. We plot a “real” trajectory (red solid lines) and a “shadow” trajectory (orange dashed lines), used to evaluate the degree of chaotic behavior. The trajectories are initialized such that the “real” starts with \hat{S} parallel to \hat{L} , and the “shadow” with \hat{S} misaligned by 10^{-6}deg with respect to \hat{L} . The parameters are $a = 1\text{AU}$, $a_b = 200\text{AU}$, $e_0 = 0.01$, $\theta_{lb}^0 = 85^\circ$, $\hat{\Omega}_* = 0.03$, $M_p = 1.025M_J$. This figure corresponds to the red points of Fig. 2.2 (bottom left) and the red curve of Fig. 2.3 (left). It is perfectly periodic: even at late times, the “real” and “shadow” trajectories match perfectly.

without extra precession effects), the eccentricity is a periodic function of time, varying between 0 and e_{\max} . We imitate this oscillatory behavior by adopting the following explicit form for Ω_{ps} :

$$\Omega_{ps}(t) = \Omega_{ps,0} f(t) \cos \theta_{sl}, \quad \text{with } f(t) \equiv \frac{1 + \varepsilon}{1 + \varepsilon \cos \Omega_0 t}, \quad (2.15)$$

where Ω_0 represents the LK oscillation frequency. The precession frequency of \hat{L} around \hat{L}_b has the approximate eccentricity dependence $\Omega_{pl} \propto [2(1 - e^2)^{-1} - 1]$

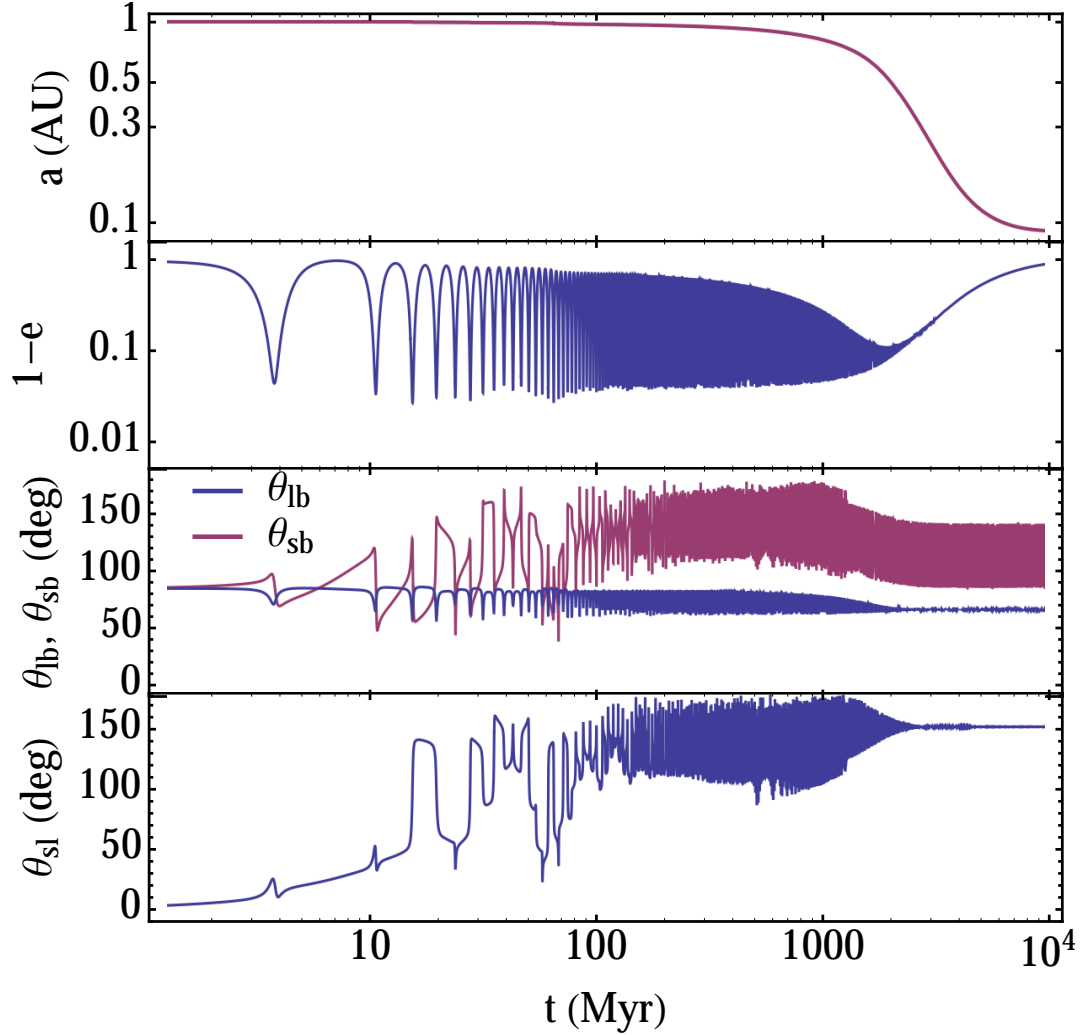


Figure 2.10: Sample orbital and spin evolution, including tidal dissipation and stellar spindown. The parameters for this run are $a_0 = 1\text{AU}$, $a_b = 200\text{AU}$, $e_0 = 0.01$, $\theta_{lb}^0 = 85^\circ$, $\hat{\Omega}_{*,0} = 0.05$, $M_p = 5M_J$, $\chi = 700$.

in the real system, and therefore in our toy model takes the form

$$\Omega_{pl} = \Omega_{pl,0}(2f^{2/3} - 1), \quad \text{where} \quad \Omega_{pl,0} = \frac{3}{4}\Omega_0 \cos \theta_{lb}. \quad (2.16)$$

During a LK cycle, Ω_{ps} varies from $\Omega_{ps,0} \cos \theta_{sl}$ to $\Omega_{ps,max} = \Omega_{ps,0}(1 + \varepsilon) \cos \theta_{sl}/(1 - \varepsilon)$. We adopt $\varepsilon = 0.99$ in our examples below. Thus, the parameter $\omega_{ps,0} \equiv \Omega_{ps,0}/\Omega_{pl,0}$ determines whether the system is nonadiabatic ($\omega_{ps,0} \lesssim 0.1$), transadiabatic ($0.1 \lesssim \omega_{ps,0} \lesssim 1$), or fully adiabatic ($\omega_{ps,0} \gtrsim 1$).

For a given $\Omega_{\text{ps},0}$, we numerically integrate Eqs. (2.6) and (2.14) for 1000 “LK cycles,” record the values of θ_{sl} and θ_{sb} at eccentricity maxima (i.e., $\Omega_0 t = \pi, 3\pi, 5\pi, \dots$), and then plot these values in the $\theta_{\text{sl}} - \omega_{\text{ps},0}$ and $\theta_{\text{sb}} - \omega_{\text{ps},0}$ planes. We repeat the process for different values of $\omega_{\text{ps},0}$. The results are shown in Fig. 2.11 for initial $\theta_{\text{lb}} = 60^\circ$ (and initial $\theta_{\text{sl}} = 0^\circ$). The range of $\omega_{\text{ps},0}$ has been chosen to illustrate the nonadiabatic, transadiabatic and fully adiabatic regimes.

As in the real system, our toy model exhibits periodic/quasiperiodic solutions and chaotic zones, and the level of chaos is determined by the parameter $\omega_{\text{ps},0}$. If we use the spreads of θ_{sl} and θ_{sb} as a measure of chaos, we see that the system generally becomes more chaotic with increasing $\omega_{\text{ps},0}$, until $\omega_{\text{ps},0}$ reaches ~ 5 , beyond which the system becomes fully-adiabatic ($\theta_{\text{sl}} \rightarrow 0$ and θ_{sb} approaches a constant). However, multiple periodic islands exist in the ocean of chaos. Figure 2.12 illustrates the time evolution of θ_{sl} and θ_{sb} in several of these periodic islands, along with an example of chaotic evolution. Figure 2.13 compares $\delta(t) = |\hat{\mathbf{S}}_{\text{real}}(t) - \hat{\mathbf{S}}_{\text{shadow}}(t)|$ (where the shadow trajectory has an initial condition nearly identical to the real one) for the different cases, clearly showing the difference between the periodic islands and chaotic evolution.

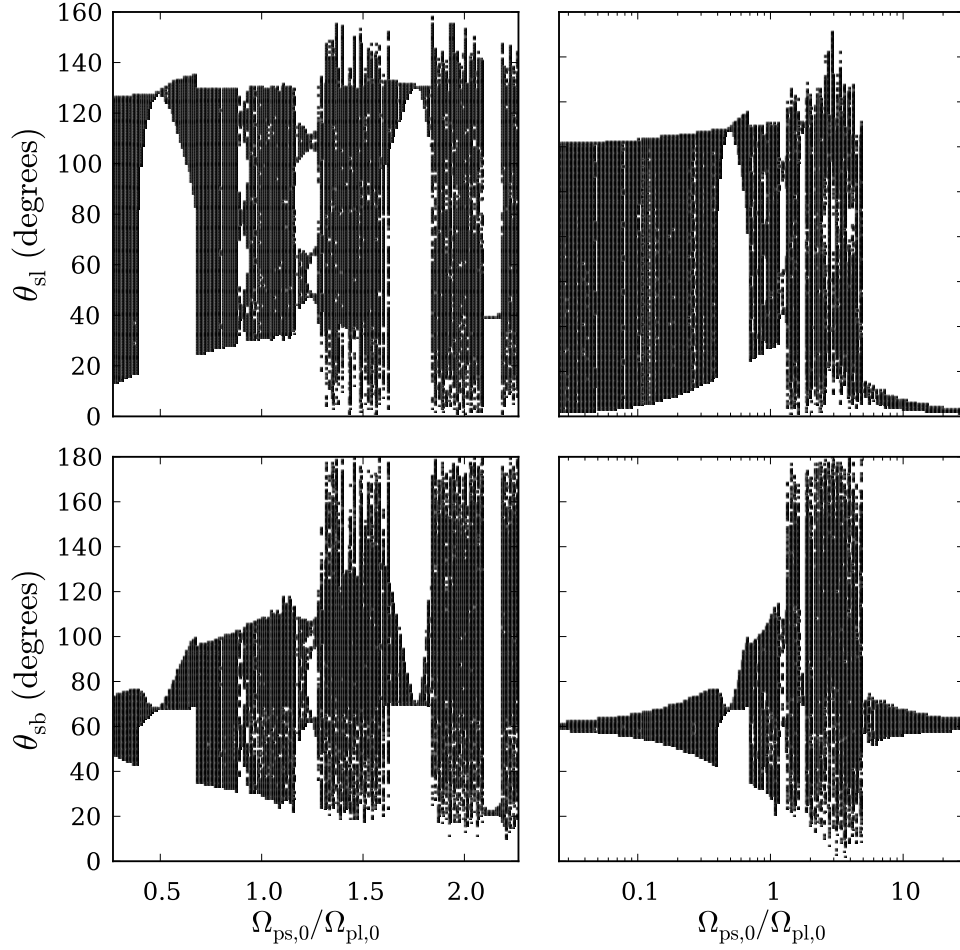


Figure 2.11: Angles θ_{sl} and θ_{sb} evaluated at maximum eccentricity (where $\Omega_0 t = \pi, 3\pi, 5\pi \dots$ for 1000 cycles) as functions of $\omega_{\text{ps},0} \equiv \Omega_{\text{ps},0}/\Omega_{\text{pl},0}$. The initial angle between $\hat{\mathbf{L}}$ and $\hat{\mathbf{L}}_b$ is $\theta_{\text{lb}}^0 = 60^\circ$, and $\hat{\mathbf{S}}$ and $\hat{\mathbf{L}}$ are initially aligned. The range of $\omega_{\text{ps},0}$ (on the logarithmic scale) in the right panels is chosen to illustrate the behavior of the three regimes (nonadiabatic, transadiabatic, and fully adiabatic). The narrow range of $\omega_{\text{ps},0}$ (on the linear scale) in the left panels exhibits the existence of periodic and quasiperiodic islands within the (chaotic) transadiabatic zones.

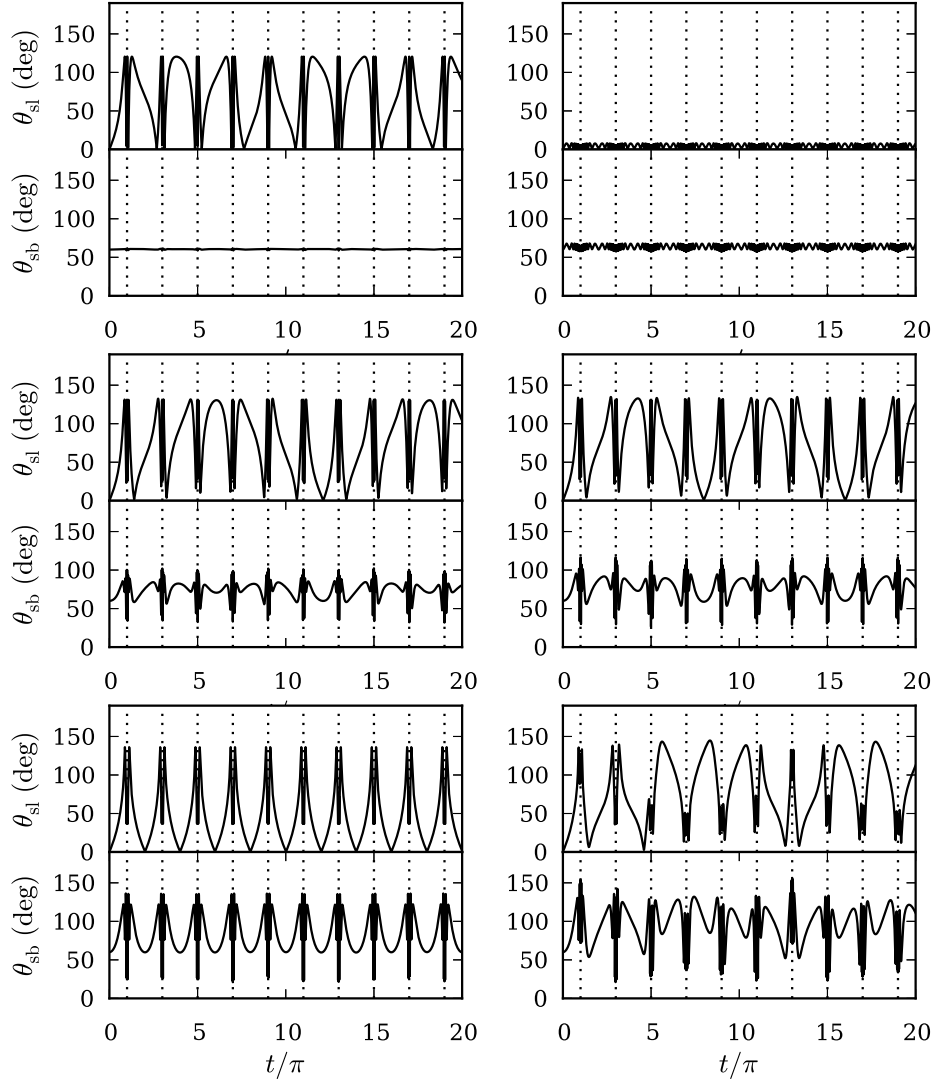


Figure 2.12: Angles θ_{sl} and θ_{sb} as functions of time, demonstrating the various behaviors of different orbits shown in Figure 2.11, including the three distinct regimes, and the difference between periodic and chaotic evolution in the transadiabatic regime. Time is in units of $\Omega_0 = 1$ (Eq. 2.15), and has been scaled by π . The dashed lines, included for reference, are located at odd-integers (when the system is at maximum eccentricity). *Upper left panel:* $\omega_{\text{ps},0} \equiv \Omega_{\text{ps},0}/\Omega_{\text{pl},0} = 0.023$, nonadiabatic, so that $\theta_{\text{sb}} \approx \text{constant}$. *Upper right panel:* $\omega_{\text{ps},0} = 13.3$, fully adiabatic, so that $\theta_{\text{sl}} \approx \theta_{\text{sl}}^0 \approx 0$. *Middle left panel:* $\omega_{\text{ps},0} = 0.89$, transadiabatic but periodic, with period= 12π . *Middle right panel:* $\omega_{\text{ps},0} = 1.25$, transadiabatic but periodic, with period= 16π . *Bottom left panel:* $\omega_{\text{ps},0} = 2.13$, transadiabatic but periodic, with period= 2π . *Bottom right panel:* $\omega_{\text{ps},0} = 2.35$, transadiabatic, with no discernible periodic behavior, chosen to illustrate chaotic evolution. See also Fig. 2.13 for further comparison between periodic and chaotic evolution.

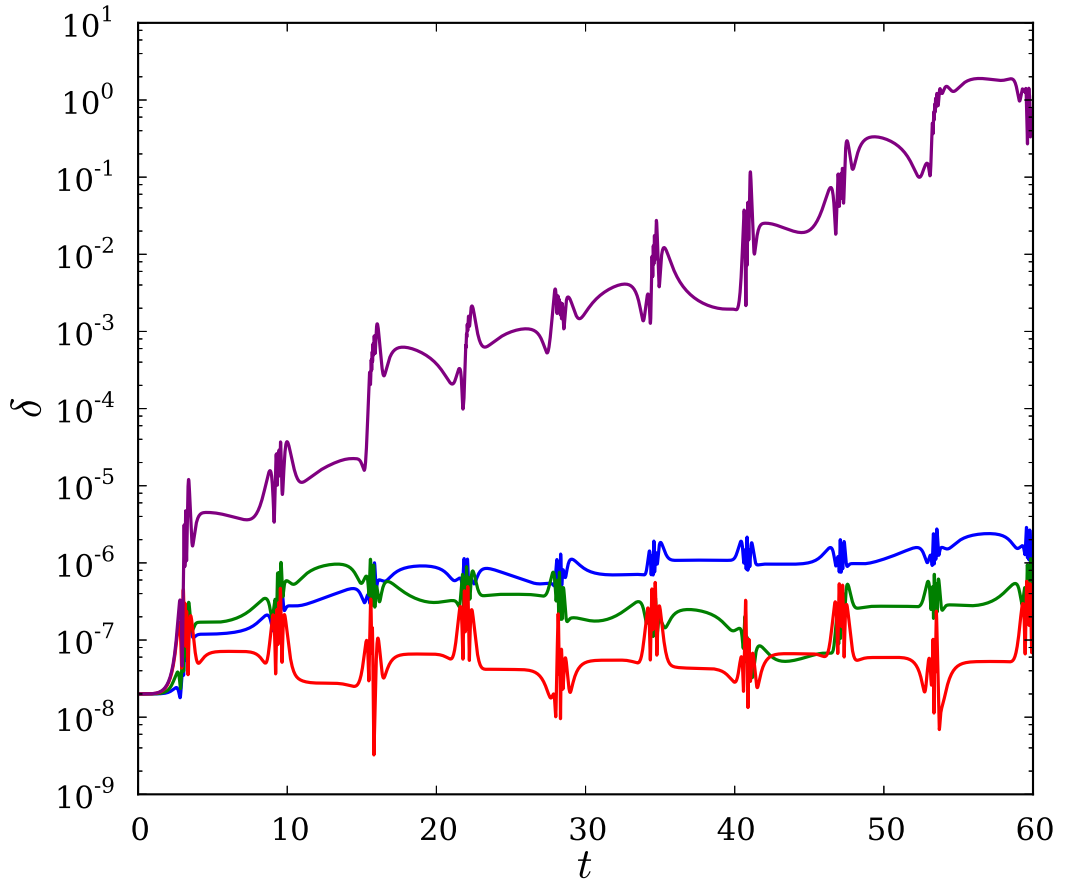


Figure 2.13: Difference (δ) in the spin vector $\hat{\mathbf{S}}$ between “real” and “shadow” trajectories for the four transadiabatic systems shown in Fig. 2.12 (bottom 4 panels), starting with an initial $\delta_0 = 10^{-8}$. Time is in units of $\Omega_0 = 1$. Three examples of periodic evolution are shown, where $\omega_{\text{ps},0} \equiv \Omega_{\text{ps},0}/\Omega_{\text{pl},0} = 0.89$ (blue), $\omega_{\text{ps},0} = 1.25$ (green), $\omega_{\text{ps},0} = 2.13$ (red), as well as a chaotic example $\omega_{\text{ps},0} = 2.35$ (purple). Compare with Figure 2.12. For the periodic examples δ remains small, while in the chaotic example, δ increases exponentially, and eventually saturates to its maximum value of $\delta = 2$.

CHAPTER 3

CHAOTIC DYNAMICS OF STELLAR SPIN DRIVEN BY PLANETS UNDERGOING LIDOV-KOZAI OSCILLATIONS: RESONANCES AND ORIGIN OF CHAOS

3.1 Abstract

Many exoplanetary systems containing hot Jupiters (HJs) are found to possess significant misalignment between the spin axis of the host star and the planet's orbital angular momentum axis. A possible channel for producing such misaligned HJs involves Lidov-Kozai oscillations of the planet's orbital eccentricity and inclination driven by a distant binary companion. We have recently shown (Storch et al., 2014) that a proto-HJ undergoing Lidov-Kozai oscillations can induce chaotic evolution of the spin axis of its host star. Here we explore the origin of the chaotic spin behavior and its various features in a simplified system where the secular oscillations of the planet's orbit are strictly periodic. Using Hamiltonian perturbation theory, we identify a set of secular spin-orbit resonances in the system, and show that resonance overlaps are responsible for the onset of wide-spread chaos in the evolution of stellar spin axis. The degree of chaos in the system depends on the adiabaticity parameter ϵ , proportional to the ratio of the Lidov-Kozai nodal precession rate and the stellar spin precession rate, and thus depends on the planet mass, semi-major axis and the stellar rotation rate. For systems with zero initial spin-orbit misalignment, our theory successfully explains the occurrence (as a function of ϵ) of large-scale chaotic vari-

The contents of this chapter were published in *MNRAS* as "Chaotic Dynamics of Stellar Spin Driven by Planets Undergoing Lidov-Kozai Oscillations: Resonances and Origin of Chaos" (Storch and Lai, 2015b)

ation, as well as regions of restricted chaos and quasi-periodic bands. Finally, we discuss a novel “adiabatic resonance advection” phenomenon, in which the spin-orbit misalignment, trapped in a resonance, gradually evolves as ϵ slowly changes. This phenomenon can occur for certain parameter regimes when tidal decay of the planetary orbit is included.

3.2 Introduction

A major surprise in exoplanetary astrophysics in recent years is the discovery of the misalignment between the orbital axis of the planet and the spin axis of the host star in systems containing “hot Jupiters”, giant planets with orbital periods $\lesssim 5$ days (Albrecht et al., 2012; Hébrard et al., 2008, 2010; Narita et al., 2009; Triaud et al., 2010; Winn et al., 2009). These planets cannot form in-situ, and must have migrated from a few AU’s distance from their host star to their current locations. Planet migration in protoplanetary disks is usually expected to produce aligned orbital and spin axes [however, see Bate et al. (2010); Batygin (2012); Batygin and Adams (2013); Lai (2014); Lai et al. (2011); Spalding and Batygin (2014)]. So the observed misalignments suggest that dynamical interaction between planets and/or companion star may play an important role in the planet’s inward migration.

One of the dynamical channels for the migration of giant planets involves Lidov-Kozai oscillations (Kozai, 1962; Lidov, 1962) of the planet’s orbit induced by a distant companion (star or planet). When the companion’s orbit is sufficiently inclined relative to the planetary orbit, the planet’s eccentricity undergoes excursions to large values while the orbital axis precesses with varying

inclination. Tidal dissipation in the planet at periastron reduces the orbital energy, leading to inward migration and circularization of the planet’s orbit (Correia et al., 2011; Fabrycky and Tremaine, 2007; Naoz et al., 2012; Petrovich, 2015*b*; Wu and Murray, 2003). A number of recent works have focused on the extreme evolution of the planetary orbit (such as orbital flip) when the octupole perturbing potential from the binary companion is included (Ford et al., 2000; Katz et al., 2011; Li et al., 2014; Liu et al., 2015; Naoz et al., 2011, 2013; Petrovich, 2015*b*).

In a recent paper [Storch et al. (2014); hereafter SAL], we have shown that during the Lidov-Kozai cycle, gravitational interaction between the planet and its oblate host star can lead to complex and chaotic evolution of the stellar spin axis, depending on the planet mass and the stellar rotation rate. In many cases, the variation of the stellar spin direction is much larger than the variation of the planet’s orbital axis. Moreover, in the presence of tidal dissipation, the complex spin evolution can leave an imprint on the final spin-orbit misalignment angle.

SAL discussed three qualitatively different regimes for the evolution of the spin-orbit misalignment angle θ_{sl} . These regimes depend on the ratio of the precession rate Ω_{pl} of the planetary orbital axis ($\hat{\mathbf{L}}$) around the (fixed) binary axis $\hat{\mathbf{L}}_b$, and the stellar precession rate Ω_{ps} driven by the planet (see Section 3.3): (i) For $|\Omega_{\text{pl}}| \gg |\Omega_{\text{ps}}|$ (“nonadiabatic” regime), the spin axis $\hat{\mathbf{S}}$ effectively precesses around $\hat{\mathbf{L}}_b$, maintaining a constant angle θ_{sb} between $\hat{\mathbf{S}}$ and $\hat{\mathbf{L}}_b$. (ii) For $|\Omega_{\text{ps}}| \gg |\Omega_{\text{pl}}|$ (“adiabatic” regime), the spin axis $\hat{\mathbf{S}}$ follows $\hat{\mathbf{L}}$ adiabatically as the latter evolves, maintaining an approximately constant θ_{sl} . (iii) For $|\Omega_{\text{ps}}| \sim |\Omega_{\text{pl}}|$ (“trans-adiabatic” regime), the evolution of $\hat{\mathbf{S}}$ is chaotic. However, the precise transitions between these regimes have not yet been explored in detail.

Since both Ω_{ps} and Ω_{pl} depend on eccentricity (Ω_{ps} also depends on θ_{sl}) and thus vary strongly during the Lidov-Kozai cycle, a useful dimensionless ratio that characterizes the evolution of $\hat{\mathbf{S}}$ is the “adiabaticity parameter”,

$$\epsilon = \left| \frac{\Omega_{\text{pl}}}{\Omega_{\text{ps}}} \right|_{e, \theta_{\text{sl}}=0}, \quad (3.1)$$

where the subscript implies that the quantity is evaluated at $e = 0$ and $\theta_{\text{sl}} = 0$. So ϵ is constant during the Lidov-Kozai cycle. For a planet of mass M_p initially in a nearly circular orbit around a star of mass M_* and radius R_* at a semimajor axis a , with a binary companion of mass M_b , semimajor axis a_b (and eccentricity $e_b = 0$), the adiabaticity parameter is given by

$$\begin{aligned} \epsilon = & 1.17 \left(\frac{k_*}{2k_q} \right) \left(\frac{R_*}{1 R_\odot} \right)^{-3/2} \left(\frac{\hat{\Omega}_*}{0.1} \right)^{-1} \left(\frac{M_b}{10^3 M_p} \right) \times \\ & \times \left(\frac{a}{1 \text{ AU}} \right)^{9/2} \left(\frac{a_b}{300 \text{ AU}} \right)^{-3} |\cos \theta_{\text{lb}}^0|, \end{aligned} \quad (3.2)$$

where $\Omega_* = (GM_*/R_*^3)^{1/2}\hat{\Omega}_*$ is the rotation rate of the star, $k_*/(2k_q) \sim 1$, and θ_{lb}^0 is the initial (at $e = 0$) planetary orbital inclination relative to the binary. Figure 3.1 shows a “bifurcation” diagram that illustrates the complex dynamics of the spin-orbit misalignment angle θ_{sb} as ϵ is varied (by changing M_p while keeping other parameters fixed). We see that in this example, wide-spread chaos occurs for $\epsilon \gtrsim 0.14$, while the evolution of θ_{sl} is largely regular for $\epsilon \lesssim 0.14$. However, in the chaotic regime, there exist multiple periodic islands in which θ_{sl} evolves regularly. Interestingly, even in the “adiabatic” regime, there exist regions of “restricted chaos”, in which θ_{sl} evolves chaotically but within a restricted range*. .

Widespread chaos in dynamical systems can be understood as arising from

*Note that, displayed in this way, it is not entirely certain that a given region of apparently “regular” behavior (i.e. not evincing obvious chaotic spread) is indeed quasi-periodic. Rather, it is possible that such a region is still chaotic but tightly isolated. Thus, Fig. 3.1 should be considered suggestive.

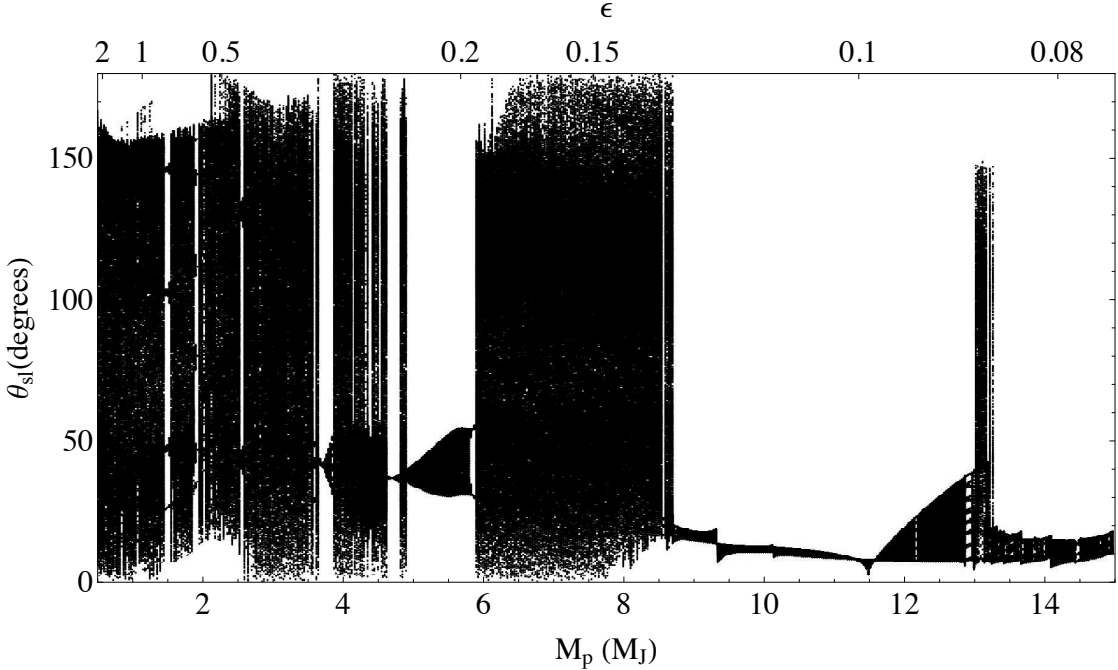


Figure 3.1: “Bifurcation” diagram of the spin-orbit misalignment angle versus planet mass and the adiabaticity parameter ϵ . For each planet mass M_p , we evolve the secular orbital evolution equations including the effects of short-range forces (periastron advances due to General Relativity, the stellar quadrupole, and the planet’s rotational bulge and tidal distortion) together with the stellar spin precession equation, starting with $\theta_{\text{sl}} = 0$, for ~ 1500 Lidov-Kozai cycles, and record θ_{sl} every time the orbital eccentricity reaches a maximum. The parameters for this plot are $a = 1$ AU, $a_b = 200$ AU, $e_0 = 0.01$, $\theta_{\text{lb}}^0 = 85^\circ$, $\hat{\Omega}_* = 0.03$. This figure is an extended version of Fig. 4 of Storch et al. (2014), demonstrating the complexity of the trans-adiabatic and even the adiabatic regimes of the spin dynamics.

overlaps of resonances in the phase space (Chirikov, 1979). What are the resonances underlying the chaotic spin behaviour found in SAL and Fig. 3.1? Since Ω_{pl} and Ω_{ps} are both strong functions of time, the answer to this question is not obvious *a priori*, even in the ideal case when the planetary orbit undergoes strictly periodic Lidov-Kozai oscillations. Using Hamiltonian perturbation theory, we show in this paper that a spin-orbit resonance occurs when the time-averaged spin precession frequency equals an integer multiple of the Lidov-Kozai oscillation frequency. We then demonstrate that overlapping resonances

can indeed explain the onset of chaos in the dynamics of stellar spin, more specifically the “adiabatic” to “trans-adiabatic” transition. We also show that many of the limited chaotic excursions found numerically in the “adiabatic” regime can be understood from overlapping resonances. Finally we show that the consideration of resonances can lead to a novel “adiabatic resonance advection” phenomenon when tidal decay of the planetary orbit is included.

The chaotic dynamics of stellar spin studied in this paper has some resemblance to the well-known problem of obliquity dynamics of Mars and other terrestrial planets (Laskar and Robutel, 1993; Li and Batygin, 2014; Touma and Wisdom, 1993). In that problem, a spin-orbit resonance arises when the spin precession frequency Ω_{ps} of Mars around its orbital axis \hat{L} driven by the Sun matches one of the eigen-frequencies (Ω_{pl} 's) for the variation of \hat{L} due to interactions with other planets. Only a small number of Ω_{pl} 's are relevant in the Solar System, and except for the $\cos \theta_{sl}$ factor, Ω_{ps} is approximately constant in time. Thus the analysis of overlapping resonances is relatively straightforward. For the problem studied in this paper, by contrast, both $(\Omega_{ps} / \cos \theta_{sl})$ and Ω_{pl} are strong functions of time, so the dynamics of the stellar spin axis exhibits a much richer set of behaviors.

Our paper is organized as follows. In Section 3.3, we review the physical system and its ingredients. In Section 3.4, we develop a Hamiltonian formulation of the problem, and derive the resonance condition for spin-orbit coupling. In Section 3.5, we discuss the behaviour of the system under the influence of a single resonance. In Section 3.6, we demonstrate the onset of chaos in the presence of two or more overlapping resonances, and derive the overlap criterion. In Section 3.7, we consider the full Lidov-Kozai driven spin precession prob-

lem, and demonstrate that resonance overlaps can explain the onset of chaos, as well as other “quasi-chaotic” features in the spin evolution. In Section 3.8, we consider the effect of a slowly evolving adiabaticity parameter, as a simplified model of tidal dissipation, and present a proof of concept for understanding the novel “adiabatic resonance advection” phenomenon. We summarize our key findings in Section 3.9.

3.3 Review of the Physical System and Ingredients

3.3.1 Lidov-Kozai (LK) Oscillations

We consider a planet of mass M_p in orbit around a host star of mass M_\star (with $M_\star \gg M_p$), and a distant companion of mass M_b . The host star and companion are in a static orbit with semi-major axis a_b , eccentricity e_b , and angular momentum axis $\hat{\mathbf{L}}_b$, which defines the invariant plane of the system. The planet’s orbit has semi-major axis a , eccentricity e , angular momentum axis $\hat{\mathbf{L}}$ and inclination θ_{lb} (the angle between $\hat{\mathbf{L}}$ and $\hat{\mathbf{L}}_b$). In the Lidov-Kozai (LK) mechanism, the quadrupole potential of the companion causes the orbit of the planet to undergo oscillations of both e and θ_{lb} , as well as nodal precession ($\dot{\Omega}$) and pericenter advance ($\dot{\omega}$), while conserving $\mathbf{L} \cdot \hat{\mathbf{L}}_b$. The equations governing these oscillations

are given by

$$\frac{de}{dt} = t_k^{-1} \frac{15}{8} e \sqrt{1 - e^2} \sin 2\omega \sin^2 \theta_{lb}, \quad (3.3)$$

$$\frac{d\Omega}{dt} = t_k^{-1} \frac{3}{4} \frac{\cos \theta_{lb} (5e^2 \cos^2 \omega - 4e^2 - 1)}{\sqrt{1 - e^2}}, \quad (3.4)$$

$$\frac{d\theta_{lb}}{dt} = -t_k^{-1} \frac{15}{16} \frac{e^2 \sin 2\omega \sin 2\theta_{lb}}{\sqrt{1 - e^2}}, \quad (3.5)$$

$$\frac{d\omega}{dt} = t_k^{-1} \frac{3 [2(1 - e^2) + 5 \sin^2 \omega (e^2 - \sin^2 \theta_{lb})]}{4\sqrt{1 - e^2}}, \quad (3.6)$$

where t_k^{-1} is the characteristic frequency of oscillation, given by

$$t_k^{-1} = \frac{n}{(1 - e_b^2)^{3/2}} \left(\frac{M_b}{M_\star} \right) \left(\frac{a}{a_b} \right)^3, \quad (3.7)$$

where $n = \sqrt{GM_\star/a^3}$ is the planet's mean motion. In this paper, we neglect all effects associated with short-range forces (General Relativity, tidal interaction, etc) and the octupole potential from the binary.

Equations (3.3)-(3.6) admit two types of analytical solutions, distinguished by whether the argument of pericenter ω circulates or librates. In the present work we will consider only the circulating case by taking $\omega = 0$ at $t = 0$. (However, we note that so long as the initial eccentricity e_0 is very small, the librating case would yield virtually the same eccentricity function. Thus our results apply, in fact, to both librating and circulating cases.) The conservation of the projected angular momentum $\mathbf{L} \cdot \hat{\mathbf{L}}_b$ gives

$$x \cos^2 \theta_{lb} = x_0 \cos^2 \theta_{lb}^0 \equiv h, \quad (3.8)$$

where

$$x \equiv 1 - e^2, \quad (3.9)$$

and energy conservation gives

$$e^2 (5 \sin^2 \theta_{lb} \sin^2 \omega - 2) = -2e_0^2. \quad (3.10)$$

For the initial eccentricity $e_0 \approx 0$, the above equations imply that the maximum eccentricity occurs at $\omega = \pi/2, 3\pi/2$, where $\sin^2 \theta_{lb} = 2/5$ and

$$e_{\max} \simeq \left(1 - \frac{5}{3} \cos^2 \theta_{lb}^0\right)^{1/2}. \quad (3.11)$$

Combining eqs. (3.8)-(3.10) with eq. (3.3), the time evolution of eccentricity can be solved explicitly (Kinoshita and Nakai, 1999):

$$x = x_0 + (x_1 - x_0) \operatorname{cn}^2(\theta, k^2), \quad (3.12)$$

where

$$\theta = \frac{K}{\pi} (n_e t + \pi), \quad (3.13)$$

$$n_e = t_k^{-1} \frac{6\pi\sqrt{6}}{8K} \sqrt{x_2 - x_1}, \quad (3.14)$$

$$k^2 = \frac{x_0 - x_1}{x_2 - x_1}. \quad (3.15)$$

In the above expressions $\operatorname{cn}(\theta, k^2)$ is the Jacobi elliptic cn function with modulus k^2 , n_e is the “mean motion” for the eccentricity variation (i.e. $2\pi/n_e$ is the period of the eccentricity oscillations), K is the complete elliptic integral of the first kind with modulus k^2 , x_0 is the value of x at $t = 0$, and x_1 and x_2 ($x_1 < x_2$) are solutions to the quadratic equation

$$x_{1,2}^2 - \frac{1}{3} (5 + 5h - 2x_0) x_{1,2} + \frac{5}{3}h = 0, \quad (3.16)$$

obtained from eqs. (3.8)-(3.10) with $\sin^2 \omega = 1$. The other orbital elements can be expressed as a function of x . Note that the period of ω circulation (ω goes from 0 to 2π) is $4\pi/n_e$.

For the remainder of this work, we use a single $x(t)$ solution in our analysis, corresponding to $e_0 = 0.01$ (so $x_0 = 1 - (0.01)^2$) and $\theta_{lb}^0 = 85^\circ$. By selecting this very high initial inclination, we effectively maximize the degree of chaos in the system.

3.3.2 Stellar spin precession

Because of the rotation-induced oblateness, the star is torqued by the planet, causing its spin axis $\hat{\mathbf{S}}$ to precess around the planet's orbital axis $\hat{\mathbf{L}}$ according to the equation

$$\frac{d\hat{\mathbf{S}}}{dt} = \Omega_{ps}\hat{\mathbf{L}} \times \hat{\mathbf{S}}, \quad (3.17)$$

where the precession frequency Ω_{ps} is given by

$$\Omega_{ps} = -\frac{3GM_p(I_3 - I_1)}{2a^3(1 - e^2)^{3/2}} \frac{\cos\theta_{sl}}{S}. \quad (3.18)$$

Here I_3 and I_1 are the principal moments of inertia of the star, S is the magnitude of the spin angular momentum, and θ_{sl} is the angle between $\hat{\mathbf{S}}$ and $\hat{\mathbf{L}}$. Our goal is to characterize how θ_{sl} changes as a function of time as the planet's orbit undergoes LK oscillations. Since e changes during the LK cycle, we write the spin precession frequency as

$$\Omega_{ps}(t) \equiv -\alpha(t)\cos\theta_{sl} = -\frac{\alpha_0}{x^{3/2}}\cos\theta_{sl}, \quad (3.19)$$

where

$$\begin{aligned} \alpha_0 &= \frac{3GM_p(I_3 - I_1)}{2a^3I_3\Omega_\star} \\ &= 1.19 \times 10^{-8} \left(\frac{2\pi}{1\text{yr}}\right) \left(\frac{2k_q}{k_\star}\right) \left(\frac{10^3M_p}{M_\star}\right) \left(\frac{\hat{\Omega}_\star}{0.05}\right) \times \\ &\quad \times \left(\frac{a}{1\text{AU}}\right)^{-3} \left(\frac{M_\star}{M_\odot}\right)^{1/2} \left(\frac{R_\star}{R_\odot}\right)^{3/2}. \end{aligned} \quad (3.20)$$

Here we have used $(I_3 - I_1) \equiv k_q M_\star R_\star^2 \hat{\Omega}_\star^2$, with $\hat{\Omega}_\star = \Omega_\star/(GM_\star/R_\star^3)^{1/2}$ the dimensionless stellar rotation rate, and $S = I_3\Omega_s \equiv k_\star M_\star R_\star^2 \Omega_\star$. For a solar-type star, $k_q \approx 0.05$, and $k_\star \approx 0.1$ (Claret and Gimenez, 1992).

During the LK cycle, the planet's orbital axis $\hat{\mathbf{L}}$ changes in two distinct ways: nodal precession around $\hat{\mathbf{L}}_b$ at the rate $\Omega_{pl}(t) = \dot{\Omega}$, and nutation at the rate $\dot{\theta}_{lb}(t)$.

Each of these acts as a driving force for the stellar spin. The variation of $\theta_{lb}(t)$ plays an important role as well since it affects $\hat{\mathbf{L}}(t)$ directly [see Eq. (3.30) below]. Note that the back-reaction torque from the stellar quadrupole on the orbit also acts to make $\hat{\mathbf{L}}$ precess around $\hat{\mathbf{S}}$; we neglect this back-reaction throughout this paper in order to focus on the spin dynamics with “pure” orbital LK cycles. Based on the analytical LK solution given in the previous sub-section, we find Ω_{pl} is given by

$$\Omega_{pl} = \dot{\Omega} = \Omega_{pl,0} \left[1 - \frac{2(x_0 - h)}{x - h} \right], \quad (3.21)$$

with x is given by Eq. (3.12) and

$$\Omega_{pl,0} = \frac{3}{4t_k} \sqrt{h} \simeq \frac{3}{4t_k} |\cos \theta_{lb}^0|, \quad (3.22)$$

where the second equality assumes $e_0 \simeq 0$. The angle θ_{lb} and its derivative are given by $\cos \theta_{lb} = \sqrt{h/x}$ and $\dot{\theta}_{lb} = \dot{x} \cos \theta_{lb} / (2x \sin \theta_{lb})$. Note that $\Omega_{pl}(t) < 0$. The quantity $\Omega_{pl,0}$ specifies the value of $|\Omega_{pl}|$ at $e = e_0 \simeq 0$, and is explicitly given by

$$\begin{aligned} \Omega_{pl,0} \simeq & \frac{3}{4} \left(\frac{2\pi}{10^6 \text{yr}} \right) \left(\frac{M_b}{M_\star} \right) \left(\frac{M_\star}{M_\odot} \right)^{1/2} \left(\frac{a}{1 \text{AU}} \right)^{3/2} \times \\ & \times \left(\frac{a_b}{100 \text{AU}} \right)^{-3} \frac{|\cos \theta_{lb}^0|}{(1 - e_b^2)^{3/2}}, \end{aligned} \quad (3.23)$$

for $x_0 = 1 - e_0^2 \simeq 1$. Taking the ratio of this and Eq. (3.20) yields the adiabaticity parameter

$$\epsilon = \frac{\Omega_{pl,0}}{\alpha_0}, \quad (3.24)$$

as given in Section 3.2 [see Eq. (3.2)].

3.4 Hamiltonian Formulation of Spin Dynamics and Resonances

3.4.1 The Spin Hamiltonian

In the inertial frame, the Hamiltonian governing the dynamics of stellar spin $\mathbf{S} = S\hat{\mathbf{S}}$ is

$$H = \frac{S^2}{2I_3} + \frac{GM_p(I_3 - I_1)}{4a^3(1 - e^2)^{3/2}} \left[1 - 3(\hat{\mathbf{S}} \cdot \hat{\mathbf{L}})^2 \right]. \quad (3.25)$$

The first term is the (constant) rotational kinetic energy and will be dropped henceforth, and the second term is the orbital-averaged interaction energy between the planet and stellar quadrupole. Since the evolution of the orbital eccentricity $e(t)$ is fixed, we only need to consider the last term in Eq. (3.25):

$$H_0 \equiv -\frac{1}{2}\alpha(t)S \left(\hat{\mathbf{S}} \cdot \hat{\mathbf{L}} \right)^2. \quad (3.26)$$

Noting that $\hat{\mathbf{S}} \cdot \hat{\mathbf{L}}_b$ and ϕ_s (the precessional phase of $\hat{\mathbf{S}}$ around $\hat{\mathbf{L}}_b$) are conjugate variables, we can check that the Hamiltonian equations for H_0 lead to Eq. (3.17).

Since we are interested in the variation of θ_{sl} , it is convenient to work in the rotating frame in which $\hat{\mathbf{L}}$ is a constant. In this frame, the Hamiltonian takes the form (Kinoshita, 1993)

$$H_{\text{rot}} = H - \mathbf{R} \cdot \mathbf{S}, \quad (3.27)$$

where the rotation “matrix” is

$$\mathbf{R} = \Omega_{\text{pl}}\hat{\mathbf{L}}_b + \dot{\theta}_{\text{lb}} \left(\frac{\hat{\mathbf{L}}_b \times \hat{\mathbf{L}}}{\sin \theta_{\text{lb}}} \right). \quad (3.28)$$

To write down the explicit expression for H_{rot} , we set up a Cartesian coordinate system with the z -axis along $\hat{\mathbf{L}}$, and the x -axis pointing to the ascending node

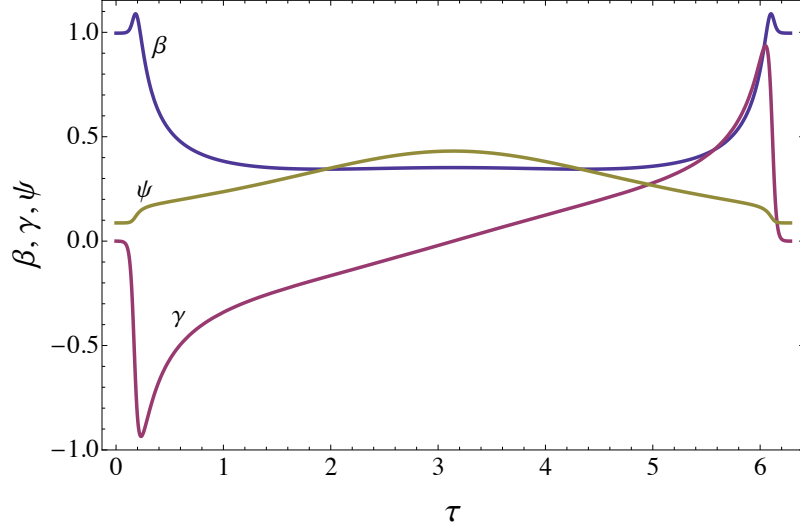


Figure 3.2: Plots of the “shape” functions $\beta(\tau)$ (blue), $\gamma(\tau)$ (red), and $\psi(\tau)$ (brown), for $x_0 = 1 - 0.01^2$ and $\cos \theta_{\text{lb}}^0 = 85^\circ$.

of the planet’s orbit in the invariant plane (the plane perpendicular to $\hat{\mathbf{L}}_b$). The spin axis is characterized by θ_{sl} and the precessional phase ϕ (the longitude of the node of the star’s rotational equator in the xy -plane), such that

$$\hat{\mathbf{S}} = \sin \theta_{\text{sl}} (\sin \phi \hat{x} - \cos \phi \hat{y}) + \cos \theta_{\text{sl}} \hat{z}. \quad (3.29)$$

Setting $S = 1$ and suppressing the subscript “rot”, we have

$$H = -\frac{1}{2}\alpha(t) (\cos \theta_{\text{sl}})^2 - \dot{\theta}_{\text{lb}}(t) \sin \theta_{\text{sl}} \sin \phi - \Omega_{\text{pl}}(t) [\cos \theta_{\text{lb}}(t) \cos \theta_{\text{sl}} - \sin \theta_{\text{lb}}(t) \sin \theta_{\text{sl}} \cos \phi], \quad (3.30)$$

Note that ϕ and $\cos \theta_{\text{sl}}$ are the conjugate pair of variables we wish to solve for. Since in this work we focus on the behavior of the system close to the adiabatic regime, in general the first term in the Hamiltonian dominates, while the others can be treated as perturbations. In the limit of no perturbation, the zeroth order Hamiltonian $H_0 \equiv -\frac{1}{2}\alpha(t) \cos^2 \theta_{\text{sl}}$ indeed conserves $\cos \theta_{\text{sl}}$, as it should based on the arguments given in Section 3.2.

3.4.2 The Rescaled Hamiltonian

The equations of motion for ϕ and $\cos \theta_{\text{sl}}$ can be derived from the Hamiltonian (3.30), and are given by

$$\begin{aligned} \frac{d\phi}{dt} &= -\alpha(t) \cos \theta_{\text{sl}} + \dot{\theta}_{\text{lb}}(t) \frac{\cos \theta_{\text{sl}}}{\sin \theta_{\text{sl}}} \sin \phi \\ &\quad - \Omega_{\text{pl}}(t) \left[\cos \theta_{\text{lb}}(t) + \sin \theta_{\text{lb}}(t) \frac{\cos \theta_{\text{sl}}}{\sin \theta_{\text{sl}}} \cos \phi \right], \end{aligned} \quad (3.31)$$

$$\begin{aligned} \frac{d \cos \theta_{\text{sl}}}{dt} &= \Omega_{\text{pl}}(t) \sin \theta_{\text{lb}}(t) \sin \theta_{\text{sl}} \sin \phi \\ &\quad + \dot{\theta}_{\text{lb}}(t) \sin \theta_{\text{sl}} \cos \phi. \end{aligned} \quad (3.32)$$

These equations can be simplified by introducing a rescaled time variable τ such that $d\tau \propto \alpha(t)dt$, i.e.,

$$\tau(t) = \frac{n_e}{\bar{\alpha}} \int_0^t \alpha(t') dt', \quad (3.33)$$

where

$$\bar{\alpha} \equiv \frac{n_e}{2\pi} \int_0^{2\pi/n_e} \alpha(t) dt. \quad (3.34)$$

Here the factor of $n_e/\bar{\alpha}$ is used to ensure that all of the time-dependent forcing functions introduced in Section 3.3 have a period of 2π in τ -space, for convenience. The equations of motion in τ space are then given by

$$\begin{aligned} \frac{d\phi}{d\tau} &= \frac{\bar{\alpha}}{n_e} \left\{ -\cos \theta_{\text{sl}} + \frac{\dot{\theta}_{\text{lb}}(\tau)}{\alpha(\tau)} \frac{\cos \theta_{\text{sl}}}{\sin \theta_{\text{sl}}} \sin \phi \right. \\ &\quad \left. - \frac{\Omega_{\text{pl}}(\tau)}{\alpha(\tau)} \left[\cos \theta_{\text{lb}}(\tau) + \sin \theta_{\text{lb}}(\tau) \frac{\cos \theta_{\text{sl}}}{\sin \theta_{\text{sl}}} \cos \phi \right] \right\}, \end{aligned} \quad (3.35)$$

$$\begin{aligned} \frac{d \cos \theta_{\text{sl}}}{d\tau} &= \frac{\bar{\alpha}}{n_e} \left\{ \frac{\Omega_{\text{pl}}(\tau)}{\alpha(\tau)} \sin \theta_{\text{lb}}(\tau) \sin \theta_{\text{sl}} \sin \phi \right. \\ &\quad \left. + \frac{\dot{\theta}_{\text{lb}}(\tau)}{\alpha(\tau)} \sin \theta_{\text{sl}} \cos \phi \right\}. \end{aligned} \quad (3.36)$$

The corresponding Hamiltonian is (Colombo, 1966; Henrard and Murigande, 1987)

$$H'(p, \phi, \tau) = \frac{\bar{\alpha}}{n_e} \left\{ -\frac{1}{2} p^2 + \epsilon \psi(\tau) p - \epsilon \sqrt{1 - p^2} \left[\beta(\tau) \cos \phi + \gamma(\tau) \sin \phi \right] \right\}, \quad (3.37)$$

where we have defined $p \equiv \cos \theta_{\text{sl}}$, and

$$\epsilon \beta(\tau) = -\frac{\Omega_{\text{pl}}(\tau)}{\alpha(\tau)} \sin \theta_{\text{lb}}(\tau), \quad (3.38)$$

$$\epsilon \gamma(\tau) = \frac{\dot{\theta}_{\text{lb}}(\tau)}{\alpha(\tau)}, \quad (3.39)$$

$$\epsilon \psi(\tau) = -\frac{\Omega_{\text{pl}}(\tau)}{\alpha(\tau)} \cos \theta_{\text{lb}}(\tau). \quad (3.40)$$

Since $\epsilon = \Omega_{\text{pl},0}/\alpha_0$ [see Eq. (3.24)], the functions $\beta(\tau)$, $\gamma(\tau)$ and $\psi(\tau)$ depend only on the “shape” of the orbit, i.e., on $e(\tau)$ (with τ varying from 0 to 2π). For a given θ_{lb}^0 (and $e_0 \simeq 0$), these functions are fixed and do not depend on any other parameters. Figure 3.2 depicts these functions for $\theta_{\text{lb}}^0 = 85^\circ$.

3.4.3 Fourier Decomposition and Resonances

We now expand $\beta(\tau)$, $\gamma(\tau)$, and $\psi(\tau)$ in Fourier series. Since β and ψ are symmetric with respect to $\tau = \pi$, while γ is anti-symmetric (see Fig. 3.2), we have

$$\beta(\tau) = \sum_{M=0}^{\infty} \beta_M \cos M\tau, \quad (3.41)$$

$$\gamma(\tau) = \sum_{M=1}^{\infty} \gamma_M \sin M\tau, \quad (3.42)$$

$$\psi(\tau) = \sum_{M=0}^{\infty} \psi_M \cos M\tau. \quad (3.43)$$

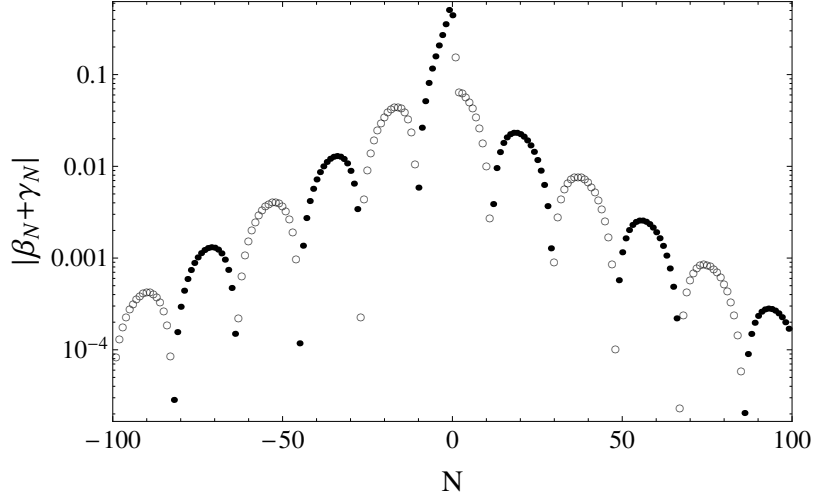


Figure 3.3: Sum of the Fourier coefficients as a function of the resonance number N . Filled circles are for positive $\beta_N + \gamma_N$, and open circles are for negative $\beta_N + \gamma_N$. Note that $\beta_{-N} = \beta_N$, while $\gamma_{-N} = -\gamma_N$, which accounts for the lack of symmetry across $N = 0$.

Obviously, β_M , γ_M and ψ_M depend only on the “shape” of the orbit $e(\tau)$. The Hamiltonian (3.37) becomes

$$\begin{aligned} H' = \frac{\bar{\alpha}}{n_e} & \left\{ -\frac{1}{2}p^2 + \epsilon \psi_0 p + \epsilon p \sum_{M=1}^{\infty} \psi_M \cos Mt \right. \\ & - \frac{\epsilon}{2} \sqrt{1-p^2} \sum_{M=0}^{\infty} \left[(\beta_M + \gamma_M) \cos(\phi - M\tau) \right. \\ & \left. \left. + (\beta_M - \gamma_M) \cos(\phi + M\tau) \right] \right\}. \end{aligned} \quad (3.44)$$

Note that γ_0 is not defined in Eq. (3.42). For convenience of notation, we will set $\gamma_0 = \beta_0$ [see discussion following Eq. (3.52)].

A resonance occurs when the argument of the cosine function, $(\phi \pm M\tau)$, in the Hamiltonian (3.44) is slowly varying, i.e., when $d\phi/d\tau = N$, where N is a positive or negative integer. In the perturbative regime ($\epsilon \ll 1$) of interest in this paper, the Hamiltonian is dominated by $H_0 = (\bar{\alpha}/n_e)(-p^2/2)$, and we have $d\phi/d\tau \simeq -\bar{\alpha}p/n_e$. So the resonance condition becomes

$$\bar{\Omega}_{\text{ps}} = -\bar{\alpha} \cos \theta_{\text{sl}} = N n_e, \quad \text{with } N = 0, \pm 1, \pm 2, \pm 3, \dots \quad (3.45)$$

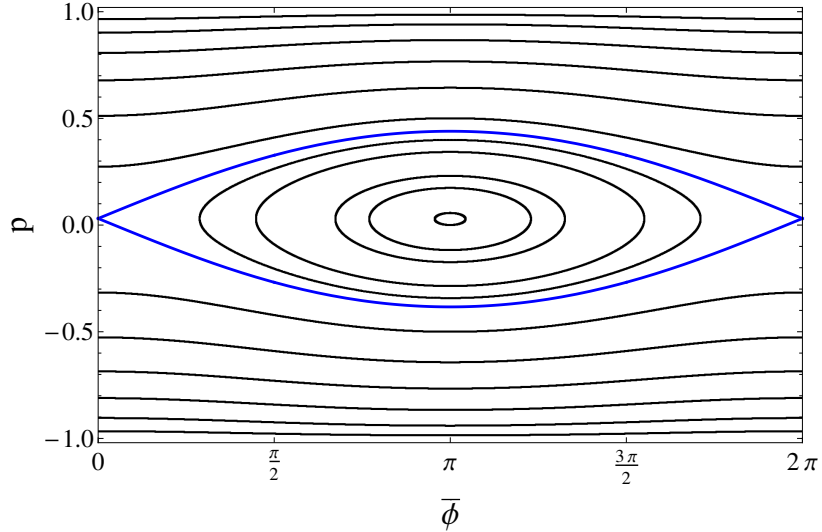


Figure 3.4: Sample constant-energy curves for the $N = 0$ single-resonance Hamiltonian [given by Eq. (3.52)], constructed by starting with a variety of initial conditions (corresponding to unique values of E) and evolving the equations of motion derived from the Hamiltonian. The blue line shows the analytical prediction for the separatrix. The adiabaticity parameter is $\epsilon = 0.1$, i.e. $\alpha_0 = 10\Omega_{\text{pl},0}$.

i.e. the averaged stellar precession frequency $\bar{\Omega}_{\text{ps}}$ equals an integer multiple of the mean eccentricity oscillation frequency in the LK cycle. Note that, since $\cos \theta_{\text{sl}}$ spans the range $\{-1, 1\}$, this means that for any given value of $\bar{\alpha}$ and of n_e there exist multiple resonances. We may then define the zeroth-order resonant momentum corresponding to each resonance as

$$p_N = (\cos \theta_{\text{sl}})_N = -\frac{N n_e}{\bar{\alpha}}. \quad (3.46)$$

Since $|p_N|$ cannot exceed 1, we also see that there exists a “maximum resonance order”,

$$N_{\text{max}} = \left\lfloor \frac{\bar{\alpha}}{n_e} \right\rfloor = \left\lfloor \frac{1}{\epsilon} \mathcal{N}(\cos \theta_{\text{lb}}^0; e_0) \right\rfloor, \quad (3.47)$$

such that $N = N_{\text{max}}$ is the maximum allowed prograde (“positive”) resonance, and $N = -N_{\text{max}}$ is the maximum allowed retrograde (“negative”) resonance.

Note that the resonant momentum p_N can be written as

$$p_N \simeq -\frac{N}{N_{\text{max}}}. \quad (3.48)$$

Thus, the stellar spin evolution is perturbed by a set of $(2N_{\max} + 1)$ resonances. The function \mathcal{N} depends mainly on $\cos \theta_{lb}^0$, and weakly on e_0 (assuming $e_0 \ll 1$). For $\theta_{lb}^0 = 85^\circ$ (adopted for our numerical examples in this paper), we find $\mathcal{N} = 0.98$.

The $N = -N_{\max}$ resonance is of particular interest, as it is the closest resonance to $p_N = 1$, the aligned configuration. Thus, if a star-planet system is born with the stellar spin axis and the planet orbital axis aligned, this resonance is the one that most directly influences the stellar spin evolution. This will be discussed in detail in Section 3.7.

We may now ask what happens if the resonance condition is satisfied: how are the dynamics of stellar spin precession affected by one - or more - resonances? To make the solution tractable analytically, we must make some simplifying assumptions. We assume ϵ is small, i.e. the system is in or close to the adiabatic regime. As a corollary, we assume that individual resonances do not affect each other significantly, i.e., that we may analyze the resonances one at a time rather than consider the coupling between them.

3.5 Dynamics of a Single Resonance

To examine the dynamics of a particular single resonance (labeled by N , which can be either positive or negative, corresponding to prograde or retrograde resonances, respectively), it is useful to transform the Hamiltonian into the frame of reference in which that resonance is stationary. To this end, we perform a canonical transformation to the new coordinates $(\bar{\phi}, \bar{p})$ such that $\bar{\phi} = \phi - N\tau$.

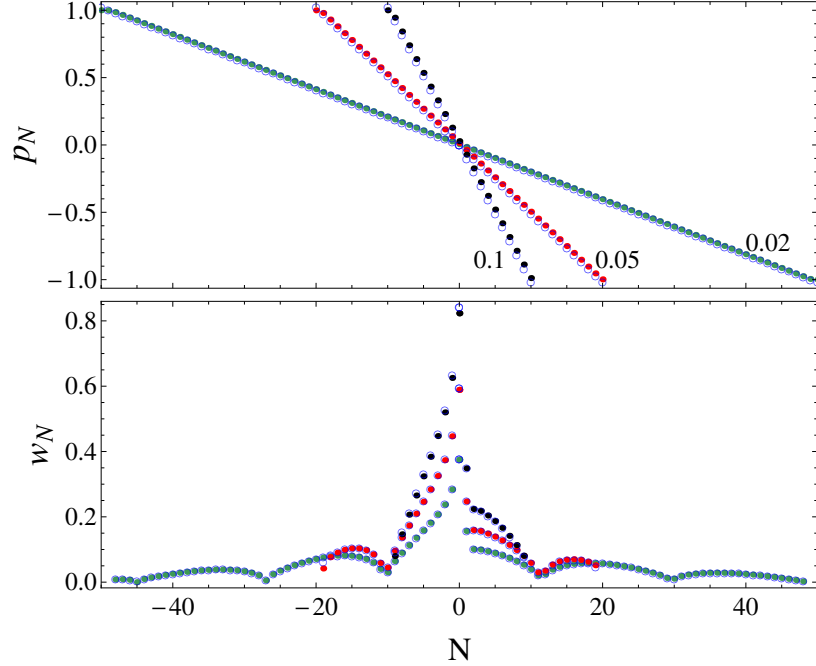


Figure 3.5: Comparison of the exact resonance locations (upper panel) and widths (bottom panel) obtained by solving Eq. (3.52) (filled circles) with simple analytical estimates (open circles). Three different values of ϵ are considered: $\epsilon = 0.1$ (blue points), $\epsilon = 0.05$ (red points), and $\epsilon = 0.02$ (green points). The agreement between the exact calculation and simple estimates is quite good, and gets better with smaller ϵ .

Using the generating function $F_2 = (\phi - N\tau)\bar{p}$, we then find

$$\bar{p} = p, \quad \bar{\phi} = \phi - N\tau, \quad (3.49)$$

$$\bar{H}' = H' [\phi(\bar{\phi}), p(\bar{p}); \tau] - N\bar{p}. \quad (3.50)$$

Thus the transformed Hamiltonian is

$$\begin{aligned} \bar{H}' = & \frac{\bar{\alpha}}{n_e} \left\{ -\frac{1}{2}p^2 - \frac{n_e}{\bar{\alpha}}Np + \epsilon p \sum_{M=0}^{\infty} \psi_M \cos M\tau \right. \\ & - \frac{\epsilon}{2} \sqrt{1-p^2} \sum_{M=0}^{\infty} \left[(\beta_M + \gamma_M) \cos [\bar{\phi} - (M-N)\tau] \right. \\ & \left. \left. + (\beta_M - \gamma_M) \cos [\bar{\phi} + (M+N)\tau] \right] \right\}, \end{aligned} \quad (3.51)$$

where we have dropped the bar over p , since $\bar{p} = p$. Under the assumption that

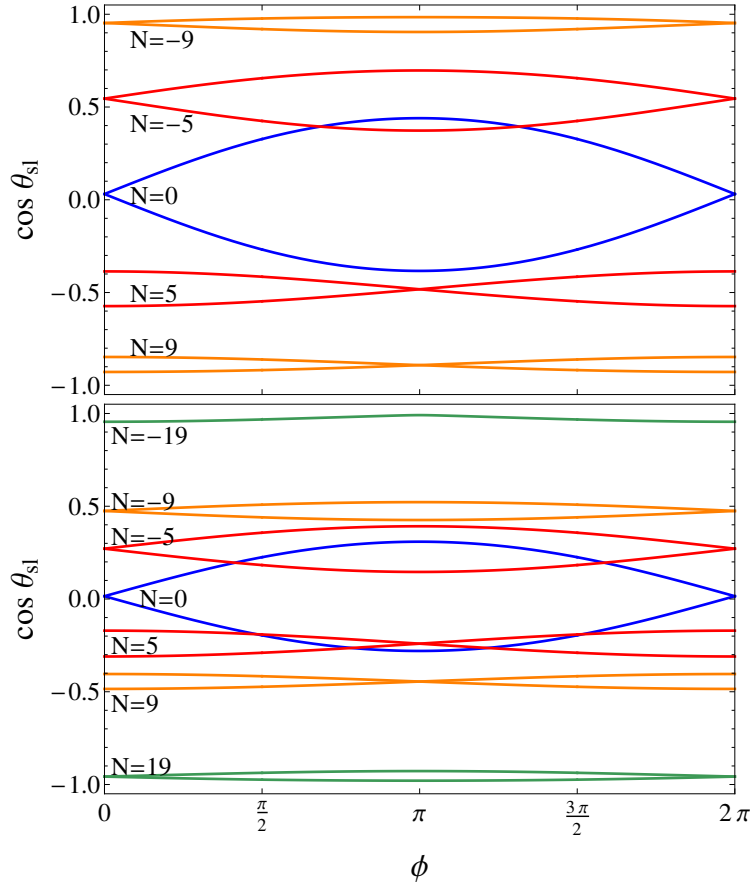


Figure 3.6: Sample separatrices for resonances of different N 's, for $\epsilon = 0.1$ (top) and $\epsilon = 0.05$ (bottom). The top panel has $N_{\max} = 9$, and the bottom panel has $N_{\max} = 19$.

resonances do not overlap, all but one harmonic can be averaged over, allowing us to examine the dynamics of a single resonance. In this case, only the $M = 0$ term in the first sum, the $M = N$ term (when $N > 0$) in the second sum, and/or the $M = -N$ term (when $N < 0$) in the third sum survive, and all the variables take on an averaged meaning. We then have

$$\begin{aligned} \bar{H}_N = \frac{\bar{\alpha}}{n_e} &\left[-\frac{1}{2}p^2 - \frac{n_e}{\bar{\alpha}} N p \right. \\ &\left. + \epsilon \psi_0 p - \frac{\epsilon}{2} \sqrt{1-p^2} (\beta_N + \gamma_N) \cos \bar{\phi} \right], \end{aligned} \quad (3.52)$$

where we have used $\beta_{-N} = \beta_N$ and $\gamma_{-N} = -\gamma_N$. In order to ensure that this expression is valid for all N 's (including $N = 0$), we set $\gamma_0 = \beta_0$.

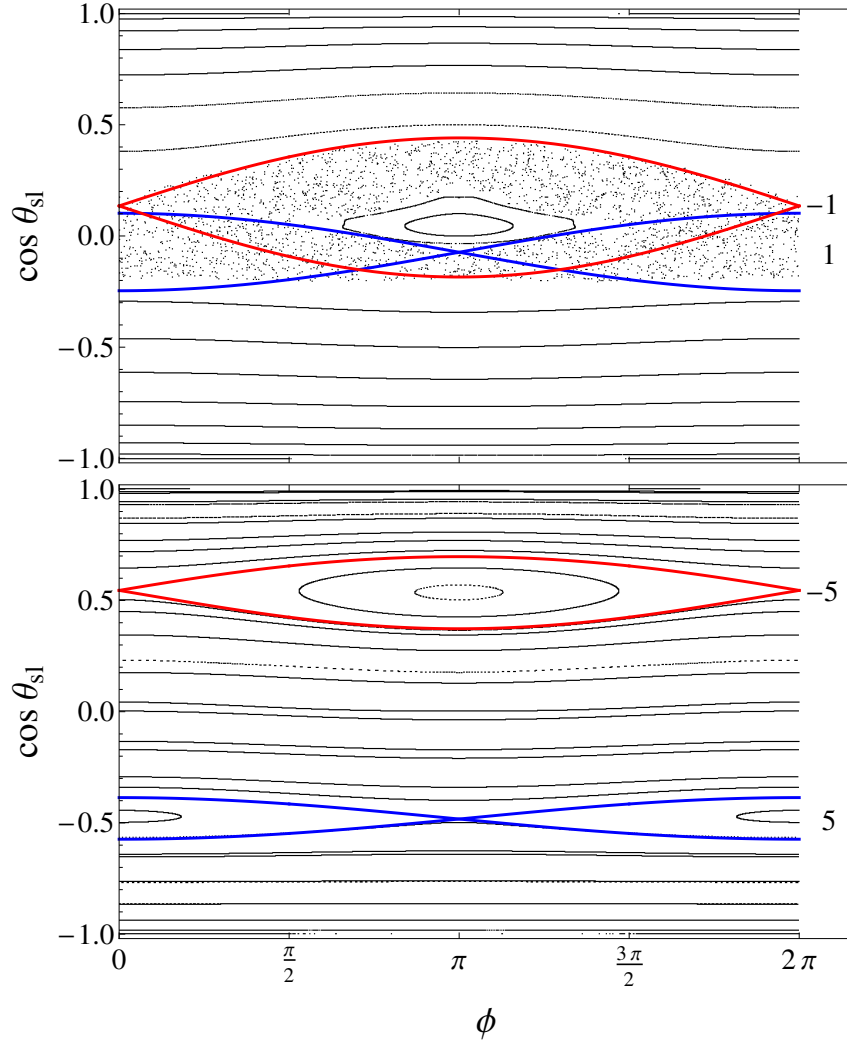


Figure 3.7: Surfaces of section for two different pairs of resonances. *Top panel* : $N = 1, M = -1$. *Bottom panel* : $N = 5, M = -5$. The adiabaticity parameter is $\epsilon = 0.1$. The red and blue curves in each panel show the analytically computed separatrices for each of the resonances, using the method of Section 3.5 (i.e. each resonance is analyzed separately).

The Hamiltonian (3.52) shows that the sum of Fourier coefficients ($\beta_N + \gamma_N$) plays a key role in determining the property of the N -resonance. Figure 3.3 plots $(\beta_N + \gamma_N)$ versus N , showing that it oscillates from positive to negative in a ringdown fashion. This oscillatory behaviour arises from individual ringdowns in β_N and γ_N , as well as from interference between the β_N and γ_N terms.

Since the Hamiltonian (3.52) is not explicitly dependent on time, energy conservation holds, i.e.

$$\bar{H}_N(\bar{\phi}, p) = \bar{H}_N(\bar{\phi}_0, p_0) \equiv E, \quad (3.53)$$

for a trajectory that starts at $(\bar{\phi}_0, p_0)$. This equation is quartic which can be solved for $p(\bar{\phi}; E)$. Figure 3.4 shows the constant-energy curves in the phase space for $N = 0$, illustrating the major features of the solution. The trajectories come in two distinct flavors: those that *circulate*, i.e. cover the entire range of $\bar{\phi}$ and do not cross $p = p_N$ [see Eq. (3.46)], and those that *librate*, i.e. are confined to some limited range of $\bar{\phi}$. The center of the librating island is the true location of the resonance, which is a stable fixed point of the equations of motion. Separating the librating and circulating regions of the phase space is a homoclinic curve known as the separatrix, which connects two saddle fixed points. The width of the separatrix (in the p axis) defines the width of the resonance.

To derive a simple expression for the resonance width, we may simplify the Hamiltonian (3.52) further by expanding it around $p = p_N$, where p_N is the zeroth-order resonant momentum given by Eq. (3.46). We take $p = p_N + \delta p$, assume the terms proportional to ϵ are already small, and expand Eq. (3.52) to second order in δp :

$$\bar{H}_N \simeq \frac{\bar{\alpha}}{n_e} \left[-\frac{1}{2} \delta p^2 - \frac{\epsilon}{2} \sqrt{1 - p_N^2} (\beta_N + \gamma_N) \cos \bar{\phi} \right], \quad (3.54)$$

where constant terms (which do not depend on δp) have been dropped. Equation (3.54) is the Hamiltonian of a simple pendulum. The resonance width is given by

$$w_N \simeq 2 \left[2 \epsilon |\beta_N + \gamma_N| \sqrt{1 - p_N^2} \right]^{1/2}. \quad (3.55)$$

Figure 3.5 shows a comparison of the exact locations of the resonances* (the

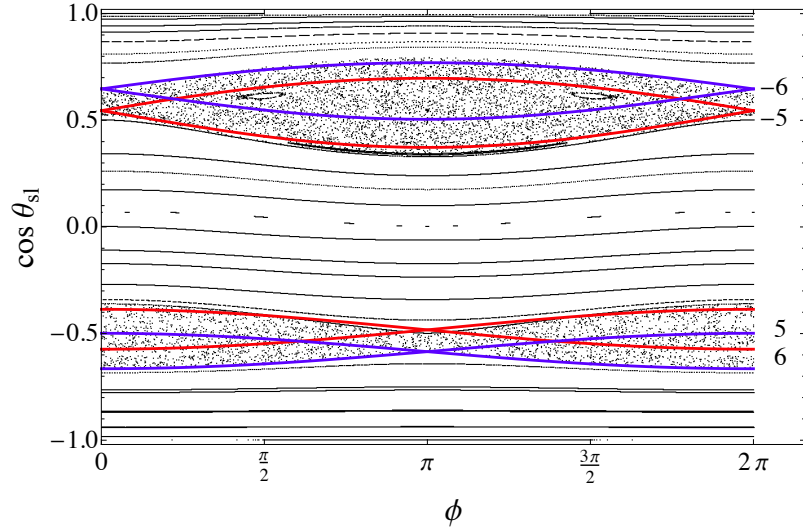


Figure 3.8: Surfaces of section for two pairs of resonances put together, with their respective analytically computed separatrices. Red: $N = 5, M = -5$; blue: $N = 6, M = -6$. The adiabaticity parameter is $\epsilon = 0.1$.

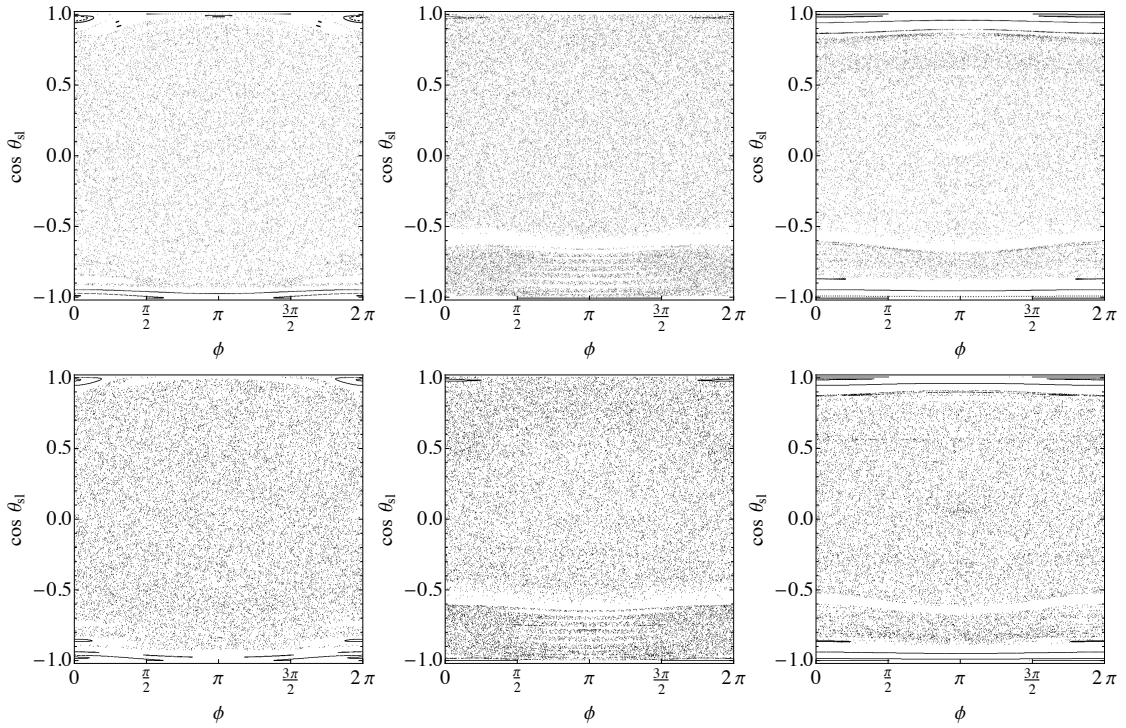


Figure 3.9: Surfaces of section computed using the exact Hamiltonian (top panels) and using the approximate Hamiltonian with only the $\{-N_{\max}, N_{\max}\}$ Fourier harmonics included in the forcing function (bottom panels). The panels from left to right correspond to $\epsilon = 0.1, 0.05, 0.02$. Note the agreement between top and bottom panels becomes better with smaller values of ϵ .

fixed points of Eq. 3.52) with the unperturbed value p_N [see Eq. (3.46)], as well as a comparison of the exact widths of the resonances with Eq. (3.55). We see that the approximate Hamiltonian (3.54) reproduces the resonance properties of the full Hamiltonian (3.52) accurately. Note that the resonance width depends on the sum of Fourier coefficients $|\beta_N + \gamma_N|$, and since β is symmetric while γ is antisymmetric with respect to N , the prograde and retrograde resonances do not have the same widths. Furthermore, since $(\beta_N + \gamma_N)$ goes through zero several times in the interval $N \in \{-100, 100\}$, the resonance width is non-monotonic as a function of N .

Figure 3.6 shows several separatrices for resonances of different orders (i.e. different N s) obtained by solving the full Hamiltonian (3.52), for two different values of ϵ . (Note we vary ϵ by varying α_0 while keeping $\Omega_{\text{pl},0}$ fixed; this means that the “shape” functions are unchanged.) Figure 3.6 illustrates several different features of the separatrices. First, decreasing ϵ tends to decrease the displacement of individual resonances from $p = 0$. Each resonance is centered at $p \simeq p_N \simeq -N/N_{\max}$. Since the maximum order of resonance, N_{\max} (recall that no resonance is possible for $|N| > N_{\max}$; see Section 3.4.3), is inversely proportional to ϵ (Eq. 3.47), we have $|p_N| \propto \epsilon$. Second, the general trend is that at smaller ϵ all the resonances are narrower, though this is not precisely true because p_N also depends on ϵ [see Eq. (3.55)]. Finally, the position of the resonance in the ϕ coordinate depends on the sign of $(\beta_N + \gamma_N)$: if $(\beta_N + \gamma_N) < 0$, the resonance is located at $\phi = \pi$, and if $(\beta_N + \gamma_N) > 0$ – at $\phi = 0$. Since $\gamma_{-N} = -\gamma_N$, this usually implies that there are significant differences between resonances with $N > 0$ and those with $N < 0$.

*Note that, in general, Eq. 3.52 admits several fixed points. Besides the resonance fixed point $p = p_N$, other fixed points exist at values of p very close to ± 1 . However, these fixed points do not globally affect the system; their separatrices are very localized. The limited influence of one such fixed point can be seen in Fig. 3.9 (left) for $p \approx 1$.

To summarize, given a particular value of the adiabaticity parameter ϵ , the stellar spin is perturbed by a set of resonances $d\phi/d\tau = N$ with $N \in \{-N_{\max}, N_{\max}\}$, where N_{\max} is given by Eq. (3.47). Each resonance governs the stellar spin evolution in the vicinity of $\cos \theta_{\text{sl}} = p_N$, with p_N approximately given by Eq. (3.46), and the width of the governed region approximately given by Eq. (3.55). As ϵ decreases (the system becomes more adiabatic), N_{\max} increases, $|p_N| \simeq |N|/N_{\max}$ (for a given N) decreases (the resonance locations move closer to $p = 0$), and the width of the resonance generally decreases. For a given ϵ , the width of the resonance is a non-monotonic function of N because of its dependence on $(\beta_N + \gamma_N)$.

3.6 Onset of Chaos: Two or More Resonances

We now consider a Hamiltonian of the form

$$H = \frac{\bar{\alpha}}{n_e} \left\{ -\frac{1}{2}p^2 + \epsilon \psi_0 p - \frac{\epsilon}{2} \sqrt{1-p^2} \left[(\beta_N + \gamma_N) \cos(\phi - N\tau) + (\beta_M + \gamma_M) \cos(\phi - M\tau) \right] \right\}, \quad (3.56)$$

where M and N are (positive or negative) integers. The system is driven by two harmonics, each with its own resonant frequency. What will happen? If the resonances are distinct enough, meaning they affect motion in different parts of the phase space, they can coexist peacefully. But supposing the resonances overlap - meaning there exist initial conditions for which the motion in the phase space is sensitive to both - what will the spin do? It does not know which resonance to "obey", and hence its motion goes chaotic. This is the essence of the Chirikov criterion for the onset of wide-spread chaos (Chirikov, 1979; Lichtenberg and

Lieberman, 1992). We note, however, that this criterion is, in fact, too strict, and chaotic motion begins somewhat before the overlap of the resonances, due to secondary resonances that arise due to the (neglected in our analysis) coupling between primary resonances.

Figure 3.7 illustrates the onset of chaos due to overlapping resonances. Note that the separatrix of each of these resonances is time-independent only in its own frame of reference. Thus, to visualize the combined effect of both resonances and be able to interpret them using resonance overlaps, we construct stroboscopic surfaces of section. Specifically, we record p and ϕ only once per eccentricity cycle at $\tau = 0, 2\pi, 4\pi, \dots$, because in this case we have $H(\bar{\phi}) = H(\phi)$ for any harmonic. This enables us to overlay analytic calculations of the separatrices on top of the surface of section in a meaningful way. By doing this, we can say that Figure 3.7 indeed demonstrates that, approximately, given two resonances N and M separated by a distance Δp , chaotic evolution of $p = \cos \theta_{\text{sl}}$ is induced when

$$\Delta p \lesssim \frac{1}{2} (w_N + w_M). \quad (3.57)$$

When this occurs, the region of chaotic evolution approximately spans the areas of both separatrices.

Figure 3.8 shows an example when four resonances are included in the Hamiltonian. In practice, a particular resonance likely only overlaps with the resonance nearest to it. Thus it is possible to observe features such as those depicted in Figure 3.8: multiple isolated regions of chaos separated by a large domain of periodic space.

3.7 Application to the Full Problem of Lidov-Kozai driven Spin Precession

We now examine the full problem of stellar spin dynamics driven by a planet undergoing LK cycles, with the Hamiltonian given by Eq. (3.37). If the chaotic behaviour of this full system is indeed determined by resonances and their overlaps, and, as discussed in Section 3.4.3, there exists a maximum resonance order N_{\max} , we expect that approximating this full system with one consisting only of all harmonics with $|N| < N_{\max}$ should reproduce the key features of the system. Thus we consider the approximate Hamiltonian

$$H'_{\text{app}} \simeq \frac{\bar{\alpha}}{n_e} \left[-\frac{1}{2} p^2 + \epsilon \psi_0 p - \frac{\epsilon}{2} \sqrt{1-p^2} \sum_{N=-N_{\max}}^{N_{\max}} (\beta_N + \gamma_N) \cos(\phi - N\tau) \right]. \quad (3.58)$$

We evolve equations of motion obtained from both Eq. (3.37) and Eq. (3.58). Figure 3.9 compares the resulting surfaces of section for several values of ϵ . It is apparent that taking only the innermost $2N_{\max} + 1$ harmonics in the perturbing functions adequately reproduces the behavior of the full system, with better agreement for smaller ϵ .

We may now consider whether the overlap of these resonances can explain the width of the chaotic region as a function of ϵ . Figure 3.10 shows that this is indeed the case. Given a value of ϵ , there exists a prograde (positive) “outermost” resonance $N = N_{\text{out}}^+$ (> 0) which overlaps with the “previous” resonance $(N_{\text{out}}^+ - 1)$ but not with the “next” one $(N_{\text{out}}^+ + 1)$. Since the separation (in p) of two neighboring resonances is $\Delta p \simeq 1/N_{\max}$ [see Eq. (3.48)], this “outermost”

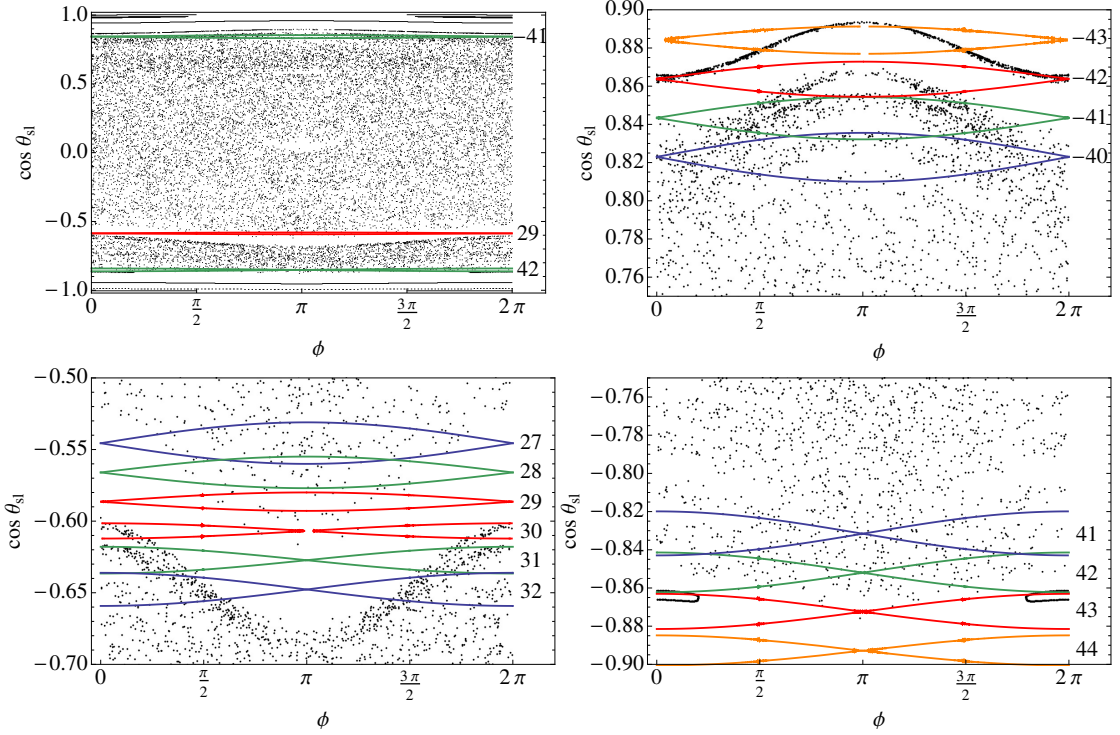


Figure 3.10: Demonstration of how overlapping resonances can explain several features of the $\epsilon = 0.02$ surface of section shown in the right panels of Fig. 3.9. *Top left panel* : The entire surface of section, with the separatrices for the $N=42$ (bottom green), 29 (red), and -41 (top green) resonances overlaid. *Top right panel* : Zoom-in on the top portion of the surface of section; the separatrices for resonances with $N = -40$ (blue), -41 (green), -42 (red), and -43 (orange) are overlaid. *Bottom left panel* : Zoom-in on the gap located at $p \approx -0.6$; from top to bottom, the separatrices for the $N = 27$ (blue), 28 (green), 29 (red), 30 (red), 31 (green), and 32 (blue) resonances are overlaid. *Bottom right panel* : Zoom-in on the bottom portion of the surface of section; the separatrices for $N = 41$ (blue), 42 (green), 43 (red), and 44 (orange) are overlaid.

resonance is determined by the conditions

$$\frac{1}{2} \left(w_{N_{\text{out}}^+} + w_{N_{\text{out}}^+ - 1} \right) > \frac{1}{N_{\text{max}}}, \quad (3.59)$$

and

$$\frac{1}{2} \left(w_{N_{\text{out}}^+} + w_{N_{\text{out}}^+ + 1} \right) < \frac{1}{N_{\text{max}}}. \quad (3.60)$$

Likewise, there exists a retrograde (negative) “outermost” resonance $N_{\text{out}}^- (< 0)$ which is the last to overlap with the “previous” one ($N_{\text{out}}^- + 1$). The locations

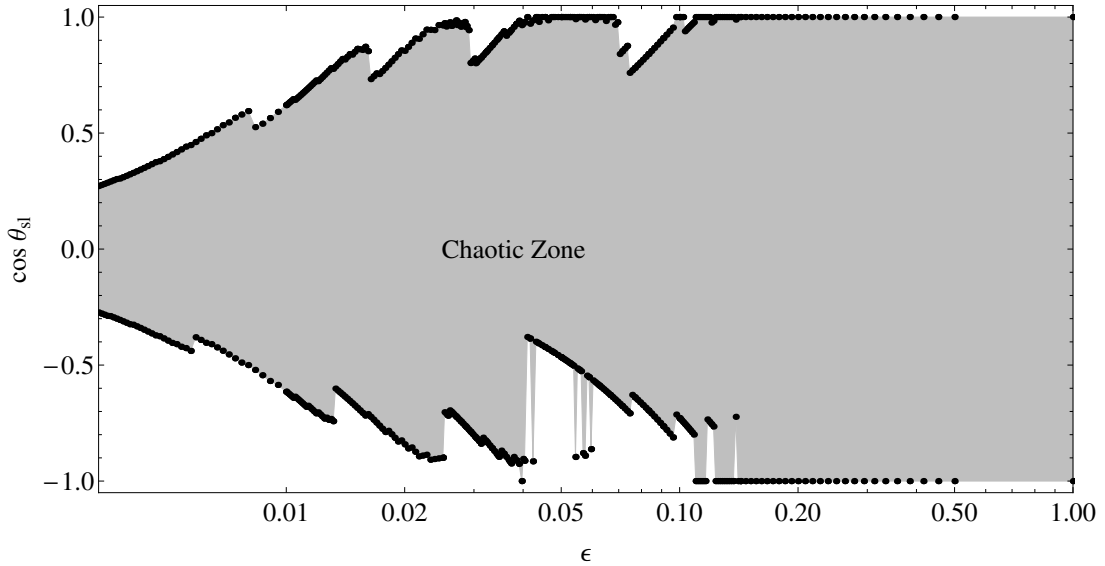


Figure 3.11: Outermost boundaries of the chaotic region as a function of ϵ , calculated by determining the outermost resonance N_{out}^{\pm} which still overlaps with the previous one. The non-monotonic nature of the width of the chaotic region is due to the non-monotonic behavior of the Fourier coefficients of the resonant forcing terms ($\beta_N + \gamma_N$; see Fig. 3.3). Note that while the spin evolution is strictly non-chaotic outside the chaotic zone (the shaded region), there could be periodic windows inside the chaotic zone.

of these two “outermost” resonances, as determined by the resonant momenta $p_{N,\text{out}}^{\pm} \simeq -N_{\text{out}}^{\pm}/N_{\text{max}}$, bound the chaotic region in the p -space*. As ϵ is varied, N_{out}^{\pm} and $p_{N,\text{out}}^{\pm}$ vary as well. Thus we may analytically compute the extent (i.e. the outermost boundaries in the p -space) of wide-spread chaos as a function of ϵ . The result is shown in Figure 3.11 (note that within the chaotic zone in p -space, there can still exist periodic islands; see below).

Figure 3.10 brings to light another interesting feature of this dynamical system: the existence of narrow isolating regions of non-chaotic behavior, spanning the entire $\{0, 2\pi\}$ range in the ϕ coordinate and thus effectively splitting the phase space into chaotic regions that cannot communicate with each other.

*Note that for sufficiently large $|N|$, the width of the resonance is small [see Eq. (3.55)]. So the outer edge of the separatrix of the outermost resonance is close to its center.

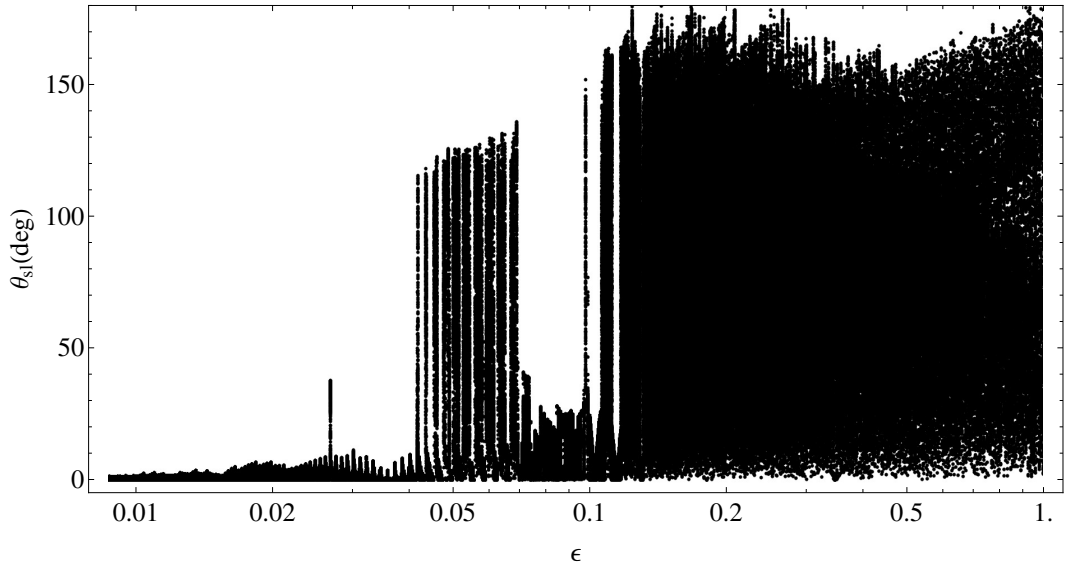


Figure 3.12: “Bifurcation” diagram of spin-orbit misalignment angle versus the adiabaticity parameter ϵ . For each ϵ , we evolve the equations of motion starting with $\theta_{\text{sl}} = 0$, for ~ 500 LK orbital eccentricity cycles, and record θ_{sl} every time the eccentricity reaches a minimum. This diagram is similar to Fig. 3.1, except that all short-range force effects and the back-reaction of the stellar spin on the orbit are turned off.

This feature arises from the strongly nonlinear variation of the Fourier coefficient $(\beta_N + \gamma_N)$, and therefore the widths, of the various resonances involved: resonances that are very narrow are isolated from the surrounding ones, and quasiperiodic behavior becomes possible in their vicinity. For example, from Figure 3.5 we see that for $\epsilon = 0.05$, the resonances of order $N = 11$ and 12 are particularly narrow, and indeed they are the ones that cause the narrow band in the middle panels of Fig. 3.9. Likewise, as demonstrated in the bottom left panel of Fig. 3.10, for $\epsilon = 0.02$, the resonances $N = 29$ and 30 are isolated from the rest and result in a band of quasi-periodicity.

We now focus on systems which start out with aligned stellar spin and planetary angular momentum axes (i.e. $\cos \theta_{\text{sl}} = 1$) – such systems are very relevant in the standard picture where planets form in protoplanetary disks aligned with

the central stars. Two questions are of interest: first, given a specific value of ϵ , will such an initially aligned state experience chaotic or quasiperiodic evolution, and second, if the evolution *is* chaotic, how much of the available phase space will it span, i.e. how much will $\cos \theta_{\text{sl}}$ vary? (A third question may also be asked - what happens if ϵ slowly evolves as a function of time, as it might in a physical system due to tidal dissipation? We address this issue in Section 3.8 below).

To address these questions, we numerically construct a “bifurcation diagram” (Fig. 3.12), using the equations of motion of the full Hamiltonian (Eq. 3.37). For each value of ϵ we compute the spin evolution trajectory starting from the initial condition $\cos \theta_{\text{sl}} = 1$. We record on the y -axis the spin-orbit misalignment angle at every eccentricity minimum (at $\tau = 0, 2\pi, 4\pi\dots$). The result is, effectively, a 1D surface of section, for a single initial condition. We then repeat the calculation for a fine grid of ϵ values. Figure 3.12 shows the result. Large spread in θ_{sl} indicates chaotic behavior, while small spread with well-defined edges indicates quasiperiodicity*. We see from Fig. 3.12 that, in general, the spread of θ_{sl} as a function of ϵ follows the trend analytically predicted in Fig. 3.11. For example, Figure 3.11 shows that for $\epsilon \gtrsim 0.1$, the spin-orbit misalignment of an initially aligned state will evolve chaotically; this is consistent with Fig. 3.12, which shows that θ_{sl} undergoes large excursion for $\epsilon \gtrsim 0.1$. Figure 3.11 also shows that only for $\epsilon \lesssim 0.02$, the aligned initial state will not evolve into the chaotic zone; this is also reflected in Fig. 3.12, where for $\epsilon \lesssim 0.02$ the spread in θ_{sl} is confined to a narrow region around $\theta_{\text{sl}} = 0$.

However, the transition between quasi-periodic evolution and chaotic evo-

*Note that rigorously speaking, it is not certain that a region with small spread is periodic; such a region could still be chaotic but tightly isolated (see also Fig. 3.1).

lution of stellar spin for an initially aligned state is fuzzy. As seen in Fig. 3.12, for ϵ between ~ 0.02 and ~ 0.1 , the regular (periodic) regions (with small spread in θ_{sl}) are interspersed with the chaotic zones (with large spread in θ_{sl}). In particular, for $\epsilon \sim 0.04 - 0.07$, the spin evolution is mostly chaotic but with somewhat regularly spaced periodic regions – “periodic islands in an ocean of chaos” (see Fig. 3.13). Toward smaller ϵ , the periodic islands expand and the chaotic regions shrink, so that for $\epsilon \lesssim 0.04$ the spin evolution becomes mostly periodic, with small finely tuned chaotic domains that are shown in Fig. 3.14 to be linearly spaced in $1/\epsilon$ – “chaotic zones in a calm sea”. To illustrate how the theory of overlapping resonances can explain these features, Figure 3.15 takes a closer look at the resonances near $\cos \theta_{\text{sl}} = 1$ for three closely spaced values of ϵ . Naturally, as discussed in Section 3.4.3, the resonance that determines the evolutionary behavior of the initially-aligned system is $N = -N_{\max}$, since it has $p_N \simeq 1$. As ϵ is varied, the trajectory of the system falls either inside the $N = -N_{\max}$ resonance, or outside it, or right on its separatrix. The proximity of the $N = -N_{\max}$ resonance to the $N = -N_{\max} + 1$ resonance then determines the evolutionary trajectory of the system. If the two resonances overlap strongly, then all trajectories in the vicinity will be chaotic, but this is not the case in Fig. 3.15. Instead, for small values of ϵ , the $N = -N_{\max}$ separatrix appears to be close to, but not quite touching, its neighbor. This, in principle, does not completely preclude chaos, since the Chirikov criterion is, in fact, too strict and chaos can still exist when two resonances are sufficiently close to each other and the trajectories are close to one of the separatrices (Chirikov, 1979; Lichtenberg and Lieberman, 1992). This is the case in Fig. 3.15: the chaotic trajectory of the middle panel falls right on the separatrix and effectively “rides” it out and onto the neighboring resonance. Thus, the series of peaks at small values of ϵ in Fig. 3.12 are due

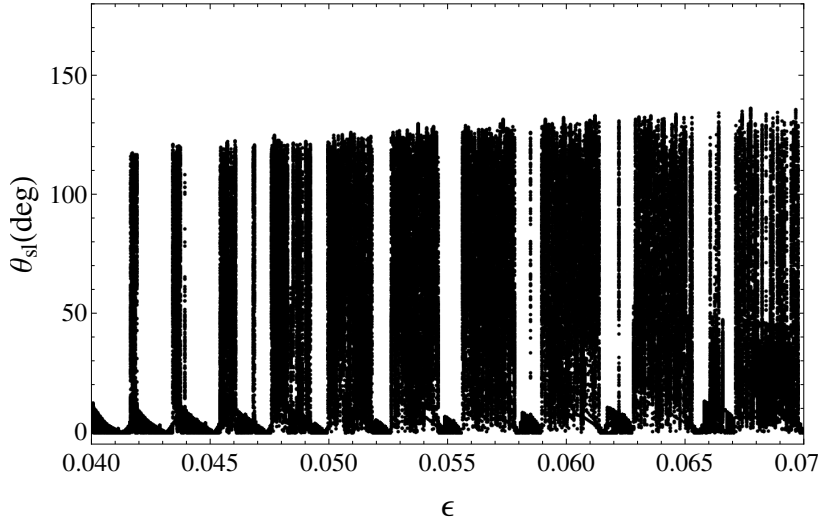


Figure 3.13: Zoom in on Fig. 3.12 in the region $0.04 < \epsilon < 0.07$. Here the spin evolution is mostly chaotic (with large scatter in θ_{sl}), with periodic regions (with θ_{sl} close to zero) appearing in the middle of the chaos. The range of chaotic excursion is limited to be less than $\sim 130^\circ$ due to a periodic island at $\cos \theta_{\text{sl}} \sim -0.5$ caused by the narrow width of the $N = 11$ and 12 resonances (see Fig. 3.5 and middle panels of Fig. 3.9).

to the varying proximity of the $N = -N_{\max}$ resonance to $\cos \theta_{\text{sl}} = 1$ and to its neighboring resonances.

3.8 Adiabatic Resonance Advection

For a non-dissipative system, the adiabaticity parameter ϵ is a constant. In the previous sections we have demonstrated that the dynamical behavior of the stellar spin axis for different values of ϵ can be understood using secular spin-orbit resonances. Here we discuss the phenomenon of “adiabatic resonance advection”, and demonstrate the importance of resonances when dissipation is introduced in our system.

As noted in Section 3.2, in the “Lidov-Kozai + tide” scenario for the forma-

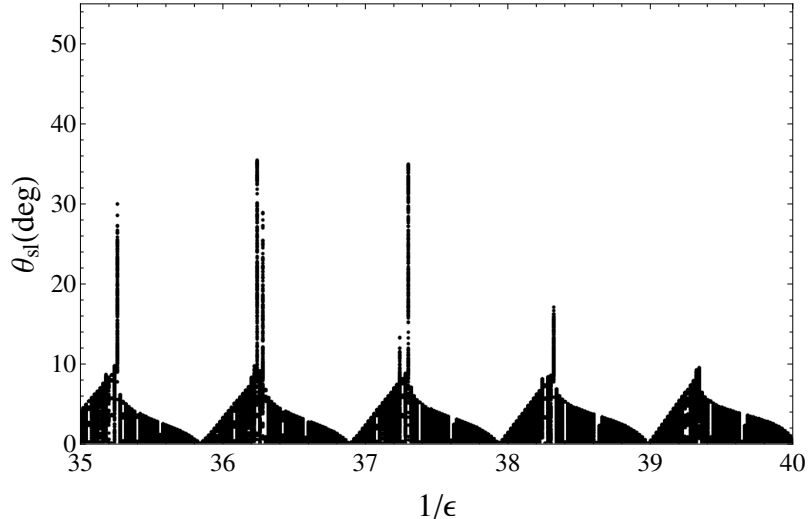


Figure 3.14: Zoom in on Fig. 3.12 in the region $0.025 < \epsilon < 0.0286$, plotted against $1/\epsilon$. Here the spin evolution is mostly regular or periodic (with small scatter in θ_{sl}), but chaotic zones (with large scatter in θ_{sl}) appear in the middle of the “calm sea”. The occurrence of the chaotic zones is approximately evenly spaced in $1/\epsilon$.

tion of hot Jupiters (Correia et al., 2011; Fabrycky and Tremaine, 2007; Naoz et al., 2012; Petrovich, 2015b; Storch et al., 2014; Wu and Murray, 2003), tidal dissipation in the planet at periastron reduces the orbital energy, and leads to gradual decrease in the orbital semi-major axis and eccentricity. In this process, ϵ slowly decreases in time. In SAL, we have considered various sample evolutionary tracks and shown that the complex spin evolution can leave an imprint on the final spin-orbit misalignment angle. A more systematic study will be presented in a future paper (Anderson, Storch, and Lai, in prep).

In Fig. 3.16, we show a particular evolutionary track of our system, obtained by integrating the full equations of motion for the LK oscillations, including the effects of all short-range forces (General Relativity, distortion of the planet due to rotation and tide, and rotational bulge of the host star) and tidal dissipation in the planet (see SAL for details). In this example, the adiabatic parameter $\epsilon \simeq 0.17$ initially and decreases as the orbit decays. So the spin evolution is always

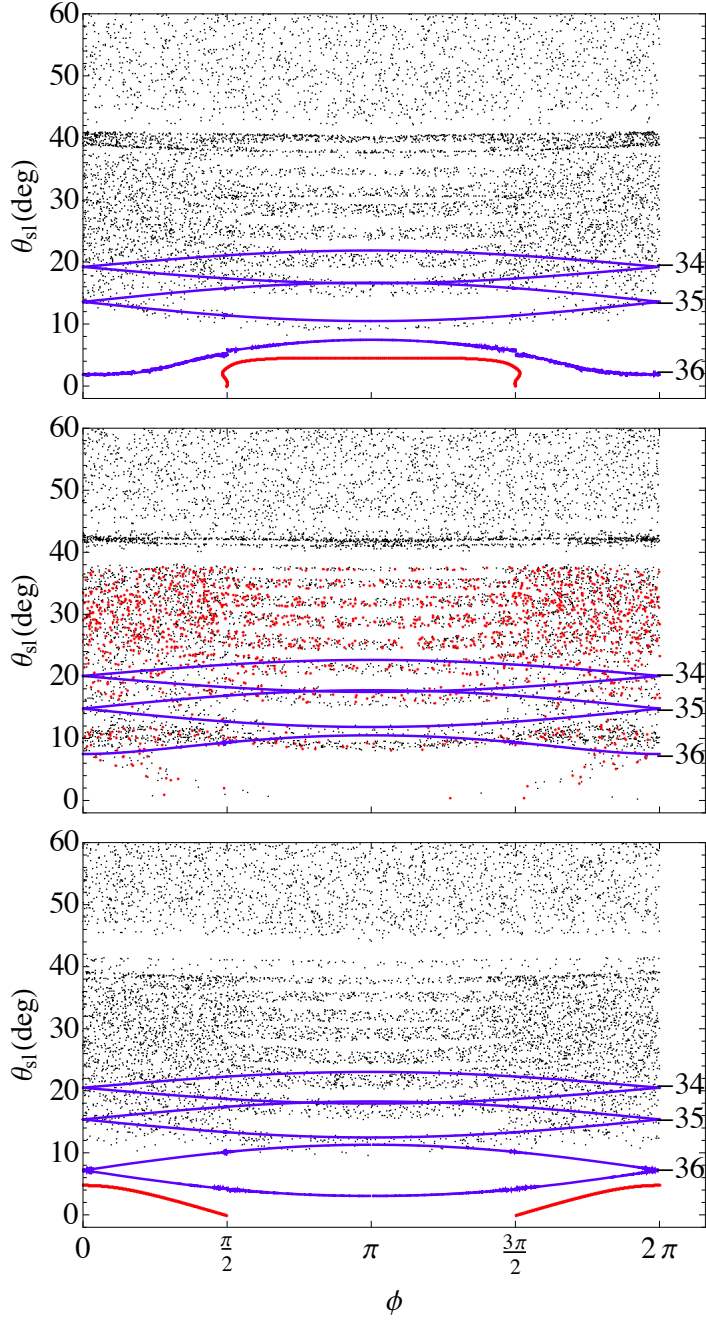


Figure 3.15: Demonstration of how the variation of resonances with ϵ leads to the peculiar oscillatory behavior seen in Fig. 3.14. The evolution of an initially aligned system is shown in red, and the analytical resonance separatrices are shown in blue. *Top panel:* $1/\epsilon = 37.1$; the initially aligned system is trapped within the $N = -36$ resonance, which is sufficiently far removed from the $N = -35$ resonance, so the trajectory is non-chaotic. *Middle panel:* $1/\epsilon = 37.3$; the $N = -36$ and $N = -35$ resonances are close, so the trajectory becomes chaotic; θ_{sl} is confined to $< 35^\circ$ because of the gap which separates the two chaotic zones. *Bottom panel:* $1/\epsilon = 37.4$; the $N = -36$ resonance has moved up sufficiently so that it no longer traps the initially aligned system, and the trajectory is regular again.

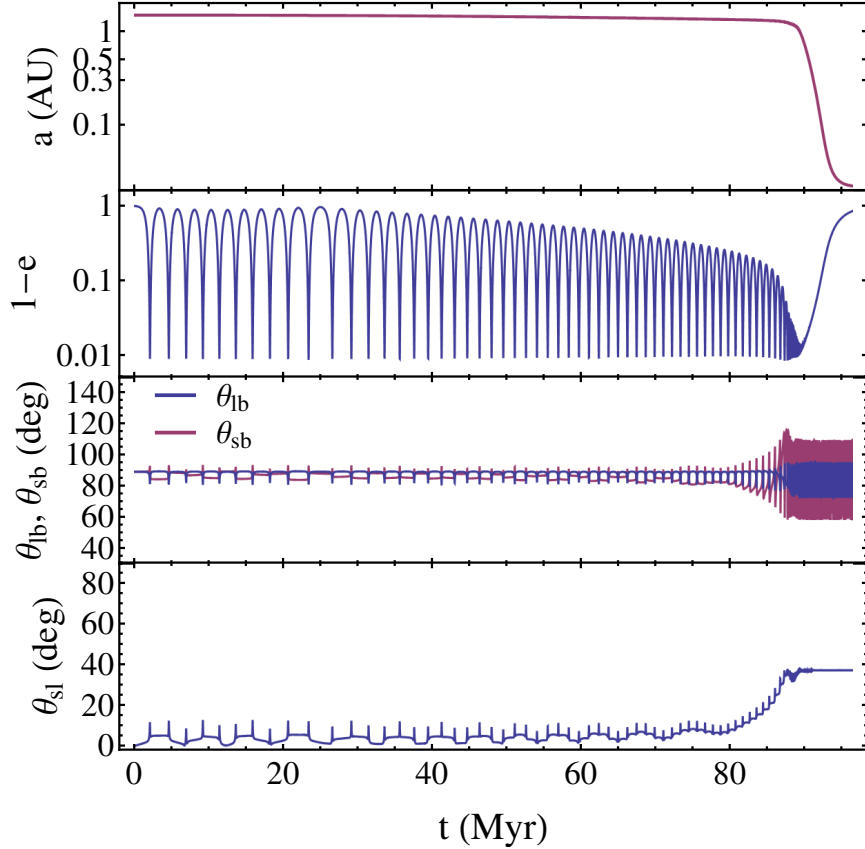


Figure 3.16: Sample time evolution demonstrating non-chaotic drift of an initially aligned system toward higher misalignment angles. The top panel shows the orbital semi-major axis, the second panel shows the eccentricity, the third panel shows the orbital inclination angle θ_{lb} and the angle θ_{sb} between \hat{S} and \hat{L}_b , and the bottom panel shows the spin-orbit misalignment angle θ_{sl} . The parameters are $M_p = 5M_J$, $\hat{\Omega}_* = 0.05$, $a_0 = 1.5\text{AU}$, $a_b = 200\text{AU}$, $\theta_{lb}^0 = 89^\circ$, and we have included all short-range effects (cf. Fig. 3.1). See SAL for details.

in the non-chaotic, adiabatic regime. Interestingly, we see that as a decreases, the initially aligned state gradually drifts toward a higher misalignment angle in a well-ordered manner.

To explain this intriguing behavior, we consider a simplified version of the problem, in which we gradually increase α_0 (thereby decreasing ϵ) while keeping the forcing due to the planet unchanged*. If the evolution of ϵ is sufficiently

*This simplification implies that the “shape” functions $[\beta(\tau), \gamma(\tau)$ and $\psi(\tau)$; see Eqs. (3.38)-(3.40)] are unchanged as ϵ evolves. In real Lidov-Kozai oscillations with tidal dissipation (de-

gradual, then given an initial state there exists an adiabatic invariant that is conserved as ϵ changes:

$$J = \oint p d\phi, \quad (3.61)$$

where the integration covers a complete cycle in the ϕ -space. This quantity is equivalent to the area enclosed by the trajectory in phase space. Since, as discussed previously, the $N = -N_{\max}$ resonance is the one that most strongly influences the initially-aligned system, we consider the single-resonance Hamiltonian (Eq. 3.52) for this resonance. Since this Hamiltonian is independent of time, it is conserved, i.e. $E = H(\phi_0, p_0)$ is a constant so long as ϵ is constant. Conversely, a single value of E corresponds to a unique phase space trajectory $p(\phi; E, \epsilon)$. It follows that the adiabatic invariant can be expressed as a function of E and ϵ , i.e., $J = J(E, \epsilon)$.

As the system evolves (ϵ slowly changes), $J(E, \epsilon)$ is kept constant, so E must change. These changes in ϵ and E lead to changes in the phase space trajectory. For an initially circulating trajectory that spans the entire $\{0, 2\pi\}$ range in ϕ , to conserve the area under the curve the most that can happen is that an initially curved trajectory must flatten, approaching $p = \text{const}$, where the constant is roughly the average of p over the initial trajectory. However, if a trajectory is librating and only encloses a small area, it can be a lot more mobile as ϵ evolves. As demonstrated in Fig. 3.15, one way for the initially-aligned trajectory to be librating is for it to be trapped inside the $-N_{\max}$ resonance. We also know that as ϵ decreases the resonance must move toward $p = 0$ [see Eqs. (3.47)-(3.48)]. We therefore posit that it is possible that the initially-aligned trajectory can be advected with the resonance, and gradually taken to higher misalignment am-

picted in Fig. 3.16), the range of eccentricity oscillations changes over time, with the minimum eccentricity e_{\min} gradually drifting from e_0 toward e_{\max} , thereby changing the shape functions. To study this phenomenon quantitatively, this effect needs to be included.

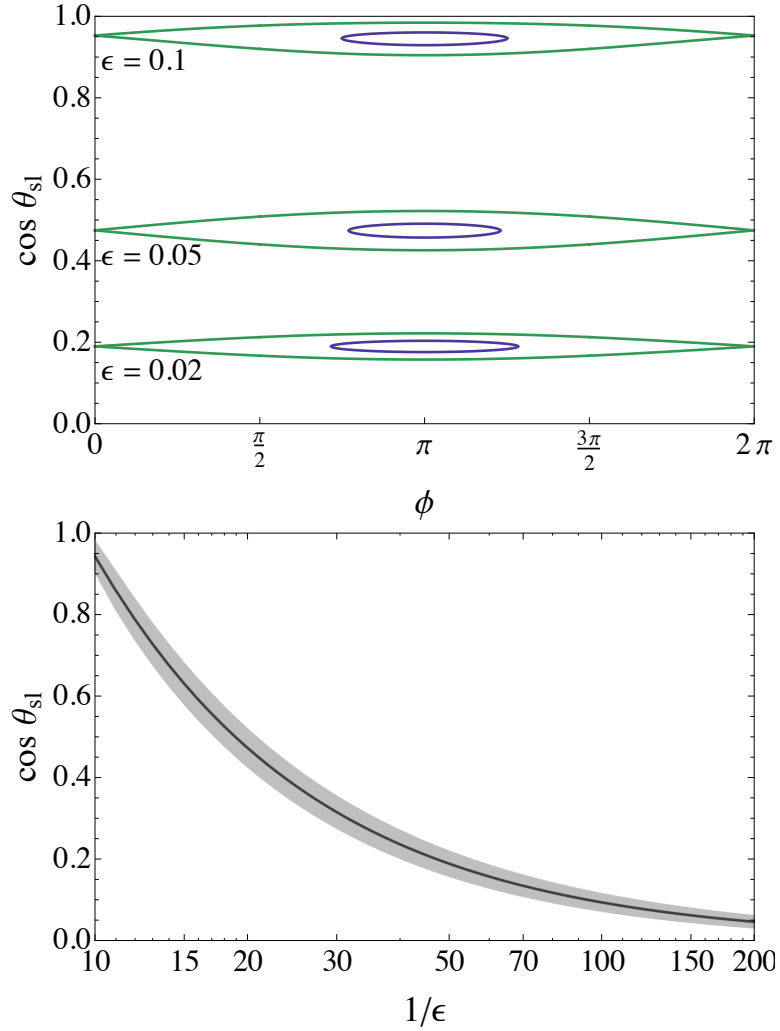


Figure 3.17: Proof of concept for “adiabatic resonance advection”. *Top panel:* Sample spin evolution trajectories (constant-energy curves in the $\cos \theta_{\text{sl}}-\phi$ phase space) for several values of ϵ . The system initially has $\epsilon = 0.1$ and is contained within the $N = -9$ resonance with $p_N \simeq 1$. As ϵ slowly decreases due to dissipation, the resonance center p_N moves to smaller values, with the sample trajectory’s area remaining constant. *Bottom panel:* Location (solid black line) and width (grey area) of the $N = -9$ resonance as a function of $1/\epsilon$, demonstrating that p_N moves toward $p = 0$ and the resonance width (in $\cos \theta_{\text{sl}}$) narrows with decreasing ϵ . The sample trajectory trapped inside the resonance must follow the resonance in accordance with the principle of adiabatic invariance.

gles. A proof of concept of this process is shown in Fig. 3.17. While a detailed study of this process (such as the condition for resonance trapping) is beyond the scope of this paper, we note that it has many well-known parallels in other physical systems, such as the trapping of mean-motion resonances when multiple planets undergo convergent migration.

3.9 Conclusion

In this work we have continued our exploration of Lidov-Kozai driven chaotic stellar spin evolution, initially discussed in Storch et al. (2014), by developing a theoretical explanation for the onset of chaos in the “adiabatic” to “trans-adiabatic” regime transition. The behaviour of the stellar spin evolution depends on the adiabaticity parameter ϵ [see Eq. (3.1) or (3.24)]. Using Hamiltonian perturbation theory, we have identified a set of spin-orbit resonances [see Eq. (3.45)] that determine the dynamical behaviour of the system. The resonance condition is satisfied when the averaged spin precession frequency of the star is an integer multiple of the Lidov-Kozai precession frequency of the planet’s orbit. We have shown that overlaps of these resonances lead to the onset of chaos, and the degree of overlap determines how wide-spread the chaos is in phase space. Some key properties of the system include the facts that the width of an individual resonance is a non-monotonic function of the resonance order N (see Fig. 3.5), and that there exists a maximum order N_{\max} [see Eq. (3.47)] that influences the spin dynamics. These properties lead to several unusual features (such as “periodic islands in an ocean of chaos”) when the system transitions (as ϵ decreases) from the fully chaotic regime to the fully adiabatic regime (see Fig. 3.12). Focusing on the systems with zero initial spin-orbit misalignment an-

gle, our theory fully predicts the region of chaotic spin evolution as a function of ϵ (see Fig. 3.11) and explains the non-trivial features found in the numerical bifurcation diagram (Fig. 3.12). Finally, we use the spin-orbit resonance and the principle of adiabatic invariance to explain the phenomenon of “adiabatic resonance advection”, in which the spin-orbit misalignment accumulates in a slow, non-chaotic way as ϵ gradually decreases as a result of dissipation (see Section 3.8).

The system we considered in this paper is idealized. We have not included the effects of short-range forces, such as periastron advances due to General Relativity, and the planet’s rotational bulge and tidal distortion. We have also ignored the back-reaction torque from the stellar quadrupole on the orbit. These simplifications have allowed us to focus on the spin dynamics with “pure” orbital Lidov-Kozai cycles. Finally, we have only briefly considered the effects of tidal dissipation, using an idealized model in which the “shape” of the Lidov-Kozai oscillations does not change as the semi-major axis decays. All of these effects will eventually need to be included, if we hope to not only understand the origin of the chaotic behavior but also make predictions for the observed spin-orbit misalignment distributions in hot Jupiter systems. We begin to systematically explore these issues numerically in a future paper (Anderson, Storch, and Lai, in prep).

3.10 Acknowledgments

We thank Kassandra Anderson for useful discussion and continued collaboration. We thank the referee, Konstantin Batygin, for comments and suggestions

that have improved the paper. This work has been supported in part by NSF grant AST-1211061, and NASA grants NNX14AG94G and NNX14AP31G.

CHAPTER 4

DYNAMICS OF STELLAR SPIN DRIVEN BY PLANETS UNDERGOING LIDOV-KOZAI OSCILLATIONS: PATHS TO MISALIGNMENT

4.1 Abstract

Many systems hosting a hot Jupiter (HJ) exhibit significant misalignment between the spin axes of the host stars and the orbital axes of the HJs (“spin-orbit misalignment”). The Lidov-Kozai (LK) mechanism of HJ formation provides a natural means of generating such misalignment, but the process is complicated due to stellar spin-orbit coupling. We have previously shown (Storch et al., 2014) that, through this coupling, a HJ undergoing LK oscillations induces complex motion in the spin axis of its host, which at times can even be chaotic. Recently (Storch and Lai, 2015b) we have analyzed the origin of this chaos in an idealized non-dissipative LK system and identified a set of secular resonances whose overlaps are responsible for the chaos. Here we extend our analysis to non-ideal systems, including the effects of short range forces, and tidal dissipation, and categorize the various paths to spin-orbit misalignment that a system can take. We identify four distinct means of generating misalignment, only two of which are capable of producing retrograde orbits, and show that the path to misalignment that a given system takes depends on only two parameters, which compare the stellar spin axis precession rate with the LK-induced rate of change of the orbital axis, and with the LK oscillation timescale itself.

The contents of this chapter are in preparation for submission to *MNRAS* as “Dynamics of Stellar Spin Driven by Planets Undergoing Lidov-Kozai Oscillations: Paths to Misalignment” (Storch et al., 2015)

4.2 Introduction

The recent discovery of misalignment between the orbital axes of hot Jupiters (HJs; giant planets found within 0.1 AU of their host stars) and the spin axes of their host stars (Albrecht et al., 2012; Hébrard et al., 2008, 2010; Narita et al., 2009; Triaud et al., 2010; Winn et al., 2009) remains a hot topic of interest in the exoplanet community. While primordial disk misalignment is a possible explanation of this (Bate et al., 2010; Batygin, 2012; Batygin and Adams, 2013; Lai, 2014; Lai et al., 2011; Spalding and Batygin, 2014), dynamical means of generating misalignment are worth exploring.

Lidov-Kozai (LK) oscillations (Kozai, 1962; Lidov, 1962) – one of the proposed channels of hot Jupiter formation – provide a natural means of generating misalignment. Lidov-Kozai oscillations occur when the proto-HJ’s host star has a binary companion. A proto-HJ is assumed to form at several AU from its host. If its orbital axis is sufficiently misaligned relative to the outer binary axis, its orbit undergoes large correlated variations in eccentricity and inclination. If the misalignment is substantial, very high eccentricities (in excess of 0.99) can be attained; during these high-eccentricity phases, tidal dissipation at periastron brings the planet close to its host, eventually creating a HJ.

Since, presumably, the LK migration happens when the host star is still relatively young and therefore spinning rapidly, significant coupling can exist between the dynamics of the proto-HJ and the dynamics of the stellar spin axis. This coupling is vital in determining the final spin-orbit misalignments of these systems. Indeed, in Storch et al. (2014), hereafter SAL, we showed that the stellar spin axis dynamics, driven by the periodic changes in the planet orbit, can

be very complex, and even chaotic. Subsequently, in Storch and Lai (2015*b*), hereafter SL15, we discussed the origin of the chaotic behavior by analyzing an idealized system with no tidal dissipation and considering only the cases in which the stellar spin precession rate was much higher than the LK oscillation frequency (the “adiabatic” regime). In the present work, we extend our analysis to the non-adiabatic regime (i.e. the regime in which the star precesses slowly), as well as account for non-ideal effects (such as periastron advance due to GR and planet oblateness), include tidal dissipation and discuss the various paths to spin-orbit misalignment that LK oscillations can induce.

This paper is organized as follows. In section 4.3, we give a review of our previous work and the most important concepts in LK-driven spin-orbit dynamics. In section 4.4, we discuss the effect that short-range forces have on the spin-orbit dynamics. In section 4.5, we classify the different regimes of non-dissipative spin dynamics. In sections 4.6 and 4.7, we include tidal dissipation and discuss the various paths toward misalignment and the parameters that determine which paths a system takes. We discuss and summarize our findings in section 4.8.

4.3 LK-Driven Spin Dynamics: Review

4.3.1 Lidov-Kozai oscillations

We consider a star of mass M_\star hosting a planet of mass M_p (such that $M_\star \gg M_p$), and a stellar binary companion with mass M_b . Note that, in all calculations presented in this paper, we assume $M_\star = M_b = 1M_\odot$.

In this work we consider LK oscillations to quadrupole order only. We assume the host star and binary companion are in a fixed circular orbit with semi-major axis a_b , and thus the binary orbital axis $\hat{\mathbf{L}}_b$ defines the invariant plane of the system.

The planet orbit is described by its semi-major axis a , eccentricity e , and angular momentum vector \mathbf{L} , which is inclined relative to $\hat{\mathbf{L}}_b$. We define $\cos \theta_{lb} \equiv \hat{\mathbf{L}} \cdot \hat{\mathbf{L}}_b$. In the LK mechanism, if $40^\circ \lesssim \theta_{lb} \lesssim 140^\circ$, the planet orbit undergoes oscillations in e and θ_{lb} , as well as nodal and periastron precession, while conserving $\mathbf{L} \cdot \hat{\mathbf{L}}_b$. The oscillations happen on a characteristic timescale given by

$$t_k^{-1} = n \left(\frac{M_b}{M_*} \right) \left(\frac{a}{a_b} \right)^3, \quad (4.1)$$

where $n \equiv (GM_*/a^3)^{1/2}$ is the mean motion frequency of the planet. In the absence of short-range forces, the maximum eccentricity achieved during an LK cycle is approximately

$$e_{\max} \simeq \left(1 - \frac{5}{3} \cos^2 \theta_{lb}^0 \right)^{1/2}. \quad (4.2)$$

A detailed discussion of the equations governing LK oscillations, and their analytical solution, can be found in SL15 [see also Kinoshita and Nakai (1999)]. For our present purposes, the one important quantity is the frequency of eccentricity oscillations, which is given by

$$n_e = \mathcal{K} t_k^{-1}, \quad (4.3)$$

where \mathcal{K} is of order 1. We also define the quantities

$$\Omega_{pl} \equiv \Omega_{pl,0} f(e) \equiv \frac{d\Omega}{dt}, \quad \dot{\theta}_{lb} \equiv \frac{d\theta_{lb}}{dt} \quad (4.4)$$

as the nodal precession rate of $\hat{\mathbf{L}}$ (with $\Omega_{pl,0}$ the nodal precession rate at $e = 0$), and the nutation rate of $\hat{\mathbf{L}}$, respectively. Each of these is a strong function of

eccentricity, and therefore time; together, they serve as driving forces for the stellar spin dynamics. Their precise forms can be found in SL15.

4.3.2 Stellar Spin Precession

Due to the star's rotation-induced quadrupole, the stellar spin axis $\hat{\mathbf{S}}$ experiences periodic torquing from the planet, which is strongest at the maximum eccentricity points of the LK cycle. This torque induces precession of $\hat{\mathbf{S}}$ around the planet's orbital angular momentum axis $\hat{\mathbf{L}}$, governed by the equation

$$\frac{d\hat{\mathbf{S}}}{dt} = \Omega_{ps}\hat{\mathbf{L}} \times \hat{\mathbf{S}}, \quad (4.5)$$

where

$$\Omega_{ps} \equiv -\frac{3GM_p(I_3 - I_1)}{2a^3(1 - e^2)^{3/2}} \frac{\cos\theta_{sl}}{S} \quad (4.6)$$

is the precession frequency. Here I_3 and I_1 are the principal moments of inertia of the star, S is the magnitude of the spin angular momentum, and θ_{sl} is the angle between $\hat{\mathbf{S}}$ and $\hat{\mathbf{L}}$. To separate out the θ_{sl} and e dependencies, we define a function $\alpha(t)$ as

$$\Omega_{ps}(t) \equiv -\alpha(t) \cos\theta_{sl} = -\frac{\alpha_0}{[1 - e(t)^2]^{3/2}} \cos\theta_{sl}, \quad (4.7)$$

where

$$\begin{aligned} \alpha_0 &= \frac{3GM_p(I_3 - I_1)}{2a^3I_3\Omega_*} \\ &= 1.19 \times 10^{-8} \left(\frac{2\pi}{1\text{yr}}\right) \left(\frac{2k_q}{k_*}\right) \left(\frac{10^3M_p}{M_*}\right) \left(\frac{\hat{\Omega}_*}{0.05}\right) \times \\ &\quad \times \left(\frac{a}{1\text{AU}}\right)^{-3} \left(\frac{M_*}{M_\odot}\right)^{1/2} \left(\frac{R_*}{R_\odot}\right)^{3/2}. \end{aligned} \quad (4.8)$$

Here we have used $(I_3 - I_1) \equiv k_q M_\star R_\star^2 \hat{\Omega}_\star^2$, with $\hat{\Omega}_\star = \Omega_\star / (GM_\star / R_\star^3)^{1/2}$ the dimensionless stellar rotation rate, and $S = I_3 \Omega_s \equiv k_\star M_\star R_\star^2 \Omega_\star$. For a solar-type star, $k_q \approx 0.05$, and $k_\star \approx 0.1$ (Claret and Gimenez, 1992).

Note that since $\alpha(t)$ is just Ω_{ps} evaluated at $\cos \theta_{sl} = 1$, it gives the maximum attainable spin precession rate at any given point in time, and α_0 gives the maximum precession rate at $e = 0$. We emphasize that these rates depends linearly on both the planet mass M_p and the stellar spin rate Ω_\star , and are strong inverse functions of the semi-major axis a .

SAL and SL15 further defined an adiabaticity parameter ϵ as

$$\epsilon \equiv \frac{\Omega_{pl,0}}{\alpha_0}, \quad (4.9)$$

and showed that, generically speaking, ϵ serves as a predictor for the behavior of the system. Given a set of initial parameters such that $\epsilon \gg 1$, the system behaves “non-adiabatically”: the nodal precession of $\hat{\mathbf{L}}$ is much faster than the precession of $\hat{\mathbf{S}}$; therefore, $\hat{\mathbf{S}}$ essentially precesses around the time average of $\hat{\mathbf{L}}$, thereby conserving θ_{sb} , the angle between the stellar spin axis and the outer binary axis. If $\epsilon \ll 1$, the system behaves “adiabatically”: the nodal precession of $\hat{\mathbf{L}}$ is much slower than the precession of $\hat{\mathbf{S}}$, and therefore $\hat{\mathbf{S}}$ has no trouble keeping up with $\hat{\mathbf{L}}$ and conserves θ_{sl} . For intermediate values of ϵ , which SAL termed the “trans-adiabatic” regime, the spin dynamics is complex and often chaotic. SL15 focused on exploring the spin dynamics in this regime but close to the adiabatic transition (i.e. for $\epsilon \lesssim 1$). We discuss their methods and findings in the rest of this section.

4.3.3 Hamiltonian Spin Dynamics

Because our primary goal is to study the behavior of the spin-orbit misalignment angle θ_{sl} , it is convenient to work in a frame of reference where $\hat{\mathbf{L}}$ is invariant. In this frame, it can be shown (SL15) that the spin dynamics are governed by the following Hamiltonian:

$$H = -\frac{1}{2}\alpha(t)(\cos\theta_{\text{sl}})^2 - \dot{\theta}_{\text{lb}}(t)\sin\theta_{\text{sl}}\sin\phi_{\text{sl}} - \Omega_{\text{pl}}(t)[\cos\theta_{\text{lb}}(t)\cos\theta_{\text{sl}} - \sin\theta_{\text{lb}}(t)\sin\theta_{\text{sl}}\cos\phi_{\text{sl}}], \quad (4.10)$$

where ϕ_{sl} is the precession phase of $\hat{\mathbf{S}}$ about $\hat{\mathbf{L}}$. Note that here ϕ_{sl} and $\cos\theta_{\text{sl}}$ constitute the conjugate pair of variables, with $\cos\theta_{\text{sl}}$ acting as the conjugate momentum. When the first term of the Hamiltonian is large compared to the others, the system is adiabatic. When it is small, the system is non-adiabatic.

In order to simplify this Hamiltonian, SL15 introduced a rescaled time variable τ , defined as

$$\tau(t) = \frac{n_e}{\bar{\alpha}} \int_0^t \alpha(t')dt', \quad (4.11)$$

where

$$\frac{\bar{\alpha}}{n_e} \equiv \frac{1}{2\pi} \int_0^{2\pi/n_e} \alpha(t)dt \quad (4.12)$$

is the ratio of the time-averaged maximum spin precession frequency $\alpha(t)$ and the LK eccentricity precession rate n_e and thus gives the maximum number of times that $\hat{\mathbf{S}}$ can go around $\hat{\mathbf{L}}$ in one LK cycle. Thus, $\bar{\alpha}/n_e$ is, in fact, a better measure of the adiabaticity of the system than ϵ , which is a fact that we discuss in more detail later in the section. Using the new rescaled time variable τ , which is normalized such that it varies from 0 to 2π in one LK eccentricity cycle, the

Hamiltonian can now be recast in the following form:

$$H'(p, \phi_{\text{sl}}, \tau) = \frac{\bar{\alpha}}{n_e} \left\{ -\frac{1}{2} p^2 + \epsilon \psi(\tau) p - \epsilon \sqrt{1 - p^2} \left[\beta(\tau) \cos \phi_{\text{sl}} + \gamma(\tau) \sin \phi_{\text{sl}} \right] \right\}, \quad (4.13)$$

where we have defined $p \equiv \cos \theta_{\text{sl}}$, and

$$\epsilon \beta(\tau) = -\frac{\Omega_{\text{pl}}(\tau)}{\alpha(\tau)} \sin \theta_{\text{lb}}(\tau), \quad (4.14)$$

$$\epsilon \gamma(\tau) = \frac{\dot{\theta}_{\text{lb}}(\tau)}{\alpha(\tau)}, \quad (4.15)$$

$$\epsilon \psi(\tau) = -\frac{\Omega_{\text{pl}}(\tau)}{\alpha(\tau)} \cos \theta_{\text{lb}}(\tau). \quad (4.16)$$

Since $\epsilon = \Omega_{\text{pl},0}/\alpha_0$, the functions $\beta(\tau)$, $\gamma(\tau)$ and $\psi(\tau)$ are “shape” functions that depend only on the “shape” of the orbit, i.e., on $e(\tau)$ (with τ varying from 0 to 2π). For a given $\theta_{\text{lb},0}$ (and $e_0 \simeq 0$), and in the absence of tidal dissipation and short-range forces, these functions are fixed and do not depend on any other parameters. These shape functions can then be decomposed into Fourier components, as

$$\beta(\tau) = \sum_{M=0}^{\infty} \beta_M \cos M\tau, \quad (4.17)$$

$$\gamma(\tau) = \sum_{M=1}^{\infty} \gamma_M \sin M\tau, \quad (4.18)$$

$$\psi(\tau) = \sum_{M=0}^{\infty} \psi_M \cos M\tau, \quad (4.19)$$

and the Hamiltonian can be written as

$$H' = \frac{\bar{\alpha}}{n_e} \left\{ -\frac{1}{2} p^2 + \epsilon \psi_0 p + \epsilon p \sum_{M=1}^{\infty} \psi_M \cos Mt - \frac{\epsilon}{2} \sqrt{1 - p^2} \sum_{M=0}^{\infty} [(\beta_M + \gamma_M) \cos(\phi_{\text{sl}} - M\tau) + (\beta_M - \gamma_M) \cos(\phi_{\text{sl}} + M\tau)] \right\}. \quad (4.20)$$

Note that γ_0 is not defined in Eq. (4.18). For convenience, we set $\gamma_0 = \beta_0$, but note that in actuality the time average of the function $\gamma(\tau)$ is 0, due to its anti-symmetric shape.

A resonance occurs when the argument of one of the cosine functions in the above Hamiltonian is slow-varying, i.e. if $d\phi_{\text{sl}}/d\tau = N$, with N an integer (positive or negative). All discussion up to this point has applied for arbitrary ϵ ; now, however, in order to acquire a tractable resonance condition, we now assume ϵ is small. In that case, the Hamiltonian is dominated by the first term and we have $d\phi_{\text{sl}}/d\tau \simeq p\bar{\alpha}/n_e$. Then the resonance condition becomes

$$\bar{\Omega}_{\text{ps}} = -\bar{\alpha} \cos \theta_{\text{sl}} = N n_e, \quad \text{with } N = 0, \pm 1, \pm 2, \pm 3, \dots \quad (4.21)$$

That is, when the time-averaged stellar spin precession frequency is equal to an integer multiple of the LK eccentricity precession rate n_e , the system experiences a resonance. When this happens, the influence of all other terms in Eq. (4.20) can be averaged out and the system is governed by the single-resonance Hamiltonian

$$H_N = \frac{\bar{\alpha}}{n_e} \left[-\frac{1}{2} p^2 + \epsilon \psi_0 p - \frac{\epsilon}{2} \sqrt{1-p^2} (\beta_N + \gamma_N) \cos(\phi_{\text{sl}} - N\tau) \right]. \quad (4.22)$$

Note that, since $\cos \theta_{\text{sl}}$ spans the range of values $\{-1, 1\}$, it follows that for a given $\bar{\alpha}$ there exists an entire set of resonances, with zeroth order resonant momenta given by

$$p_N = (\cos \theta_{\text{sl}})_N = -\frac{N n_e}{\bar{\alpha}}. \quad (4.23)$$

Since $\cos \theta_{\text{sl}}$ cannot exceed 1, that means there exists a maximum resonance order

$$N_{\text{max}} = \frac{\bar{\alpha}}{n_e}, \quad (4.24)$$

which we allow to be non-integer because, as discussed previously, it also has physical significance as simply the maximum number of times $\hat{\mathbf{S}}$ can go around $\hat{\mathbf{L}}$ in one LK cycle. In later sections we show that, when tidal dissipation is introduced, this parameter is a key parameter in determining the dynamics of the system.

As discussed in great detail in SL15, in $\cos \theta_{\text{sl}}$ vs $\phi_{\text{sl}} - N\tau$ phase space, the region of influence of each resonance is defined by its separatrix, which has a distinctive cat-eye shape centered on $\cos \theta_{\text{sl}} = p_N$ and $\phi_{\text{sl}} - N\tau = 0$ or π , depending on the sign of $(\beta_N + \gamma_N)$ (see Fig. 4.3). The Chirikov criterion (Chirikov, 1979) states that overlaps in the separatrices of two or more resonances leads to chaos. We thoroughly explored this idea in SL15 and showed that, indeed, the appearance of chaos in the system can be explained by overlaps between resonances of different N 's.

One final point needs to be made. Recall, once again, that the above discussion of resonances applies solely in the regime where the first term of the Hamiltonian (4.20) dominates over the others. We stated, above, and in SL15, that this regime corresponds roughly with $\epsilon \lesssim 1$. More precisely, however, since in general (see SL15) we have $(\beta_0 + \gamma_0) > (\beta_N + \gamma_N)$ for $N \neq 0$, the boundary of this regime can be defined more accurately as $\epsilon(\beta_0 + \gamma_0) \lesssim 1$. We thus define

$$\bar{\mathcal{A}} \equiv \epsilon^{-1}(\beta_0 + \gamma_0)^{-1} \quad (4.25)$$

as a new, more precise, adiabaticity parameter, such that when $\bar{\mathcal{A}} \gtrsim 1$ the system is adiabatic. $\bar{\mathcal{A}}$ is related to N_{\max} via

$$\bar{\mathcal{A}} = \frac{N_{\max} n_e}{2\langle \Omega_{\text{pl}} \sin \theta_{\text{lb}} \rangle}, \quad (4.26)$$

where the triangle brackets denote time averaging, and physically represents the ratio of the maximum change in $\hat{\mathbf{S}}$ to the change in $\hat{\mathbf{L}}$ during one LK cycle.

Thus, if $\bar{\mathcal{A}} \ll 1$, the spin vector hardly moves compared with the orbital angular momentum vector and the system behaves non-adiabatically, whereas when $\bar{\mathcal{A}} \gg 1$ the system behaves adiabatically as long as $\cos \theta_{\text{sl}}$ is not very close to 0.

The quantity $n_e/\langle \Omega_{\text{pl}} \sin \theta_{\text{lb}} \rangle$ is invariant so long as the “shape” of the orbit remains the same, i.e. it depends only on a , $\theta_{\text{lb},0}$ and $e(\tau)$. Thus, so long as the “shape” of the orbit is unchanged, only one parameter (either $\bar{\mathcal{A}}$ or N_{\max}) need be used to determine the behavior of the system. In comparing the behavior of systems with orbits of different “shapes”, however, both parameters are crucial. To recap, $\bar{\mathcal{A}}$ compares the rate of change of $\hat{\mathbf{S}}$ with the rate of change of $\hat{\mathbf{L}}$, whereas N_{\max} compares the rate of change of $\hat{\mathbf{S}}$ with the LK eccentricity oscillation frequency n_e and sets the maximum resonance order. Physically, it is of note that both N_{\max} and $\bar{\mathcal{A}}$ scale linearly with the stellar spin rate and the planet mass. In the remainder of the paper, we will show how the values that these two parameters take determine the behavior of the system and, in the presence of tidal dissipation, the ultimate fate of the spin-orbit misalignment angle.

4.4 Effect of Short-Range Forces

The analysis of SL15 focused solely on the “pure” Lidov-Kozai system described briefly in Section 4.3.1. As a step toward realism, we now account for extra periastron advance induced in the system by perturbations due to GR and the tidally- and rotationally-induced quadrupole moments of the planet (Wu and Murray, 2003). The extra periastron advance affects the LK+spin dynamics in two ways.

First, it slightly changes the LK eccentricity timescale n_e ; this change is

largely unimportant.

Second, it (sometimes significantly) reduces the maximum eccentricity attained during each LK cycle (Liu et al., 2015), thus changing the “shape” of $e(t)$. The new maximum eccentricity depends not on $\theta_{lb,0}$ (cf Eq. 4.2), but on the physical parameters of the system, including the planet mass M_p , semi-major axis a , and binary separation a_b . This leads to significant changes in the shape functions defined in Eqs. (4.14)-(4.16) and hence in the Fourier coefficients β_N , γ_N and ψ_N . Figure 4.1 demonstrates this effect: in general, the variation in the shape functions becomes smoother and less pronounced. We note that from Fig. 4.1 it is obvious that short-range forces increase β_0 (the τ -average of Eq. 4.14) and therefore decrease $\bar{\mathcal{A}}$ (Eq. 4.25), making the system less adiabatic.

Due to the reduction of e_{\max} , the maximum of $\alpha(t)$ (Eq. 4.7) is also reduced, leading to a significant decrease in $\bar{\alpha}$ (Eq. 4.12). Thus, another consequence of the inclusion of short-range forces is a decrease in the parameter N_{\max} (Eq. 4.24). Figure 4.2 presents N_{\max} as a function of the initial orbital inclination $\theta_{lb,0}$ with and without short-range forces, to illustrate this effect. We see that, in general, N_{\max} is greatly reduced when short-range forces are present. Furthermore, because short range forces tend to set the maximum eccentricity to a value that is not sensitive to $\theta_{lb,0}$ (Liu et al., 2015), N_{\max} in the presence of short range forces becomes nearly independent of the initial inclination. It is worth noting that N_{\max} still scales linearly with the stellar spin rate (or inversely with the spin period), but its dependence on M_p is no longer as simple, since M_p now plays a role in setting the maximum eccentricity.

For comparison, Figure 4.3 demonstrates how a sample phase space previously presented in SL15 (Fig. 6) changes when short-range forces are added to

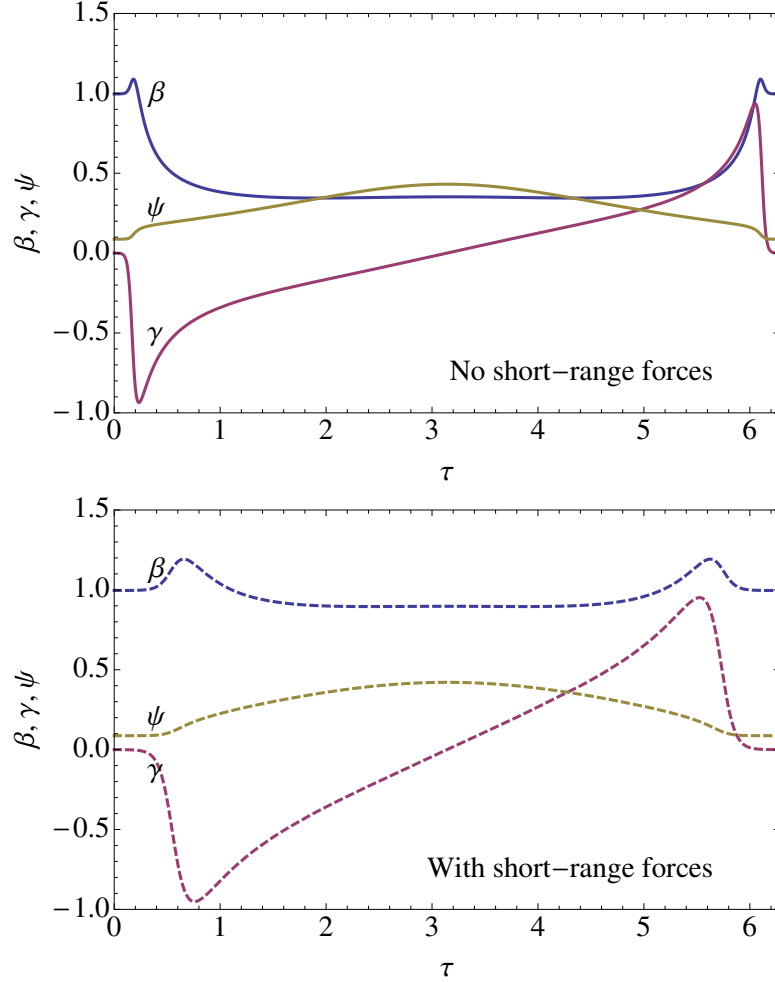


Figure 4.1: Shape functions β , γ , and ψ for $\theta_{lb,0} = 85^\circ$ as a function of the rescaled time variable τ , without (top panel) and with (bottom panel) short range forces. Physical parameters for bottom panel are $M_p = 5M_J$, $a_b = 300$ AU, $a = 1.5$ AU.

the system: as expected, the number of resonances is significantly reduced, and on the whole most resonances become wider. In summary, given a system with a set of initial parameters, the inclusion of short-range forces changes the shape functions that drive the spin precession dynamics, and generally decreases both \bar{A} and N_{\max} , reducing the degree of adiabaticity of the system.

Finally, note that there is one more non-ideal effect we have continued to ignore: the perturbation of the planet's orbit due to the rotationally-induced

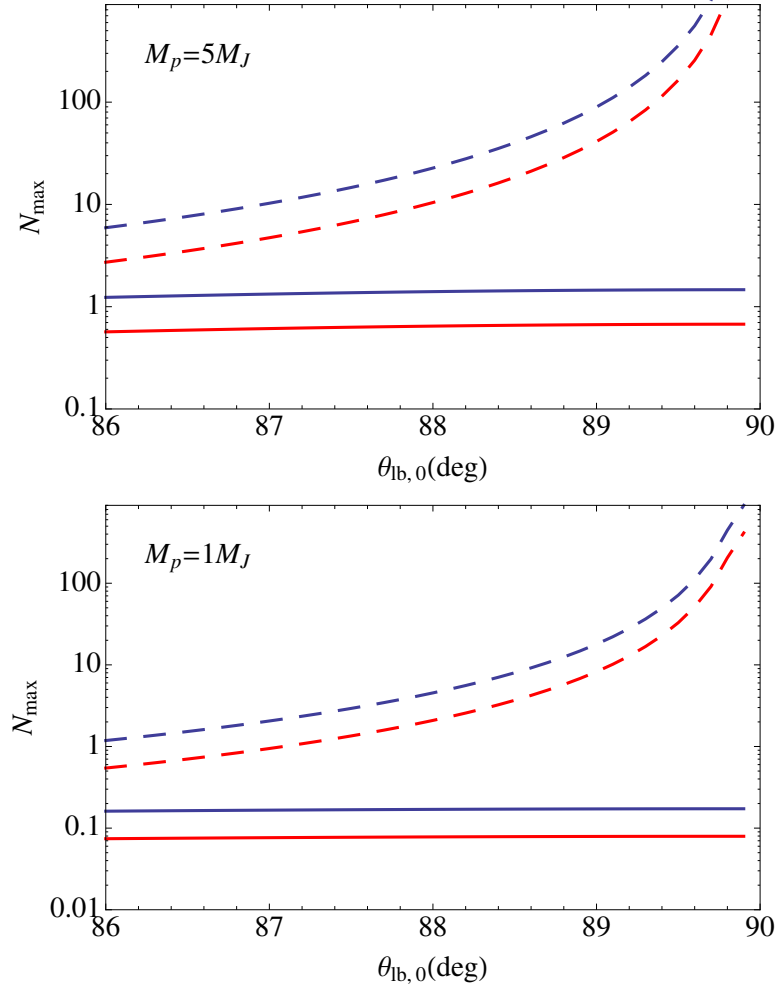


Figure 4.2: N_{\max} as a function of initial inclination for two planet masses (top panel: $M_p = 5M_J$; bottom panel: $M_p = 1M_J$) and two stellar spin periods (red: $P_\star = 5$ days; blue: $P_\star = 2.3$ days). Dashed: without short-range forces. Solid: with short-range forces.

stellar quadrupole. This perturbation comes in two forms: first, just as \hat{S} precesses about \hat{L} , so should \hat{L} precess about \hat{S} . Second, the stellar quadrupole induces additional periastron advance in the orbit, similar to the other short range forces. We ignore these effects because, by creating feedback between stellar spin precession and orbit precession, they break the integrability of the Hamiltonian system by introducing more degrees of freedom (i.e. $e(t)$, $\Omega_{pl}(t)$, etc would no longer be solely determined by LK dynamics and would not act

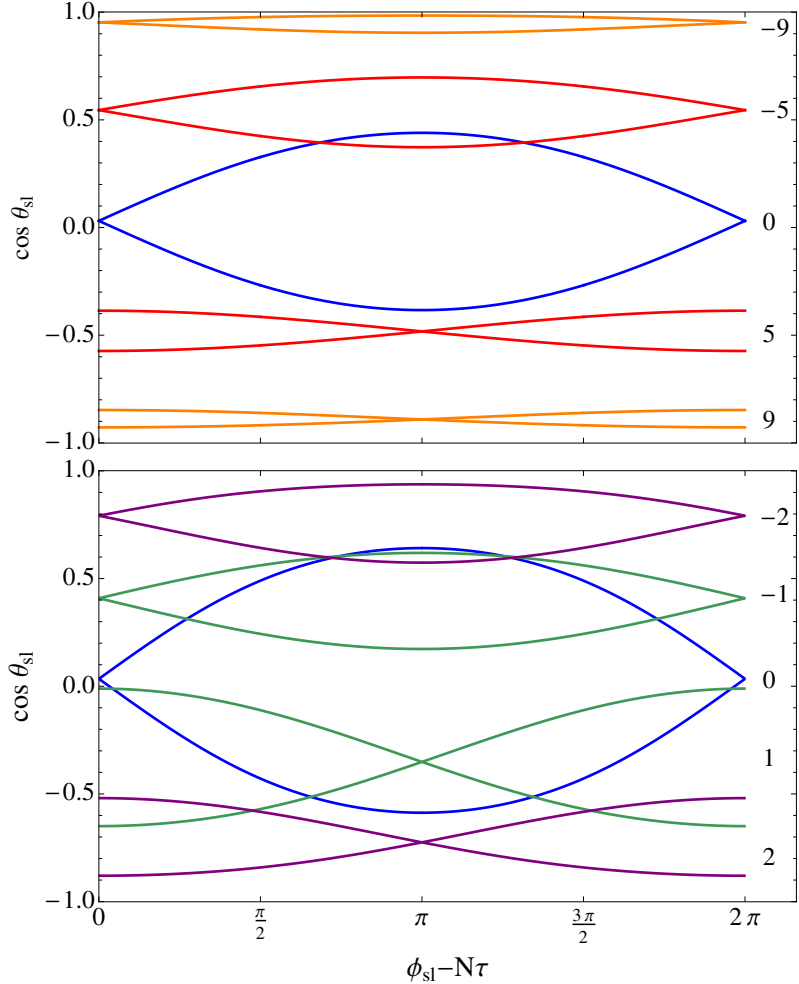


Figure 4.3: Locations of several resonances, labeled on the right-hand side with their corresponding N , for the shape functions presented in Fig. 4.1 ($\theta_{lb,0} = 85^\circ$), with $\epsilon = 0.1$, without (top panel) and with (bottom panel) short range forces.

as known externally-imposed forcing functions in our Hamiltonian).

Omission of the feedback effect is the single biggest simplifying assumption we make in our analysis. Particularly for low planet masses and high stellar rotation rates, this makes our subsequent analysis of the spin dynamics somewhat pedagogical. For higher planet masses and lower stellar spin rates, however, for which feedback is not as important, our conclusions should still be more or less robust.

4.5 Non-dissipative Regime Classification

In this section we discuss the differences in the behavior of a given non-dissipative system in the non-adiabatic vs adiabatic regimes. For the remainder of the section, we fix the “shape” of the LK orbit by considering systems with $M_p = 5M_J$, $\theta_{lb,0} = 89^\circ$, $a = 1.5$ AU, and $a_b = 300$ AU and varying only the stellar spin period, which scales up/down both N_{\max} and $\bar{\mathcal{A}}$. Note that, in order to explore the entire range of possible behaviors, we consider a somewhat unphysical range of stellar spin periods, from as large as 50 days to as small as 1 day.

We first consider spin dynamics in the non-adiabatic regime, with $\bar{\mathcal{A}} \lesssim 1$ and $N_{\max} \ll 1$. We then consider the adiabatic regime with $\bar{\mathcal{A}} \gtrsim 1$, which further breaks into two sub-regimes with $N_{\max} \lesssim 1$ and $N_{\max} \gtrsim 1$. Finally, we specialize to the dynamics of trajectories that start with $\cos \theta_{sl} = 1$ (i.e. zero initial spin-orbit misalignment) and discuss their behavior in each of the aforementioned regimes.

4.5.1 Non-adiabatic Regime: $\bar{\mathcal{A}} \lesssim 1$

The form of the Hamiltonian (4.20) is such that the non-adiabatic regime of spin dynamics does not easily lend itself to perturbation theory and cannot easily be formally explored. Nevertheless, the non-adiabatic regime is very important (especially for Jupiter-mass planets) and we therefore endeavor to study it based on our intuition and empirical findings.

We classify the non-adiabatic regime as having $\bar{\mathcal{A}} \lesssim 1$ and $N_{\max} \ll 1$ (note

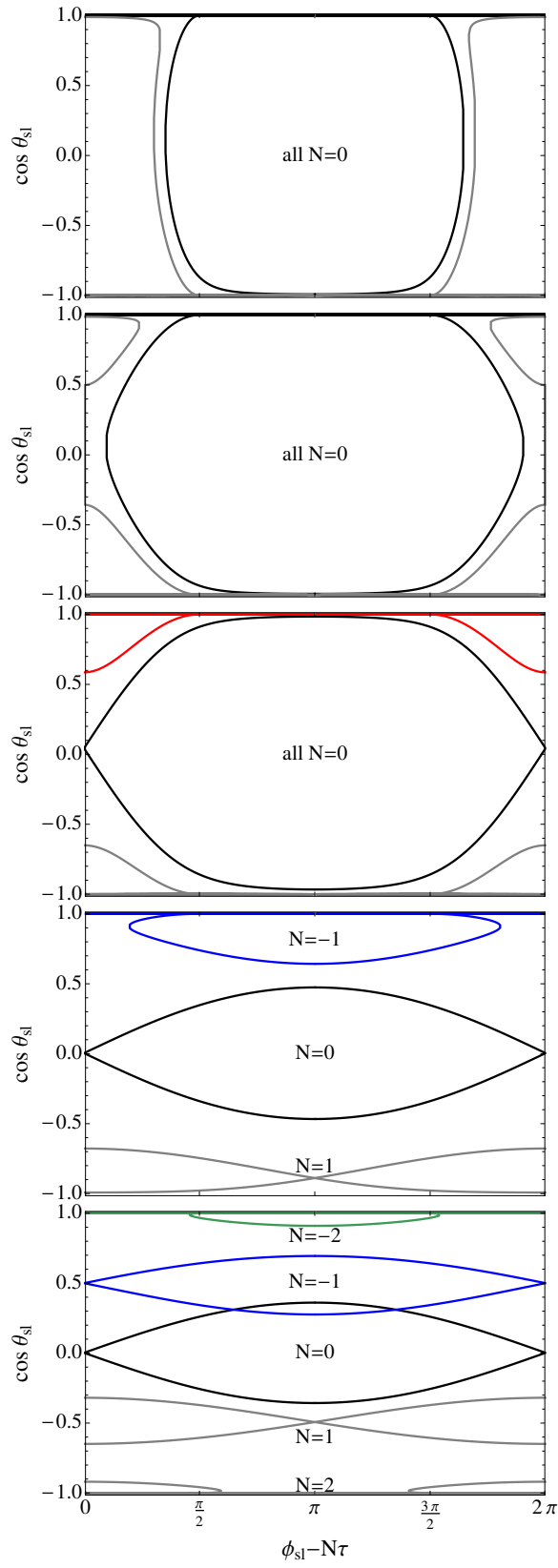


Figure 4.4: Sample separatrices in phase space for $M_p = 5M_J$, $\theta_{lb,0} = 89^\circ$ and, top to bottom, $P_\star = 50, 25, 20, 3$, and 1.7 days.

that N_{\max} can never be larger than $\bar{\mathcal{A}}$). In this case, the stellar spin vector $\hat{\mathbf{S}}$ is changing slowly compared to both the rate of change of $\hat{\mathbf{L}}$ and the LK oscillation frequency. We therefore surmise that most of the relevant spin dynamics can be captured using a time-independent Hamiltonian whose coefficients are the time averages of the externally imposed shape functions (β, ψ, γ) . In other words, we assume that most of the dynamics can be understood by analyzing the $N = 0$ Hamiltonian (cf. Eq. 4.22)

$$H_0 = \frac{\bar{\alpha}}{n_e} \left[-\frac{1}{2} p^2 + \epsilon \psi_0 p - \frac{1}{2\bar{\mathcal{A}}} \sqrt{1-p^2} \cos \phi_{\text{sl}} \right], \quad (4.27)$$

where we have replaced $\epsilon(\beta_0 + \gamma_0)$ using the definition of $\bar{\mathcal{A}}$. The top two panels of Figure 4.4 present example phase spaces calculated based on this Hamiltonian. The curves shown in each panel are separatrices that cannot be crossed by any trajectory. Thus, the shapes of the separatrices determine the possible trajectories. An analysis of the separatrix shapes, therefore, sheds light on the possible behaviors of the system.

At very low values of $\bar{\mathcal{A}}$ (Fig. 4.4, top panel), the phase space is roughly split into two islands of libration. The separatrix of one of them touches $\cos \theta_{\text{sl}} = 1$, whereas the other touches $\cos \theta_{\text{sl}} = -1$. The centers of these islands (the fixed points) are closely related to the well-known Cassini states [e.g. Fabrycky et al. (2007)]. A trajectory starting inside one of these separatrices will librate about the corresponding fixed point in the center of the island. Trajectories starting in the narrow region in-between the two separatrices are able to circulate.

As $\bar{\mathcal{A}}$ gets closer to 1, the central (centered on $\phi_{\text{sl}} = \pi$) libration island expands, while the other island shrinks and eventually cleaves into two separate islands, one of which still touches $\cos \theta_{\text{sl}} = -1$ (Fig. 4.4, second panel).

As $\bar{\mathcal{A}}$ increases, the center libration island spans an increasingly larger range

of ϕ_{sl} , until, when $\bar{\mathcal{A}} \simeq 1$, it spans the entire $\{0, 2\pi\}$ range and detaches from $\cos \theta_{\text{sl}} = 1$, forming the standard cat-eye shaped $N = 0$ resonance. (Fig. 4.4, middle panel). This marks the transition from non-adiabatic to adiabatic behavior.

4.5.2 Adiabatic Regime: $\bar{\mathcal{A}} \gtrsim 1$

$$N_{\max} \lesssim 1$$

Shortly after the non-adiabatic to adiabatic transition, N_{\max} is still small, and therefore the spin dynamics are still essentially governed by the $N = 0$ Hamiltonian. After the central $N = 0$ island/resonance has detached from $\cos \theta_{\text{sl}} = 1$, one of the side islands merges upward and *attaches* to $\cos \theta_{\text{sl}} = 1$ (Fig. 4.4, middle panel, shown in red). As $\bar{\mathcal{A}}$ and N_{\max} continue to increase, this new top island rapidly shrinks and is soon overtaken in importance by the newly forming $N = -1$ resonance. Likewise, the bottom island shrinks as well and is soon dominated by the $N = 1$ resonance.

$$N_{\max} \gtrsim 1$$

As N_{\max} approaches 1, the stellar spin dynamics are no longer determined solely by the $N = 0$ Hamiltonian. Rather, Hamiltonians for $N = 1$ and $N = -1$ must also be considered (cf. Eq. 4.22). For $0.5 \lesssim N_{\max} \lesssim 1$, each of these Hamiltonians produces a separatrix that is attached to $\cos \theta_{\text{sl}} = 1$ (for $N = -1$) and $\cos \theta_{\text{sl}} = -1$ (for $N = 1$). As N_{\max} continues to increase, the separatrices “emerge” more fully into the phase space until eventually they detach from the top and bottom

edges and form standard cat-eye shapes. Note that, due to the slight asymmetry in the Hamiltonians introduced by the $\psi_0 p$ term, the bottom resonance detaches slightly earlier than $N_{\max} \simeq 1$, whereas the top resonance detaches slightly later than $N_{\max} \simeq 1$ (Fig. 4.4, fourth panel).

After the $N = \pm 1$ resonances have emerged fully, the $N = \pm 2$ resonances begin to grow, and likewise detach and form cat-eye shapes when $N_{\max} \simeq 2$ (Fig. 4.4, bottom panel).

4.5.3 The initially-aligned trajectory

In the standard planetary system formation scenario, the final outcome is usually a system in which the stellar spin axis and the planet orbital axis are aligned. Although in recent years several methods of generating primordial misalignment have been suggested (Bate et al., 2010; Batygin, 2012; Batygin and Adams, 2013; Lai, 2014; Lai et al., 2011; Spalding and Batygin, 2014), for the remainder of this paper we choose to focus solely on systems with $\cos \theta_{\text{sl},0} = 1$, i.e. no initial spin-orbit misalignment. What determines the behavior of these systems?

One key observation can be taken away from the five panels presented in Fig. 4.4: regardless of what regime the system is in, there is *always* a separatrix “attached” to $\cos \theta_{\text{sl}} = 1$. In the non-adiabatic regime this separatrix is the $N = 0$ center island. In the adiabatic regime, this separatrix is the $N = 0$ top island when N_{\max} is small, and then $N = -1$ for $N_{\max} \lesssim 1$, $N = -2$ for $N_{\max} \lesssim 2$, and so on. These are the separatrices that determine the behavior of the initially aligned trajectory.

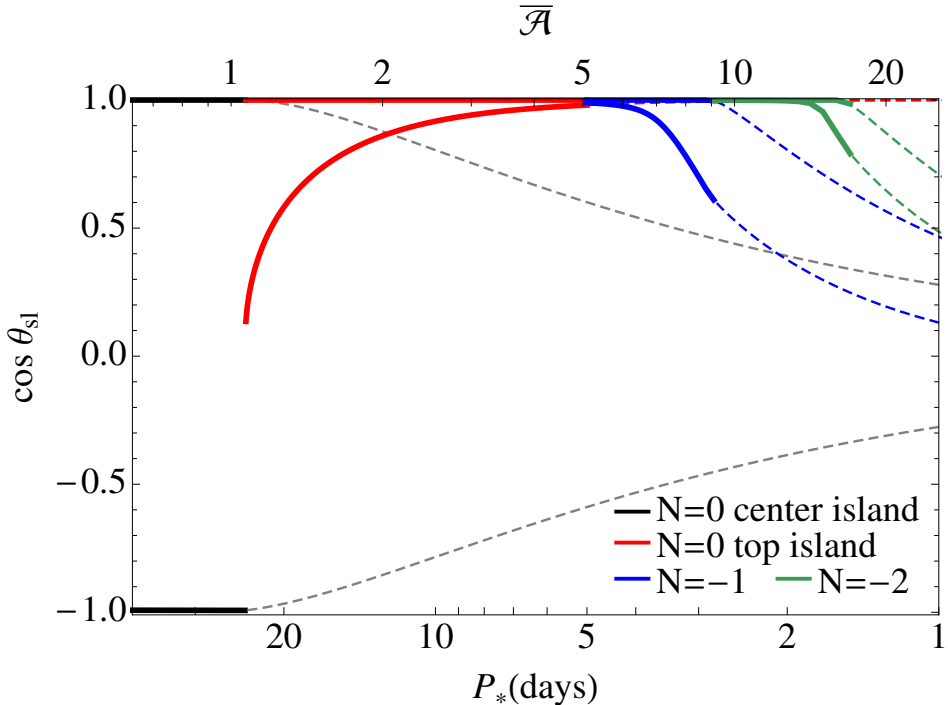


Figure 4.5: Maximum widths of each of the sample separatrices presented in Fig. 4.4 as a function of stellar spin period for $\theta_{lb,0} = 89^\circ$, $M_p = 5M_J$. Colors have been chosen to match those of Fig. 4.4. The separatrix widths are shown in bold solid lines whenever they touch $\cos \theta_{sl} = 1$, since they then determine the behavior of the initially-aligned trajectory. After detaching from $\cos \theta_{sl} = 1$, each separatrix is shown in thin dashed lines of the same color. Note the transition from non-adiabatic behavior (controlled by the $N = 0$ center island) to adiabatic behavior happens at $\bar{A} \simeq 1$.

Figure 4.5 presents a different way of visualizing this information. It shows the maximum vertical width of each of the relevant (“attached” to $\cos \theta_{sl} = 1$) separatrices as a function of the stellar spin period P_* , with the corresponding values of \bar{A} given on the top axes. Note that although we do not show both \bar{A} and N_{\max} , in this case, since only the stellar spin period is varied, the two numbers are always related by the same factor, with $\bar{A} \simeq 8N_{\max}$. Since, in each case, the initially-aligned trajectory *starts out* on the relevant separatrix, its maximum vertical width represents the maximum range of spin-orbit misalignments that the trajectory can cover. Thus, in the non-adiabatic regime the stellar spin has

the most “freedom” and is able to cover the largest range of $\cos \theta_{\text{sl}}$. As $\bar{\mathcal{A}}$ increases, the spin axis’ range of excursion becomes progressively more and more limited, though not monotonically so.

4.6 Inclusion of Tides: Paths to Misalignment

We now include tidal dissipation in the planet interior and allow the semi-major axis of the planet to decay, and ask how the non-dissipative regimes outlined in the previous section map onto final spin-orbit misalignment angle distributions. We use the standard weak friction model for tidal dissipation; see SAL for details.

Under the influence of tides, several things happen. First, the semi-major axis decays, and consequently, the stellar spin precession rate increases (Eq. 4.8). The orbital and LK precession rates increase too, but not as dramatically, leading to an overall gradual increase in both $\bar{\mathcal{A}}$ and N_{\max} . As the semi-major axis decays, the shape of the LK orbit also changes, with the minimum eccentricity slowly increasing; thus, the shape functions that drive the stellar spin dynamics also slowly change in time. All of these changes, however, are slow enough for the system to be treated as quasi-static: we assume that for any given LK cycle the spin dynamics of the initially-aligned trajectory are still governed by one non-dissipative Hamiltonian, as described in the previous section. However, over time, i.e. over many LK cycles, the coefficients in the Hamiltonian slowly change, and the background non-dissipative phase space slowly evolves through a procession similar to that depicted in Figs. 4.4 and 4.5.

There are two consequences to this very slow evolution of the Hamiltonian

coefficients. First, since at any given point in time the system is still governed by a Hamiltonian, a (non-chaotic) trajectory still cannot cross a separatrix (unless it has no choice – more on this later). The implication of this is that if a trajectory starts out on or inside a certain separatrix, its behavior will continue to be governed by that (slowly evolving) separatrix.

Second, because the system evolves so gradually (or *adiabatically* - not to be confused with the adiabatic regime!), an adiabatic invariant emerges: the area enclosed by a trajectory in $\cos \theta_{\text{sl}} - (\phi_{\text{sl}} - N\tau)$ space is an approximately conserved quantity. Together, these two ideas (avoidance of separatrix crossings, and conservation of area) are all that is necessary to understand this dissipative system. Thus, in principle, knowing what separatrix governs the behavior of the initially-aligned trajectory at $t = 0$, plus knowledge of how that separatrix changes under the influence of tides, should be enough to determine the fate of the trajectory.

Since we have reasoned that it is the governing separatrix at $t = 0$ that determines the fate of the system, we define

$$\bar{\mathcal{A}}_0 \equiv \bar{\mathcal{A}}(t = 0), \quad N_{\max,0} \equiv N_{\max}(t = 0). \quad (4.28)$$

In the presence of tides, we expect that all possible outcomes may be classified using these two parameters.

4.6.1 Varying the stellar spin period

We begin by repeating the experiment of Section 4.5, including the influence of tides. That is, we fix the “shape” of the LK orbit by setting $M_p = 5M_J, \theta_{\text{lb},0} = 89^\circ$,

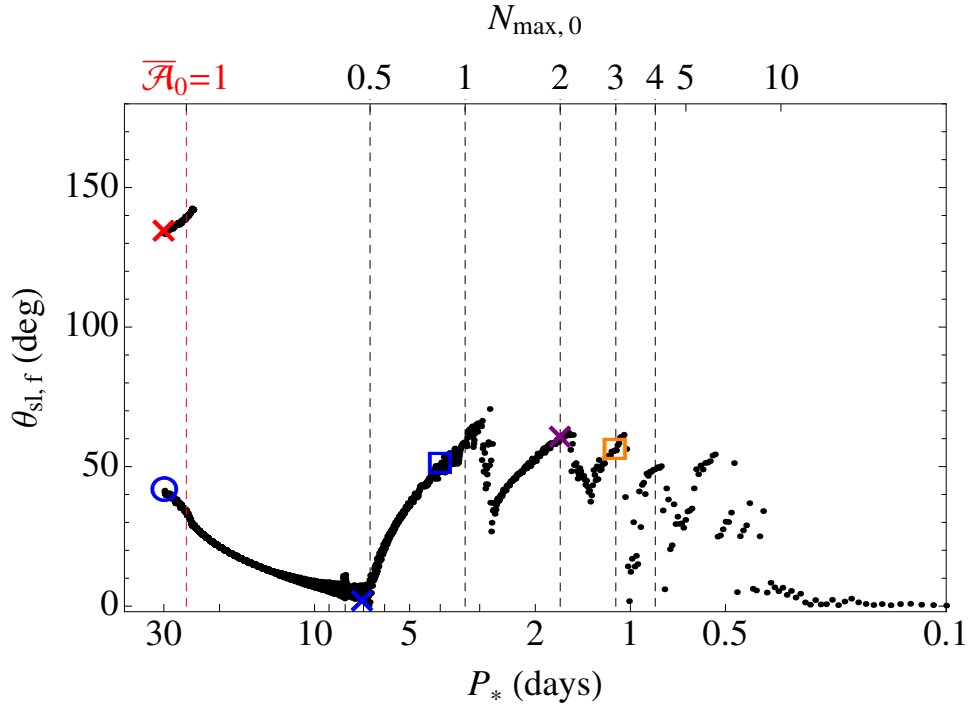


Figure 4.6: Final spin-orbit misalignments after tidal dissipation, as a function of stellar spin period, for $M_p = 5M_J$, $\theta_{lb,0} = 89^\circ$, $a_0 = 1.5$ AU, $a_b = 300$ AU. The blue, red, and purple X symbols correspond to the left, middle, and right example trajectories shown in Fig. 4.7, respectively. The blue O symbol corresponds to the blue trajectory in Fig. 4.8. The blue and orange square symbols correspond to the left and right panels of Fig. 4.10, respectively.

$a_0 = 1.5$ AU (the initial semi-major axis), and $a_b = 300$ AU and varying only the stellar spin period (which remains constant throughout the tidal evolution). We set $\theta_{sl,0} = 0$ and plot $\theta_{sl,f}$, the final spin-orbit misalignment angle, as a function of the stellar spin period in Figure 4.6. As before, we cover a somewhat unphysical range of stellar spin periods in order to capture all possible behaviors.

Three distinct categories of outcomes in Fig. 4.6 are rather easily identified. First: the distinct bimodal distribution at very high spin periods. Second: the unimodal, monotonically decreasing distribution at high to intermediate spin periods. Third: the striated pattern of spin-orbit misalignments at low and very low spin periods. We show an example of time evolutions resulting in each of

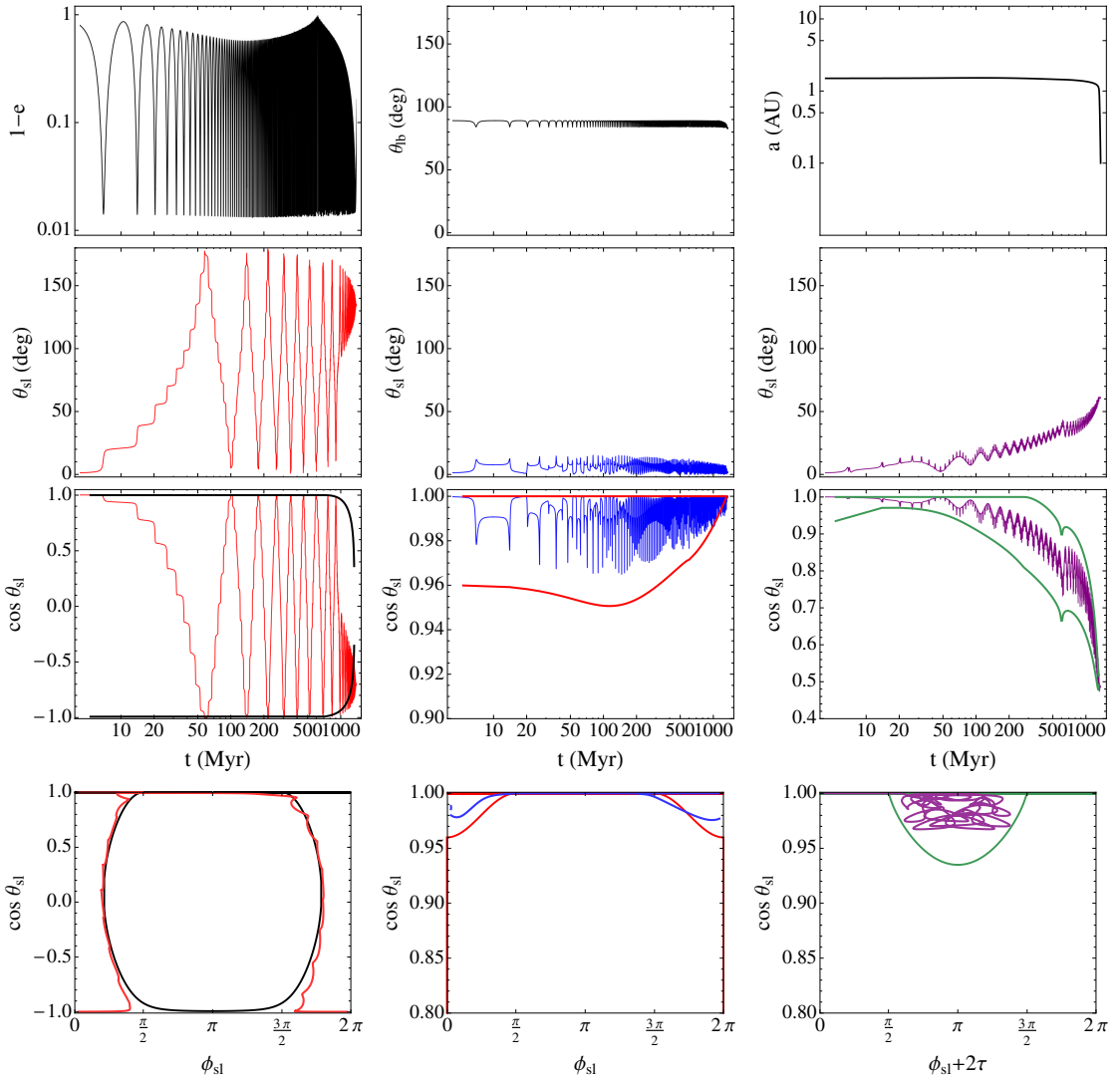


Figure 4.7: Sample evolution trajectories, including tidal dissipation, for $\theta_{lb,0} = 89^\circ$, $M_p = 5M_J$ and three different values of the stellar spin period. Left panels: $P_\star = 30$ days; middle panels: $P_\star = 7.07$ days; right panels: $P_\star = 1.67$ days. Top row: evolution of the orbital elements. Note the orbital elements' evolution is independent of the stellar spin period and is therefore the same for all three cases. Second row: evolution of the spin-orbit misalignment angle θ_{sl} . Third row: evolution of $\cos \theta_{\text{sl}}$ as well as the relevant background separatrix (see next). Bottom row: the initial background phase space (cf. Fig 4.4) as well as the first full cycle of evolution of $\cos \theta_{\text{sl}}$, showing that the relevant background separatrices, from left to right, are the $N = 0$ center island (shown in black), the $N = 0$ top island (shown in red), and the $N = -2$ resonance (shown in green).

these outcomes in Figure 4.7. We discuss each category of outcomes individually in the following subsections.

4.6.2 Non-adiabatic behavior: bimodality

In order to understand the clean bimodal spin-orbit misalignment distribution found at high stellar spin periods in Fig. 4.6, we first need to know which separatrix governs the behavior of the $\theta_{\text{sl},0} = 0$ trajectory at $t = 0$. Two simple clues point us to the answer: first, the left panels of Fig. 4.7 show an example of a time evolution from the bimodal outcome regime, as well as the $t = 0$ phase space for that evolution. We see that, clearly, the separatrix governing the behavior of the trajectory at $t = 0$ is the $N = 0$ central island. Second, in Fig. 4.6 the bimodal region ends very close to $\bar{\mathcal{A}}_0 \simeq 1$, i.e. at the stellar spin period for which at $t = 0$ we have $\bar{\mathcal{A}} \simeq 1$. From Section 4.5, we know that $\bar{\mathcal{A}} \simeq 1$ corresponds to the transition between non-adiabatic and adiabatic behavior, and that at $\bar{\mathcal{A}} \simeq 1$ the governing separatrix for the initially aligned trajectory switches from being the $N = 0$ center island to the $N = 0$ top island (see Fig. 4.4, middle panel, and Fig. 4.5). Thus, it follows that the bimodality found at high stellar spin periods in Fig. 4.6 corresponds to the initially non-adiabatic regime.

To understand why the outcome is bimodal, we now need to know two things: how the $N = 0$ center separatrix changes in time (due to tides), and how the trajectory interacts with it.

The $N = 0$ center separatrix changes in time (Fig. 4.7, left, third panel) in a way exactly analogous to the progression shown in Figs. 4.4 and 4.5. To start with, the separatrix is attached to $\cos \theta_{\text{sl}} = 1$. As tides act to reduce the semi-

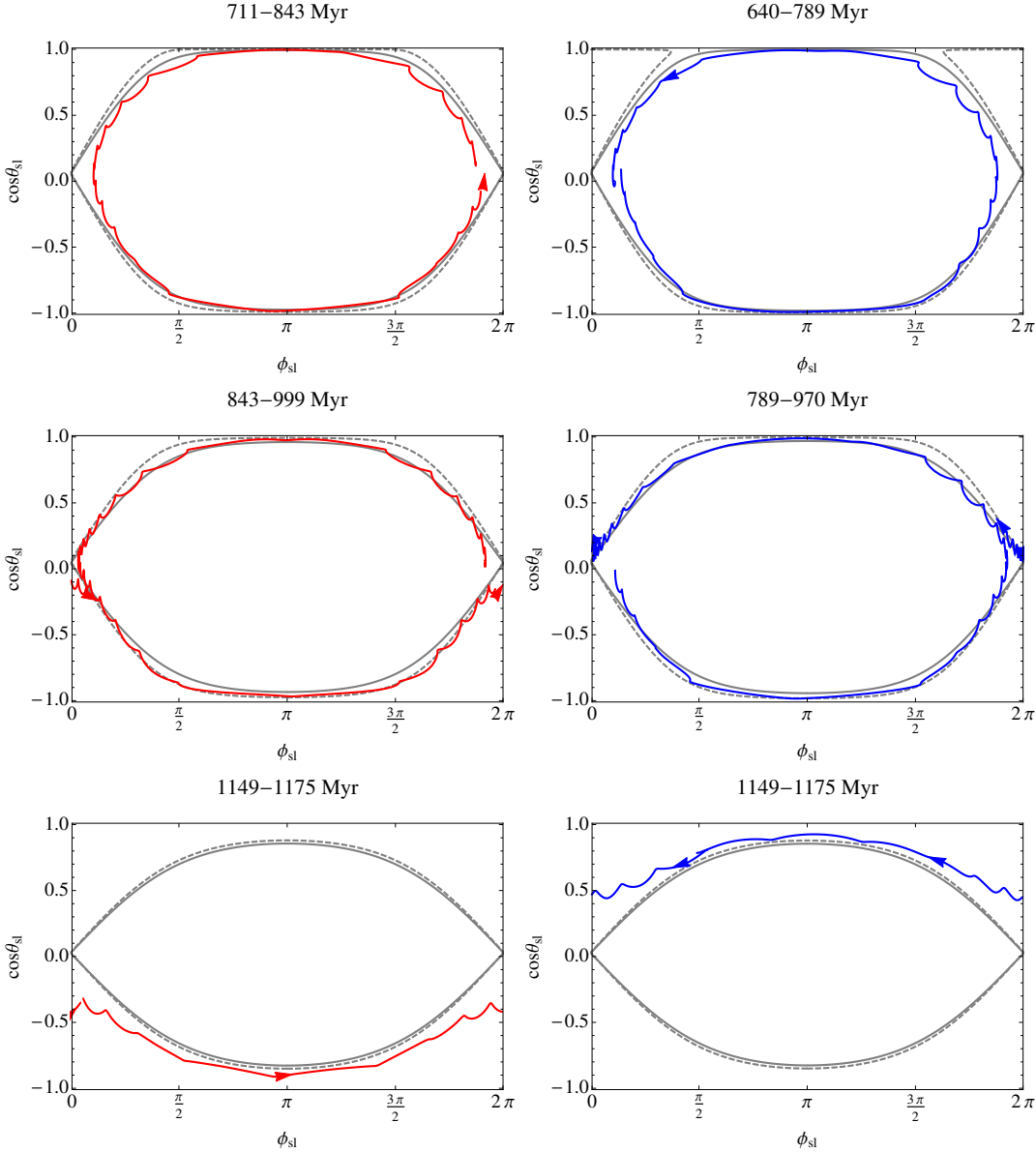


Figure 4.8: Demonstration of the process that gives rise to the bimodality found in the non-adiabatic regime of Fig. 4.6. In each panel, the dashed (solid) grey line shows the $N = 0$ separatrix at the beginning (end) of the time interval indicated at the top of the panel, while the colored line shows the actual time evolution of $\cos \theta_{\text{sl}}$ during that time interval. The red trajectory (left panels) has $P_* = 30$ days and is the trajectory shown in Fig. 4.7 (left) and marked with a red X in Fig. 4.6. The blue trajectory (right panels) has $P_* = 29.87$ days and is marked with a blue O in Fig. 4.6. Top panels: both trajectories are contained within the $N = 0$ separatrix and their areas are smaller than the separatrix area. Middle panels: the $N = 0$ separatrix has shrunk such that its area now matches the areas of the trajectories, thus the trajectories have no choice but to exist the resonance. The red (blue) trajectory's location at time of exit is such that it exits below (above) the separatrix. Bottom panels: both trajectories are now caught in their respective part of phase space.

major axis and increase \bar{A} and N_{\max} , the separatrix detaches from $\cos \theta_{\text{sl}} = 1$ and slowly shrinks.

On the other hand, the actual trajectory cannot shrink, due to the aforementioned adiabatic invariance of the area it encloses. Its initial area is set by the area of the separatrix at $t = 0$. At intermediate times the separatrix actually expands (analogously to the transition between panels 1 and 2 of Fig. 4.4) and the trajectory remains inside the separatrix. After the separatrix detaches and begins to shrink again, there comes a point when the area of the separatrix is equal to the area of the trajectory. At that point, the trajectory has no choice but to cross the separatrix. Figure 4.8 illustrates this idea. At time of crossing, the trajectory can cross either the top or the bottom part of the separatrix, depending on its phase. Two trajectories that start very close together can, over time, accumulate enough difference in phase that one ends up exiting through the top, and the other through the bottom. This is the origin of the bimodality seen in Fig. 4.6.

This “bifurcation” phenomenon is analogous to the case of a pendulum whose length is slowly decreased with time. The shorter the pendulum gets, the larger its amplitude of oscillation becomes, until at some point it must transition to circulating rather than oscillating. At that point, the pendulum will either “choose” to circulate clockwise or counterclockwise – corresponding to a positive or negative conjugate momentum – depending on its phase at the time of transition.

4.6.3 Stationary adiabatic behavior

For $\bar{\mathcal{A}}_0 \gtrsim 1$ and $N_{\max,0} \lesssim 0.5$, Fig. 4.6 shows a smooth unimodal distribution of final spin-orbit misalignments, with $\theta_{\text{sl},f}$ decreasing with decreasing P_* . In the previous subsection, we have already determined that the behavior in this regime must be governed by the $N = 0$ top island. The middle bottom panel of Fig. 4.7 shows that this is indeed the case. In order to understand the distribution of misalignments, we again need to ask how the $N = 0$ top separatrix evolves with time, and how the trajectory interacts with it.

Based on Figure 4.5, we know that an increase in $\bar{\mathcal{A}}$ or N_{\max} leads to a rapid decrease in the width of the $N = 0$ top island. On the other hand, again, the actual trajectory area cannot decrease and is set by the initial area of the top island. Thus, as soon as any significant semi-major axis decay occurs, the trajectory area should exceed the area of the top island, and the trajectory should circulate on the outside of the island.

For a circulating trajectory, the conserved area becomes the area between the trajectory and the $\cos \theta_{\text{sl}} = 0$ axis. Thus, as more semi-major axis decay occurs, the trajectory cannot move up/down, it can only straighten out, eventually settling on a constant $\cos \theta_{\text{sl},f}$ equal approximately to its mean $\cos \theta_{\text{sl}}$ at the time of decoupling from the top island.

Thus, if the top island is initially large, the final $\theta_{\text{sl},f}$ should be (relatively) large. For smaller stellar spin periods, the top island decreases in size; therefore, $\theta_{\text{sl},f}$ gets closer and closer to 0.

A caveat to the above discussion is the following: farther into the adiabatic regime, the assumption that only the $N = 0$ Hamiltonian determines the spin

dynamics becomes increasingly erroneous, since the stellar spin vector now precesses at rates comparable to the precession of $\hat{\mathbf{L}}$ and thus sees more than just the time average of the forcing functions. Thus, although the above discussion is suggestive and sound, the actual behavior of the trajectory can be a lot more random and need not obey these rules. This is why, for example, the trajectory depicted in the middle panels of Figure 4.7 actually remains level with, or inside, the top island for most of its evolution.

We term this regime of behavior “stationary adiabatic” because the trajectory essentially cannot move away from its initial location. This is to be contrasted with the behavior discussed in the following section.

4.6.4 Adiabatic advection

The concept of adiabatic advection was first considered by SL15 in a rather speculative manner. Here we demonstrate that the suppositions of SL15 were, in fact, exactly correct, and that adiabatic advection is a novel, interesting way of generating spin-orbit misalignment.

The idea behind adiabatic advection is simple: if at $t = 0$ the behavior of the $\cos \theta_{\text{sl},0} = 1$ trajectory is governed by a resonance $N = -1, -2, \dots$, then as tidal dissipation reduces the semi-major axis of the orbit, the trajectory can be advected by the governing resonance to non-zero misalignments. Figure 4.9 shows an example of exactly this behavior: in the top panel, at $t = 0$ we see that the trajectory is trapped inside the $N = -2$ resonance, which is still “attached” to $\cos \theta_{\text{sl}} = 1$. Just over a Gyr later, the resonance has detached and moved down significantly, and the trajectory has likewise moved down and remains

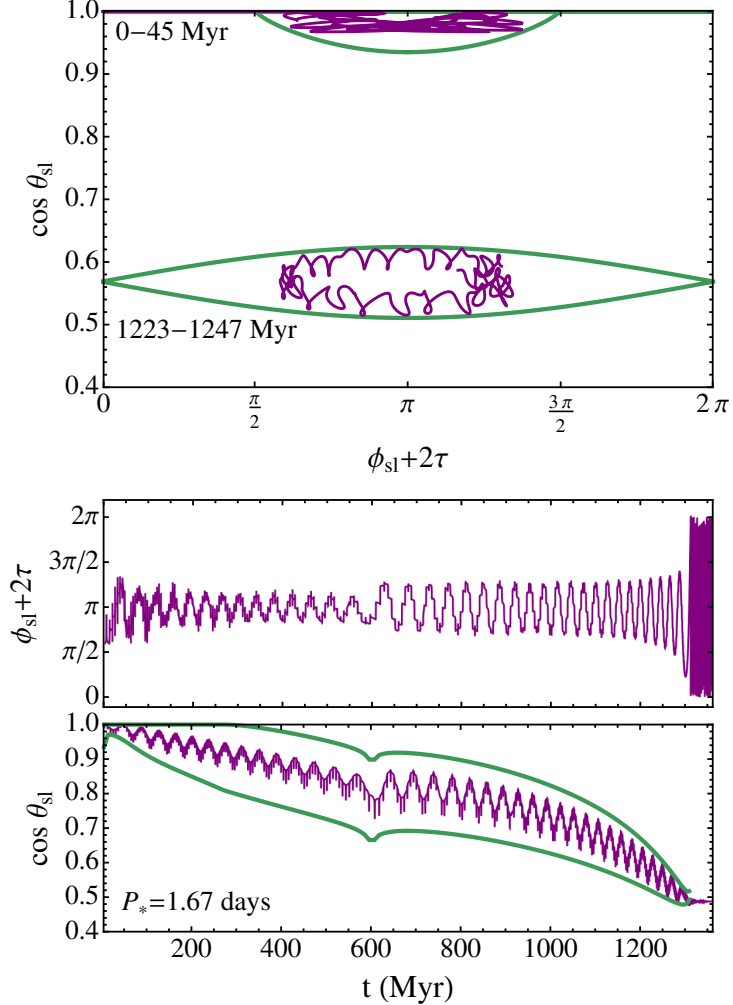


Figure 4.9: Demonstration of the process of adiabatic advection by an $N = -2$ resonance. In both panels, the purple time evolution corresponds to that of Fig. 4.7 (right) and is marked with a purple X in Fig. 4.6. Top panel: the median shape of the $N = -2$ resonance and the time evolution of $\cos \theta_{\text{sl}}$ is shown at two different time intervals. In both cases, the trajectory is contained inside the resonance. Bottom panel: the full evolution of $\phi_{\text{sl}} + 2\tau$ (top sub-panel) and $\cos \theta_{\text{sl}}$ (bottom sub-panel, purple) as well as the maximum width of the $N = -2$ resonance vs time (bottom sub-panel, green), confirming that the trajectory advects with the resonance until the resonance shrinks significantly and the trajectory has no choice but to exit.

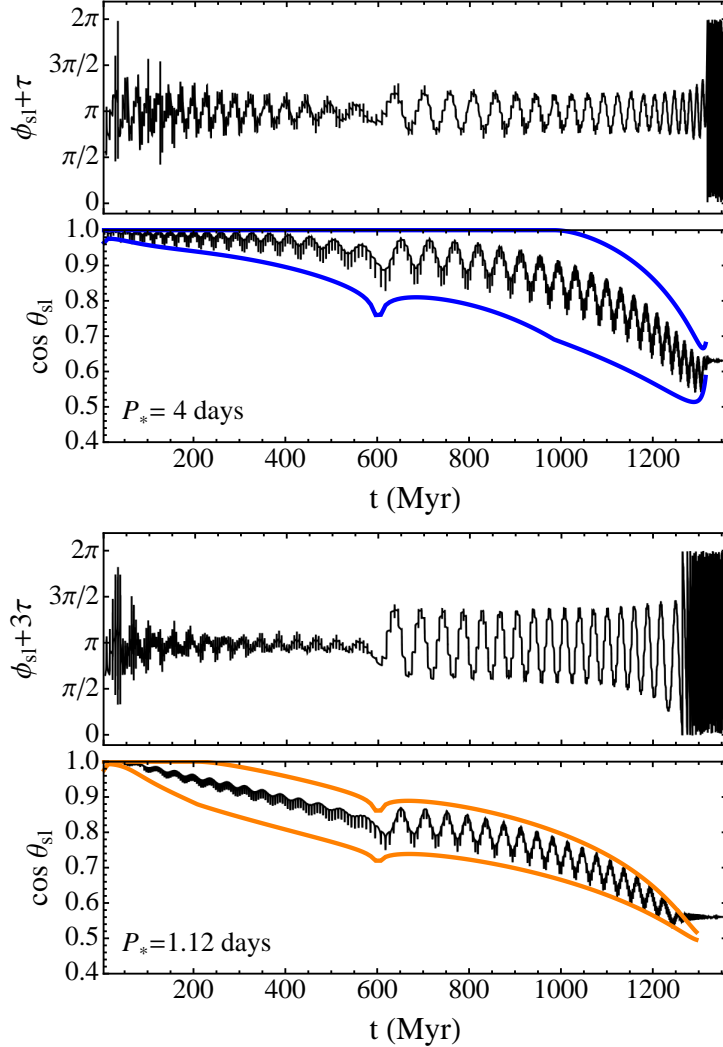


Figure 4.10: Demonstration of the process of adiabatic advection by an $N = -1$ (top) and an $N = -3$ (bottom) resonance. The top (bottom) time evolution is marked in Fig. 4.6 with a blue (orange) square symbol. Just like in Fig. 4.9 the two sample trajectories remain trapped in their respective resonances (top: $N = -1$, shown in blue; bottom: $N = -3$, shown in orange) and are advected with them.

inside the resonance.

As another means of looking at the situation, we note that at the center of a resonance of order N we have, by definition, $\phi_{\text{sl}} - N\tau = 0$. Thus, a trajectory trapped inside a resonance circulates about this point; that is, $\phi_{\text{sl}} - N\tau$ of such a

trajectory should exhibit moderate variation about 0. In the bottom panel of Fig. 4.9, we show that this is indeed the case: $\phi_{\text{sl}} + 2\tau$ oscillates about 0, indicating that the trajectory is trapped inside the $N = -2$ resonance. Likewise, the oscillations of $\cos \theta_{\text{sl}}$ never exceed the maximum width of the $N = -2$ resonance, thus also demonstrating that the trajectory is always contained inside.

Similarly, Figure 4.10 shows sample advections by $N = -1$ (top) and $N = -3$ (bottom) resonances. By locating these examples on the $\theta_{\text{sl},f}$ vs P_* plot (Fig. 4.6), we can conclude that each of the diagonally striated lines in Fig. 4.6, located at $0.5 \lesssim N_{\max,0} \lesssim 1$, $1 \lesssim N_{\max,0} \lesssim 2$, etc., corresponds to advection by a resonance of a different N .

4.7 Predictive Power

In the previous two sections, we have focused solely on experiments that changed the spin dynamics in the simplest way possible: by changing the stellar spin period, while keeping all other system parameters fixed. We would now like to check whether the understanding of the different outcomes for $\theta_{\text{sl},f}$ we developed in the previous section holds up when we change something other than the stellar spin period. Thus, in Figure 4.11 we present the distributions of final spin-orbit misalignment angles as a function of the initial orbital inclination $\theta_{\text{lb},0}$, for two values of the stellar spin period and two planet masses.

We find that, indeed, our classification of outcomes holds up well. For Jupiter-mass planets, the outcomes are either bimodal or stationary adiabatic, with the transition between the two regimes falling on $\bar{\mathcal{A}}_0 \simeq 1$, as expected. For the heavier, $5M_J$ planets, a chaotic band appears at lower misalignments - some-

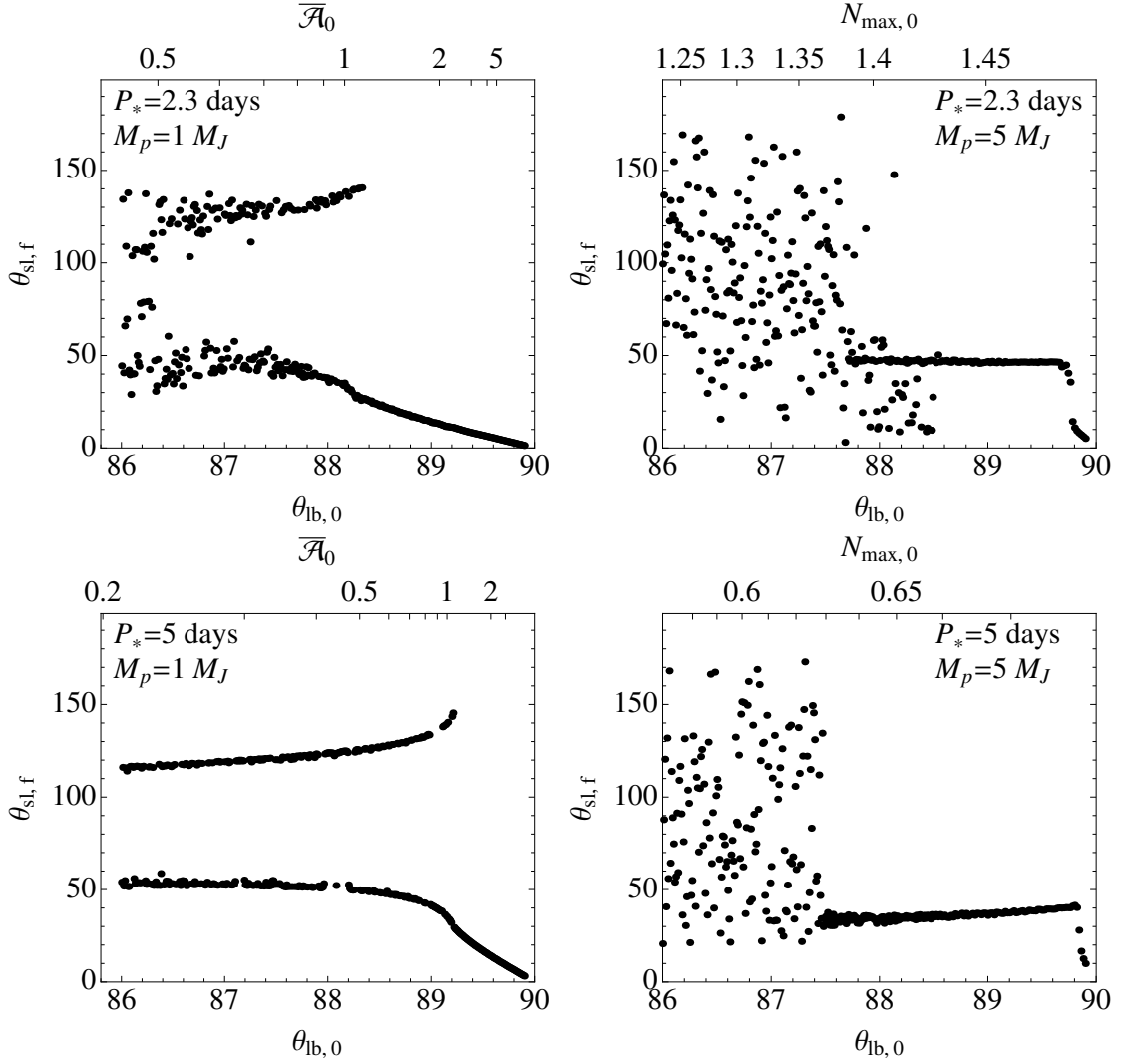


Figure 4.11: Final spin-orbit misalignment angle as a function of initial inclination $\theta_{lb,0}$, for two different planet masses and two stellar spin periods. The $M_p = 1 M_J$ panels (left) exhibit non-adiabatic (bimodal) and stationary adiabatic behavior, with the transition from one to the other happening, as expected, at $\bar{\mathcal{A}}_0 \simeq 1$. The $M_p = 5 M_J$ panels (right) exhibit chaos and adiabatic advection by the $N = -2$ (top) and $N = -1$ (bottom) resonances. Because $N_{max,0}$ is very weakly sensitive to the initial inclination (cf. Fig. 4.2), the final angle after advection is nearly independent of $\theta_{lb,0}$.

thing we have not yet addressed. Aside from that, however, in the non-chaotic regions we find that $\theta_{\text{sl},f}$ is nearly constant, consistent with the fact that $N_{\max,0}$ is moderately large and nearly independent of $\theta_{\text{lb},0}$ (as expected based on Fig. 4.2). We conclude that the top right panel of Fig. 4.11 shows an extended region of adiabatic advection by the $N = -2$ resonance, whereas the bottom right panel of Fig. 4.11 shows a region of advection by the $N = -1$ resonance.

The appearance of the chaotic band is not something we had previously discussed or directly foreseen. We surmise, however, that the chaotic band appears whenever, at $t = 0$, the resonance governing the $\cos \theta_{\text{sl},0} = 1$ trajectory (e.g. $N = -2$, as is the case in Fig. 4.11, top right) overlaps with its neighboring resonance (e.g. $N = -1$). Based on Fig. 4.5 we know that this is *not* the case for $\theta_{\text{lb},0} = 89^\circ$, and thus it is not surprising that the chaotic region does not extend all the way to $\theta_{\text{lb},0} = 89^\circ$. Although we do not plot it, we have checked that, in fact, for $\theta_{\text{lb},0} = 87^\circ$ the governing separatrices in both the top and bottom panels of Fig. 4.11 do indeed overlap with their neighbors, which explains the randomly distributed final outcomes.

In general, we expect the appearance of chaos to be correlated with the widths of the resonances. Since the widths of the resonances generally decrease with increasing $\bar{\mathcal{A}}_0$ (see SL15), we expect chaotic bands to be confined to lower values of $\bar{\mathcal{A}}_0$ (but high enough that multiple resonances exist).

Finally, taking one step further, we consider a more general suite of time evolutions with various initial conditions, such as different planet masses, stellar spin periods, binary separations, and initial inclinations. We categorize each time evolution according to its outcome: bimodal (non-adiabatic), stationary adiabatic, adiabatically advected, or chaotic, and plot these outcomes in $N_{\max,0}$

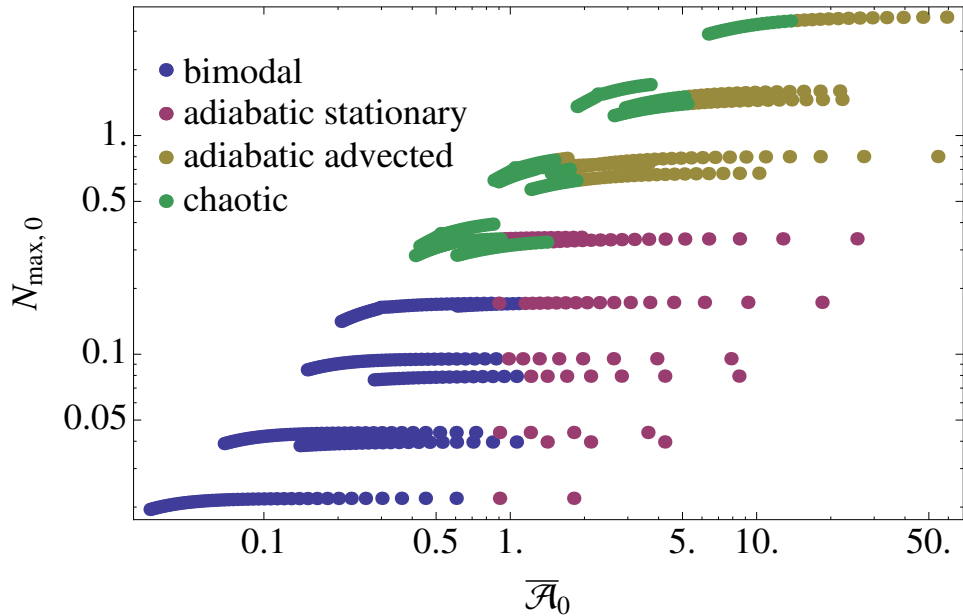


Figure 4.12: Compilation of the outcomes of a suite of time evolutions with variable initial conditions, plotted in $N_{\max,0}$ vs \bar{A}_0 space. Each outcome is classified into the categories discussed in section 4.6, plus an extra “chaotic” category. The variable initial conditions include combinations of various planet masses, stellar spin periods, binary separations, and initial inclinations. Despite varying all of these initial parameters, we see that the outcomes still obey the guidelines set out in Section 4.6: non-adiabatic (bimodal) and adiabatic stationary behaviors happen at low $N_{\max,0}$, and are separated by $\bar{A}_0 \simeq 1$. At higher $N_{\max,0}$, advection and chaotic behavior become possible, with chaotic behavior being restricted to lower values of \bar{A}_0 (for which, generally speaking, all the resonances are wider and more likely to overlap).

vs \bar{A}_0 space (Fig. 4.12). From this figure, it is clear that our understanding of the different outcomes is sound: at $\bar{A}_0 \lesssim 1$, bimodality dominates; at $\bar{A}_0 \gtrsim 1$ but $N_{\max,0} \lesssim 0.5$ stationary adiabatic behavior is prevalent; for $\bar{A}_0 \gtrsim 1$ and $N_{\max,0} \gtrsim 0.5$, adiabatic advection is dominant, except where the evolution is chaotic, with the chaotic evolution restricted to lower values of \bar{A}_0 .

Thus, we conclude that knowledge of the two parameters \bar{A}_0 and $N_{\max,0}$ is, in many cases, sufficient in order to predict whether the final spin-orbit misalignment angle of a given system can be high. For $\bar{A}_0 \lesssim 1$, the final misalignment

distribution is bimodal, and thus a system is equally as likely to have low misalignment as high misalignment. For $\bar{A}_0 \gtrsim 1$ but $N_{\max,0} \lesssim 0.5$ the system is incapable of achieving a significantly misaligned state. For $\bar{A}_0 \gtrsim 1$ and $N_{\max,0} \gtrsim 0.5$ a calculation of resonance widths must be carried out to determine whether the system is chaotic or advecting, but in general it can be expected that if \bar{A}_0 is relatively high then the system is not chaotic, and will attain non-zero, but strictly prograde and fairly modest, misalignment.

4.8 Discussion and Conclusion

4.8.1 Complications due to feedback

As explained in Section 4.4, a major simplifying assumption in the analysis laid out in this paper, as well as in SL15, is the omission of the extra precession the planet’s orbit experiences due to perturbation from the stellar quadrupole. This omission enables us to considerably simplify the spin dynamics problem by reducing it to a 1D Hamiltonian system. It is important, however, to understand under what conditions this assumption is valid.

Feedback in the system becomes important if the star has nearly as much, or more, angular momentum as the planet’s orbit. Thus, it is questionable whether our analysis is truly applicable to Jupiter-mass (as opposed to heavier) planets and rapidly rotating stars. However, in a recent work (Anderson et al., 2015), in prep, we have run a comprehensive suite of numerical simulations *including* feedback and all other important effects, including octupole-order Lidov-Kozai. We found that, while under certain conditions the bimodal and stationary adia-

batic behaviors expected to dominate for Jupiter-mass planets can be disrupted, on the whole, bimodality remains nearly ubiquitous. Thus, we conclude that, even with the omission of feedback, we have still been able to classify the dominant modes and outcomes of stellar spin dynamics in LK systems.

4.8.2 Primordial misalignment

In this paper we have focused solely on stellar spin dynamics in systems that have no initial spin-orbit misalignment. However, since several ways of generating primordial misalignment have been proposed (Bate et al., 2010; Batygin, 2012; Batygin and Adams, 2013; Lai, 2014; Lai et al., 2011; Spalding and Batygin, 2014), the dynamics of initially misaligned systems are of potential interest. A thorough exploration of these dynamics may merit a future paper.

We can state, however, that we believe the ideas outlined in this work, and particularly the importance of the parameters \bar{A}_0 and $N_{\max,0}$, are still applicable to initially misaligned systems. The fate of the system should still be determined by the initial $t = 0$ phase space of the system and where in that phase space the system is initialized. For example, for trajectories starting anywhere inside the $N = 0$ center island (cf. Fig. 4.4 top panel), the final outcome should be bimodal just like it is for initially aligned systems - however, the peaks of the bimodal distribution would lie closer to 90° due to the smaller initial area of the trajectory. In Anderson et al. (2015), in prep, we demonstrate that this is the case.

Thus, the guidelines developed here for the special case of initially aligned systems can likely be easily generalized to systems with arbitrary initial mis-

alignments and phases.

4.8.3 Summary of key findings

The goal of this work has been to explore in detail, and classify, the various regimes of stellar spin dynamics driven by planets undergoing Lidov-Kozai migration. Whereas in previous work (SL15) we analyzed solely the idealized non-dissipative LK system, and only in the adiabatic regime, here we generalize our analysis to include the effects of short-range forces and tidal dissipation, and consider all possible dynamical regimes. The only simplifying assumption we make is the omission of feedback due to the stellar quadrupole onto the planet’s orbital dynamics. We also consider solely cases with zero initial spin-orbit misalignment

We find that, in general, the behavior of a system with a given set of initial conditions, planet mass, and stellar spin rate is governed primarily by two parameters: N_{\max} , which compares the average precession frequency of the stellar spin vector $\hat{\mathbf{S}}$ with the LK eccentricity oscillation timescale; and $\bar{\mathcal{A}}$, which compares the average precession frequency of the stellar spin vector $\hat{\mathbf{S}}$ with the rate of change of the orbital angular momentum vector $\hat{\mathbf{L}}$.

In the presence of tides, N_{\max} and $\bar{\mathcal{A}}$ vary slowly with time, but the fate of the system is entirely determined by the values of these parameters at $t = 0$ (i.e. during the first LK cycle). We find that when $\bar{\mathcal{A}}_0 \lesssim 1$ and $N_{\max,0} \ll 1$, the final spin-orbit misalignment distribution is bimodal, and thus the system is equally as likely to attain low final misalignment as high misalignment. When $\bar{\mathcal{A}}_0 \gtrsim 1$ and $N_{\max,0} \lesssim 0.5$, the system experiences “stationary adiabatic” behavior and

cannot achieve high misalignments. When $\bar{A}_0 \gtrsim 1$ and $N_{\max,0} \gtrsim 0.5$, the system is either chaotic or experiences “adiabatic advection”, wherein it can slowly accumulate a modest amount of spin-orbit misalignment (never more than 90°). The chaotic regime is typically restricted to lower values of \bar{A}_0 .

CHAPTER 5

**VISCOELASTIC TIDAL DISSIPATION IN GIANT PLANETS AND
FORMATION OF HOT JUPITERS THROUGH HIGH-ECCENTRICITY
MIGRATION**

5.1 Abstract

We study the possibility of tidal dissipation in the solid cores of giant planets and its implication for the formation of hot Jupiters through high-eccentricity migration. We present a general framework by which the tidal evolution of planetary systems can be computed for any form of tidal dissipation, characterized by the imaginary part of the complex tidal Love number, $\text{Im}[\tilde{k}_2(\omega)]$, as a function of the forcing frequency ω . Using the simplest viscoelastic dissipation model (the Maxwell model) for the rocky core and including the effect of a nondissipative fluid envelope, we show that with reasonable (but uncertain) physical parameters for the core (size, viscosity and shear modulus), tidal dissipation in the core can accommodate the tidal-Q constraint of the Solar System gas giants and at the same time allows exoplanetary hot Jupiters to form via tidal circularization in the high-e migration scenario. By contrast, the often-used weak friction theory of equilibrium tide would lead to a discrepancy between the Solar System constraint and the amount of dissipation necessary for high-e migration. We also show that tidal heating in the rocky core can lead to modest radius inflation of the planets, particularly when the planets are in the high-eccentricity phase ($e \sim 0.6$) during their high-e migration. Finally, as an in-

The contents of this chapter were published in *MNRAS* as "Viscoelastic Tidal Dissipation in Giant Planets and Formation of Hot Jupiters Through High-Eccentricity Migration" (Storch and Lai, 2014)

teresting by-product of our study, we note that for a generic tidal response function $\text{Im}[\tilde{k}_2(\omega)]$, it is possible that spin equilibrium (zero torque) can be achieved for multiple spin frequencies (at a given e), and the actual pseudosynchronized spin rate depends on the evolutionary history of the system.

5.2 Introduction

In recent years high-eccentricity migration has emerged as one of the dominant mechanisms responsible for the formation of hot Jupiters. In this mechanism, a gas giant which is formed beyond the snow line is first excited into a state of very high eccentricity ($e \gtrsim 0.9$) by few-body interactions, either via dynamical planet-planet scatterings (Chatterjee et al., 2008; Jurić and Tremaine, 2008; Rasio and Ford, 1996; Weidenschilling and Marzari, 1996; Zhou et al., 2007) or/and secular interactions between multiple planets, or Lidov-Kozai effect induced by a distant companion (Dawson and Murray-Clay, 2013; Fabrycky and Tremaine, 2007; Katz et al., 2011; Nagasawa et al., 2008; Naoz et al., 2011, 2012, 2013; Wu and Lithwick, 2011; Wu and Murray, 2003; Wu et al., 2007). Due to the high eccentricity, the planet passes quite close to its host star at periastron, and tidal dissipation in the planet extracts energy from the orbit, leading to inward migration and circularization of the planet's orbit.

Tidal effects on the orbital evolution of binaries are often discussed using the weak friction theory of equilibrium tides (Alexander, 1973; Eggleton et al., 1998; Hut, 1981), according to which the rate of decay of the semi-major axis (a) for a pseudosynchronized planet can be written as

$$\left| \frac{\dot{a}}{a} \right| = 6k_2\tau \left(\frac{GM_\star}{a_F^3} \right) \left(\frac{R_p}{a_F} \right)^5 \frac{M_\star}{M_p} \sqrt{\frac{a_F}{a}} F(e). \quad (5.1)$$

Here M_p and R_p are the mass and radius of the planet, M_* is the mass of the central star, $a_F \equiv a(1 - e^2)$ is the final circularization radius (assuming orbital angular momentum conservation), k_2 the tidal Love number, τ is the tidal lag time (assumed constant in the weak friction theory), and $F(e)$ is a function of eccentricity of order $(1 - 10)$ and given by $F(e) = f_1(e) - f_2^2(e)/f_5(e)$, where f_1 , f_2 and f_5 are given by Eq. (11) of Hut (1981). By requiring that the high-e migration happens on a timescale less than 10 Gyrs we can place a constraint on τ :

$$\left(\frac{GM_*}{a_F^3}\right)^{1/2} \tau \gtrsim 3 \times 10^{-5} \left(\frac{a}{5\text{AU}}\right)^{1/2} \left(\frac{a_F}{0.06\text{AU}}\right)^6 \times \left(\frac{M_*}{M_\odot}\right)^{-3/2} \frac{M_p}{M_J} \left(\frac{R_p}{R_J}\right)^{-5} \left(\frac{k_2}{0.38}\right)^{-1}. \quad (5.2)$$

Note that instead of τ , tidal dissipation is often parameterized by the tidal quality factor $Q \equiv (\tau\omega)^{-1}$, where ω is the tidal forcing frequency. Thus, the above constraint on τ translates to $Q \lesssim 3 \times 10^4$ at $\omega \sim (GM_*/a_F^3)^{1/2} \sim 2\pi/(5\text{ d})$ [for the canonical parameters adopted in Eq. (5.2)]. A similar constraint can be obtained by integration over the planets' orbital evolution (Fabrycky and Tremaine, 2007; Hansen, 2012; Leconte et al., 2010; Matsumura et al., 2010; Naoz et al., 2012; Socrates et al., 2012a).

The tidal Q for Solar System giant planets can be measured or constrained by the tidal evolution of their satellites (Goldreich and Soter, 1966). For Jupiter, Yoder and Peale (1981) derived a bound $2 \times 10^{-7} < k_2/Q_J < 6 \times 10^{-6}$ based on Io's long-term orbital evolution (particularly the eccentricity equilibrium), with the upper limit following from the limited expansion of satellite orbits. Recent analysis of the astrometric data of Galilean moons gave $k_2/Q_J = (1.1 \pm 0.2) \times 10^{-5}$ for the current Jupiter-Io system (Lainey et al., 2009), corresponding to $Q_J \simeq 3.5 \times 10^4$ for the conventional value of the Love number $k_2 = 0.38$ (Gavrilov

and Zharkov, 1977). With Jupiter's spin period 9.9 hrs and Io's orbital period 42.5 hrs, the tidal forcing frequency on Jupiter from Io is $\omega = 2\pi/(6.5 \text{ hr})$, and the tidal lag time is then $\tau_J = (Q_J \omega)^{-1} \simeq 0.1 \text{ s}$.

For Saturn, theoretical considerations based on the long-term evolution of Mimas and other main moons (with the assumption that they formed above the synchronous orbit 4.5 Gyr ago) lead to the constraint $3 \times 10^{-6} < k_2/Q_S < 2 \times 10^{-5}$ (Peale, 1999; Sinclair, 1983). However, using astrometric data spanning more than a century, Lainey et al. (2012) found a much larger $k_2/Q_S = (2.3 \pm 0.7) \times 10^{-4}$, corresponding to $Q_S = (1 - 2) \times 10^3$ for $k_2 = 0.34$; they also found that Q_S depends weakly on the tidal period in the range between $2\pi/\omega = 5.8 \text{ hrs}$ (Rhea) and 7.8 hrs (Enceladus).

Assuming that extra-solar giant planets are close analogs of our own gas giants, we can ask whether the aforementioned empirical constraints on k_2/Q for Jupiter and Saturn are compatible with the extra-solar constraint [see Eq. 5.2]. The difference between the two sets of constraints is the tidal forcing frequencies: For example, the Jupiter-Io constraint involves a single frequency ($P = 6.5 \text{ hrs}$), while high-e migration involves tidal potentials of many harmonics, all of them with periods longer than a few days. Socrates et al. (2012a) showed that the two sets of constraints are incompatible with the weak friction theory [see also Naoz et al. (2012)]: In order for hot Jupiters to undergo high-e migration within the age of their host stars, their required tidal lag times must be more than an order of magnitude larger than the Jupiter-Io constraint.

Tidal dissipation in giant planets is complex, and depends strongly on the internal structure of the planet, such as the stratification of the liquid envelope and the presence and properties of a solid core. There have been some

attempts to understand the physics of tidal Q in giant planets [see Ogilvie and Lin (2004) for a review]. It has long been known (Goldreich and Nicholson, 1977) that simple turbulent viscosity in the fluid envelopes of giant planets is many orders of magnitude lower than required by observations. Ioannou and Lindzen (1993*a,b*) considered a prescribed model of Jupiter where the envelope is not fully convective (contrary to the conventional model where the envelope is neutrally buoyant to a high degree; see Guillot (2005)) and showed that the excitation and radiative damping of gravity waves in the envelope provide efficient tidal dissipation only at specific “resonant” frequencies. Lubow et al. (1997) examined similar gravity wave excitations in the radiative layer above the convective envelope of hot Jupiters. So far the most sophisticated study of dynamical tides in giant planets is that by Ogilvie and Lin (2004) [see also Goodman and Lackner (2009); Ogilvie (2009, 2013)], who focused on the tidal forcing of inertial waves (short-wavelength disturbances restored primarily by Coriolis force) in the convective envelope of a rotating planet [see Ivanov and Papaloizou (2007); Papaloizou and Ivanov (2010) for highly eccentric orbits, and Wu (2005) for a different approach]. They showed that because of the rocky core, the excited inertial waves are concentrated on a web of “rays”, leading to tidal dissipation which depends on the forcing frequency in a highly erratic way. The tidal Q obtained is typically of order 10^{6-7} . It remains unclear whether this mechanism can provide sufficient tidal dissipation compared to the observational constraints.

The possibility of core dissipation in giant planets was first considered by Dermott (1979) but has not received much attention since. Recently, Remus et al. (2012*b*) showed that dissipation in the solid core could in principle satisfy the constraints on tidal Q obtained by Lainey et al. (2009) for Jupiter and by Lainey

et al. (2012) for Saturn.

In this paper, we continue the study of tidal dissipation in the solid core of giant planets and examine its consequences for the high-e migration scenario and for the thermal evolution of hot Jupiters. In section 5.3 we present the general tidal theory which may be used with any tidal response model. In section 5.4 we discuss a simple viscoelastic tidal response model and its range of applicability. In section 5.5 we use the general theory of section 5.3 in conjunction with the model of section 5.4 to compute high-e migration timescales and compare with the weak friction theory. We also examine the effect of tidal heating in the core for the radius evolution of the planets. We summarize our findings and conclude in section 5.6.

5.3 Evolution of Eccentric Systems with General Tidal Responses

Here we formulate the tidal evolution equations for eccentric binary systems. These equations can be applied to any tidal response model, where the complex Love number (defined below) is an arbitrary function of the tidal forcing frequency [see also Efroimsky and Makarov (2013); Mathis and Le Poncin-Lafitte (2009); Remus et al. (2012b) for similar formalisms]. This formulation is valid as long as the responses of the body to different tidal components are independent of each other.

We consider a planet of mass M_p , radius R_p and rotation rate Ω_s (assumed to be aligned with the orbital angular momentum axis), moving around a star

(mass M_\star) in an eccentric orbit with semi-major axis a and mean motion frequency Ω . The tidal potential exerted on the planet by the star is given by

$$U(\mathbf{r}, t) = -GM_\star \sum_m \frac{W_{2m}r^2}{D(t)^3} e^{-im\Phi(t)} Y_{2m}(\theta, \phi), \quad (5.3)$$

where (r, θ, ϕ) is the position vector (in spherical coordinates) relative to the center of mass of the planet, $D(t)$ and $\Phi(t)$ are the time-dependent separation and phase of the orbit, and $m = 0, \pm 2$, with $W_{20} = -(\pi/5)^{1/2}$ and $W_{2\pm 2} = (3\pi/10)^{1/2}$. The potential $U(\mathbf{r}, t)$ can be decomposed into an infinite series of circular harmonics:

$$U(\mathbf{r}, t) = - \sum_{m,N} U_{mN} r^2 Y_{2m}(\theta, \phi) e^{-iN\Omega t}, \quad (5.4)$$

where $N \in (-\infty, \infty)$ and

$$U_{mN} \equiv \frac{GM_\star}{a^3} W_{2m} F_{mN}(e), \quad (5.5)$$

with $F_{mN}(e)$ being the Hansen coefficient (e.g., called X_{2m}^N in Murray and Dermott (2000)), given by

$$F_{mN}(e) = \frac{1}{\pi} \int_0^\pi \frac{\cos [N(\Psi - e \sin \Psi) - m\Phi(t)]}{(1 - e \cos \Psi)^2} d\Psi, \quad (5.6)$$

with

$$\cos \Phi(t) = \frac{\cos \Psi - e}{1 - e \cos \Psi}. \quad (5.7)$$

Each harmonic of the tidal potential produces a perturbative response in the planet, expressible in terms of the Lagrangian displacement ξ_{mN} and the Eulerian density perturbation $\delta\rho_{mN}$. These responses are proportional to the dimensionless ratio, $U_{mN}/\omega_0^2 = (M_\star/M_p)(R_p/a)^3 W_{2m} F_{mN}$, where $\omega_0 \equiv (GM_p/R_p^3)^{1/2}$ is the dynamical frequency of the planet. Without loss of generality, we can write

the tidal responses as (Lai, 2012)

$$\xi_{mN}(\mathbf{r}, t) = \frac{U_{mN}}{\omega_0^2} \bar{\xi}_{mN}(r, \theta) e^{im\phi - iN\Omega t}, \quad (5.8)$$

$$\delta\rho_{mN}(\mathbf{r}, t) = \frac{U_{mN}}{\omega_0^2} \delta\bar{\rho}_{mN}(r, \theta) e^{im\phi - iN\Omega t}, \quad (5.9)$$

with

$$\delta\rho_{mN} = -\nabla \cdot (\rho \xi_{mN}). \quad (5.10)$$

Note that $\delta\bar{\rho}_{mN}$ and $\bar{\xi}_{mN}$ are in general complex functions (implying that the tidal response is phased-shifted relative to the tidal potential), and they depend on the forcing frequency ω_{mN} of each harmonic in the rotating frame of the primary,

$$\omega_{mN} \equiv N\Omega - m\Omega_s. \quad (5.11)$$

Given the Eulerian density perturbation, we can obtain the perturbation to the gravitational potential of the planet, $\delta\Phi_{mN}$, by solving the Poisson equation, $\nabla^2\delta\Phi_{mN} = 4\pi G\delta\rho_{mN}$. We define the dimensionless Love number \tilde{k}_2^{mN} as the ratio of $\delta\Phi_{mN}$ and the (mN) -component of the tidal potential $[U(\mathbf{r}, t)]_{mN} = -r^2 U_{mN} Y_{2m}(\theta, \phi) \exp(-iN\Omega t)$, evaluated at the planet's surface:

$$\tilde{k}_2^{mN} \equiv \left. \frac{\delta\Phi_{mN}}{[U(\mathbf{r}, t)]_{mN}} \right|_{r=R_p}. \quad (5.12)$$

Note that, just as $\delta\rho_{mN}$ is complex, so in general is \tilde{k}_2^{mN} . We find that

$$\tilde{k}_2^{mN} = \frac{4\pi}{5} \frac{1}{M_p R_p^2} \int \delta\bar{\rho}_{mN}(r, \theta) e^{im\phi} r^2 Y_{2m}^* d^3x. \quad (5.13)$$

We now have all the information necessary to calculate the time-averaged torque and energy transfer rate (from the orbit to the planet):

$$\mathbf{T} = \text{Re} \left\langle \int d^3x \delta\rho(\mathbf{r}, t) \mathbf{r} \times [-\nabla U^*(\mathbf{r}, t)] \right\rangle, \quad (5.14)$$

$$\dot{E} = \text{Re} \left\langle \int d^3x \rho(\mathbf{r}) \frac{\partial \xi(\mathbf{r}, t)}{\partial t} \cdot [-\nabla U^*(\mathbf{r}, t)] \right\rangle, \quad (5.15)$$

where $\langle \rangle$ denotes time averaging. After plugging in the ansatz for ξ and $\delta\rho$ [Eqs. (5.8)-(5.9)] and the expression for \tilde{k}_2^{mN} [Eq. (5.13)], we find

$$T_z = \frac{5}{4\pi} T_0 \sum_{m,N} m [W_{2m} F_{mN}(e)]^2 \text{Im}(\tilde{k}_2^{mN}), \quad (5.16)$$

$$\dot{E} = \frac{5}{4\pi} T_0 \Omega \sum_{m,N} N [W_{2m} F_{mN}(e)]^2 \text{Im}(\tilde{k}_2^{mN}), \quad (5.17)$$

where $T_0 \equiv G(M_\star/a^3)^2 R_p^5$. The tidal evolution equations for the planet's spin Ω_s , the orbital semi-major axis a and the eccentricity e are

$$\dot{\Omega}_s = \frac{T_z}{I}, \quad (5.18)$$

$$\frac{\dot{a}}{a} = -\frac{2a\dot{E}}{GM_\star M_p}, \quad (5.19)$$

$$\frac{e\dot{e}}{1-e^2} = -\frac{a\dot{E}}{GM_\star M_p} + \frac{T_z}{L}, \quad (5.20)$$

where I is the moment of inertia of the planet and $L = M_\star M_p [Ga(1-e^2)/(M_\star + M_p)]^{1/2}$ is the orbital angular momentum.

As noted before, \tilde{k}_2^{mN} depends on the forcing frequency $\omega_{mN} = N\Omega - m\Omega_s$ and physical properties of the planet. We can write $\tilde{k}_2^{mN} = \tilde{k}_2(\omega_{mN})$. In general, given a model for $\tilde{k}_2(\omega)$, the sum over (mN) must be computed numerically. Note that $\text{Im}(\tilde{k}_2^{mN})$ is related to the often-defined tidal quality factor Q by

$$\text{Im}(\tilde{k}_2^{mN}) \equiv \left(\frac{k_2}{Q} \right)_{mN}, \quad (5.21)$$

with k_2 the usual (real) Love number, except that in our general case $(k_2/Q)_{mN}$ is for a specific (mN) -tidal component.

In the special case of the weak friction theory of equilibrium tide*, one assumes $\text{Im}[\tilde{k}_2(\omega)] = k_2 \tau \omega$, with k_2 and the lag time τ being independent of the

*Note that for equilibrium tides in general, the tidal response $\text{Im}[\tilde{k}_2(\omega)]$ does not have to be a linear function of ω (i.e., constant lag time). For example, Remus et al. (2012a) showed that for convective stars/planets, $\text{Im}[\tilde{k}_2(\omega)]$ is independent of ω (i.e., constant lag angle) when ω exceeds the convective turnover rate.

frequency ω . In this case, the sum over (mN) can be carried out analytically, giving the usual expressions (Alexander, 1973; Hut, 1981):

$$T_z = \frac{3 T_0 \Omega k_2 \tau}{(1 - e^2)^6} \left[f_2 - (1 - e^2)^{3/2} f_5 \frac{\Omega_s}{\Omega} \right], \quad (5.22)$$

$$\dot{E} = \frac{3 T_0 \Omega^2 k_2 \tau}{(1 - e^2)^{15/2}} \left[f_1 - (1 - e^2)^{3/2} f_2 \frac{\Omega_s}{\Omega} \right], \quad (5.23)$$

where f_1 , f_2 , and f_5 are functions of eccentricity given by (Hut 1981)

$$f_1(e) = 1 + \frac{31}{2}e^2 + \frac{255}{8}e^4 + \frac{185}{16}e^6 + \frac{25}{64}e^8, \quad (5.24)$$

$$f_2(e) = 1 + \frac{15}{2}e^2 + \frac{45}{8}e^4 + \frac{5}{16}e^6, \text{ and} \quad (5.25)$$

$$f_5(e) = 1 + 3e^2 + \frac{3}{8}e^4. \quad (5.26)$$

5.4 Viscoelastic Dissipation in Giant Planets with Rocky Cores

We now discuss a theoretical model of $k_2(\omega)$ for giant planets based on viscoelastic dissipation in rocky cores. We consider first a homogeneous solid core, and subsequently introduce a homogeneous non-dissipative liquid envelope.

5.4.1 Viscoelastic Solid Core

The rocky/icy core of a giant planet can possess the characteristics of both elastic solid and viscous fluid, depending on the frequency of the imposed periodic shear stress or strain. Dissipation in rocks arises from thermally activated creep processes associated with the diffusion of atoms or the motion of dislocations when the rocks are subjected to stress. We use the simplest phenomenological model, the Maxwell model, to describe such viscoelastic materials (Turcotte and

Schubert, 2002). The model contain two free parameters, the shear modulus (rigidity) μ and viscosity η . Other rheologies are possible (Henning et al., 2009), but contain more free parameters and are not warranted at present given the large uncertainties associated with the solid cores of giant planets.

The incompressible constitutive relation of a Maxwell solid core takes the form

$$\dot{\varepsilon}_{ij} = \frac{1}{2\mu}\dot{\sigma}_{ij} + \frac{1}{2\eta}\sigma_{ij}, \quad (5.27)$$

where ε_{ij} and σ_{ij} are strain and stress tensors, respectively, and a dot denotes time derivative. For periodic forcing $\varepsilon_{ij}, \sigma_{ij} \propto e^{-i\omega t}$, the complex shear modulus, $\tilde{\mu} \equiv \sigma_{ij}/(2\varepsilon_{ij})$, is given by

$$\tilde{\mu} = \frac{\omega\mu\eta}{\omega\eta + i\mu} = \frac{\mu}{1 + i(\omega_M/\omega)}, \quad (5.28)$$

where the Maxwell frequency is

$$\omega_M \equiv \mu/\eta. \quad (5.29)$$

Clearly, the core behaves as an elastic solid (with $\tilde{\mu} \simeq \mu$) for $\omega \gg \omega_M$, and as a viscous fluid (with $\tilde{\mu} \simeq -i\omega\eta$) for $\omega \ll \omega_M$.

Consider a homogeneous rocky core (mass M_c , radius R_c and density ρ_c) with a constant $\tilde{\mu}$. When the tidal forcing frequency ω is much less than the dynamical frequency of the body, i.e., when $\omega \ll (GM_c/R_c^3)^{1/2}$ and $\omega \ll (\mu/\rho_c R_c^2)^{1/2}$, the tidal Love number in the purely elastic case ($\text{Im}[\tilde{\mu}] = 0$) can be obtained analytically (Love, 1927). Following Remus et al. (2012b) we invoke the correspondence principle (Biot, 1954), which allows us to simply replace the real shear modulus in the elastic solution by the full complex shear modulus in order to obtain the viscoelastic solution, yielding

$$\tilde{k}_{2c} = \frac{3}{2} \frac{1}{1 + \bar{\mu}}, \quad (5.30)$$

where $\bar{\mu}$ is the body's (dimensionless) effective rigidity

$$\bar{\mu} \equiv \bar{\mu}_1 + i\bar{\mu}_2 \equiv \frac{19\hat{\mu}}{2\beta}, \quad (5.31)$$

with $\beta \equiv \rho_c g_c R_c$ and $g_c = GM_c/R_c^2$. Thus we have

$$\text{Im}(\tilde{k}_{2c}) = \frac{57\omega\eta}{4\beta} \left[1 + \left(\frac{\omega\eta}{\mu} \right)^2 \left(1 + \frac{19\mu}{2\beta} \right)^2 \right]^{-1}. \quad (5.32)$$

Note that $\text{Im}(\tilde{k}_{2c})$ is a non-monotonic function of ω (see Fig. 5.1, top panel). For $\omega \ll \omega_M$, we have $\text{Im}(\tilde{k}_{2c}) \simeq 57\omega\eta/(4\beta)$; for $\omega \gg \omega_M$, we have $\text{Im}(\tilde{k}_{2c}) \propto \omega^{-1}$.

For a given core model, the maximum

$$\text{Im}(\tilde{k}_{2c})_{\max} = \frac{3\hat{\mu}}{4(1 + \hat{\mu})} \quad (5.33)$$

is attained at $\omega = \omega_M/(1 + \hat{\mu})$, where $\hat{\mu} \equiv 19\mu/(2\beta)$.

5.4.2 Application to a giant planet with a rocky core

In order to apply the results of section 5.4.1 to a gas giant, we introduce a non-dissipative fluid envelope on top of the rocky body. While the fluid envelope does not, itself, dissipate energy, it is deformed by the tidal potential and interacts with the central solid body by exerting variable pressure on its surface, thus creating additional stress. We consider a core of radius R_c and density ρ_c within a planet of radius R_p , with a fluid envelope of density ρ_F . We then use the analytical expression of Remus et al. (2012b), who used Dermott's 1979 solution for the effect of a liquid envelope on the deformation of an elastic core, together with the correspondence principle (Biot, 1954), to calculate the resulting modified Love number of the core, defined as the ratio of the potential generated by

the deformed core and the tidal potential, evaluated at the core radius (R_c):

$$\tilde{k}_{2c} = \frac{1}{(B + \bar{\mu}_1)^2 + \bar{\mu}_2^2} \left\{ \left[(B + \bar{\mu}_1) \left(C + \frac{3}{2\alpha} \bar{\mu}_1 \right) + \frac{3}{2\alpha} \bar{\mu}_2^2 \right] - iAD\bar{\mu}_2 \right\}, \quad (5.34)$$

where (Remus et al., 2012b)

$$\begin{aligned} \alpha &= 1 + \frac{5}{2} \frac{\rho_c}{\rho_F} \left(\frac{R_c}{R_p} \right)^3 \left(1 - \frac{\rho_F}{\rho_c} \right), \\ A &= \left(1 - \frac{\rho_F}{\rho_c} \right) \left(1 + \frac{3}{2\alpha} \right), \\ B &= 1 - \frac{\rho_F}{\rho_c} + \frac{3}{2} \frac{\rho_F}{\rho_c} \left(1 - \frac{\rho_F}{\rho_c} \right) - \frac{9}{4\alpha} \left(\frac{R_c}{R_p} \right)^5 \left(1 - \frac{\rho_F}{\rho_c} \right)^2, \\ C &= \frac{3}{2} \left(1 - \frac{\rho_F}{\rho_c} \right) \left(1 - \frac{\rho_F}{\rho_c} + \frac{5}{2\alpha} \right) + \frac{9}{4\alpha} \left(\frac{R_c}{R_p} \right)^5 \left(1 - \frac{\rho_F}{\rho_c} \right)^2, \\ D &= \frac{3}{2} \left(1 - \frac{\rho_F}{\rho_c} \right) \left[1 + \frac{3}{2\alpha} \left(\frac{R_c}{R_p} \right)^5 \right]. \end{aligned}$$

Since in our model, all the dissipation happens in the core, we then have, from section 5.3,

$$\dot{E} = \frac{5}{4\pi} \left(\frac{GM_*^2 R_c^5}{a^6} \right) \Omega \sum_{m,N} N [W_{2m} F_{mN}(e)]^2 \text{Im}[\tilde{k}_{2c}^{mN}], \quad (5.35)$$

where $\tilde{k}_{2c}^{mN} = \tilde{k}_{2c}(N\Omega - m\Omega_s)$. However, rather than keep the explicit dependence on R_c , we prefer to re-cast the equation such that all core parameters appear in \tilde{k}_2 only. We write,

$$\dot{E} = \frac{5}{4\pi} \left(\frac{GM_*^2 R_p^5}{a^6} \right) \Omega \sum_{m,N} N [W_{2m} F_{mN}(e)]^2 \text{Im}[\tilde{k}_2^{mN}], \quad (5.36)$$

where

$$\tilde{k}_2(\omega) \equiv \left(\frac{R_c}{R_p} \right)^5 \tilde{k}_{2c}(\omega). \quad (5.37)$$

This (complex) Love number is now, effectively, the Love number for the entire planet rather than for the core only.

5.4.3 The specific case of Jupiter

The size of the rocky/icy core of Jupiter is uncertain, with estimates in the range of $\sim (0 - 10)M_{\oplus}$ (Guillot, 2005) and $\sim (14 - 18)M_{\oplus}$ (Militzer et al., 2008). The viscous and elastic properties of materials at the high pressure (~ 40 Mbar) found at the center of giant planets are also poorly known. We mention here values of η and μ for several materials to give the reader an idea for the range of parameter space involved. The inner core of the Earth has a measured viscosity of $\eta \sim 10^{8\pm 3}$ bar · s (Jeanloz, 1990) and a shear modulus of $\mu \sim 1500$ kbar, while the central pressure is ~ 3600 kbar (Montagner and Kennett, 1996). In contrast, the Earth's mantle has $\eta \sim 10^{15} - 10^{18}$ bar · s, depending on depth (Mitrovica and Forte, 2004), and shear modulus similar to the core. Icy materials have $\eta \sim 10^6 - 10^9$ bar · s, and $\mu \sim 50$ kbar (Goldsby and Kohlstedt, 2001; Poirier et al., 1981). Evidently, η in particular has a very large dynamical range, and since very little is known about the interior of Jupiter, all of this range is hypothetically accessible. In addition to varying η and μ , we may also vary the size of the core R_c and the core density ρ_c .

Figure 5.1 presents three models for the tidal response $\text{Im}(\tilde{k}_{2c})$ of Jupiter's rocky core (upper panel), and the corresponding effective tidal response of the entire planet $\text{Im}(\tilde{k}_2)$ (lower panel). For each curve, different values of η and R_c were chosen such that the Jupiter-Io tidal dissipation constraint is satisfied (see also Fig. 10 of Remus et al. (2012b)). Also plotted is the weak friction theory, similarly calibrated. For all the theoretical curves of Figure 5.1, we choose to fix μ and ρ_c , due to their smaller dynamical ranges. We note that of the remaining parameters, changing η acts primarily to alter the transition frequency $\omega_M \sim \mu\eta^{-1}$, effectively moving the curve horizontally left-right, while changing R_c

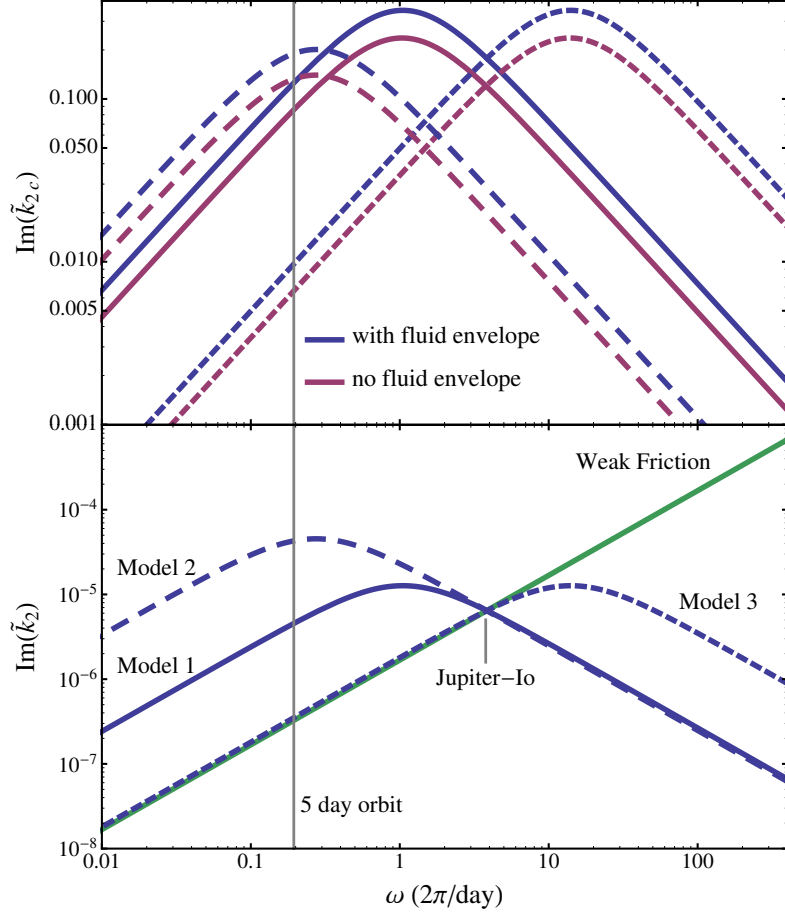


Figure 5.1: Theoretical curves for the tidal Love number of a Jupiter-mass planet as a function of the tidal forcing frequency, for several values of R_c/R_p and η , each calibrated to satisfy the Jupiter-Io constraint. *Top:* The intrinsic Love number of the rocky core with (blue lines) and without (red lines) the presence of liquid envelope. *Bottom:* The effective Love number for the entire planet with fluid envelope. The density ratio of the core and envelope is $\rho_c/\rho_F = 5$ and the core rigidity is $\mu = 485$ kbar for all models. The other model parameters are as follows. *Model 1* (blue solid line): $R_c/R_p = 0.13$, $\eta = 4.4 \times 10^9$ bar · s; *Model 2* (blue long-dashed line): $R_c/R_p = 0.19$, $\eta = 2 \times 10^{10}$ bar · s; *Model 3* (blue short-dashed line): $R_c/R_p = 0.13$, $\eta = 3.3 \times 10^8$ bar · s. *Green solid line:* weak friction theory with $\tau = 0.06$ s (the lag time obtained using the value of k_2/Q from Lainey et al. (2009) and assuming $k_2 = 0.38$).

effectively moves the curve up-down due to the strong dependence of \tilde{k}_2 on R_c/R_p .

From Figure 5.1, it is evident that the use of weak friction theory, which due to having only one parameter needs only one data point to be completely constrained, can lead to strong over- or under- estimation of tidal dissipation at different frequencies, as compared to more realistic models.

5.5 High-eccentricity migration of a giant planet with a rocky core

5.5.1 Orbital Evolution

We now compute the rates of high-e migration for a giant planet with a rocky core for different viscoelastic dissipation models depicted in Fig. 5.1, and compare the results with weak friction theory. We numerically carry out the sums in Eqs. (5.16)-(5.17) for different values of orbital eccentricity and a fixed final semi-major axis, i.e., the semi-major axis a and eccentricity e always satisfy $a(1 - e^2) \equiv a_F = \text{constant}$, corresponding to a final circular orbital period of 5 days.

Since the timescale for changing the planet's spin is much shorter than the orbital evolution time, we assume that the planet is in the equilibrium spin state ($T_z = 0$) at all times. For the weak friction theory, the result is [see Eq. (5.22)] $\Omega_{ps}/\Omega_{peri} = (1 + e)^{-3/2} f_2/f_5$, where $\Omega_{peri} = \Omega/(1 - e)^{3/2}$ is the orbital frequency at the pericenter. For general viscoelastic models, we set the right-hand-side

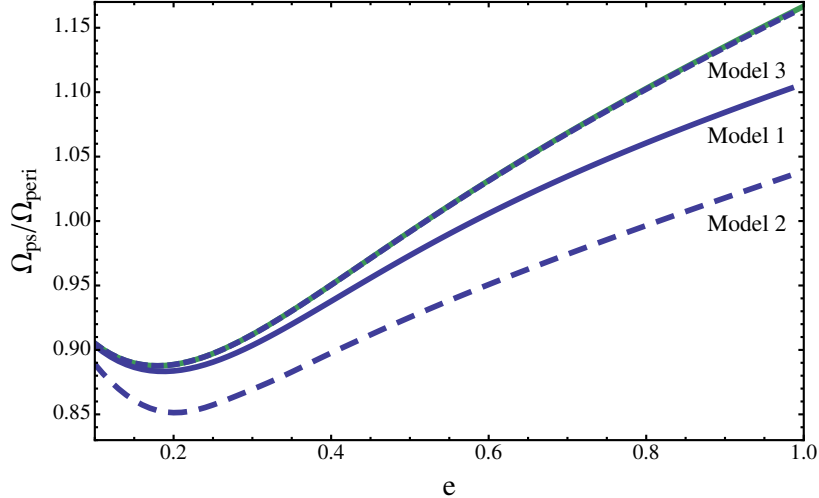


Figure 5.2: Ratio of the pseudosynchronized spin frequency Ω_{ps} to the pericenter frequency Ω_{peri} for each of the viscoelastic models of Figure 5.1, as well as for the (analytical) weak friction model. Each blue curve corresponds to one of the Maxwell model curves depicted in Fig. 5.1. The green curve shows the result of the weak friction theory.

of Eq. (5.16) to 0 and numerically solve for the equilibrium spin rate Ω_{ps} . The results are shown in Fig. 5.2. We note that while for the model parameters considered in Figs. 5.1 and 5.2, there exists a single Ω_{ps} for a given e (for a given model), as in the weak friction theory, for other model parameters where the torque is created by a primarily elastic rather than viscous response ($\omega \gtrsim \omega_M$), it is possible to find *multiple* spin frequencies for which $T_z = 0$, some of which are resonant in nature, for a given e . We discuss this interesting phenomenon in the Appendix.

Figures 5.3 and 5.4 present the results of the orbital evolution for different viscoelastic tidal dissipation models. While all these models satisfy the same Jupiter-Io tidal Q constraint as the weak friction theory, the predicted high- e migration rate can be easily larger, by a factor of 10 or more, than that predicted by the weak friction theory. For example, while it takes ~ 100 Gyrs to complete the orbital circularization in the weak friction theory, only 10 Gyrs is needed in

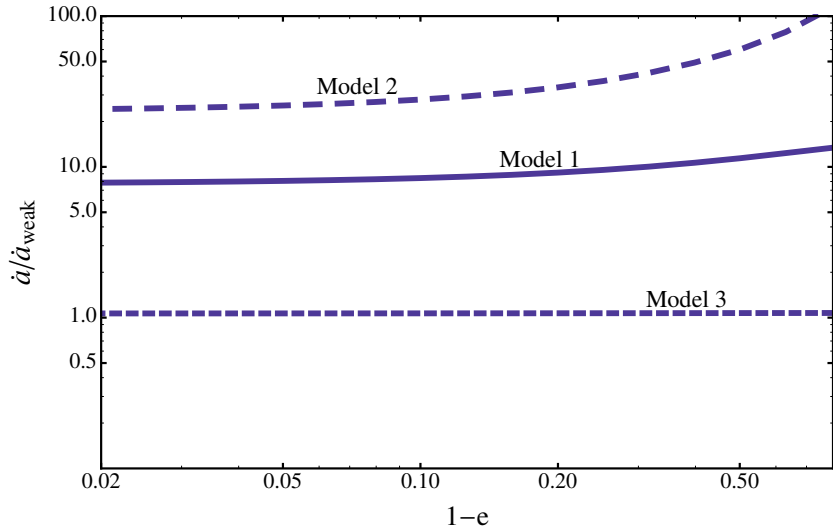


Figure 5.3: Ratio of the orbital decay rate \dot{a} for different viscoelastic tidal dissipation models and \dot{a}_{weak} for the weak friction theory, as a function of eccentricity, for a fixed $a_F = a(1 - e^2)$ corresponding to final mean motion period of 5 days. Each curve corresponds to one of the blue Maxwell model curves of Fig. 5.1. In all cases, the weak friction theory is that of the green curve in Fig. 5.1.

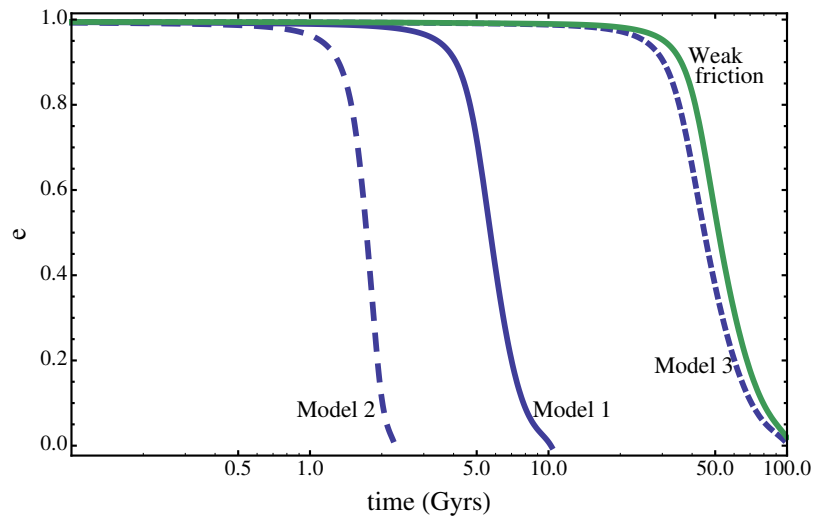


Figure 5.4: Eccentricity as a function of time, for an initial eccentricity of 0.9945 and a final mean motion period of 5 days. Each blue curve corresponds to one of the blue theoretical Maxwell model curves of Fig. 5.1. The green curve corresponds to the weak friction theory of Fig. 5.1.

Model 1 and only ~ 2 Gyrs is needed in Model 2.

5.5.2 Tidal heating of giant planets during migration

Many hot Jupiters are found to have much larger radii than predictions based on “standard” gas giant theory (Baraffe et al., 2010). A number of possible explanations for the “radius inflation” have been suggested, including tidal heating (Bodenheimer et al., 2001, 2003; Ibgui et al., 2010; Leconte et al., 2010; Miller et al., 2009), the effect of thermal tides (Arras and Socrates, 2010; Socrates, 2013), enhanced envelope opacity (Burrows et al., 2007), double-diffusive envelope convection (Chabrier and Baraffe, 2007; Leconte and Chabrier, 2012) and Ohmic dissipation of planetary magnetic fields (Batygin and Stevenson, 2010; Batygin et al., 2011; Huang and Cumming, 2012; Menou, 2012; Perna et al., 2010; Rauscher and Menou, 2013; Wu and Lithwick, 2013). It is possible that more than one mechanism is needed to explain all of the observed radius anomalies of hot Jupiters (Fortney and Nettelmann, 2010; Spiegel and Burrows, 2013).

Several papers have already pointed out the potential importance of tidal heating in solving the radius anomaly puzzle (see above for references). In particular, Leconte et al. (2010) studied the combined evolutions of the planet’s orbit (starting from high eccentricity) and thermal structure including tidal heating, and showed that tidal dissipation in the planet provides a substantial contribution to the planet’s heat budget and can explain some of the moderately bloated hot Jupiters but not the most inflated objects (Ibgui et al., 2010; Miller et al., 2009). However, all these studies were based on equilibrium tide theory with a parameterized tidal quality factor Q or lag time, and assume that the heating is

distributed uniformly across the planet.

Here we study the heating of proto-hot-Jupiters via tidal dissipation in the core. To model this effect, we use the MESA code (Paxton et al., 2011, 2013) to evolve the internal structure of giant planets in conjunction with the orbital evolution starting from high eccentricity. We create a zero-age Jupiter-mass giant planet (initially hot and inflated) with an inert rocky core, for which we can prescribe a time-varying luminosity. Assuming the core is in thermal equilibrium with its surroundings, we consider the core luminosity to be equal to \dot{E} as given by Eq. (5.17) (with $\Omega_s = \Omega_{ps}$ such that $T_z = 0$). We assume the planet starts at a high eccentricity of $e = 0.9945$ and circularizes to a 5-day orbit, while conserving orbital angular momentum (so that $a_F = a(1 - e^2)$ at all times). These assumptions enable us to calculate $\dot{E}(t)$ and observe its effect on the radius of the planet.

Figure 5.5 presents the planet heating rate and radius vs age curves. Evidently, it is possible to inflate a proto-hot-Jupiter by up to 40% via tidal heating in the core. However, this happens early in the planet's evolution, around eccentricities of 0.6, when the heating rate is largest. By the time the planet's orbit has circularized ($e \lesssim 0.05$), its radius is only $\sim 10\%$ larger than the zero-temperature planet and continues to decline over time. Therefore, regardless of the details of the tidal models, it appears that tidal heating cannot fully explain the population of observed hot Jupiters with significant radius inflation. Nevertheless, tidal effects can significantly delay the radius contraction of gas giants. By keeping the planet somewhat inflated until (possibly) another effect due to proximity to the host star takes over, tidal dissipation may still play an important role in the creation of inflated hot Jupiters.

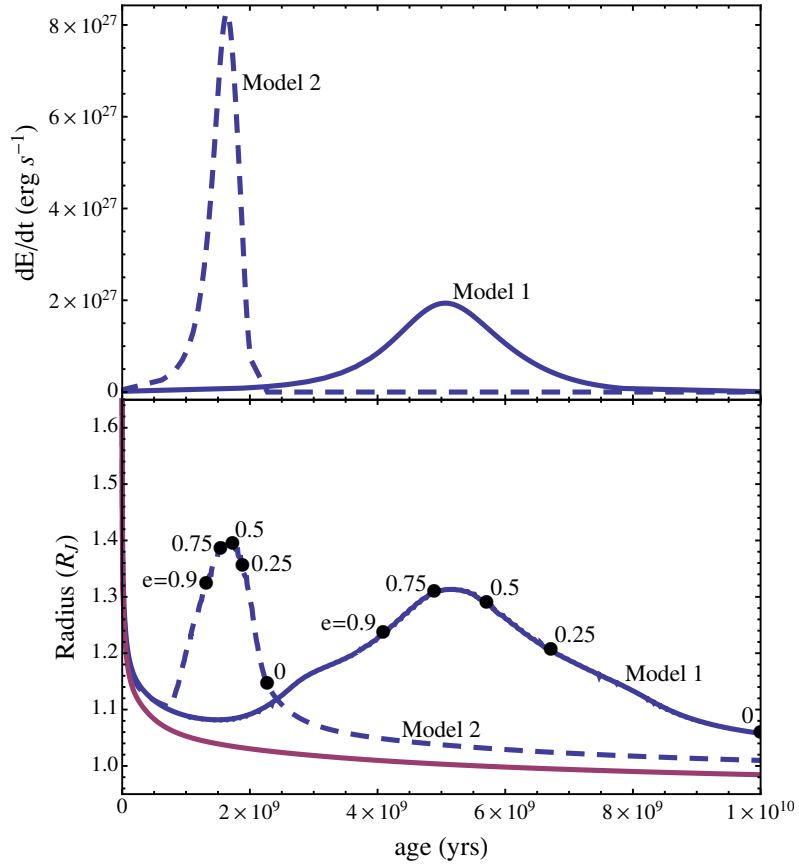


Figure 5.5: *Top:* Core luminosity due to viscoelastic tidal dissipation in a Jupiter-mass gas giant. The blue solid curve corresponds to Model 1 of Fig. 5.1, and the blue long-dashed curve corresponds to Model 2 of Fig. 5.1. *Bottom:* Evolution of radius vs time for each of the models (top), assuming an initial eccentricity of 0.9945 and a final circularized orbital period of 5 days. The red solid curve has no tidal heating and asymptotes to the zero-temperature radius at later times. Black dots and labels on each curve denote when the particular planet model passes through that value of eccentricity in its orbital evolution. Note that since Model 2 is more dissipative than Model 1, the maximum heating rate and radius inflation (around $e = 0.6$) occur earlier in time than Model 1.

Interestingly, these cooling curves suggest that if tidal dissipation in the core is indeed strong enough to play a significant role in circularizing the planet's orbit, as we have shown to be possible in this paper, we may expect to observe a population of gas giants (proto-hot-Jupiters) in wide, eccentric orbits, which are nevertheless inflated more than expected (Dawson and Murray-Clay, 2013; Socrates et al., 2012*b*).

5.6 Conclusion

The physical mechanisms for tidal dissipations in giant planets are uncertain. Recent works have focused on mechanisms of dissipation in the planet's fluid envelope, but it is not clear whether they are adequate to satisfy the constraints from the Solar System gas giants and the formation of close-in exoplanetary systems via high- e migration.

In this paper, we have studied the possibility of tidal dissipation in the solid cores of giant planets. We have presented a general framework by which the effects of tidal dissipation on the spin and orbital evolution of planetary systems can be computed. This requires only one input - the imaginary part of the complex tidal Love number, $\text{Im}[\tilde{k}_2(\omega)]$, as a function of the forcing frequency ω . We discussed the simplest model of tidal response in solids - the Maxwell viscoelastic model, which is characterized by a transition frequency ω_M , above which the solid responds elastically, below - viscously. Using the Maxwell model for the rocky/icy core, and including the effect of a non-dissipative fluid envelope, we have demonstrated that with a modest-sized rocky core and reasonable (but uncertain) physical core parameters, tidal dissipation in the core can account

for the Jupiter-Io tidal- Q constraint (Remus et al., 2012*b*) and at the same time allows exoplanetary hot Jupiters to form via tidal circularization in the high- e migration scenario. By contrast, in the often-used weak friction theory of equilibrium tide, when the tidal lag is calibrated with the Jupiter-Io constraint, hot Jupiters would not be able to go through high- e migration within the lifetime of their host stars.

We have also examined the consequence of tidal heating in the rocky cores of giant planets. Such heating can lead to modest radius inflation of the planets, particularly when the planets are in the high-eccentricity phase ($e \sim 0.6$) during their high- e migration.

As an interesting by-product of our study, we have shown that when $\text{Im}(\tilde{k}_2)$ exhibits nontrivial dependence on ω (as opposed to the linear dependence in the weak friction theory), there may exist multiple spin frequencies at which the torque on the planet vanishes (see Appendix).

We emphasize that there remain large uncertainties in the physical properties of solid cores inside giant planets, including the size, density, composition, viscosity and elastic shear modulus. These uncertainties make it difficult to draw any definitive conclusion about the importance of core dissipation. Nevertheless, our study in this paper suggests that within the range of uncertainties, viscoelastic dissipation in the core is a possible mechanism of tidal dissipation in giant planets and has several desirable features when confronting the current observational constraints. Thus, core dissipation should be kept in mind as observations in the coming years provide more data on tidal dissipations in giant planets.

5.7 Acknowledgments

We thank M. Efroimsky, M.-H. Lee, J. Lunine, P. Nicholson and Y. Wu for discussions and information. This work has been supported in part by NSF grants AST-1008245, 1211061 and NASA grant NNX12AF85G.

5.8 Appendix: Spin Equilibrium/Pseudosynchronization in Viscoelastic Tidal Models

In the weak friction theory, the tidal Love number $\text{Im}(\tilde{k}_2)$ is a linear function of the tidal frequency ω , and thus spin equilibrium ($T_z = 0$) occurs at a unique value of Ω_s , termed the pseudosynchronous frequency, for a given orbital eccentricity e . When $\text{Im}(\tilde{k}_2)$ depends on ω in a more general way, as in the case of viscoelastic tidal models of giant planets, it is possible that multiple solutions for the equilibrium spin frequency Ω_{ps} exist at a given e .

The reason for the existence of multiple pseudo-synchronized spins can be understood in simple algebraic terms. For clarity here we demonstrate how multiple roots arise naturally even at low eccentricities. Consider Eq. (5.16), which we rewrite here to make the dependence on spin frequency explicit:

$$T_z = \frac{5}{4\pi} T_0 \sum_{m,N} m [W_{2m} F_{mN}(e)]^2 \text{Im}[\tilde{k}_2(N\Omega - m\Omega_s)]. \quad (5.38)$$

For very low eccentricities $e \ll 1$, the Hansen coefficients F_{mN} are negligible for all except the following combinations of (m, N) : $(0, 0)$, $(0, \pm 1)$, $(\pm 2, \pm 2)$, and $(\pm 2, \pm 3)$. We can then rewrite T_z as

$$T_z = \text{Im}[A\tilde{k}_2(2\Omega - 2\Omega_s) + B\tilde{k}_2(3\Omega - 2\Omega_s)], \quad (5.39)$$

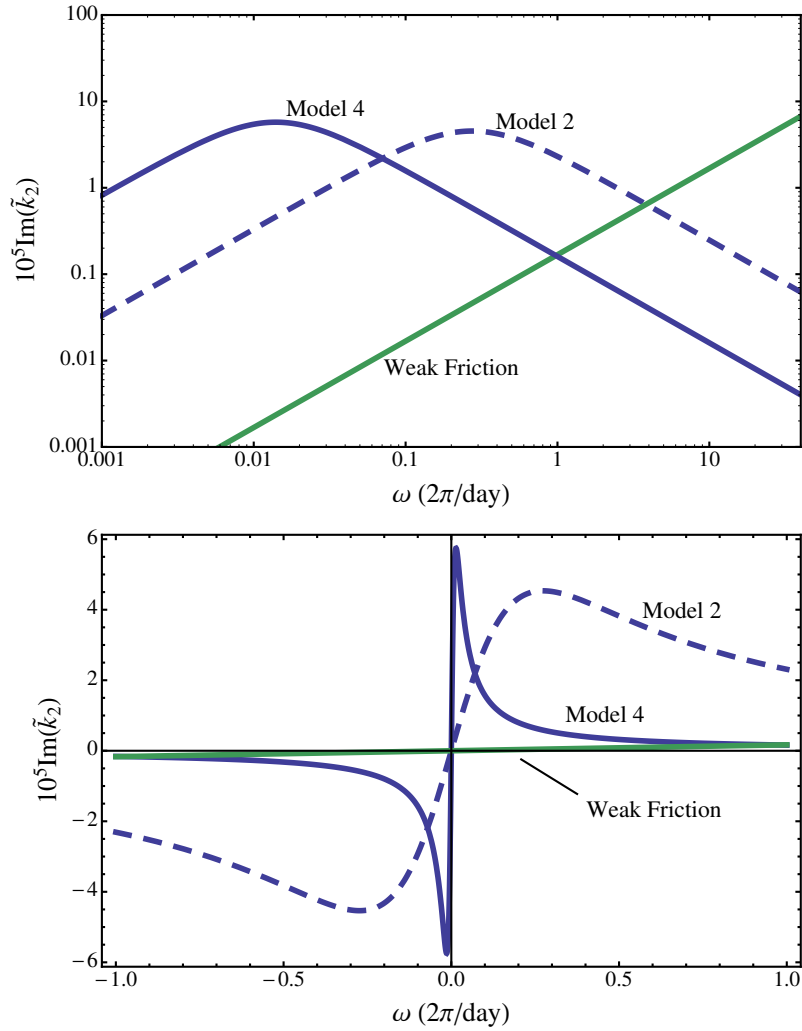


Figure 5.6: Theoretical curves for the tidal Love number of a Jupiter-mass planet as a function of the tidal forcing frequency. The blue dashed curve is the same as Model 2 of Fig. 5.1, and the green solid curve corresponds to the weak friction model of Fig. 5.1. The blue solid curve is a viscoelastic Maxwell model (model 4), with $R_c/R_p = 0.2$ and $\eta = 4 \times 10^{11} \text{ bar} \cdot \text{s}$. In the top panel, the models are plotted on a log-log scale, as in Fig. 5.1, while in the bottom panel we plot the models on a linear scale to clarify how the shape of the tidal response curve leads to resonant equilibrium spin states.

with A and B real constants. Plugging in for \tilde{k}_2 using the Maxwell model (Eq. 5.32) (neglecting fluid envelope for simplicity), we have:

$$T_z = \bar{A} \frac{(2\Omega - 2\Omega_s)}{1 + C(2\Omega - 2\Omega_s)^2} + \bar{B} \frac{(3\Omega - 2\Omega_s)}{1 + C(3\Omega - 2\Omega_s)^2}, \quad (5.40)$$

where \bar{A} , \bar{B} , and C are constants. Thus, when solving for Ω_s from $T_z(\Omega_s) = 0$, it is obvious that upon finding the least common denominator, we end up solving a cubic equation for Ω_s . The above discussion can be generalized to higher eccentricities: the pseudosynchronized spin Ω_{ps} is determined by solving equations of increasingly higher (always odd) degree in Ω_s .

The top panel of Figure 5.7 shows the two terms on the RHS of Eq. (5.40), as well as their sum, for the viscoelastic Model 4 of Figure 5.6 at an eccentricity of 0.13. This demonstrates the way in which multiple solutions for Ω_{ps} arise. Furthermore, we see that two (out of three) of the solutions are resonant in nature: that is, they occur, roughly, at multiples of $\Omega/2$, where Ω is the orbital frequency. This can be understood by considering that the viscoelastic response (Figure 5.6) is quite sharply peaked and localized. Each term on the RHS of Eq. (5.40) vanishes when $\Omega_s = \Omega$ and 1.5Ω , respectively. Due to the sharply peaked nature of the viscoelastic response, to which T_z is proportional, the sum of the two terms then shows resonant crossings at both of these values.

This generalizes easily to the case of arbitrary eccentricity, where each (m, N) harmonic of the sum for T_z (Eq. 5.38) vanishes when $N\Omega - m\Omega_s = 0$. The number and location of the resonant crossings then depends on the relative importance of each of the harmonics; the strongest crossing is expected to occur $\Omega_s \sim \Omega_{peri}$. This is demonstrated in Figure 5.7 (bottom) and Figure 5.8.

Thus, the nonlinearity of the function $\text{Im}[\tilde{k}_2(\omega)]$ of the viscoelastic Maxwell model is responsible for the existence of multiple pseudosynchronized spins. As

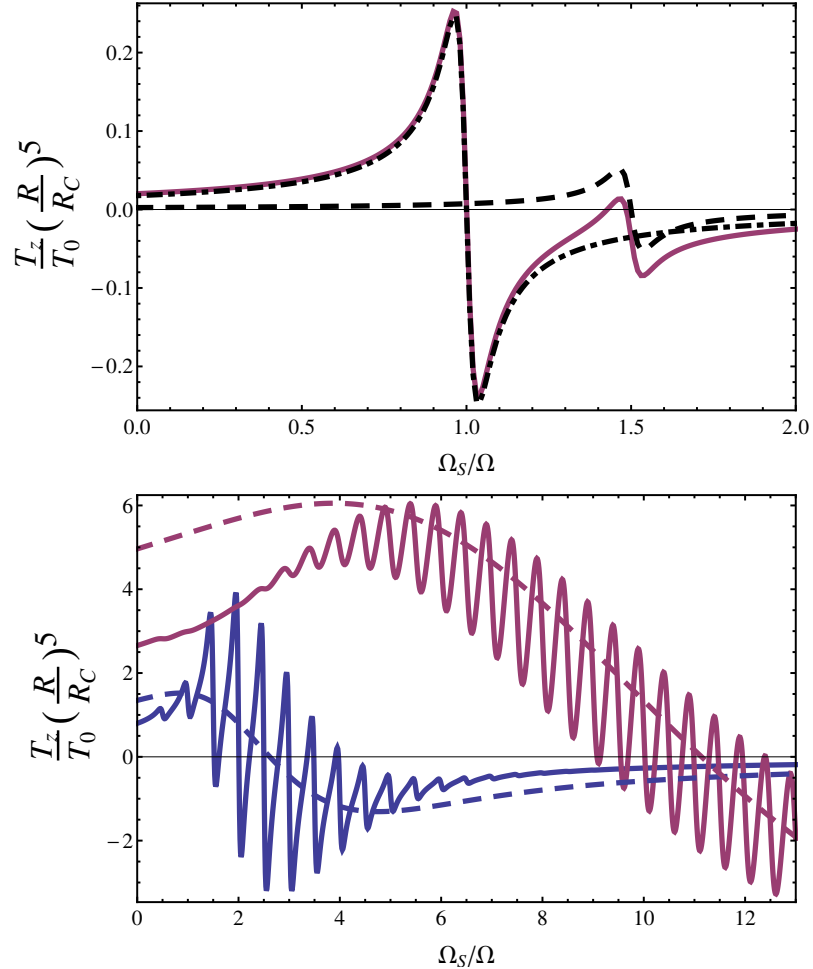


Figure 5.7: Tidal torque on the planet as a function of the spin frequency for different values of eccentricity and different tidal dissipation models. *Top:* Model 4 (solid blue) of Figure 5.6, for $e = 0.13$. The black dot-dashed and dashed curves show the $(m, N) = (\pm 2, \pm 2)$ and $(\pm 2, \pm 3)$ terms of Eq. 5.40, respectively. The red curve shows their sum. The resonant features in each of the harmonics combine into three different zero-crossings in the sum. *Bottom:* Model 4 (solid) and Model 2 (dashed) of Figure 5.6. The red curves have $e = 0.8$, while the blue curves have $e = 0.5$. In order to fit all the curves on the same plot, we show $10T_z$ for the blue solid curve, and $0.1T_z$ for the red dashed curve. Equilibrium spins are determined by $T_z = 0$. Evidently, in the case of Model 2, the viscoelastic response is not localized enough to permit more than one resonant solution.

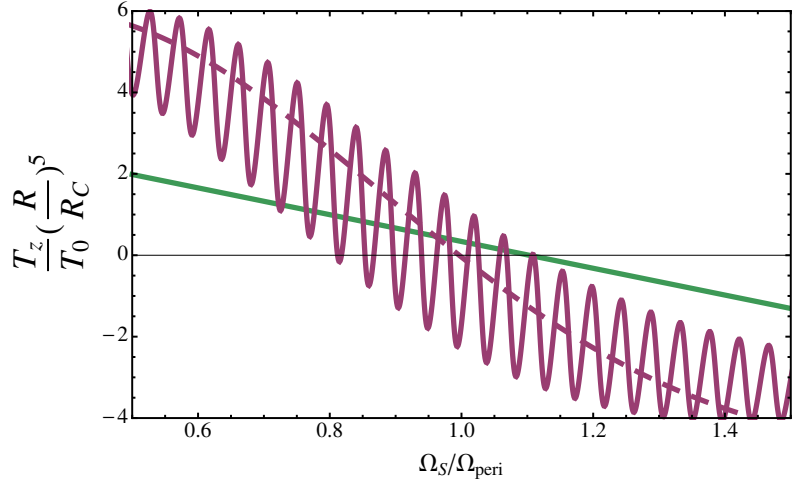


Figure 5.8: Tidal torque on the planet as a function of the ratio of spin frequency to pericenter frequency for $e = 0.8$ and different tidal dissipation models. *Red solid:* Model 4 of Figure 5.6; *red dashed:* $0.1T_z$ for Model 2 of Figure 5.6; *green solid:* Weak friction model of Figure 5.6. Note that the equilibrium spin frequencies of the viscoelastic models can differ from the weak friction pseudosynchronous spin by as much as $\sim 10 - 20\%$.

shown in Figure 5.7 (bottom panel), there will not be multiple solutions if the viscoelastic response is not localized enough, compared with the mean motion frequency Ω (that is, the width of the resonant transition $\Delta \sim \omega_M \gtrsim \Omega$), and all important harmonics of T_z are solidly on the viscous (linear) side of the Maxwell curve. On the other hand, there may exist multiple solutions when $\Delta \sim \omega_M \ll \Omega$ and the relevant tidal forcing frequencies lie on the elastic side of the Maxwell curve.

Finally, we note that all the resonant zero crossings of T_z are stable (negative slope), while the non-resonant crossings are necessarily unstable (positive slope). The innermost and outermost crossings are always resonant. This phenomenon is analogous to that discussed by Makarov and Efroimsky (2013), who used a different model for viscoelastic dissipation in solid bodies to analyze the pseudosynchronization of telluric planets. They demonstrated the presence of

multiple equilibrium spin solutions, and showed that only the resonant solutions are stable equilibria, thus concluding that the telluric planets possess no true (non-resonant) pseudosynchronous state.

The implications of our finding may be of practical interest when it becomes possible to measure the spin of exoplanets on eccentric orbits. We may then look for evidence of the existence of multiple stable spin equilibria in rocky planets or gas giants with rocky cores.

CHAPTER 6

**ANALYTICAL MODEL OF TIDAL DISTORTION AND DISSIPATION
FOR A GIANT PLANET WITH A VISCOELASTIC CORE**

6.1 Abstract

We present analytical expressions for the tidal Love numbers of a giant planet with a solid core and a fluid envelope. We model the core as a uniform, incompressible, elastic solid, and the envelope as a non-viscous fluid satisfying the $n = 1$ polytropic equation of state. We discuss how the Love numbers depend on the size, density, and shear modulus of the core. We then model the core as a viscoelastic Maxwell solid and compute the tidal dissipation rate in the planet as characterized by the imaginary part of the Love number k_2 . Our results improve upon existing calculations based on planetary models with a solid core and a uniform ($n = 0$) envelope. Our analytical expressions for the Love numbers can be applied to study tidal distortion and viscoelastic dissipation of giant planets with solid cores of various rheological properties, and our general method can be extended to study tidal distortion/dissipation of super-earths.

6.2 Introduction

Tidal effects play an important role in understanding many puzzles associated with planet/exoplanet formation and evolution. One example involves high-eccentricity migration of giant planets: tidal dissipation in the planet is respon-

The contents of this chapter were published in *MNRAS* as "Analytical Model of Tidal Distortion and Dissipation for a Giant Planet with a Viscoelastic Core" (Storch and Lai, 2015a)

sible for circularizing the planet’s orbit, leading to the creation of hot Jupiters (Correia et al., 2011; Fabrycky and Tremaine, 2007; Naoz et al., 2012; Petrovich, 2015b; Storch et al., 2014; Wu and Murray, 2003).

The levels of tidal dissipation in giant planets suggested by both Solar System (Goldreich and Soter, 1966; Lainey et al., 2009, 2012; Yoder and Peale, 1981) and extrasolar (Socrates et al., 2012a; Storch and Lai, 2014) constraints cannot easily be explained by simple viscous dissipation in the turbulent fluid envelope (Goldreich and Nicholson, 1977). While several mechanisms based on wave excitation and dissipation in the envelope (ocean) have been studied (Ivanov and Papaloizou, 2007; Ogilvie, 2014; Ogilvie and Lin, 2004), it remains unclear whether they can provide sufficient dissipation.

Dissipation in the solid cores of giants planets is another possible source of dissipation. Previous works (Remus et al., 2012b, 2015; Storch and Lai, 2014) have employed analytical formulae for the tidal dissipation in a two-layer planet consisting of a uniform, incompressible, viscoelastic core and a uniform non-dissipative ocean (Dermott, 1979). These works demonstrate that, while there are significant uncertainties in the rheologies of the solid core, it is in principle possible for dissipation in the core to be substantial enough to account for existing constraints, particularly the dependence of dissipation on the tidal forcing frequency (Storch and Lai, 2014).

The advantage of analytical models for the tidal deformation lies in the use of the “correspondence principle”, in which the analytical formulae derived for the tidal deformation of an elastic body may be generalized to a *viscoelastic* body via introduction of a complex shear modulus (Biot, 1954). This allows various rheologies for the solid core to be employed in calculating the tidal dissipation.

In this paper, we extend previous works by considering a fluid envelope (ocean) of non-uniform density, rather than a uniform one. In particular, we show that if the ocean obeys the $n = 1$ polytropic equation of state ($P \propto \rho^2$), relatively simple analytical expressions for the tidal Love numbers can be obtained. The $n = 1$ polytrope is appropriate for giant planets, as it correctly reproduces the fact that their radii are nearly independent of their masses.

In section 6.3, we set up the analytical problem of calculating the tidal distortion in a two-layer giant planet. In section 6.4, we present the solution for the tidal radial deformation of the core, characterized by the Love number h_{2c} , and the change in the self-gravity of the planet, characterized by the Love number k_2 . In section 6.5 we give several examples of the uses of these formulae. We discuss our results and conclude in section 6.6.

6.3 Setup and Schematic Solution

We consider distortion of a planet by an $l = 2$ tidal potential. Let the perturber have mass M_\star and be a distance a away. Let the planet have mass M_p and radius R , and possess a solid core of radius R_c . We assume the core is incompressible, with uniform density ρ_c and shear modulus μ . We model the planet's fluid envelope as an $n = 1$ polytrope, such that its pressure (P) and density (ρ) profiles satisfy the relation

$$P(r) = K\rho(r)^2, \quad (6.1)$$

where K is a constant.

6.3.1 Equilibrium Structure

In the absence of a perturber, the planet is in hydrostatic equilibrium. The planet's gravitational potential Φ and pressure profile P satisfy the equations

$$\nabla^2 \Phi = 4\pi G \rho, \quad (6.2)$$

$$\nabla P = -\rho \nabla \Phi. \quad (6.3)$$

It follows that the density profile in the fluid ocean is given by

$$\rho(r) = \rho_0 \frac{\sin[q(1-r/R)]}{qr/R}, \quad (6.4)$$

where

$$q^2 = \frac{2\pi G R^2}{K}, \quad (6.5)$$

$$\rho_0 = \frac{q^2 M_p}{4\pi R^3}. \quad (6.6)$$

For clarity, we define ρ_{\max} to be the fluid density at $r = R_c +$ (just outside R_c):

$$\rho_{\max} \equiv \rho_0 \frac{\sin[q(1-R_c/R)]}{qR_c/R}. \quad (6.7)$$

Since we demand the planet to be of mass M_p and radius R , and the core to have radius R_c , this leads to a constraint on the core-to-fluid density jump:

$$\frac{\rho_c}{\rho_{\max}} = \frac{3R^2}{q^2 R_c^2} \left[\frac{qR_c}{R} \cot[q(1-R_c/R)] + 1 \right]. \quad (6.8)$$

In practice, for given M_p , R , ρ_c and R_c (or M_c), we solve for q from equations (6.6)-(6.8). For completeness, we give the potential Φ inside the planet:

$$\Phi(r) = \begin{cases} \frac{2}{3}\pi G \rho_c (r^2 - R_c^2) - \frac{GM_p}{R} \left[\frac{\sin[q(1-R_c/R)]}{qR_c/R} + 1 \right] & (r \leq R_c) \\ -\frac{GM_p}{R} \left[\frac{\sin[q(1-r/R)]}{qr/R} + 1 \right] & (R_c \leq r \leq R). \end{cases} \quad (6.9)$$

6.3.2 Tidal Perturbation

We now turn on the $l = 2$ tidal perturbation and calculate the resulting deformation of the planet. We set up the problem such that the z axis joins the centers of the planet and the perturber. In this way, the problem has azimuthal symmetry. The perturbing tidal potential (assumed small) is given by

$$\bar{U}(r, \theta) \equiv U(r)Y_{20}(\theta) = -\sqrt{\frac{4\pi}{5}} \frac{GM_\star}{a^3} r^2 Y_{20}(\theta), \quad (6.10)$$

Hence we can assume all perturbed quantities are proportional to Y_{20} . The perturbed Poisson's equation is given by

$$\nabla^2 \bar{\delta\Phi} = 4\pi G \bar{\delta\rho}, \quad (6.11)$$

where $\bar{\delta X} \equiv \delta X(r)Y_{20}(\theta)$ indicates the Eulerian perturbation to the variable X , and the perturbed equation of hydrostatic equilibrium in the liquid layer of the planet is given by

$$\nabla \bar{\delta P} = -\bar{\delta\rho} \nabla \Phi - \rho \nabla \bar{V}, \quad (6.12)$$

where $\bar{V} \equiv V(r)Y_{20}(\theta) \equiv \bar{\delta\Phi} + \bar{U}$, and $\rho(r)$ and $\Phi(r)$ are the unperturbed density profile and unperturbed gravitational potential as derived in the previous subsection. The transverse component of Eq. (6.12) is $\bar{\delta P} = -\bar{\delta\rho} \bar{V}$, while the radial component is $(\bar{\delta P})' = -\bar{\delta\rho} \Phi' - \rho \bar{V}'$, where ' stands for $\partial/\partial r$. These imply that $\bar{\delta\rho} = (\rho'/\Phi') \bar{V}$.

Inside the core, and outside the planet, the perturbed Poisson equation reduces to $\nabla^2 \bar{\delta\Phi} = 0$, and is easily solved, yielding $\delta\Phi = b_1 r^2$ inside the core and $\delta\Phi = b_4 r^{-3}$ outside the planet, with b_1 and b_4 as yet unknown constants. In the fluid envelope, the Poisson equation reduces to

$$\nabla^2 \bar{V} = 4\pi G \bar{\delta\rho} = 4\pi G \frac{\rho'}{\Phi'} \bar{V}. \quad (6.13)$$

So far the equations in this subsection are general (valid for all envelope equation of state). for the $n = 1$ EOS, $P' = -\rho\Phi'$ gives $(\rho'/\Phi') = -1/(2K)$ and we have

$$\nabla^2 \bar{V} = - \left(\frac{q}{R} \right)^2 \bar{V}. \quad (6.14)$$

This equation admits a standard solution in the form of spherical Bessel functions (j_2 and y_2):

$$V(r) = b_2 j_2 \left(q \frac{r}{R} \right) + b_3 y_2 \left(q \frac{r}{R} \right) \quad (6.15)$$

inside the fluid envelope, with b_2 and b_3 constants to be determined.

The unknown constants b_1, b_2, b_3, b_4 may now be solved for by matching boundary conditions at $r = R$ and at $r = R_c$:

$$\delta\Phi(R_+) = \delta\Phi(R_-), \quad (6.16)$$

$$\delta\Phi(R_{c,+}) = \delta\Phi(R_{c,-}), \quad (6.17)$$

$$(\delta\Phi')_{R_-} = (\delta\Phi')_{R_+} = -\frac{3}{R} \delta\Phi(R_+), \quad (6.18)$$

$$(\delta\Phi' + 4\pi G\rho\xi_r)_{R_{c,-}} = (\delta\Phi' + 4\pi G\rho\xi_r)_{R_{c,+}}. \quad (6.19)$$

Since the fluid density vanishes at surface of planet, these introduce only one additional unknown: the radial displacement at the core-fluid interface, $\xi_r(R_c)$. Determining $\xi_r(R_c)$ requires solving for the deformation of the core, matching the radial and transverse tractions across the core-fluid interface. The procedure to follow is similar to Love's classic solution for the deformation of an incompressible, uniform, self-gravitating elastic body under an external potential (Greff-Lefftz et al., 2005; Love, 1911), with the addition of an external pressure force due to the fluid envelope. We find the final boundary condition is given by

$$\begin{aligned} \frac{19}{5}\mu \frac{\xi_r(R_c)}{R_c} &= - \left(\frac{dP}{dr} + \rho_c g_c \right) \xi_r \\ &+ (\rho_{\max} - \rho_c)(b_1 R_c^2 + U), \end{aligned} \quad (6.20)$$

where $g_c \equiv (4/3)\pi G\rho_c R_c$ is the gravitational acceleration at $r = R_c$, and all the quantities on the RHS are evaluated at $r = R_{c,+}$. Note that equation (6.20) is valid for any envelope EOS. Together, the five boundary conditions, Eqs. (6.16) – (6.20), can be solved for all the unknowns.

6.4 Analytical Love Number Formulae

6.4.1 Non-dissipative tide

We are interested in two dimensionless Love numbers. The first is the tidal Love number of the planet, defined as

$$k_2 \equiv \frac{\delta\Phi(R)}{U(R)}. \quad (6.21)$$

This specifies the magnitude of the quadrupole potential produced by the distorted planet, $\overline{\delta\Phi} = k_2 U(R)(R/r)^3 Y_{20}(\theta)$ (for $r > R$), and therefore determines the effect of tidal distortion on the planet's orbit. The second is the radial displacement Love number of the core, defined by

$$h_{2c} \equiv -\frac{\xi_r(R_c)g_c}{U(R_c)}. \quad (6.22)$$

This specifies the shape of the inner core under the combined influences of the external tidal field and the loading due to the fluid envelope.

Following the schematic procedure outlined in the previous section, we find

$$h_{2c} = \frac{5}{q^2} \left(\frac{R}{R_c} \right)^3 \left\{ \alpha \left[1 + \frac{2\bar{\mu}}{5 \left(1 - \frac{\rho_{\max}}{\rho_c} \right)} \right] - 3\lambda \left(1 - \frac{\rho_{\max}}{\rho_c} \right) \right\}^{-1}, \quad (6.23)$$

$$k_2 = \frac{3h_{2c}}{q\alpha} \left(\frac{R_c}{R} \right)^2 \left(1 - \frac{\rho_{\max}}{\rho_c} \right) + \frac{5\gamma}{q\alpha} - 1, \quad (6.24)$$

where

$$\bar{\mu} \equiv 19\mu/(2\rho_c g_c R_c), \quad (6.25)$$

and

$$\begin{aligned} \alpha &= j_1(q) [\chi_c y_1(\chi_c) - 5y_2(\chi_c)] - y_1(q) [\chi_c j_1(\chi_c) - 5j_2(\chi_c)], \\ \lambda &= y_1(q) j_2(\chi_c) - j_1(q) y_2(\chi_c), \\ \gamma &= j_2(q) [\chi_c y_1(\chi_c) - 5y_2(\chi_c)] - y_2(q) [\chi_c j_1(\chi_c) - 5j_2(\chi_c)], \end{aligned} \quad (6.26)$$

with $\chi_c \equiv qR_c/R$.

6.4.2 Dissipative tide

We now consider the effects of viscous dissipation in the solid core. According to the correspondence principle (Biot, 1954), we may generalize the calculation of tidal distortion of a non-dissipative elastic core by adopting a complex shear modulus μ , where the imaginary part of μ accounts for dissipation in the viscoelastic core. In general, the complex μ depends on the tidal forcing frequency ω in the rest frame of the planet, and its actual form depends on the rheology of the solid (Henning et al., 2009; Remus et al., 2012b). Thus the complex $k_2 = k_2(\omega)$ also depends on the forcing frequency.

For example, assume the perturber is in a circular orbit with orbital frequency Ω and the planet is spinning with frequency Ω_s . The forcing frequency is then $\omega = 2\Omega - 2\Omega_s$. The torque on the planet and the energy transfer rate from the orbit to the planet due to dissipation may be calculated as (Storch and Lai, 2014)

$$T_z = \frac{3}{2}T_0 \operatorname{Im}[k_2(2\Omega - 2\Omega_s)], \quad (6.27)$$

$$\dot{E} = \frac{3}{2}T_0\Omega \operatorname{Im}[k_2(2\Omega - 2\Omega_s)], \quad (6.28)$$

where $T_0 \equiv G(M_\star/a^3)^2 R^5$. See Storch and Lai (2014) for the more general case of a perturber on an eccentric orbit.

Note that \dot{E} includes contributions both from dissipation into heat, which occurs solely in the viscoelastic core, and from the torque T_z that acts to synchronize the rotation rate of the planet with the orbital frequency of the perturber. Thus, the true tidal heating rate received by the core is given by

$$\dot{E}_{\text{heat}} = \dot{E} - \Omega_s T_z. \quad (6.29)$$

6.5 Applications of Love Number Formulae

In this section we present several sample applications of the formulae derived in the previous section. First we consider planets with non-dissipative cores, then generalize to a complex shear modulus and compute the tidal dissipation.

6.5.1 Non-dissipative elastic core

In Figure 6.1 we present the Love numbers for a giant planet (mass $M_p = M_J$, radius $R = R_J$) with a core of constant density, $\rho_c = 6 \text{ g cm}^{-3}$, but varying size, for several values of the core shear modulus μ . Our nominal reference value for μ is that of undamaged rocky material at Earth-like pressures and temperatures, $\mu_0 = 900 \text{ kbar}$. Damaged rocky, or icy material can have a lower shear modulus $\sim 40 \text{ kbar}$ (Goldsby and Kohlstedt, 2001; Henning et al., 2009). However, little is known about both the composition of giant cores and the behavior of rocky/icy materials under high pressures and thus the value of μ is largely a free parameter.

Based on Fig. 6.1, we note that the Love numbers generally behave as expected. Cores with higher shear moduli are harder to deform, resulting in smaller Love numbers. Planets with cores of larger radii have more mass concentrated in the center, and thus k_2 decreases as a function of R_c . At $R_c = 0$, i.e. in the absence of a core, k_2 correctly defaults to the standard value for an $n = 1$ envelope, $(15/\pi^2) - 1$. At $R_c/R \approx 0.6$, the core mass is equal to planet mass, i.e. the envelope has zero mass but still artificially extends to $R = R_J$. In this case k_2 and h_{2c} default to values for a bare core:

$$h_{2c,0} = \frac{5}{2(1 + \bar{\mu})}, \quad k_{2,0} = \frac{3}{2(1 + \bar{\mu})} \left(\frac{R_c}{R} \right)^5. \quad (6.30)$$

In Figure 6.2 we present the Love numbers for a planet with a core of constant mass, $M_c = 5M_\oplus$, as a function of the core shear modulus μ , for three different core radii. For the range of core sizes considered (up to $R_c/R = 0.15$), changing the shear modulus by 4 orders of magnitude apparently hardly changes the surface tidal k_2 (bottom panel). Core radius plays a slightly more important

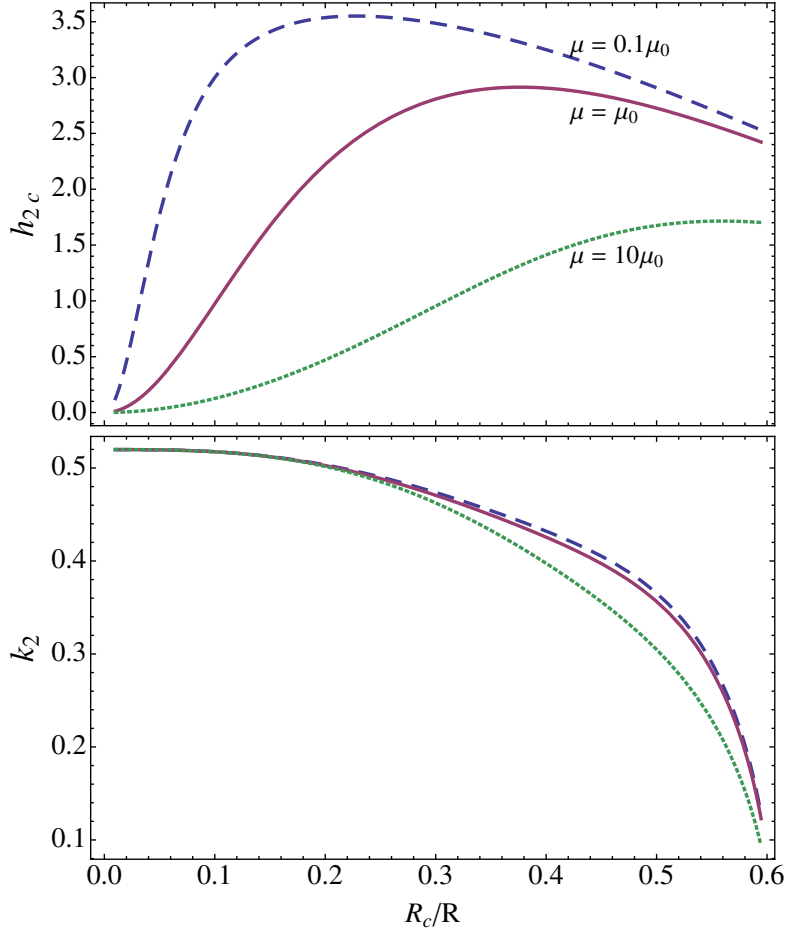


Figure 6.1: Sample tidal Love numbers h_{2c} (top) and k_2 (bottom) for a gas giant with mass M_J , radius R_J , and core density $\rho_c = 6 \text{ g cm}^{-3}$, as a function of core radius for several values of core shear modulus, where $\mu_0 = 900 \text{ kbar}$.

role, with smaller cores yielding smaller k_2 , as expected (note this is opposite to Fig. 6.1 because here we are keeping core mass rather than core density constant). Perhaps surprisingly, smaller cores are deformed more than larger cores (top panel). This can be understood by noting that the amount of deformation depends on $\bar{\mu}$, the ratio of the core shear modulus to the gravitational rigidity $\rho_c g_c R_c$ of the core, with larger ratios yielding smaller deformations (cf. Eq. 6.30). For constant core mass, this ratio scales as $\bar{\mu} \propto R_c^4$, and therefore the core deforms less at higher radii.

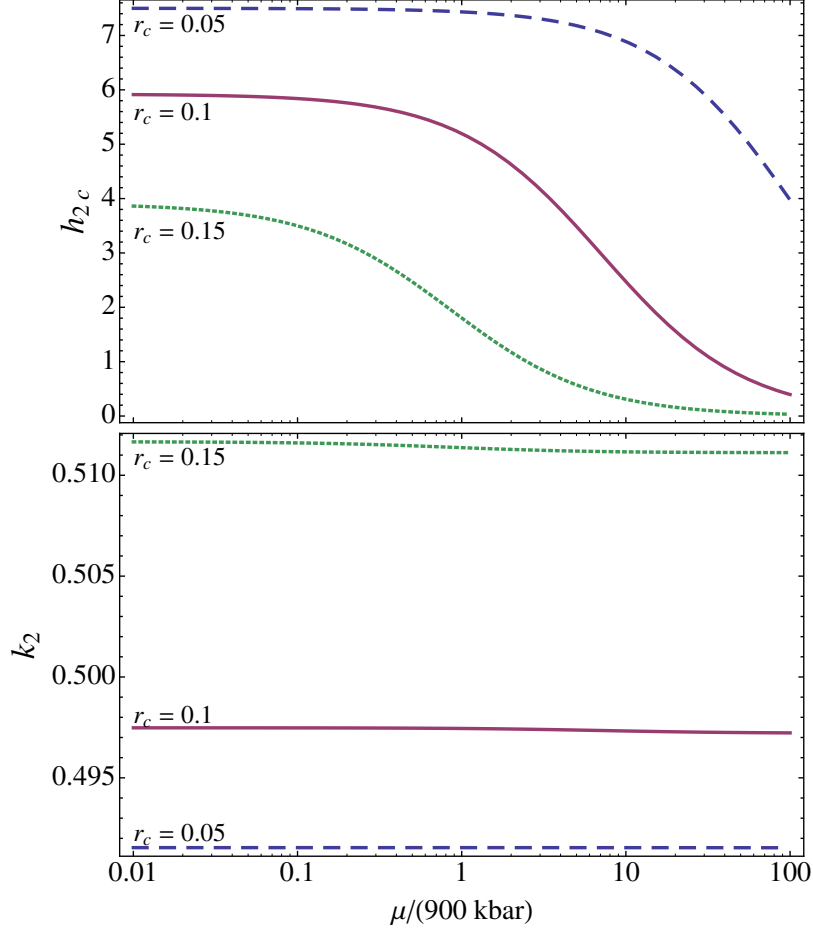


Figure 6.2: Sample tidal Love numbers h_{2c} (top) and k_2 (bottom) for a gas giant with mass M_J , radius R_J , and core mass $M_c = 5M_\oplus$, as a function of shear modulus μ for several values of fractional core radius $r_c \equiv R_c/R$.

6.5.2 Dissipation of viscoelastic core

We now consider tidal dissipation of a viscoelastic core, modeled by a complex shear modulus. We take

$$\mu \rightarrow \tilde{\mu} \equiv \tilde{\mu}_1 + i\tilde{\mu}_2, \quad (6.31)$$

and assume the simplest viscoelastic model - the Maxwell model, such that (Henning et al., 2009)

$$\tilde{\mu}_1 = \frac{\mu (\omega/\omega_M)^2}{1 + (\omega/\omega_M)^2}, \quad (6.32)$$

$$\tilde{\mu}_2 = -\frac{\mu (\omega/\omega_M)}{1 + (\omega/\omega_M)^2}, \quad (6.33)$$

where ω is the forcing frequency in the reference frame of the planet, and ω_M is the Maxwell frequency given by $\omega_M \equiv \mu/\eta$, where μ is the normal shear modulus of the core and η the viscosity of the core. Under the Maxwell model, the solid core responds viscously for $\omega \lesssim \omega_M$ and elastically for $\omega \gtrsim \omega_M$.

Figure 6.3 shows tidal dissipation rates, characterized by $\text{Im}[k_2]$, as a function of the forcing frequency, for different values of μ and η . Since η only enters into the expression for μ through the ratio ω/ω_M , it is not surprising that changing η simply shifts the tidal dissipation curve horizontally without changing the strength (Fig. 6.3, bottom). The effect of μ is more complicated (Fig. 6.3, top panel) and can shift the curve up/down as well. Since μ does not directly affect the viscous properties of the core, it makes sense that a change in μ shifts the curve such that the tidal response on the viscous side ($\omega \lesssim \omega_M$) remains unchanged.

6.5.3 Comparison with planet models with uniform-density envelope

An analytical formula for the tidal number k_2 was previously derived for giant planet models with uniform envelope density (Dermott, 1979). Recent works have used viscoelastic dissipation in the solid cores of such models to explain

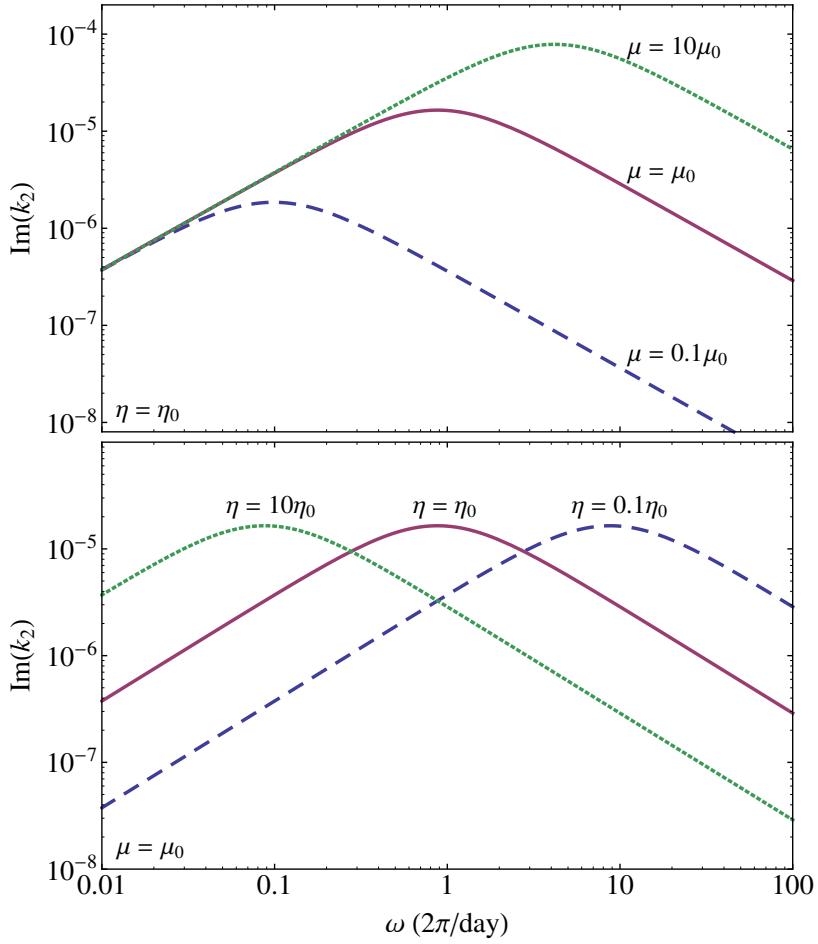


Figure 6.3: Sample tidal dissipation rates for a gas giant with mass M_J , radius R_J with an $n = 1$ envelope, characterized by $\text{Im}[k_2]$, as a function of the forcing frequency ω . Here $R_c = 0.1R$, and $M_c = 5M_\oplus$. Top panel: for a fixed viscosity $\eta = \eta_0 \approx 12.3 \text{ Gbar} \cdot \text{s}$ and three values of μ , were $\mu_0 = 900 \text{ kbar}$. Bottom panel: for a fixed $\mu = \mu_0$ and three values of η .

the amount of tidal dissipation inferred from the evolution of Jupiter's and Saturn's satellites (Remus et al., 2012b, 2015) and from constraints on high-eccentricity migration of hot Jupiters (Storch and Lai, 2014). In Figure 6.4 we compare the dissipation levels in planets with $n = 1$ vs uniform-density envelopes. While we do not attempt to explore the full parameter space here, Figure 6.4 suggests that the difference between the two depends most strongly on the density of the core, with the $n = 1$ dissipation being stronger in more

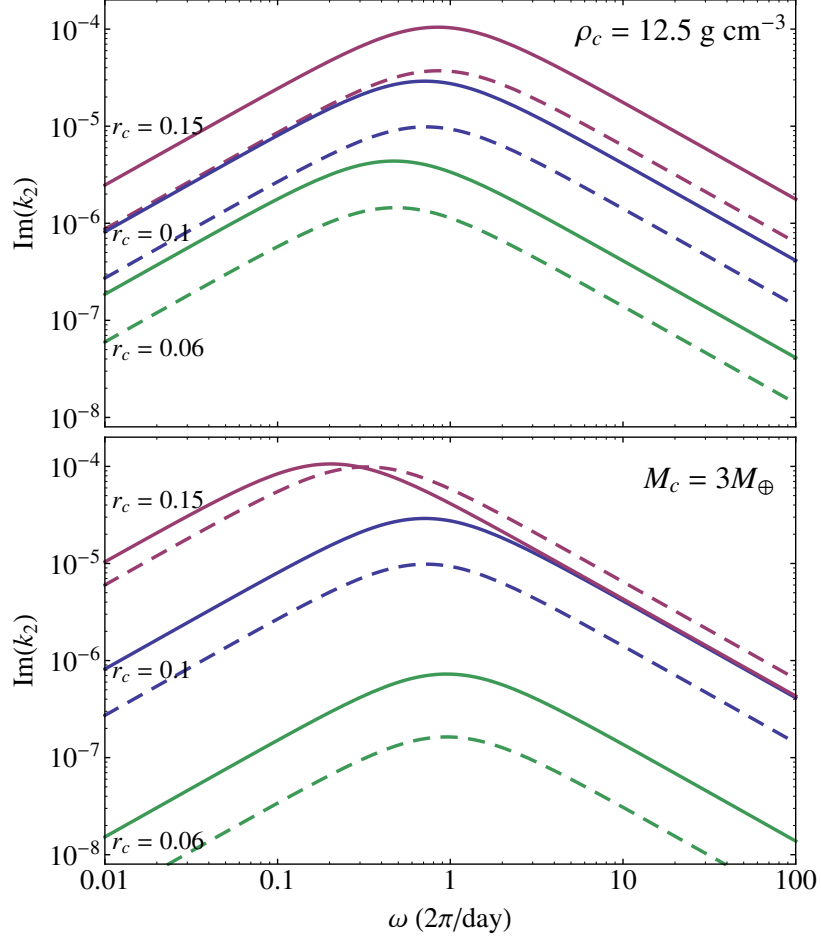


Figure 6.4: Comparison of tidal response curves for a gas giant with mass M_J , radius R_J with an $n = 1$ envelope (solid lines) vs $n = 0$ envelope (dashed lines). Top panel: for a solid core of fixed density $\rho_c = 12.5 \text{ g cm}^{-3}$ but varying radii $r_c \equiv R_c/R$. Bottom panel: for a solid core of fixed mass $M_c = 3M_{\oplus}$ but varying radii. The core mass and density in each panel have been selected such that the $r = 0.1$ curves are identical in the top and bottom panels. We assume $\mu = \mu_0 = 900 \text{ kbar}$ and $\eta = \eta_0 = 12 \text{ Gbar} \cdot \text{s}$.

compact cores by as much as a factor of few.

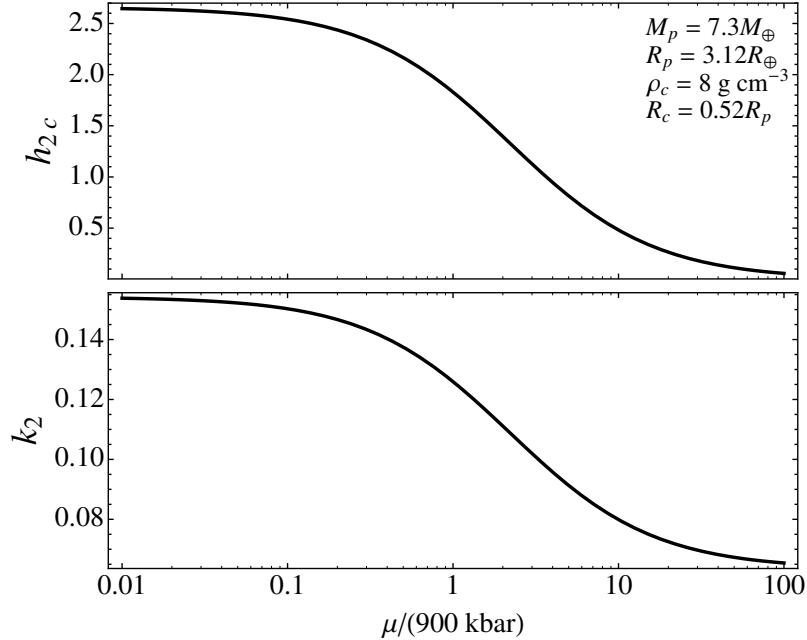


Figure 6.5: Tidal response for a super-Earth analogue similar to Kepler-11d, assuming an $n = 1$ envelope.

6.5.4 Application to Super-Earths

While in this work we focus mainly on gas giants, the formulae presented in section 6.4 do not assume the core radius to be small. Thus, in principle, they may be applied to super-Earths - with the caveat that super-Earths are not likely to be well-described by $n = 1$ envelopes. In Figure 6.5 we present the Love numbers for a super-Earth analogue similar to Kepler-11d (Lissauer et al., 2013), consisting of a solid core and a $n = 1$ gas envelope that is $\sim 15\%$ by mass, but $\sim 50\%$ by radius. In this case the effect of the “core” shear modulus on the surface k_2 is significant when μ is varied by a few orders of magnitude.

6.6 Conclusion

We have presented a general method of computing the tidal Love numbers of giant planets consisting of a uniform elastic solid core and a non-uniform fluid envelope. We show that if the envelope obeys the $n = 1$ polytropic equation of state ($P \propto \rho^2$), simple analytical expressions for the tidal Love numbers can be obtained [see Eqs. (6.23)-(6.26)]. These expressions are valid for any core size, density, and shear modulus. They allow us to compute the tidal dissipation rate in the viscoelastic core of a planet by using a complex shear modulus that characterizes the rheology of the solid core. Our results improve upon previous works that are based on planetary models with a solid core and a uniform ($n = 0$) envelope. In general, we find that while for diffuse (low density, larger size) cores, the dissipation rates of the $n = 0$ envelope models can be higher than the $n = 1$ models, for more compact cores the $n = 1$ envelope models have higher dissipation rates by as much as a factor of few.

While we have focused on analytical expressions for the Love numbers in this paper, our method and equations can be adapted for numerical computation of the real (non-dissipative) Love numbers for any envelope equation of state. In particular, they can be used to study tidal distortion of super-earths, which typically contain a H-He envelope (a few percent by mass) surrounding a rocky core (Lissauer et al., 2014), or tidal distortion in gas giants with more realistic equations of state. It is possible that for some exoplanetary systems, particularly those containing hot Jupiters, the tidal Love number k_2 can be constrained or measured using secular planet-planet interactions (Becker and Batygin, 2013; Mardling, 2010). This would provide a useful probe of the interior structure of the planet.

In the presence of viscosity in the solid core, additional work is still needed to obtain the tidal viscoelastic dissipation rate even when numerical results for the real Love numbers are available. Thus, our analytical expressions will be useful, as they allow for simple computation of the tidal dissipation rate via the correspondence principle, and can serve as a calibration of numerical results.

6.7 Acknowledgments

This work has been supported in part by NSF grant AST-1211061, and NASA grants NNX14AG94G and NNX14AP31G.

CHAPTER 7

CONCLUSION

The purpose of this thesis work has been to consider two separate topics that may have relevance to the theoretical puzzles hot Jupiter (HJ) formation presents: the generation of spin-orbit misalignment via the Lidov-Kozai mechanism, and tidal dissipation in the cores of proto-HJs.

In chapter 2, first published in *Science* in 2014 (Storch et al., 2014), we demonstrated that coupling between the stellar spin vector and the proto-HJ orbital angular momentum vector during Lidov-Kozai cycles results in a rich variety of dynamical behaviors for the stellar spin axis orientation. We showed that, under certain conditions, the stellar spin axis may tumble chaotically, and that the final, potentially observable, distributions of HJ spin-orbit misalignments should be a function of the planet mass. Because the stellar spin precession rate depends on both the planet mass and on the spin rate of the star, we have also suggested that different stellar spin rates and spindown histories should also affect the final distribution of misalignments.

In chapter 3, first published in *MNRAS* in 2015 (Storch and Lai, 2015b), we further explored the stellar spin-orbit dynamics by considering an idealized Lidov-Kozai system, unaffected by short-range forces and tidal dissipation. We showed that much of the chaotic behavior discussed in the previous chapter can be explained via the Chirikov criterion of resonance overlap (Chirikov, 1979). We showed that a resonance occurs in the system whenever the averaged stellar spin precession rate is equal to an integer multiple of the Lidov-Kozai rate, and we discussed in detail the various features and interactions of these resonances. Finally, we suggested that a novel mechanism termed “adiabatic advec-

tion” could be another, previously unexplored, mode of generating spin-orbit misalignment during Lidov-Kozai cycles.

In chapter 4, based on work that is in preparation for submission to *MNRAS*, we relaxed the idealized assumptions made in the previous chapter by considering both the effects of short-range forces and tidal dissipation. We discussed four non-trivial regimes of outcomes for the stellar spin-orbit misalignment distributions, and identified two parameters that determine these outcomes. We showed that “adiabatic advection”, introduced in the previous chapter, is, indeed, one of these outcomes. Based on our work, under the simplifying assumption that the stellar quadrupole does not induce precession in the planet’s orbit, given a system with a set of initial orbital parameters, a planet mass, and a stellar spin rate, it is possible to predict whether the system will be able to achieve large spin-orbit misalignment.

In chapter 5, first published in *MNRAS* in 2014 (Storch and Lai, 2014) we addressed the existing issues surrounding tidal dissipation in the interiors of giant planets, and hot Jupiters in particular, by considering the effects of tidal dissipation in the (hypothetical) solid cores of these planets. By assuming a simplified model of a two-layer planet with a solid core and a uniform fluid envelope, we showed that, for certain core viscosities and shear moduli, it is possible to construct tidal dissipation models that reconcile all existing constraints on tidal dissipation in giant planets.

In chapter 6, first published in *MNRAS* in 2015 (Storch and Lai, 2015a), we extended the analysis of chapter 5 to models of giant planets with a solid core and a polytropic $n = 1$, rather than uniform, envelope. This model is more appropriate for the description of giant planets, as it correctly reproduces the fact

that their radii are nearly independent of their masses. Using this model, we provided simple semi-analytical formulae for the tidal dissipation as a function core viscosity, size, and modulus, thus facilitating potential future use in simulations of high-eccentricity migration of HJs and other potential applications.

In spite of the wealth of HJ formation theories that have been developed, HJs remain largely enigmatic, with no definitive answers reached. The next few years promise to be an exciting time for HJ research, however, as more and more HJs are discovered and characterized via radial velocity surveys. Slowly but steadily, soon our knowledge of HJs will begin to reach critical mass, and we will begin to be able to discriminate between different formation theories. Exciting times are coming, and that's something to look forward to.

BIBLIOGRAPHY

- Albrecht, S., S. Reffert, I. A. G. Snellen, and J. N. Winn. 2009. Misaligned spin and orbital axes cause the anomalous precession of DI Herculis. *Nature* 461:373–376.
- Albrecht, S., J. N. Winn, J. A. Johnson, A. W. Howard, G. W. Marcy, R. P. Butler, P. Arriagada, J. D. Crane, S. A. Shectman, I. B. Thompson, T. Hirano, G. Bakos, and J. D. Hartman. 2012. Obliquities of Hot Jupiter Host Stars: Evidence for Tidal Interactions and Primordial Misalignments. *ApJ* 757:18.
- Albrecht, S., J. N. Winn, G. Torres, D. C. Fabrycky, J. Setiawan, M. Gillon, E. Jehin, A. Triaud, D. Queloz, I. Snellen, and P. Eggleton. 2014. The BANANA Project. V. Misaligned and Precessing Stellar Rotation Axes in CV Velorum. *ApJ* 785:83.
- Alexander, M. E. 1973. The Weak Friction Approximation and Tidal Evolution in Close Binary Systems. *Ap&SS* 23:459–510.
- Anderson, K. R., N. I. Storch, and D. Lai. 2015. Formation of Misaligned Hot Jupiters due to Lidov-Kozai Oscillations in Stellar Binaries. *in prep*.
- Arras, P., and A. Socrates. 2010. Thermal Tides in Fluid Extrasolar Planets. *ApJ* 714:1–12.
- Baraffe, I., G. Chabrier, and T. Barman. 2010. The physical properties of extrasolar planets. *Reports on Progress in Physics* 73:016901.
- Bate, M. R., G. Lodato, and J. E. Pringle. 2010. Chaotic star formation and the alignment of stellar rotation with disc and planetary orbital axes. *MNRAS* 401:1505–1513.

- Batygin, K. 2012. A primordial origin for misalignments between stellar spin axes and planetary orbits. *Nature* 491:418–420.
- Batygin, K., and F. C. Adams. 2013. Magnetic and Gravitational Disk-Star Interactions: An Interdependence of PMS Stellar Rotation Rates and Spin-Orbit Misalignments. *ApJ* 778:169.
- Batygin, K., and D. J. Stevenson. 2010. Inflating Hot Jupiters with Ohmic Dissipation. *ApJ* 714:L238–L243.
- Batygin, K., D. J. Stevenson, and P. H. Bodenheimer. 2011. Evolution of Ohmically Heated Hot Jupiters. *ApJ* 738:1.
- Becker, J. C., and K. Batygin. 2013. Dynamical Measurements of the Interior Structure of Exoplanets. *ApJ* 778:100.
- Biot, M. A. 1954. Theory of Stress-Strain Relations in Anisotropic Viscoelasticity and Relaxation Phenomena. *Journal of Applied Physics* 25:1385–1391.
- Bodenheimer, P., D. N. C. Lin, and R. A. Mardling. 2001. On the Tidal Inflation of Short-Period Extrasolar Planets. *ApJ* 548:466–472.
- Bodenheimer, P., G. Laughlin, and D. N. C. Lin. 2003. On the Radii of Extrasolar Giant Planets. *ApJ* 592:555–563.
- Burrows, A., I. Hubeny, J. Budaj, and W. B. Hubbard. 2007. Possible Solutions to the Radius Anomalies of Transiting Giant Planets. *ApJ* 661:502–514.
- Chabrier, G., and I. Baraffe. 2007. Heat Transport in Giant (Exo)planets: A New Perspective. *ApJ* 661:L81–L84.
- Chatterjee, S., E. B. Ford, S. Matsumura, and F. A. Rasio. 2008. Dynamical Outcomes of Planet-Planet Scattering. *ApJ* 686:580–602.

- Chirikov, B. V. 1979. A universal instability of many-dimensional oscillator systems. *Phys. Rep.* 52:263–379.
- Claret, A., and A. Gimenez. 1992. Evolutionary stellar models using Rogers and Iglesias opacities, with particular attention to internal structure constants. *A&AS* 96:255–268.
- Colombo, G. 1966. Cassini’s second and third laws. *AJ* 71:891.
- Correia, A. C. M., J. Laskar, F. Farago, and G. Boué. 2011. Tidal evolution of hierarchical and inclined systems. *Celestial Mechanics and Dynamical Astronomy* 111:105–130.
- Dawson, R. I., and R. A. Murray-Clay. 2013. Giant Planets Orbiting Metal-rich Stars Show Signatures of Planet-Planet Interactions. *ApJ* 767:L24.
- Dermott, S. F. 1979. Tidal dissipation in the solid cores of the major planets. *Icarus* 37:310–321.
- Dong, S., B. Katz, and A. Socrates. 2014. Warm Jupiters Need Close “Friends” for High-eccentricity Migration – a Stringent Upper Limit on the Perturber’s Separation. *ApJ* 781:L5.
- Efroimsky, M., and V. V. Makarov. 2013. Tidal Friction and Tidal Lagging. Applicability Limitations of a Popular Formula for the Tidal Torque. *ApJ* 764:26.
- Eggleton, P. P., and L. Kiseleva-Eggleton. 2001. Orbital Evolution in Binary and Triple Stars, with an Application to SS Lacertae. *ApJ* 562:1012–1030.
- Eggleton, P. P., L. G. Kiseleva, and P. Hut. 1998. The Equilibrium Tide Model for Tidal Friction. *ApJ* 499:853–870.

- Fabrycky, D., and S. Tremaine. 2007. Shrinking Binary and Planetary Orbits by Kozai Cycles with Tidal Friction. *ApJ* 669:1298–1315.
- Fabrycky, D. C., E. T. Johnson, and J. Goodman. 2007. Cassini States with Dissipation: Why Obliquity Tides Cannot Inflate Hot Jupiters. *ApJ* 665:754–766.
- Ford, E. B., and F. A. Rasio. 2008. Origins of Eccentric Extrasolar Planets: Testing the Planet-Planet Scattering Model. *ApJ* 686:621–636.
- Ford, E. B., B. Kozinsky, and F. A. Rasio. 2000. Secular Evolution of Hierarchical Triple Star Systems. *ApJ* 535:385–401.
- Fortney, J. J., and N. Nettelmann. 2010. The Interior Structure, Composition, and Evolution of Giant Planets. *Space Sci. Rev.* 152:423–447.
- Gallet, F., and J. Bouvier. 2013. Improved angular momentum evolution model for solar-like stars. *A&A* 556:A36.
- Gavrillov, S. V., and V. N. Zharkov. 1977. Love numbers of the giant planets. *Icarus* 32:443–449.
- Goldreich, P., and P. D. Nicholson. 1977. Turbulent viscosity and Jupiter's tidal Q. *Icarus* 30:301–304.
- Goldreich, P., and S. Soter. 1966. Q in the Solar System. *Icarus* 5:375–389.
- Goldreich, P., and S. Tremaine. 1980. Disk-satellite interactions. *ApJ* 241:425–441.
- Goldsby, D. L., and D. L. Kohlstedt. 2001. Superplastic deformation of ice: Experimental observations. *J. Geophys. Res.* 106:11017.
- Goodman, J., and C. Lackner. 2009. Dynamical Tides in Rotating Planets and Stars. *ApJ* 696:2054–2067.

- Greff-Lefftz, M., L. Métivier, and H. Legros. 2005. Analytical Solutions of Love Numbers for a Hydrostatic Ellipsoidal Incompressible Homogeneous Earth. *Celestial Mechanics and Dynamical Astronomy* 93:113–146.
- Guillot, T. 2005. THE INTERIORS OF GIANT PLANETS: Models and Outstanding Questions. *Annual Review of Earth and Planetary Sciences* 33:493–530.
- Hansen, B. M. S. 2012. Calibration of Equilibrium Tide Theory for Extrasolar Planet Systems. II. *ApJ* 757:6.
- Hébrard, G., F. Bouchy, F. Pont, B. Loeillet, M. Rabus, X. Bonfils, C. Moutou, I. Boisse, X. Delfosse, M. Desort, A. Eggenberger, D. Ehrenreich, T. Forveille, A.-M. Lagrange, C. Lovis, M. Mayor, F. Pepe, C. Perrier, D. Queloz, N. C. Santos, D. Ségransan, S. Udry, and A. Vidal-Madjar. 2008. Misaligned spin-orbit in the XO-3 planetary system? *A&A* 488:763–770.
- Hébrard, G., J.-M. Désert, R. F. Díaz, I. Boisse, F. Bouchy, A. Lecavelier Des Etangs, C. Moutou, D. Ehrenreich, L. Arnold, X. Bonfils, X. Delfosse, M. Desort, A. Eggenberger, T. Forveille, J. Gregorio, A.-M. Lagrange, C. Lovis, F. Pepe, C. Perrier, F. Pont, D. Queloz, A. Santerne, N. C. Santos, D. Ségransan, D. K. Sing, S. Udry, and A. Vidal-Madjar. 2010. Observation of the full 12-hour-long transit of the exoplanet HD 80606b. Warm-Spitzer photometry and SOPHIE spectroscopy. *A&A* 516:A95.
- Henning, W. G., R. J. O’Connell, and D. D. Sasselov. 2009. Tidally Heated Terrestrial Exoplanets: Viscoelastic Response Models. *ApJ* 707:1000–1015.
- Henrard, J., and C. Murigande. 1987. Colombo’s top. *Celestial Mechanics* 40:345–366.

- Holman, M., J. Touma, and S. Tremaine. 1997. Chaotic variations in the eccentricity of the planet orbiting 16 Cygni B. *Nature* 386:254–256.
- Huang, X., and A. Cumming. 2012. Ohmic Dissipation in the Interiors of Hot Jupiters. *ApJ* 757:47.
- Hut, P. 1981. Tidal evolution in close binary systems. *A&A* 99:126–140.
- Ibgui, L., A. Burrows, and D. S. Spiegel. 2010. Tidal Heating Models for the Radii of the Inflated Transiting Giant Planets WASP-4b, WASP-6b, WASP-12b, WASP-15b, and TrES-4. *ApJ* 713:751–763.
- Ioannou, P. J., and R. S. Lindzen. 1993a. Gravitational tides in the outer planets. I - Implications of classical tidal theory. II - Interior calculations and estimation of the tidal dissipation factor. *ApJ* 406:252–278.
- . 1993b. Gravitational Tides in the Outer Planets. II. Interior Calculations and Estimation of the Tidal Dissipation Factor. *ApJ* 406:266.
- Ivanov, P. B., and J. C. B. Papaloizou. 2007. Dynamic tides in rotating objects: orbital circularization of extrasolar planets for realistic planet models. *MNRAS* 376:682–704.
- Jeanloz, R. 1990. The nature of the earth's core. *Annual Review of Earth and Planetary Sciences* 18:357–386.
- Jurić, M., and S. Tremaine. 2008. Dynamical Origin of Extrasolar Planet Eccentricity Distribution. *ApJ* 686:603–620.
- Katz, B., S. Dong, and R. Malhotra. 2011. Long-Term Cycling of Kozai-Lidov Cycles: Extreme Eccentricities and Inclinations Excited by a Distant Eccentric Perturber. *Physical Review Letters* 107:181101.

- Kinoshita, H. 1993. Motion of the orbital plane of a satellite due to a secular change of the obliquity of its mother planet. *Celestial Mechanics and Dynamical Astronomy* 57:359–368.
- Kinoshita, H., and H. Nakai. 1999. Analytical Solution of the Kozai Resonance and its Application. *Celestial Mechanics and Dynamical Astronomy* 75:125–147.
- Knutson, H. A., B. J. Fulton, B. T. Montet, M. Kao, H. Ngo, A. W. Howard, J. R. Crepp, S. Hinkley, G. Á. Bakos, K. Batygin, J. A. Johnson, T. D. Morton, and P. S. Muirhead. 2014. Friends of Hot Jupiters. I. A Radial Velocity Search for Massive, Long-period Companions to Close-in Gas Giant Planets. *ApJ* 785:126.
- Kozai, Y. 1962. Secular perturbations of asteroids with high inclination and eccentricity. *AJ* 67:591.
- Lai, D. 2012. Tidal dissipation in planet-hosting stars: damping of spin-orbit misalignment and survival of hot Jupiters. *MNRAS* 423:486–492.
- . 2014. Star-disc-binary interactions in protoplanetary disc systems and primordial spin-orbit misalignments. *MNRAS* 440:3532–3544.
- Lai, D., F. Foucart, and D. N. C. Lin. 2011. Evolution of spin direction of accreting magnetic protostars and spin-orbit misalignment in exoplanetary systems. *MNRAS* 412:2790–2798.
- Lainey, V., J.-E. Arlot, Ö. Karatekin, and T. van Hoolst. 2009. Strong tidal dissipation in Io and Jupiter from astrometric observations. *Nature* 459:957–959.
- Lainey, V., Ö. Karatekin, J. Desmars, S. Charnoz, J.-E. Arlot, N. Emelyanov, C. Le Poncin-Lafitte, S. Mathis, F. Remus, G. Tobie, and J.-P. Zahn. 2012. Strong

- Tidal Dissipation in Saturn and Constraints on Enceladus' Thermal State from Astrometry. *ApJ* 752:14.
- Laskar, J., and P. Robutel. 1993. The chaotic obliquity of the planets. *Nature* 361:608–612.
- Leconte, J., and G. Chabrier. 2012. A new vision of giant planet interiors: Impact of double diffusive convection. *A&A* 540:A20.
- Leconte, J., G. Chabrier, I. Baraffe, and B. Levrard. 2010. Is tidal heating sufficient to explain bloated exoplanets? Consistent calculations accounting for finite initial eccentricity. *A&A* 516:A64.
- Li, G., and K. Batygin. 2014. On the Spin-axis Dynamics of a Moonless Earth. *ApJ* 790:69.
- Li, G., S. Naoz, M. Holman, and A. Loeb. 2014. Chaos in the Test Particle Eccentric Kozai-Lidov Mechanism. *ApJ* 791:86.
- Lichtenberg, A. J., and M. A. Lieberman. 1992. *Regular and Chaotic Dynamics*. Springer, New York, NY.
- Lidov, M. L. 1962. The evolution of orbits of artificial satellites of planets under the action of gravitational perturbations of external bodies. *Planet. Space Sci.* 9:719–759.
- Lin, D. N. C., P. Bodenheimer, and D. C. Richardson. 1996. Orbital migration of the planetary companion of 51 Pegasi to its present location. *Nature* 380:606–607.
- Lissauer, J. J., D. Jontof-Hutter, J. F. Rowe, D. C. Fabrycky, E. D. Lopez, E. Agol, G. W. Marcy, K. M. Deck, D. A. Fischer, J. J. Fortney, S. B. Howell, H. Isaacson,

- J. M. Jenkins, R. Kolbl, D. Sasselov, D. R. Short, and W. F. Welsh. 2013. All Six Planets Known to Orbit Kepler-11 Have Low Densities. *ApJ* 770:131.
- Lissauer, J. J., R. I. Dawson, and S. Tremaine. 2014. Advances in exoplanet science from Kepler. *Nature* 513:336–344.
- Lithwick, Y., and Y. Wu. 2014. Secular chaos and its application to Mercury, hot Jupiters, and the organization of planetary systems. *Proceedings of the National Academy of Science* 111:12610–12615.
- Liu, B., D. J. Muñoz, and D. Lai. 2015. Suppression of extreme orbital evolution in triple systems with short-range forces. *MNRAS* 447:747–764.
- Love, A. E. H. 1911. Some Problems of Geodynamics. Dover, NY.
- . 1927. A Treatise on the Mathematical Theory of Elasticity. Dover, NY.
- Lubow, S. H., C. A. Tout, and M. Livio. 1997. Resonant Tides in Close Orbiting Planets. *ApJ* 484:866–870.
- Makarov, V. V., and M. Efroimsky. 2013. No Pseudosynchronous Rotation for Terrestrial Planets and Moons. *ApJ* 764:27.
- Mardling, R. A. 2010. The determination of planetary structure in tidally relaxed inclined systems. *MNRAS* 407:1048–1069.
- Mathis, S., and C. Le Poncin-Lafitte. 2009. Tidal dynamics of extended bodies in planetary systems and multiple stars. *A&A* 497:889–910.
- Matsumura, S., S. J. Peale, and F. A. Rasio. 2010. Tidal Evolution of Close-in Planets. *ApJ* 725:1995–2016.
- Menou, K. 2012. Magnetic Scaling Laws for the Atmospheres of Hot Giant Exoplanets. *ApJ* 745:138.

- Militzer, B., W. B. Hubbard, J. Vorberger, I. Tamblyn, and S. A. Bonev. 2008. A Massive Core in Jupiter Predicted from First-Principles Simulations. *ApJ* 688:L45–L48.
- Miller, N., J. J. Fortney, and B. Jackson. 2009. Inflating and Deflating Hot Jupiters: Coupled Tidal and Thermal Evolution of Known Transiting Planets. *ApJ* 702:1413–1427.
- Mitrovica, J. X., and A. M. Forte. 2004. A new inference of mantle viscosity based upon joint inversion of convection and glacial isostatic adjustment data. *Earth and Planetary Science Letters* 225:177–189.
- Montagner, J.-P., and B. L. N. Kennett. 1996. How to reconcile body-wave and normal-mode reference earth models. *Geophysical Journal International* 125:229–248.
- Murray, C. D., and S. F. Dermott. 2000. *Solar System Dynamics*. Cambridge U. Press, Cambridge, MA.
- Nagasawa, M., S. Ida, and T. Bessho. 2008. Formation of Hot Planets by a Combination of Planet Scattering, Tidal Circularization, and the Kozai Mechanism. *ApJ* 678:498–508.
- Naoz, S., W. M. Farr, Y. Lithwick, F. A. Rasio, and J. Teyssandier. 2011. Hot Jupiters from secular planet-planet interactions. *Nature* 473:187–189.
- Naoz, S., W. M. Farr, and F. A. Rasio. 2012. On the Formation of Hot Jupiters in Stellar Binaries. *ApJ* 754:L36.
- Naoz, S., W. M. Farr, Y. Lithwick, F. A. Rasio, and J. Teyssandier. 2013. Secular dynamics in hierarchical three-body systems. *MNRAS* 431:2155–2171.

- Narita, N., B. Sato, T. Hirano, and M. Tamura. 2009. First Evidence of a Retrograde Orbit of a Transiting Exoplanet HAT-P-7b. *PASJ* 61:L35–L40.
- Ogilvie, G. I. 2009. Tidal dissipation in rotating fluid bodies: a simplified model. *MNRAS* 396:794–806.
- . 2013. Tides in rotating barotropic fluid bodies: the contribution of inertial waves and the role of internal structure. *MNRAS* 429:613–632.
- . 2014. Tidal Dissipation in Stars and Giant Planets. *ARA&A* 52:171–210.
- Ogilvie, G. I., and D. N. C. Lin. 2004. Tidal Dissipation in Rotating Giant Planets. *ApJ* 610:477–509.
- Papaloizou, J. C. B., and P. B. Ivanov. 2010. Dynamic tides in rotating objects: a numerical investigation of inertial waves in fully convective or barotropic stars and planets. *MNRAS* 407:1631–1656.
- Paxton, B., L. Bildsten, A. Dotter, F. Herwig, P. Lesaffre, and F. Timmes. 2011. Modules for Experiments in Stellar Astrophysics (MESA). *ApJS* 192:3.
- Paxton, B., M. Cantiello, P. Arras, L. Bildsten, E. F. Brown, A. Dotter, C. Mankovich, M. H. Montgomery, D. Stello, F. X. Timmes, and R. Townsend. 2013. Modules for Experiments in Stellar Astrophysics (MESA): Planets, Oscillations, Rotation, and Massive Stars. *ApJS* 208:4.
- Peale, S. J. 1999. Origin and Evolution of the Natural Satellites. *ARA&A* 37:533–602.
- Perna, R., K. Menou, and E. Rauscher. 2010. Ohmic Dissipation in the Atmospheres of Hot Jupiters. *ApJ* 724:313–317.

- Petrovich, C. 2015a. Hot Jupiters from Coplanar High-eccentricity Migration. *ApJ* 805:75.
- . 2015b. Steady-state Planet Migration by the Kozai-Lidov Mechanism in Stellar Binaries. *ApJ* 799:27.
- Poirier, J. P., C. Sotin, and J. Peyronneau. 1981. Viscosity of high-pressure ice VI and evolution and dynamics of Ganymede. *Nature* 292:225–227.
- Rasio, F. A., and E. B. Ford. 1996. Dynamical instabilities and the formation of extrasolar planetary systems. *Science* 274:954–956.
- Rauscher, E., and K. Menou. 2013. Three-dimensional Atmospheric Circulation Models of HD 189733b and HD 209458b with Consistent Magnetic Drag and Ohmic Dissipation. *ApJ* 764:103.
- Remus, F., S. Mathis, and J.-P. Zahn. 2012a. The equilibrium tide in stars and giant planets. I. The coplanar case. *A&A* 544:A132.
- Remus, F., S. Mathis, J.-P. Zahn, and V. Lainey. 2012b. Anelastic tidal dissipation in multi-layer planets. *A&A* 541:A165.
- . 2015. The surface signature of the tidal dissipation of the core in a two-layer planet. *A&A* 573:A23.
- Sinclair, A. T. 1983. A re-consideration of the evolution hypothesis of the origin of the resonances among Saturn's satellites. In V. V. Markellos, and Y. Kozai, eds., IAU Colloq. 74: Dynamical Trapping and Evolution in the Solar System, volume 106 of *Astrophysics and Space Science Library*, pages 19–25.
- Skumanich, A. 1972. Time Scales for CA II Emission Decay, Rotational Braking, and Lithium Depletion. *ApJ* 171:565. doi:10.1086/151310.

- Socrates, A. 2013. Relationship Between Thermal Tides and Radius Excess. ArXiv e-prints .
- Socrates, A., B. Katz, and S. Dong. 2012a. Q in Other Solar Systems. ArXiv e-prints .
- Socrates, A., B. Katz, S. Dong, and S. Tremaine. 2012b. Super-eccentric Migrating Jupiters. ApJ 750:106.
- Spalding, C., and K. Batygin. 2014. Early Excitation of Spin-Orbit Misalignments in Close-in Planetary Systems. ApJ 790:42.
- Spiegel, D. S., and A. Burrows. 2013. Thermal Processes Governing Hot-Jupiter Radii. ApJ 772:76.
- Storch, N. I., and D. Lai. 2014. Viscoelastic tidal dissipation in giant planets and formation of hot Jupiters through high-eccentricity migration. MNRAS 438:1526–1534.
- . 2015a. Analytical model of tidal distortion and dissipation for a giant planet with a viscoelastic core. MNRAS 450:3952–3957.
- . 2015b. Chaotic dynamics of stellar spin driven by planets undergoing Lidov-Kozai oscillations: resonances and origin of chaos (SL15). MNRAS 448:1821–1834.
- Storch, N. I., K. R. Anderson, and D. Lai. 2014. Chaotic dynamics of stellar spin in binaries and the production of misaligned hot Jupiters (SAL). Science 345:1317–1321.
- Storch, N. I., D. Lai, and K. R. Anderson. 2015. Dynamics of Stellar Spin Driven

by Planets Undergoing Lidov-Kozai Oscillations: Paths to Misalignment. in prep .

Strogatz, S. H. 1994. Nonlinear Dynamics and Chaos: With Applications to Physics, Biology, Chemistry, and Engineering. Perseus Books, Reading, MA.

Touma, J., and J. Wisdom. 1993. The chaotic obliquity of Mars. *Science* 259:1294–1297.

Triaud, A. H. M. J., A. Collier Cameron, D. Queloz, D. R. Anderson, M. Gillon, L. Hebb, C. Hellier, B. Loeillet, P. F. L. Maxted, M. Mayor, F. Pepe, D. Pollacco, D. Ségransan, B. Smalley, S. Udry, R. G. West, and P. J. Wheatley. 2010. Spin-orbit angle measurements for six southern transiting planets. New insights into the dynamical origins of hot Jupiters. *A&A* 524:A25.

Triaud, A. H. M. J., L. Hebb, D. R. Anderson, P. Cargile, A. Collier Cameron, A. P. Doyle, F. Faedi, M. Gillon, Y. Gomez Maqueo Chew, C. Hellier, E. Jehin, P. Maxted, D. Naef, F. Pepe, D. Pollacco, D. Queloz, D. Ségransan, B. Smalley, K. Stassun, S. Udry, and R. G. West. 2013. The EBLM project. I. Physical and orbital parameters, including spin-orbit angles, of two low-mass eclipsing binaries on opposite sides of the brown dwarf limit. *A&A* 549:A18.

Tsang, D., N. J. Turner, and A. Cumming. 2014. Shedding Light on the Eccentricity Valley: Gap Heating and Eccentricity Excitation of Giant Planets in Protoplanetary Disks. *ApJ* 782:113.

Turcotte, D. L., and G. Schubert. 2002. Geodynamics. Cambridge U. Press, Cambridge, MA.

Udry, S., and N. C. Santos. 2007. Statistical Properties of Exoplanets. *ARA&A* 45:397–439.

- Weidenschilling, S. J., and F. Marzari. 1996. Gravitational scattering as a possible origin for giant planets at small stellar distances. *Nature* 384:619–621.
- Winn, J. N., J. A. Johnson, S. Albrecht, A. W. Howard, G. W. Marcy, I. J. Crossfield, and M. J. Holman. 2009. HAT-P-7: A Retrograde or Polar Orbit, and a Third Body. *ApJ* 703:L99–L103.
- Wisdom, J., S. J. Peale, and F. Mignard. 1984. The chaotic rotation of Hyperion. *Icarus* 58:137–152.
- Wu, Y. 2005. Origin of Tidal Dissipation in Jupiter. II. The Value of Q. *ApJ* 635:688–710.
- Wu, Y., and Y. Lithwick. 2011. Secular Chaos and the Production of Hot Jupiters. *ApJ* 735:109.
- . 2013. Ohmic Heating Suspends, Not Reverses, the Cooling Contraction of Hot Jupiters. *ApJ* 763:13.
- Wu, Y., and N. Murray. 2003. Planet Migration and Binary Companions: The Case of HD 80606b. *ApJ* 589:605–614.
- Wu, Y., N. W. Murray, and J. M. Ramsahai. 2007. Hot Jupiters in Binary Star Systems. *ApJ* 670:820–825.
- Yoder, C. F., and S. J. Peale. 1981. The tides of Io. *Icarus* 47:1–35.
- Zhou, J.-L., D. N. C. Lin, and Y.-S. Sun. 2007. Post-oligarchic Evolution of Proto-planetary Embryos and the Stability of Planetary Systems. *ApJ* 666:423–435.